TWO-BODY PHOTODISINTEGRATION OF THE DEUTERON AT INCIDENT PHOTON ENERGIES OF 0.8 - 4.0 GEV

BY

CHRISTOPHER WALDEMAR BOCHNA

B.S., Carnegie-Mellon University, 1992
M.S., University of Illinois at Urbana-Champaign, 1993

THESIS

Submitted in partial fulfillment of the requirements
for the degree of Doctor of Philosophy in Physics
in the Graduate College of the
University of Illinois at Urbana-Champaign, 1999

Urbana, Illinois

TWO-BODY PHOTODISINTEGRATION OF THE DEUTERON
AT INCIDENT PHOTON ENERGIES OF 0.8 - 4.0 GEV

Christopher Waldemar Bochna, Ph.D.
Department of Physics
University of Illinois at Urbana-Champaign, 1999
Douglas H. Beck, Advisor

The differential cross section for two-body deuteron photodisintegration was measured during experiment E89-012 which took place at the Continuous Electron Beam Accelerator Facility in the Spring of 1996. The newly commissioned High Momentum Spectrometer was used to detect the recoil proton of the photodisintegration reaction at center of mass angles 36°, 52°, 69°, and 89° with incident photon energies 0.8, 1.6, 2.4, 3.2, and 4.0 GeV. Constituent counting rules predict that the invariant cross section should scale as s^{-11} at asymptotic energies. Previous data show evidence of this scaling starting at about $E_\gamma = 1.2 - 1.5$ GeV for $\theta_{cm} = 90°$. Results from this experiment show that asymptotic scaling is evident for $\theta_{cm} = 89°$ and 69°, but no evidence of asymptotic scaling is seen for $\theta_{cm} = 52°$ and 36°. Experimental results disagree with the prediction given by the reduced nuclear amplitude model. Comparisons of data to other theoretical predictions given by meson-exchange theories, asymptotic amplitudes, and quark-gluon string model are also shown.

Acknowledgments

As I near the end of my graduate education, some of my friends have already asked me the question: If I had the chance to start over, would I do it all again? Absolutely. These past few years have been an excellent opportunity for me to play a role in an important research project. It's been an honor to have worked alongside such an incredible team of scientists.

I would first like to thank my parents for all their support throughout my childhood and in my education. They taught me that anything is achievable through hard work and persistence. My parents spent the time and effort to rear me and to teach me the lessons that have carried me to this stage in my life; lessons that will continue to stay with me in the future. They gave me the freedom to explore opportunities in the world, so that I could decide on my own which roads to take. Only with their support and guidance have I been able to achieve this milestone in my life.

My advisor, Douglas Beck, has done a fantastic job of guiding me through the rigors of graduate school. I thank him for all the hard work he has put into furthering my education. He always made himself available for questions, and allowed me a great deal of independence in my experimental work and analysis; but also made sure that I didn't stray too far. Throughout the years, he has stressed the importance of academic integrity and professionalism—as I progressed along my career path from student to scientist.

I must give special thanks to Roy Holt for allowing me to analyze the data from his experiment, for use in my thesis. Roy taught me all I know about the deuteron, and much of what I know about nuclear physics in general. I only wish I could have retained more from the impromptu lessons he gave at his office whiteboard.

My undergraduate education at Carnegie Mellon University gave me a wonderful opportunity to meet and work with an excellent faculty. Hugh Young, Helmet Vogel, Robert Schumacher, Richard Edelstein, and Brian Quinn are just a few of the many wonderful professors who helped me build the basics of my education in physics. I must also thank Stephen Garoff for being my undergraduate advisor while I was a student there. He always had a cheerful attitude, and donated his time to help provide me with insight into the decisions I had to make for my future.

At the University of Illinois, I learned about the degree of hard work that is necessary to excel in physics. I was overwhelmed initially, but with the help of my friends I managed to get back to speed and kept on learning. I would like to specifically thank Nathan Yanasak who always had an unusual view of what goes on in life. He helped me to gain the confidence to explore some different avenues that I probably would not have tried otherwise.

This thesis is about the experiment that took place at what is now the Thomas Jefferson National Accelerator Facility. I am grateful for the staff of the lab who put together a first-class accelerator. At this facility, I had the unique opportunity both to perform research at a large-scale electron accelerator and to assist with the commissioning of the spectrometers in Hall C. I became part of a team of incredibly hard-working physicists and graduate students. I only wish I could have matched the effort they put into understanding the results. Dave Mack, Rolf Ent, Joe Mitchell, Thia Keppel, Steve Wood, Paul Gueye, Bill Vulcan, Hamlet Mkrtchyan, Ketevi Assamagan, Jim Dunne, and Keith Baker are just a few of the people who each showed me something new to learn about the experimental part of physics. Their insights helped me to understand at some minor level the methodology and philosophy behind experimental physics.

My fellow graduate students at the facility were a great resource of knowledge and experience. They put in an extreme amount of work into getting Hall C ready for experimental use. I'm sure I've forgotten a great number of people who deserve

mention here, but I'll try my best to name them. To John Arrington, Derek van Westrum, Dipangkar Dutta, Gabriel Niculescu, Chris Armstrong, Chris Cothran, and Ken Gustafson–thank you for your help during my experiment.

While I spent much time at what was then CEBAF, I also spent a large amount of my free time with Joe Grames. Joe is a great friend of mine, from way back in high school. At CEBAF, he was a fellow graduate student. We enjoyed quite a few beers while de-stressing, talking about the past, present and future. Joe has always amazed me with his energy. Somehow, he has always shown an interest and has participated in virtually every aspect of projects at the accelerator. I learned quite a few interesting details about the accelerator from him, thanks to his non-stop efforts to know all the nuances of the accelerator design.

Two graduate students who deserve particular praise are Bart Terburg and Dave Meekins–the other two students who obtained a PhD using data from this experiment. Dave Meekins seemed to know absolutely everything about every instrument in Hall C and in the counting house. Whenever I needed an answer about how something worked, or if something ever needed fixing, Meekins had the solution. Bart helped to build an excellent target for the experiment, and his help was invaluable in during the data analysis. I would probably still be beating my head against the monitor in frustration if he hadn't been around to help me.

Mike Miller and Haiyan Gao, the post-docs for this experiment, were a great help to me during the experiment and later with the data analysis. I also thank Eric Belz for his advice and help as a veteran of deuteron photodisintegration.

I am deeply indebted to Penny Sigler and Gaylon Reeves, the office staff at the Nuclear Physics Laboratory here at the university. Thanks to their expertise, they helped make many arrangements during my stay here. They made sure that all the necessary forms were signed and processed everything expeditiously. They looked out for me well beyond the call of duty, especially during times when I was completely oblivious to university procedures.

Bart Terburg, Tony Forest, and Nevin Simicevic graciously made themselves avail-

able for the informal seminars we held every Friday evening. There were always many interesting discussions revolving around a few drinks, and I thank them for the opportunity to hear their personal views on a number of topics.

I feel I must also mention a group of people that might seem unusual for a document like this. I would like to thank the staff and workers of The Raptor Trust. The director, Leonard Soucy, has had more of an impact on the development of my career than any might suspect. I spent two summers as a part-time volunteer there, where I assisted in rehabilitating and caring for injured and orphaned birds. I gained a lot of experience in helping out there, and took part in owl and hawk banding projects that are important for understanding the population dynamics of different species. Most importantly, I was able to help a few birds out there have a second chance at a natural life in the wild.

Finally, I'd like to thank some of my friends from around town and out of town. They did their best to deal with all of my bitching when work got tough. They also helped me to take my mind off of work so I could just relax. I thank my friends in town, especially James Miles, Paul Defenbaugh, and Tom Rogers. I want to thank Bowen Goletz, for flying over every so often from Purdue thanks to his pilot's license. I hope he enjoys the hundred-dollar burgers he gets to eat while he's here. I want to thank my friends over in Ohio, George Nemeyer, David Orth, Jeff Storey, and Mark Brown, whom I've travelled to see on many occasions when I just needed to get out of town for a while. I want to thank Michael O'Donnell for taking the time to look through this thesis, and for editing some of the more glaring grammatical errors within it. I wish I could have incorporated more of his suggestions. I want to thank some of my other long-distance friends who helped encourage me to finish my graduate education, including Cody Buchmann, Tony DeMatio, and Michael Merow.

This material is based on work supported by the National Science Foundation under grants NSF PHY 89-21146, NSF PHY 92-57057, NSF PHY 93-10871, and NSF PHY 94-20787.

Contents

Chapter 1 Introduction 1

Chapter 2 Theory 4

2.1 QCD and Nuclear Physics 4

2.1.1 QCD 5

2.1.2 Meson Exchange Theory 7

2.1.3 Summary of theoretical models for deuteron photodisintegration . 8

2.1.4 Why Deuteron Photodisintegration 9

2.2 Constituent Counting Rules 11

2.3 Reduced Nuclear Amplitudes 20

2.4 Quark-Gluon String Model 23

2.5 QCD Rescattering 26

2.6 Conventional Meson Theory 28

2.7 Asymptotic Amplitudes 33

Chapter 3 Experiment 37

3.1 General Overview of Apparatus 37

3.2 Electron Beam 38

3.3 Beam Charge Measurement 39

3.4 Fast Rastering System 39

3.5 Radiator 40

3.6 Target 41

3.7 High Momentum Spectrometer 42
3.7.1 Coordinate Systems 44
3.7.2 Collimator 44
3.7.3 Drift Chambers 47
3.7.4 Scintillator Hodoscopes 49
3.7.5 Cerenkov Detector 51
3.7.6 Lead Glass Calorimeter 52
3.8 Data Acquisition and Trigger 53
3.9 Run Plan 56

Chapter 4 Event Level Analysis 58
4.1 Analysis Software 58
4.2 Particle ID 59
4.2.1 Hodoscope Time of Flight 59
4.2.2 Gas Cerenkov Detector 66
4.2.3 Particle ID Analysis Cuts 69
4.3 Tracking 71
4.3.1 Tracking Algorithm 71
4.3.2 Tracking Efficiency 72
4.3.3 Drift chamber calibration 76
4.4 Event Reconstruction 77
4.4.1 Methods for event reconstruction 78
4.4.2 Choice for data analysis 82

Chapter 5 Measurement of the Cross Section 88
5.1 Measuring Cross Section from Experimental Quantities 88
5.1.1 Photodisintegration Yield 89
5.1.2 Cross Section 94
5.2 Monte Carlo 96

5.3 Background Sources . . . 98
5.3.1 Gate valve . . . 99
5.3.2 Pion production . . . 107
5.3.3 Background . . . 109
5.4 Other Cross Section Factors . . . 111
5.4.1 Solid Angle . . . 112
5.4.2 Total Charge . . . 115
5.4.3 Bremsstrahlung Photon Yield . . . 117
5.4.4 Target Density . . . 119
5.4.5 Proton Absorption . . . 126
5.4.6 Trigger Efficiency . . . 129
5.4.7 Dead Time Corrections . . . 129
5.5 Systematic Uncertainties . . . 131

Chapter 6 Experimental Results . . . 136
6.1 Kinematic Variables . . . 136
6.2 Results . . . 138
6.3 Comparison to Theoretical Models . . . 148
6.3.1 Constituent Counting Rules . . . 148
6.3.2 Reduced Nuclear Amplitudes . . . 149
6.3.3 Traditional Meson-exchange Theory . . . 151
6.3.4 Asymptotic Amplitudes . . . 152
6.3.5 Quark Gluon String Theory . . . 152
6.4 Changes from Published Data . . . 153
6.5 Summary . . . 154

Chapter 7 Conclusions . . . 156
7.1 Comments on Experiment Quality . . . 157
7.2 Future Considerations . . . 157

Appendix A Beam Current Monitors 158
A.1 Description and Location 158
A.2 Theory of Operation 159
A.2.1 Unser PCT 159
A.2.2 Resonant cavities 160
A.2.3 Support Electronics 163
A.3 Calibration 166
A.3.1 Absolute Calibration 167
A.3.2 Relative Calibration 167
A.4 Performance 168
A.4.1 Definitions 168
A.4.2 Unser 168
A.4.3 Power Meter 171
A.4.4 Mixer/rms-dc converter 180
A.4.5 Preamplifiers 180
A.4.6 Voltage-Frequency Converters 181
A.4.7 Temperature Stability System 182

Appendix B Derivation of Kinematic Quantities 183
B.1 Center of Mass Quantities 185
B.2 Center-of-Mass Frame Velocity 187
B.3 Jacobian $\frac{d\Omega_{cm}}{dt}$ 187
B.4 Jacobian $\frac{d\Omega}{d\Omega_{cm}}$ 188
B.5 Reconstructed Photon Energy E_γ 189
B.6 Pion Production Threshold 190

References 193

Vita 199

List of Tables

2.1 Measured s dependence for many scattering processes compared to the prediction made by dimensional scaling rules, $\frac{d\sigma}{dt} \propto s^{-n}$. 14

3.1 Nominal and actual thicknesses of copper radiators used in experiment E89-012, including thicknesses for each foil that form the radiators. . 40

3.2 Measured dimensions of nominal 15 cm target cells in the CEBAF cryotarget. 42

3.3 CEBAF Hall C HMS performance limits 43

3.4 The LeCroy 8LM output logic table. The symbol $\otimes$ implies a logical AND. 55

3.5 Expected statistical errors for each kinematics setting. 57

4.1 Upper and lower limits in mass-squared used in data analysis for each kinematics. 70

4.2 Charge weighted tracking efficiencies for the four measurement configurations of each kinematics. No standard deviations are given for those configurations where only one run is taken. For the kinematics marked with †, the tracking efficiencies T^{in}_{empty} and T^{out}_{empty} are replaced by $T^{in}_{LH_2}$ and $T^{out}_{LH_2}$ respectively, reflecting the configurations using a hydrogen target. See Section 5.1.1 for the list of configurations. 75

5.1 Actual center-of-mass angles in degrees for the half acceptance that is not obscured by the gate valve. The bottom portion of the table list the center-of-mass angles for the full acceptance for kinematic settings where the gate valve is not present. Note that for $E_{beam} = 0.845$ GeV, the data for $\theta_{nom} = 89°$ are separated into two different regions in E_γ in the analysis (see Section 5.4.3), which correspond to different values for θ_{cm}. 105

5.2 Thresholds for pion production for the kinematics studied. Above the threshold, all kinematically allowed events come from $\gamma d \to pn$. The angles shown above are central values. The actual proton angles used to find the thresholds correspond to the forward edge of the collimator aperture. 108

5.3 Effective solid angles used for data analysis. Values are given for the half of the spectrometer acceptances that is not obscured by the presence of the gate valve. Values for full acceptances are given at the end of the table for kinematics where the gate valve was not present. . . . 116

5.4 Integrated photon yields per microcoulomb of electrons incident on a copper radiator. Radiator thickness is 3.49% radiation length for $E_{beam} = 0.845$ GeV, and 6.02% radiation length for all other kinematics. The photon energy window upper limit is $E_{\gamma,high} = E_{beam} - 25$ MeV, where E_{beam} is the bremsstrahlung endpoint, except for $E_{beam} = 0.845$ GeV, $\theta_{cm} = 89.1°$, where the window has been split into two regions of 50 MeV width. The average photon energy is calculated with Equation 5.11. 120

5.5 Results of target gas analysis by Lawrence Livermore National Laboratory. 121

5.6 Densities of cryogenic targets used in the experiment. Errors include uncertainties in overall temperature and pressure, and localized temperature effects. 121

5.7 The region in y_{tar} used in data analysis for all kinematics. 122
5.8 Normalized integrated photo-proton yield for different target lengths. The errors given for the yield are statistical only. 123
5.9 Apparent target lengths obtained by measuring the distance between the peaks for empty target cells for many kinematics settings. This shows the inaccuracy of the COSY matrix elements in reconstructing the position of the event at the target. 125
5.10 Materials in the HMS. The actual amount of LD_2 material depends on scattering angle. 128
5.11 Summary of systematic errors that affect calculation of the $\gamma d \to pn$ cross section. 132

6.1 Kinematic variables for all settings where only half of the acceptance is used in the analysis. This is necessary due to the gate valve obscuring half of the acceptance for most kinematics. 137
6.2 Kinematic variables for full acceptance settings. The failure of the gate valve mechanism did not affect these settings, allowing for data analysis for the full acceptance. 137
6.3 Center-of-mass differential cross sections for $\gamma d \to pn$ measured during the CEBAF experiment E89-012 for half-acceptance data analysis at all kinematics settings. The errors listed are for statistical and systematic uncertainties. 139
6.4 Center-of-mass differential cross sections for $\gamma d \to pn$ measured with full acceptance for those kinematic settings where the gate valve was completely removed from the acceptance. The errors listed are for statistical and systematic uncertainties. 139
6.5 Individual measurement of differential cross sections using data analysis for half-acceptance for two seperate measurements. The weighted mean of these values are used for their respective entries in Table 6.3. 140

6.6 Fits to the energy behavior of $d\sigma/dt \propto s^{-n}$ where n is the parameter that is fit. Data used in the fit include only the results from the half-acceptance analysis given in Table 6.3. 149
6.7 Center-of-mass angles, θ_{cm}, used to calculate the RNA curves in Figures 6.1 - 6.6 and incident photon energies, E_γ used to calculate RNA angular dependence curves in Figure 6.7. 151

A.1 Estimated quality factors and measured loaded quality factors for resonant cavities BCM1 and BCM2 162
A.2 Location of the Temperature stability system thermocouples 166
A.3 Results from absolute Unser PCT calibrations over the course of several months. 171

List of Figures

2.1 Pictorial of momentum transfer to each nucleon for a) elastic electron-deuteron scattering, and b) deuteron photodisintegration. 10

2.2 General diagram for $AB \to CD$. The four momentum for each particle is given by p_i. 12

2.3 Example of Landshoff diagram for $pp \to pp$ scattering where there are multiple interactions between the quarks of different protons. Such diagrams are assumed to be suppressed in the constituent counting rule model. 13

2.4 Invariant cross section $d\sigma/dt$ for $pp \to pp$ elastic scattering. The data are taken from [27]. 14

2.5 Invariant cross section for $d(\gamma,p)n$ for a) $\theta_{cm} = 90°$, b) 53°, c) 37°. References for the data: Dougan *et. al.* [33], Ching and Schaerf [34], Myers *et. al.* [35], Arends *et. al.* [36], SLAC NE8 [2,37], and SLAC NE17 [3]. The figure is adapted from [38]. 16

2.6 Lowest order QCD diagram for ep elastic scattering. 17

2.7 QCD diagram for deuteron photodisintegration $\gamma d \to pn$. 17

2.8 Hadronic form factors $F_H(Q^2)$ scaled by $(Q^2)^{n_H-1}$. Figure is adapted from [40]. 19

2.9 Deuteron form factor $F_D(Q^2)$ scaled by $(Q^2)^5$. Figure is adapted from [41]. 19

2.10 Quark-interchange diagram for electron-deuteron elastic scattering as described by the reduced form factor. 21

2.11 Measurement of reduced deuteron form factor. The figure is adapted from [43]. Additional data are from [41]. 22
2.12 Three-quark exchange diagram for $\gamma d \to pn$, at high s and low $|t|$ or $|u|$. The three quarks that are exchanged along with any number of gluons that are exchanged between them correspond to a Reggeon. . . 24
2.13 Differential cross sections for θ_{cm} = a) 37°, b) 53°, c) 90° from NE17. The solid line indicates the prediction given by the QGS model. Figure is adapted from [46]. 27
2.14 Quark rescattering diagram. The photon is absorbed by one quark which then performs a hard scattering with a quark from the other nucleon. 28
2.15 Meson exchange calculations using Reid soft-core potential. A cut-off mass of $\Lambda_\pi = 1.2$ GeV and a ρ-baryon coupling constant ratio of $G_\rho^2/G_\pi^2 = 1.6$ are chosen. The dotted line indicates the result for the calculation without any meson exchange current. The dashed line gives the result with the meson exchange current. The dash-dot and solid lines also include final state interactions between the nucleons in the S state only and the S and P states respectively. The figure is taken from [51]. 30
2.16 Meson exchange diagram for Lee's Coupled-Channel Model. The photon is absorbed by one nucleon, which goes into an intermediate excited state, F. It then emits a meson which is absorbed by the other nucleon. Finally, there are final state interactions shown in t in the form of meson exchange between the nucleons. 31
2.17 Predicted cross section for $\gamma d \to pn$ using a front-form calculation by Lee [20] laid over data taken at $\theta_{cm} = 90°$ in the SLAC NE8 experiment. The dotted line shows the results of the calculation if final state interactions are ignored. 32

2.18 Tree level diagrams for deuteron photodisintegration at asymptotic energies considered in [21]. Figures a), b), d), and f) correspond to NN configurations of the deuteron. Figures c) and e) correspond to NN* configurations. Figure f) is the contact term and is important at asymptotic energies. 34

3.1 Schematic diagram of experimental setup. The electron beam strikes a copper foil radiator. The resulting bremsstrahlung photons strike the cryogenic deuterium target. Recoil protons from photodisintegration are then detected by the High Momentum Spectrometer. 37

3.2 Overhead schematic of the accelerator at CEBAF. 39

3.3 Schematic of the CEBAF Hall C cryogenic target stack. 41

3.4 Side view of the High Momentum Spectrometer (HMS) 43

3.5 Schematic diagram showing the relative locations of the detectors in the High Momentum Spectrometer (HMS). 45

3.6 Coordinate systems as seen from above for the beam before it strikes the target, and for reaction products detected by the HMS. 46

3.7 Coordinate system for the HMS as seen from the side before and after the dipole bend. 46

3.8 Schematic of HMS collimator. All dimensions are in inches. 47

3.9 HMS drift chamber planes. An incoming particle traverses each of the six planes shown above from left to right. 48

3.10 Front view of the HMS drift chamber wire layout. The lines show the direction the sense wires lay for each of the six planes. 48

3.11 Wire layout for a typical plane in the HMS drift chamber. Electrons ionized by the charged incoming particle drift along the electric field gradient created by the field wires toward a grounded sense wire. . . . 49

3.12 Layout for part of an HMS scintillator hodoscope plane. The x planes have 16 scintillators and the y planes have 10 scintillators staggered as above. 50
3.13 Layout of HMS hodoscope paddles in each of the four planes. 51
3.14 Schematic of the pretrigger electronics used in the experiment. 54
3.15 Schematic of the Trigger Supervisor. 55

4.1 Raw particle mass spectrum. Figures a) through d) show the particle mass reconstructed from velocity determined through hodoscope time of flight and particle momentum reconstructed from tracking. Included are all events which reconstruct to a position within the target. . . . 61
4.2 Raw particle mass spectrum. Figures a) through d) show the particle mass reconstructed from velocity determined through hodoscope time of flight and particle momentum reconstructed from tracking. These figures show the mass spectrum for events which reconstruct to a position within the target but only for -85 MeV $< E_\gamma - E_{beam} <$ -25 MeV. 62
4.3 Example of the presence of pions in the raw particle mass spectrum for E_{beam} = 2.445 GeV, θ_{cm} = 88.8°. The proton peak extends to the right. The height of the pion peak is enhanced in this figure by including background events which come from $Al(\gamma, \pi)X$ reaction from the target endcaps. 63
4.4 Relation between the width of the mass spectrum proton peak determined from TOF and p^2_{HMS} for all kinematics studied in this experiment. The relation can be used to determine the time resolution of the HMS hodoscope. Limitations in hodoscope calibration may give a value that is higher than expected. 64

4.5 HMS time of flight and timing resolution for $E_{beam} = 3.245$ GeV, $\theta_{cm} = 68.7°$. Figure a) gives the velocity of the protons used in the calibration determined from tome of flight. Figure b) shows the distribution of standard deviations for time measurements made for each event. For each scintillator plane, a time is generated for the event to reach the focal plane. The standard deviation is calculated from the three or four measurements made by the hodoscope planes. 67

4.6 Raw mass spectrum for $E_{beam} = 4.045$ GeV, $\theta_{cm} = 51.5°$. The main curve (a) shows all events that reconstruct to the middle of the target region. The crosshatched area (b) shows those events which trigger the HMS Gas Cerenkov, identifying them as pions. Note that the peak is centered near $M^2 = 0.02$ GeV^2 where the pion peak is expected. . . . 68

4.7 Ratio of total pions to total protons for each kinematics using time-of-flight and the Gas Cerenkov for particle identification. The ratio is calculated by considering the number of pions and protons in the region where only photodisintegration is expected. No subtractions are made for background measurements. 69

4.8 Fiducial area used to determine tracking efficiency. Tracking efficiency is calculated using only those events which fall within the central part of the spectrometer acceptance. The event must be triggered by hodoscope paddles in the shaded area. 73

4.9 Figure a) shows the calorimeter energy spectrum for $E_{beam} = 3.245$ GeV, $\theta_{cm} = 88.8°$. Tracking efficiency calculations only include those events which are sure to be protons. This is done by requiring the events to be within a narrow window in β and that they deposit a minimum amount of energy in the calorimeter. For these kinematics, the value is $E_{cal} > 0.45$. The dashed curve in Figure b) shows the protons that pass both the β and the calorimeter energy cuts. 74

4.10 Drift time and drift distance spectra for events in the HMS drift chambers. Drift times are mapped into a uniform distribution of distances to the sense wire in the center of each cell. 77

4.11 Pictorial of target position and angle parameters. 79

4.12 Pictorial of focal plane position and angle parameters. 79

4.13 HMS sieve slit diagram. The sieve slit is used in fitting reverse optics matrix elements. Two holes are filled to visually guarantee correct orientation in the final reconstruction. The center hole is smaller to facilitate measurement of angular resolution. 81

4.14 a) Position of events at the plane of the collimator (z = 126 cm) using the COSY model set of reconstruction matrix elements for E_{beam} = 4.045 GeV, $\theta_{cm} = 35.4°$. b) Corresponding reconstructed E_γ spectrum. 84

4.15 a) Position of events at the plane of the collimator (z = 126 cm) using the fitted set of reconstruction matrix elements for E_{beam} = 4.045 GeV, $\theta_{cm} = 35.4°$. b) Corresponding reconstructed E_γ spectrum. 85

4.16 Position of events at the plane of the collimator (z = 126 cm) for E_{beam} = 4.045 GeV, $\theta_{cm} = 53.2°$. Figure a) shows the results for the COSY model of reconstruction matrix elements. Figure b) uses the fitted set of matrix elements. 86

5.1 Normalized photo-proton yields as a function of E_γ for E_{beam} = 2.445 GeV, $\theta_{cm} = 51.6°$ for each of the four configurations, LD_2^{in}, LD_2^{out}, MT^{in}, MT^{out} in figures a), b), c), d), respectively. 91

5.2 The correction factor $f(E_\gamma)$ for an electron beam with initial energy E_{beam} = 4.045 GeV striking a 6.02% copper radiator. This factor corrects for the difference in the photon spectra created by the electron beam in the target. This difference is caused by the change in the energy distribution of the incident electron beam as it passes through the copper radiator. 93

5.3 Photo-proton yield for $\theta_{cm} = 53.0^{\circ}$, $E_{beam} = 2.445$ GeV as a function of E_{γ}. Background configurations have been subtracted in accordance with Equation 5.5. The crosshatched area shows the portion of the photo-proton yield that is used in calculating the deuteron photodisintegration cross section. 94
5.4 Schematic diagram of gate valve and mechanism. 99
5.5 Attenuation from gate valve. Shown here are the reconstructed particle positions at ($z_{HMS} = 145$ cm) downstream from the target for data taken at $\theta_{cm} = 89.0^{\circ}$, $E_{beam} = 1.645$ GeV. An outline of the edge of the valve is overlaid on the data. 100
5.6 Reconstructed particle positions at ($z_{HMS} = 145$ cm) for a simulation of $E_{beam} = 1.645$ GeV, $\theta_{cm} = 89^{\circ}$. 103
5.7 Difference in reconstructed and initial parameters for a simulation of $E_{beam} = 1.645$ GeV, $\theta_{cm} = 89^{\circ}$. Figures a), b), c) on left show the difference in δ, y_{target}, and E_{γ}, respectively, for events which are not obstructed by the gate valve. Figures d), e), f) on right show the difference in δ, y_{target}, and E_{γ}, respectively, for events for those events which pass through the gate valve and enter the spectrometer. 104
5.8 Monte Carlo simulation of the reconstructed position along $\hat{y}_{HMS}$ for $E_{beam} = 1.645$ GeV, $\theta_{cm} = 89^{\circ}$, at the position of the gate valve ($z_{HMS} = 145$ cm). The main graph shows the histogrammed position for all events that are within the spectrometer acceptance. The 'unobstructed' half of the acceptance corresponds to the region $y_{HMS} < 0$. The crosshatched area shows the events which are scattered by the gate valve, showing the portion of those events which leak into the half-acceptance used in data analysis for those kinematics affected by the gate valve. 106
5.9 Pion production in the deuteron photodisintegration reaction in the center of mass and the lab frame. 107

5.10 Proton events reconstructed back to the plane of the collimator ($z_{HMS} =$ 126 cm) for the LD_2^{in} configuration for $E_{beam} = 4.045$ GeV, $\theta_{cm} = 53.2°$. The inner box shows the software cuts used in data analysis. The area between the outer box and the inner box is equal in area to that of the inner box and is used to estimate the amount of accidental background which remains after all other background subtraction. 110

5.11 Normalized photo-proton yields for $E_{beam} = 4.045$ GeV, $\theta_{cm} = 35.4°$ as a function of E_γ. The crosshatched area shows the normalized spectrum for background events which lie in an area around the perimeter of the spectrometer acceptance. 112

5.12 Acceptance for Monte Carlo for x'_{tar}, y'_{tar}, δ, and y_{tar}. Shown are the ratios of final reconstructed target parameters to the initial target parameters for a simulation run at $p_{HMS} = 1.920$ GeV, $\theta_{HMS} = 51.5°$. A ratio of 1 indicates that all events in that parameter space successfully track into the spectrometer. 114

5.13 Bremsstrahlung energy spectrum for a 4.045 GeV electron beam incident on a 6.02% copper radiator. The dashed line corresponds to the spectrum in the thin radiator limit. The solid line includes corrections for finite radiator thickness. 119

5.14 Event yields, $\frac{dN}{dZ}$, in arbitrary units over the length of the target. Empty target configurations are used which presents data that comes solely from the aluminum target windows. Figures a) - d) are labeled showing the kinematics that are histogrammed. 124

5.15 Correction for target length due to inaccuracy of COSY matrix element reconstruction of y_{tar}. Plotted is the ratio of actual target length to apparent target length as a function of the central spectrometer momentum. The errors include only the uncertainty of determining the centroids of the two target windows for each data set combined with the uncertainty of the physical measurement of the target lengths. . . 126

6.1 Results for $s^{11}d\sigma/dt$ for $\theta_{cm} = 87.9 - 91.0°$. Data for previous measurements are also shown [3, 33, 34, 37]. Data for E89-012 and SLAC NE17 include statistical and total uncertainties. For information regarding theoretical curves, see Section 6.3. 141
6.2 Results for $s^{11}d\sigma/dt$ for $\theta_{cm} = 68.7 - 68.8°$. Data for E89-012 include statistical and total uncertainties. For information regarding theoretical curves, see Section 6.3. 142
6.3 Results for $s^{11}d\sigma/dt$ for $\theta_{cm} = 51.5 - 53.8°$. Data for previous measurements are also shown [3, 33, 37]. Data for E89-012 and SLAC NE17 include statistical and total uncertainties. For information regarding theoretical curves, see Section 6.3. 143
6.4 Results for $s^{11}d\sigma/dt$ for $\theta_{cm} = 35.4 - 37.5°$. Data for previous measurements are also shown [3, 33]. Data for E89-012 and SLAC NE17 include statistical and total uncertainties. For information regarding theoretical curves, see Section 6.3. 144
6.5 Results for $d\sigma/d\Omega_{cm}$ for a) $\theta_{cm} = 87.9 - 91.0°$ and b) $\theta_{cm} = 68.7 - 68.8°$. Data for previous measurements are also shown [3, 33, 34, 37]. Data for E89-012 and SLAC NE17 include statistical and total uncertainties. For information regarding theoretical curves, see Section 6.3. 145
6.6 Results for $d\sigma/d\Omega_{cm}$ for a) $\theta_{cm} = 51.5 - 53.8°$ and b) $\theta_{cm} = 35.4 - 37.5°$. Data for previous measurements are also shown [3, 33, 37]. Data for E89-012 and SLAC NE17 include statistical and total uncertainties. For information regarding theoretical curves, see Section 6.3. 146
6.7 Angular behavior of $d\sigma/d\Omega_{cm}$ for a) $E_\gamma = 1.52 - 1.60$ GeV, b) $E_\gamma = 2.32 - 2.40$ GeV, c) $E_\gamma = 3.16 - 3.20$ GeV, d) $E_\gamma = 3.96 - 4.00$ GeV. Data for previous measurements are also shown [3, 37]. Data for E89-012 and SLAC NE17 include statistical and total uncertainties. For information regarding theoretical curves, see Section 6.3. 147

6.8 Graph for $f^2(\theta_{cm} = 90^\circ)$, the angular factor in the differential cross section prediction of the reduced nuclear amplitude model. 151

A.1 Relative locations of the beam current monitors on the beamline. Distances are not to scale. 158
A.2 Pictorial of TM_{010} mode in cylindrical cavity. 161
A.3 Block diagram of electronics associated with the signal from the Unser PCT. 164
A.4 Block diagram of electronics associated with the signal from the resonant cavities. 165
A.5 Example of short term noise in the Unser monitor. 169
A.6 Histogram of current readings from the Unser PCT from data shown in Figure A.5. 170
A.7 Residuals from a linear fit for the absolute calibration of the Unser PCT in November 1995. 172
A.8 Residuals from a linear fit for the absolute calibration of the Unser PCT in February 1996. 172
A.9 Relative short-term noise between BCM1 and BCM2 at $I_{beam} \approx 25\mu$A. 173
A.10 Changes in the zero offset with respect to time for BCM1. 174
A.11 Changes in the zero offset with respect to time for BCM2. 174
A.12 Relative gain of BCM1 for successive calibrations. 175
A.13 Gain of BCM1 as a function of cavity temperature for calibrations made during late 1995. 176
A.14 Gain of BCM2 as a function of cavity temperature for calibrations made during late 1995. 176
A.15 Figure a) Expected behavior of beam current during measurement interval. Figure b) Sudden drop in beam current during a measurement interval. The quantity, α, is the fraction of the time interval that the beam remains on. 177

A.16 Ratio of beam current readings from BCM3 to BCM1 normalized at $I_{beam} = 25\ \mu$A. 181

B.1 General diagram for $AB \rightarrow CD$ in the lab frame. 183

B.2 General diagram for $AB \rightarrow CD$ in the center-of-mass frame. 184

B.3 Pictorial of $\gamma d \rightarrow pn$ in the lab frame. 184

B.4 Pictorial of $\gamma d \rightarrow pn$ in the center-of-mass frame. 184

B.5 Pion production in the deuteron photodisintegration reaction in the center of mass and the lab frame. 191

Chapter 1

Introduction

The deuteron has been the subject of much interest over the past few decades, owing to the fact that it is the simplest nucleus. This has offered experimentalists and theorists the opportunity to explore the nucleon-nucleon interaction in a bound system. The properties of the deuteron are as important in nuclear theory as the hydrogen atom is in atomic theory [1]. Deuteron photodisintegration ($\gamma d \to pn$) is a powerful method of probing the properties of the deuteron, because the photon probe is well understood and the absorption of the photon by the nucleons can lead to a much higher momentum transfer than more conventional electron-deuteron elastic scattering.

Traditionally, meson exchange theory has been used to model the nucleon-nucleon interaction. A vast amount of low and medium energy scattering data have been collected for the deuteron. From those data, theoretical models have been created to describe the interaction between the nucleons, and thus the binding mechanism of the deuteron. In the low energy limit, meson exchange theory has been successful at describing these interactions in terms of meson and baryon degrees of freedom.

These theoretical models, such as the theoretical description of the $\gamma d \to pn$ process, have run into difficulties upon being extended to higher energies. There are many possible reasons for these difficulties which may be overcome with further development. Perhaps the models may require consideration of higher mass meson exchanges and higher excitation states of the nucleons, or perhaps a fully relativistic treatment is necessary. It is possible the short-range interactions evident with a higher energy probe are not well described by the nucleon potentials of past models.

Since the discovery of subnucleon degrees of freedom and the advent of Quantum Chromodynamics (QCD), attention has shifted to explaining nucleon interactions in terms of gluon exchange between the quarks rather than the meson-baryon picture which is used at low energies.

At very high energies, QCD predicts asymptotic freedom, where the inter-quark interactions vanish in the infinite energy limit. Thus, quark-gluon interactions can be treated with perturbative QCD (PQCD). This simplification is important as performing theoretical calculations with non-perturbative methods has thus far proven prohibitive. The utility of QCD to model nuclear reactions in the low energy regime is limited. Efforts have, however, been made to see how far down the high energy limit can be applied to describe nuclear processes such as deuteron photodisintegration.

The region where meson-exchange theories give way to the quark-gluon degrees of freedom is an area rich with controversy and speculation. Obtaining experimental data in this energy region is essential in the effort to describe the complex transition that takes place in this intermediate region. This experiment hopes to improve the theoretical interpretation of the deuteron in this transition region.

This document presents the results from experiment E89-012 which took place at the Continuous Electron Beam Accelerator Facility (CEBAF) during 1996. The experiment focused on studying the energy dependence of differential cross section for exclusive two-body photodisintegration of the deuteron ($\gamma d \to pn$) at several center-of-mass angles in a photon energy range of 0.8 - 4.0 GeV. This experiment used the many advantages offered by the CEBAF accelerator to extend measurements of these cross sections to a higher energy range. These measurements build upon results from experiments NE8 [2] and NE17 [3] which took place in previous years at the Stanford Linear Collider (SLAC).

Chapter 2 discusses the many theoretical models that have been made to describe the deuteron photodisintegration reaction in this energy region. Chapter 3 describes the experimental apparatus including the detector package of the spectrometer. Chapter 4 and 5 discuss the aspects considered in data analysis. Chapter 4 focuses on the analysis of individual events while Chapter 5 includes calculation of the cross section and the corrections that are made for background in the measurement. The final results are presented in Chapter 6 along with a short discussion as they apply to the present theoretical models. A summary and an outlook to the future are given in the final chapter.

Chapter 2

Theory

2.1 QCD and Nuclear Physics

The many models that attempt to describe the behavior of the deuteron can be placed in one of two major categories. The first category consists of models inspired by Quantum Chromodynamics (QCD), where the deuteron and its interactions are discussed in terms of quark and gluon degrees of freedom. Here, perturbative QCD (PQCD) is used to describe the behavior of the deuteron in the high energy limit, where the quark gluon interaction can be investigated in terms of lowest order diagrams. The second category contains the traditional meson-exchange models that dominate the low energy region. These calculations disregard the quark substructure and concentrate solely on the baryon and meson degrees of freedom. In the low energy limit, the distances probed are much too large to distinguish the underlying quarks that make up each hadron.

The main focus of interest is the intermediate region, where the traditional picture of nuclear reactions consisting of baryon constituents interacting through the exchange of mesons gives way to the substructure of quarks and gluons that make up each hadron. Nuclear reactions in this region are not easily explainable by models used at either extreme.

2.1.1 QCD

Quantum Chromodynamics (QCD) is widely accepted as the theory that describes the strong force, in the same way that Quantum Electrodynamics (QED) has adequately described the electromagnetic force [4]. QCD is a field theory which describes the interactions between quarks and gluons, much the same way that QED describes the interactions between photons and charged particles. Quarks are described as point-like spin 1/2 particles with charge +2/3 or -1/3 and color from a basis of (red, green, blue). Gluons act as the mediator of the strong force by exchanging color between quarks. By combining quarks, composite particles can be constructed that are "colorless". This construction leads to two lowest-order examples of colorless particles. The quark-antiquark pair, which has a quark in some color state and an anti-quark in the opposite color state, is the basis of the meson. The three-quark state, whose color states combine to give an equal amount of all three colors, corresponds to the baryon.

The nature of SU(3) color symmetry is that of a non-Abelian field theory where not only do gluons couple to quarks, but gluons can couple to other gluons as well. Thus, vertices where three, four, or more gluons interact with each other are allowed. This is because there is a basis set of eight different gluons which can interact with each other, exchanging color in the same way gluons exchange color in quarks. This interaction gives rise to the QCD running coupling constant given by [5]

$$\alpha_s(Q^2) = \frac{12\pi}{(33 - 2n_f)\ln\left(\frac{Q^2}{\Lambda^2_{QCD}}\right)}, \tag{2.1}$$

where n_f gives the number of flavors of quarks (up, down, strange, etc...), and Λ_{QCD} is the basic mass scale of QCD. Current estimates give $\Lambda_{QCD} \approx 100 - 300$ MeV [6] which come from theoretical fits to experimental data.

One of the features of the QCD strong coupling constant is that for $n_f = 6$, the total number of quark flavors observed now, the coupling constant vanishes at very high momentum transfer, Q^2. This is the phenomenon known as asymptotic freedom. Asymptotic freedom allows interactions between quarks and gluons to be calculated through a perturbative version of QCD (PQCD). In PQCD, interactions are calculated using an expansion in terms of the coupling constant, α_s. PQCD also allows for factorization of hard and soft contributions in nuclear reactions [7]. This allows for perturbative calculations of process dependent hard contributions, while the soft part is left to be calculated through other methods.

PQCD is calculable for interactions at very high energies, but in the low energy limit, PQCD is no longer valid. The strong coupling constant in this region becomes too large and higher order diagrams must be considered. However, a full QCD treatment of low energy reactions is beyond present capabilities. PQCD sometimes requires the calculations of millions of lowest-order diagrams. Including all possible diagrams for higher orders which would be necessary for a non-perturbative calculation renders the situation incalculable.

QCD has been successful in describing the features of many hadronic phenomena in the high energy region including quark-based spectroscopy, point-like parton structure in deep inelastic scattering, and the magnitude and scaling of the ($e^+e^- \rightarrow$ hadrons) cross section, as well as the hadronic jet formation in such reactions [4]. Although PQCD is expected to be valid only at very high energies, it may also be applicable in the intermediate energy range studied by this experiment. This is due to the relatively low mass scale of $\Lambda_{QCD} \approx 200$ MeV. This gives a characteristic length scale of about 1 fm which is comparable to the radius of the nucleon.

QCD does not explicitly describe bound light quark states observed in the laboratory such as mesons and baryons, and thus it is difficult to perform quantitative calculations in perturbative QCD concerning bound states. It is difficult to determine if the specific formulation of QCD even allows for such bound states [8]. Even though bound states are difficult to describe in QCD, a set of empirical relations, dimensional scaling rules (also called constituent counting rules), make it possible to deal with asymptotic behavior of scattering cross sections of such bound states in terms of the number of elementary constituents involved [8]. Many experiments have been done to test the quark structure in bound systems by using high energy electromagnetic probes. These experiments typically investigated quark structure through elastic scattering of electrons from hadrons where the scaling appears to hold. However, asymptotic scaling behavior is believed to apply not only for mesons and baryons, but for nuclei as well [4]. Again, the deuteron would be an excellent candidate for such study as it is the simplest example of a bound nucleus. (An excellent review of the QCD view of the deuteron can be found in [7].) Previous experiments, however, involving elastic electron-deuteron scattering have failed to show the onset of asymptotic scaling of the deuteron form factor up to momentum transfer of $Q^2 = 4$ GeV^2.

While PQCD is expected to reign in the asymptotic limit of high energies, there are still many questions about the applicability of such theories in the intermediate energy region probed in this experiment [9]. The contributions due to non-perturbative processes may still be quite significant when compared to the PQCD prediction. In fact, one estimate shows that PQCD should dominate the description of the deuteron form factor only at a minimum momentum transfer of $Q^2 \geq 60$ GeV^2 [10]. Many QCD inspired models try to improve upon the asymptotic QCD prediction by adding corrections for the non-perturbative portion which could account for the deviation in the behavior from the PQCD picture. With the controversy concerning where PQCD can be used to accurately describe nuclear interactions, experimental data in this intermediate energy region is crucial in the determination of the transition between the non-perturbative and the perturbative models.

2.1.2 Meson Exchange Theory

Meson-exchange models have had great success in describing nuclear reactions in the low energy limit in terms of meson exchange between nucleons. While these models accurately describe the low energy regime, attempts to extend the energy range of these models have been met with difficulty.

Although these models do not include quark and gluon degrees of freedom, they are not inconsistent with the assumption that hadrons are made of quarks which interact through gluon exchange. If QCD is the correct theory to describe the strong force, then meson exchange models are possibly the low energy approximation of QCD. However, this has not yet been proven. Meson-exchange models investigate the interactions between baryons and mesons, which are empirically described by QCD to be color singlet three-quark states (qqq) and color singlet quark-antiquark states ($q\bar{q}$). But in nuclei such as the deuteron, QCD does not rule out the possibility of six-quark color singlet states. The success of meson-exchange models implies that, in the low energy limit, contributions from hidden-color states are negligible. However, at higher energies, these hidden-color contributions may be significant. Some calculations of PQCD imply that contributions from such hidden-color states become dominant in the regime of small quark separation [11]. This would preclude an exact treatment of nuclear interactions based on meson-baryon degrees of freedom as such models do not describe the full basis of QCD [12]. Meson theories are also deficient in that mesons and baryons are only approximate degrees of freedom—the energy behavior of form factors are not reproduced and nucleon-antinucleon terms in intermediate states are not properly suppressed [7].

2.1.3 Summary of theoretical models for deuteron photodisintegration

Constituent counting rules [13, 14], which came about through an empirical argument to be later predicted by QCD, look upon the nuclear reactions purely in terms of hard gluon scattering between quarks at asymptotically high energies. Soft interaction effects between the quarks within each nucleon are added in terms of the nucleon form factors in an attempt to regain the energy scaling picture at lower energies [15, 16]. Another method to describe this region has been to claim that one hard scattering occurs between a pair of quarks, one from each nucleon, while the remaining reactions can be described by low energy NN potentials [17].

Meson-exchange theories have attacked the problem from the other end of the energy scale. At very low energies, the underlying quark substructure of the nucleons are not probed, due to the large wavelength of the electromagnetic probe being used. Therefore, nuclear reactions use mesons such as pions to act as the mediator of the nuclear force. There are many successful calculations of such models [18, 19] which consider different intermediate nucleon resonances and mesons which are exchanged between the nucleons. Attempts to improve the calculations are made to extend the energy range by use of a relativistic model [20]. Another attempt has been to consider the asymptotic energy behavior of the deuteron wave-function [21]. The characteristic distances probed at high energies include the nuclear core of the deuteron where conventional NN potentials cannot accurately describe the deuteron wave-function.

The differing models show the importance of obtaining further experimental data for deuteron photodisintegration in this energy region. The transition from baryon-meson to quark-gluon degrees of freedom seems to be quite complicated and the mixture of theoretical models are presently somewhat muddled as efforts continue to be made to tie together predictions from either end of the energy spectrum. The experimental data from this and other intermediate energy region experiments can hopefully be used to gain a clearer understanding of nuclear reactions.

2.1.4 Why Deuteron Photodisintegration

Photodisintegration holds one large advantage over elastic scattering for deuterons [22]. For photodisintegration, a photon is absorbed by the deuteron in the breakup process. This imparts a much larger momentum transfer to each of the nucleons than in elastic electron-deuteron scattering. This is represented in Figure 2.1. For elastic scattering, the momentum transfer from the electron to the deuteron is given by $-Q^2 = (p'_d - p_d)^2$. Assuming that each nucleon carries half of the momentum of the deuteron, the momentum transfer for each nucleon is given by

$$t_N = (\frac{p'_d}{2} - \frac{p_d}{2})^2 = \frac{-Q^2}{4}. \tag{2.2}$$

By contrast, the momentum imparted to each nucleon in photodisintegration is given by

$$
\begin{aligned}
t_N &= (p_N - \frac{p_d}{2})^2 &(2.3)\\
&= m_N^2 + \left(\frac{m_d}{2}\right)^2 - m_d E_N &(2.4)
\end{aligned}
$$

where E_N is the total energy of the nucleon. Using the approximation, $m_d \approx 2m_N$, the momentum transfer is roughly

$$t_N \approx -2m_N(E_N - m_N). \tag{2.5}$$

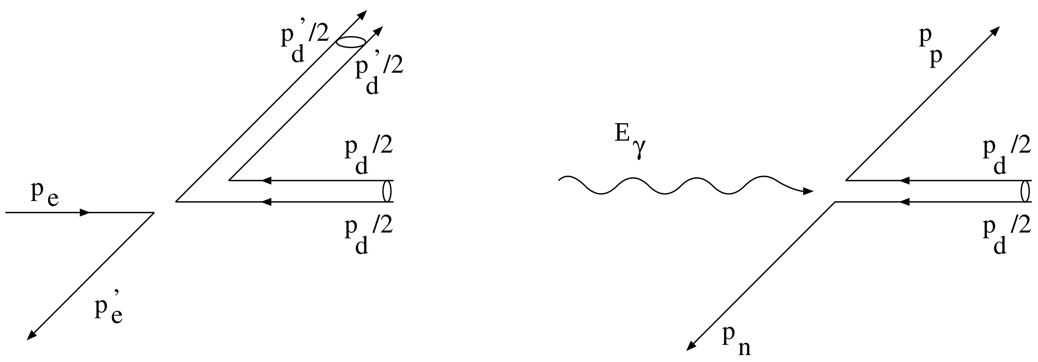

a) ed -> ed

b) γd -> pn

Figure 2.1: Pictorial of momentum transfer to each nucleon for a) elastic electron-deuteron scattering, and b) deuteron photodisintegration.

For the highest beam energy proposed for experiment E89-012, photodisintegration at $]theta_{cm} = 90°$ offers a momentum transfer of about $Q^2 = 15$ GeV^2 in an equivalent elastic deuteron scattering experiment [23]. This would allow the energy scaling behavior predicted by QCD to be observed with photons at a lower energy than with electrons. Present accelerators cannot perform such an elastic scattering experiment at such high momentum transfer as the cross section is too low to make an accurate measurement. This makes photodisintegration an ideal reaction for study.

This experiment also takes advantage of a new facility designed for study of nuclear processes. The Continuous Electron Beam Accelerator Facility (CEBAF) offers many enhancements over other accelerators. Most accelerators function with a pulsed beam, where a high current particle beam strikes the target in short time pulses. The low duty factor of these beams force the averaged current to be very small. CEBAF, on the other hand, uses a continuous beam which offers a 100% duty factor. This allows for a much greater average current, which in turn allows experiments to obtain better statistical accuracy in their measurements in the same amount of time.

2.2 Constituent Counting Rules

Brodsky and Farrar [13] and, independently, Matveev, Muradyan, and Tavkhelidze [14] identified constituent counting rules, also known as dimensional scaling rules. They theorize that the invariant cross section for any fixed-angle two body exclusive process ($AB \to CD$) as pictured in Figure 2.2 should scale at asymptotically high energies as a function of the center of mass energy. The scaling goes as

$$\frac{d\sigma}{dt}(AB \to CD) \sim s^{-(n_A+n_B+n_C+n_D)+2} f\left(\frac{t}{s}\right) \tag{2.6}$$

where t/s remains fixed, $n_A + n_B + n_C + n_D$ are the number of external elementary particles (quarks, leptons, gluons, photons, etc) that take part in the reaction, and s, t are the Mandelstam variables

$$s = (p_A + p_B)^2 \tag{2.7}$$

$$t = (p_A - p_C)^2 \tag{2.8}$$

$$u = (p_A - p_D)^2 . \tag{2.9}$$

At high s, t/s is constant at fixed center of mass scattering angle θ_{cm}.

The scaling behavior in Equation 2.6 is derived empirically through dimensional analysis following Brodsky and Farrar [24]. Using the conventional normalization $\langle p|p'\rangle = 2E\delta(p - p')$, the invariant amplitude for a collection of free constituents,

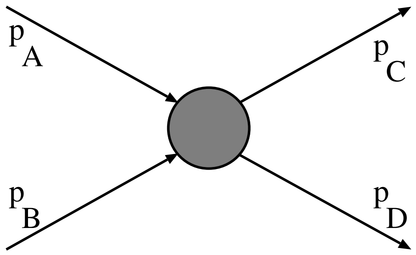

Figure 2.2: General diagram for $AB \to CD$. The four momentum for each particle is given by p_i.

$\mathcal{M}_n(AB \to CD)$, has the dimensions of $[\text{length}]^{n-4}$. At asymptotically high energy and momentum transfer, the only length scale available is a function of s. This implies that the amplitude can be given as

$$\mathcal{M}_n(AB \to CD) \sim \left(\frac{1}{\sqrt{s}}\right)^{n-4} f(\theta_{cm}) \tag{2.10}$$

where $f(\theta_{cm})$ is a function dependent only on the center of mass scattering angle. Assuming each constituent carries a finite part of the total momentum, integrating over all possible momenta for all constituents does not introduce any new dependence on s. Thus, the invariant amplitude, $\mathcal{M}$, for bound constituents should exhibit the same scaling behavior as the amplitude, $\mathcal{M}_n$, for a collection of free constituents.

The center of mass cross section for the generic process $(AB \to CD)$ is expressed as [25]

$$\frac{d\sigma}{d\Omega_{cm}} = \frac{1}{64\pi^2 s}\frac{p_f}{p_i}|\mathcal{M}|^2 \tag{2.11}$$

where $p_i = |\vec{p}_A| = |\vec{p}_B|$ and $p_f = |\vec{p}_C| = |\vec{p}_D|$. The invariant cross section, $\frac{d\sigma}{dt}$, is found through the use of the Jacobian, $\frac{d\Omega_{cm}}{dt}$,

$$\frac{d\sigma}{dt} = \frac{d\sigma}{d\Omega_{cm}}\frac{d\Omega_{cm}}{dt} \tag{2.12}$$

$$= \frac{1}{64\pi s}\frac{1}{p_i^2}|\mathcal{M}|^2. \tag{2.13}$$

The initial momentum, p_i^2, in the center of mass frame in the limit of high s is given as

$$\lim_{s\to\infty} |p_i|^2 \approx \frac{s}{4}. \tag{2.14}$$

Placing this into Equation 2.13 gives the scaling relation for the invariant cross section,

$$\frac{d\sigma}{dt} \approx \frac{|\mathcal{M}|^2}{16\pi s^2} \propto s^{-(n-2)}, \tag{2.15}$$

returning the relation in Equation 2.6.

Brodsky and Farrar further state that this scaling is correct if three assumptions are made:

1. Bound constituents can be described by ground state wave functions that are finite at zero quark distance and vanish at large separation.

2. Large momentum transfers between the constituents are asymptotically scale invariant.

3. Multiple interactions between constituents of different hadrons can be ignored.

The first assumption guarantees that the corrections for the binding energy are small. The second assumption ensures that s is the only scaling variable available for the amplitude. The third assumption is used to eliminate contributions from disconnected graphs described by Landshoff scattering [26] (see Figure 2.3).

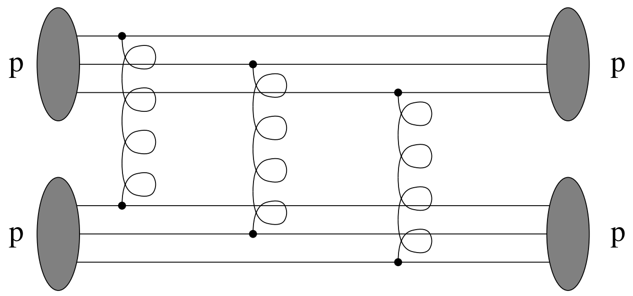

Figure 2.3: Example of Landshoff diagram for $pp \rightarrow pp$ scattering where there are multiple interactions between the quarks of different protons. Such diagrams are assumed to be suppressed in the constituent counting rule model.

The scaling rules outlined above still allow for logarithmic corrections to affect the scaling behavior. Such corrections are expected from QCD [4].

Constituent scaling has been successful in describing the energy behavior of many processes. The most striking example is in elastic proton-proton scattering [27].

Figure 2.4 shows the experimental results of elastic proton-proton scattering for many center of mass angles. For very large s, constituent counting rules would predict that the invariant cross section would fall as s^{-10}. From a fit to the data, the falloff is found to be $\frac{d\sigma}{dt} \sim s^{-9.7\pm0.5}$. Table 2.1 gives a summary of the measured and predicted s scaling for $\gamma p \to \gamma p$ [28], $\gamma p \to \pi^0 p$ [29], $\gamma p \to \pi^+ n$ [30], $\pi^- p \to p\pi^-$ [31], $pp \to pp$ [27], $\gamma d \to d\pi^0$ [32].

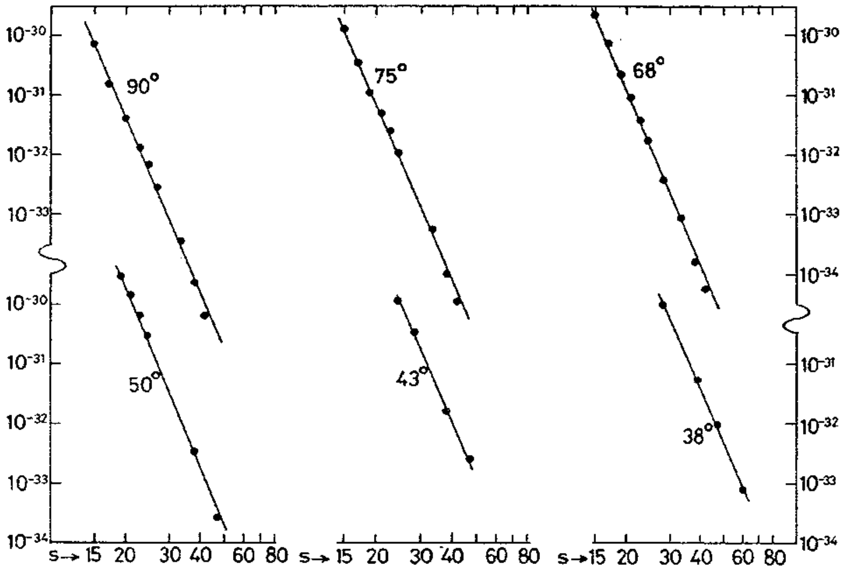

Figure 2.4: Invariant cross section $d\sigma/dt$ for $pp \to pp$ elastic scattering. The data are taken from [27].

Reaction	θ_{cm}	Energy	Predicted s Dependence	Measured s Dependence
$\gamma p \to \gamma p$	60°	$7 < s < 12$ GeV^2	-6	-5.9 ± 0.3
$\gamma p \to \pi^0 p$	90°	$8 < s < 10$ GeV^2	-7	-7.6 ± 0.7
$\gamma p \to \pi^+ n$	90°	$1 < s < 20$ GeV^2	-7	-7.3 ± 0.4
$\pi^- p \to p\pi^-$	90°	$12 < s < 20$ GeV^2	-8	-7.5 ± 0.3
$pp \to pp$	38° – 90°	$15 < s < 60$ GeV^2	-10	-9.7 ± 0.5
$\gamma d \to d\pi^0$	136°	$6.5 < s < 12.5$ GeV^2	-13	-13.1 ± 0.2

Table 2.1: Measured s dependence for many scattering processes compared to the prediction made by dimensional scaling rules, $\frac{d\sigma}{dt} \propto s^{-n}$.

The constituent scaling rule prediction can be applied to deuteron photodisintegration, $\gamma d \to pn$. The number of elementary fields for each constituent is $n_\gamma = 1$, $n_d = 6$, $n_p = 3$, and $n_n = 3$. The expected scaling behavior is found by placing the number of fields into Equation 2.6,

$$\frac{d\sigma}{dt}(\gamma d \to pn) \to s^{-11} f(\theta_{cm}) \tag{2.16}$$

where in the high energy limit, t/s remains fixed at constant θ_{cm}.

Figure 2.5 shows the previous experimental data obtained for deuteron photodisintegration, including the data from Stanford Linear Accelerator (SLAC) Experiment NE17 for $\theta_{cm} = 90°$, $53°$, and $37°$. At $\theta_{cm} = 90°$, constituent scaling seems to start at about 1.2 - 1.5 GeV. The data at $\theta_{cm} = 53°$ shows the possibility of scaling, while at $\theta_{cm} = 37°$ scaling is still not evident.

Carlson gives an alternate derivation for the scaling laws in terms of quark rescattering where momentum transfer between all the constituents are required [39]. As an example, consider ep elastic scattering as pictured in Figure 2.6. A virtual photon with four-momentum, q, scatters with one of the constituent quarks of the proton. The quark then scatters with the other two quarks in the proton through a hard gluon exchange. Assuming terms in m/q are ignored, where m is some mass scale, the scale in q is governed by the following:

- Each internal fermion propagator counts as $1/q$.
- Each internal boson propagator counts as $1/q^2$.
- Each external quark line scales as q if the helicity of the Dirac spinor is conserved.

So in this example, there are three internal boson propagators, two internal fermion propagators, and four external lines where helicity is conserved. By applying the above rules, the amplitude is predicted to scale as

$$\mathcal{M} \sim \left(\frac{1}{q}\right)^2 \left(\frac{1}{q^2}\right)^3 q^4 = \frac{1}{q^4} \sim \frac{1}{\sqrt{s}^4}. \tag{2.17}$$

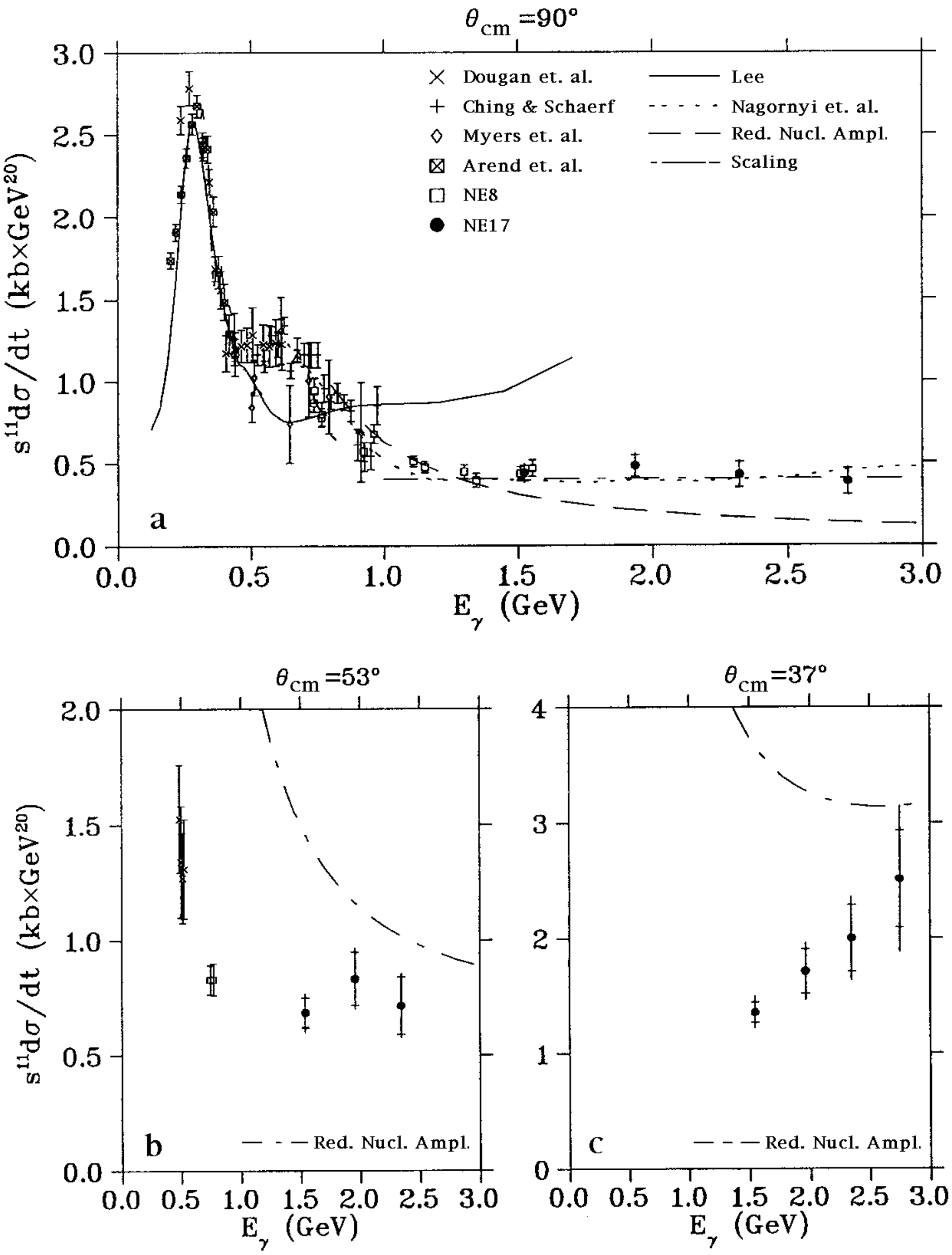

Figure 2.5: Invariant cross section for $d(\gamma,p)n$ for a) θ_{cm} = 90°, b) 53°, c) 37°. References for the data: Dougan *et. al.* [33], Ching and Schaerf [34], Myers *et. al.* [35], Arends *et. al.* [36], SLAC NE8 [2,37], and SLAC NE17 [3]. The figure is adapted from [38].

Substituting the above into Equation 2.13 gives the expected scaling results in Equation 2.6 predicted by the dimensional derivation of constituent scaling rules.

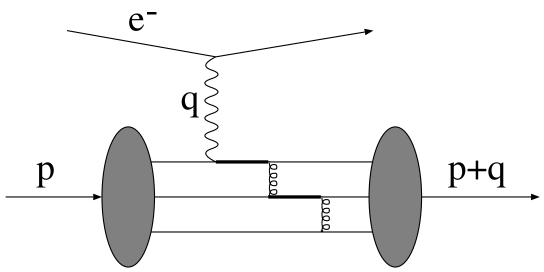

Figure 2.6: Lowest order QCD diagram for *ep* elastic scattering.

This idea can be applied to verify that the scaling behavior for deuteron photodisintegration is the same as expected in Equation 2.16. Figure 2.7 gives a pictorial of the diagram to be studied where there is a single hard gluon exchange between each of the quarks to distribute the momentum gained by absorption of a real photon. There are six external quark lines whose helicity is conserved, five internal fermion propagators and five internal gluon propagators. Following the scaling rules outlined by Carlson, the amplitude is expected to scale as

$$\mathcal{M} \sim \left(\frac{1}{q}\right)^5 \left(\frac{1}{q^2}\right)^5 q^6 = \frac{1}{q^9} \sim \frac{1}{\sqrt{s}^9}. \tag{2.18}$$

Substituting the amplitude into Equation 2.13 gives the expected scaling as s^{-11}.

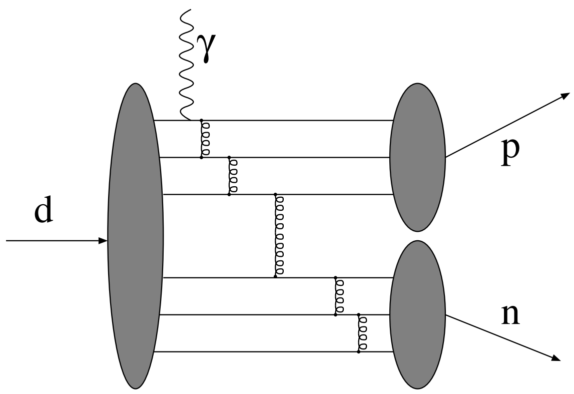

Figure 2.7: QCD diagram for deuteron photodisintegration $\gamma d \to pn$.

Dimensional scaling can also be used to predict the behavior in q^2 of electromagnetic form factors for hadrons. For $eH \to eH$ scattering, the electron counts as one elementary field ($n_e = 1$), and the hadron contains n_H elementary fields equal to the number of quarks in the hadron. Each is counted twice as the electron and hadron are incoming and outgoing particles in the reaction. The scaling rules would predict

$$\frac{d\sigma}{dt}(eH \to eH) \simeq s^{-(2(n_H+n_e)-2)} f(\theta_{cm}) \tag{2.19}$$

$$\simeq s^{-2n_H} f(\theta_{cm}). \tag{2.20}$$

The invariant cross section for elastic hadron scattering is given in terms of the hadron form factor [15]

$$\frac{d\sigma}{dt}(eH \to eH) = \frac{4\pi\alpha^2}{|t|^2} |F_H(t)|^2 f(t/s) \tag{2.21}$$

which implies that for asymptotically high t

$$|F_H(t)|^2 \propto \frac{1}{|t|^{n_H - 1}} \tag{2.22}$$

where $t = q^2$, the momentum transfer from the electron to the hadron. This can be understood by looking at an example of ep elastic scattering pictured in Figure 2.6. The electron scatters from a quark, imparting a momentum, q, onto the quark. The momentum must be shared by the other quarks in the proton through a gluon exchange, each carrying a factor of $1/q^2 = 1/t$.

There has been some controversy surrounding the applicability of dimensional scaling at such low momentum transfer [9]. However, it has shown to be quite useful in describing the monopole form factor behavior for the pion and dipole form factor behavior for the proton and neutron where $Q^2 > 2$ GeV^2 as seen in Figure 2.8. Figure 2.8 indicates that scaling for the deuteron form factor has not yet been reached, but this can be expected as at $Q^2 = 4$ GeV^2, the average momentum transfer per nucleon is on the order of $|t_N| \approx 1$ GeV^2, where the individual nucleon form factors also do not exhibit scaling. However, recent results [41] shown in Figure 2.9 indicate that the deuteron form factor does exhibit asymptotic scaling in measurements extended to $Q^2 \approx 6$ GeV^2.

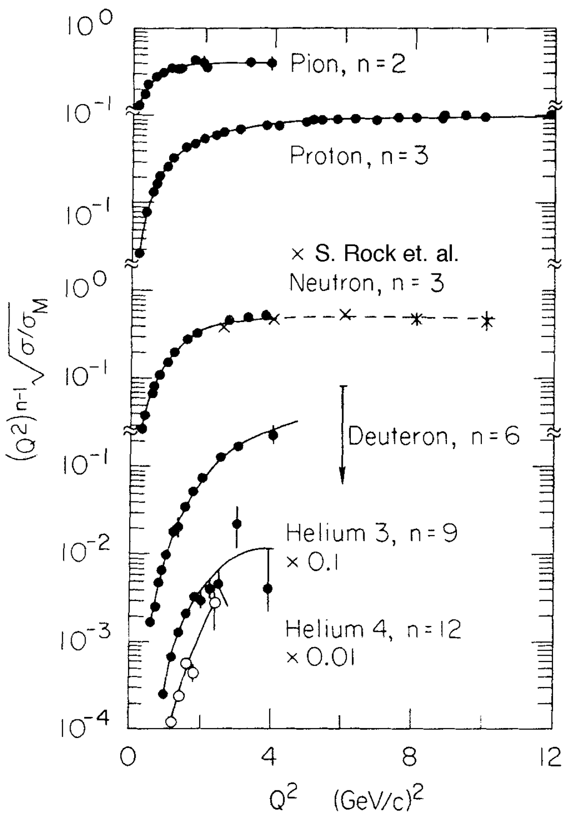

Figure 2.8: Hadronic form factors $F_H(Q^2)$ scaled by $(Q^2)^{n_H-1}$. Figure is adapted from [40].

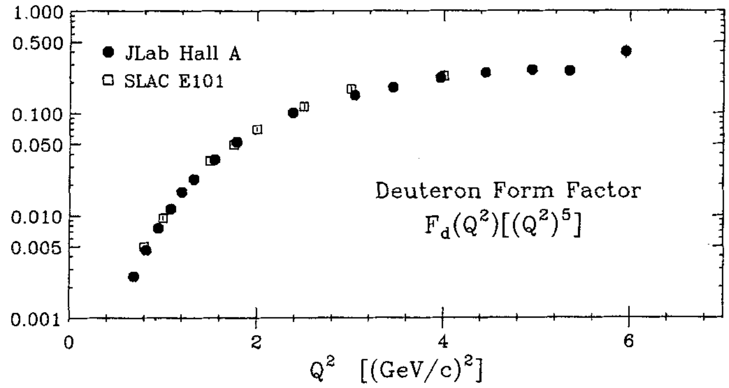

Figure 2.9: Deuteron form factor $F_D(Q^2)$ scaled by $(Q^2)^5$. Figure is adapted from [41].

2.3 Reduced Nuclear Amplitudes

The inability of the constituent counting rules to predict the scaling behavior of the deuteron form factor up to $Q^2 = 4$ GeV^2 led Brodsky and Chertok to formulate a new model in an attempt to show that scaling can occur at a lower threshold value of Q^2 [15, 16].

They claim that at high momentum transfer, the binding energy between the two nucleons can be neglected. The deuteron can then be described as two nucleons, each carrying half of the deuteron momentum. The deuteron form factor can be viewed as the probability that the deuteron remains intact after absorbing a momentum transfer Q^2. It also includes the probability that each nucleon remains intact after absorbing half of the momentum transfer.

In the asymptotic scaling of the constituent scaling rules, the deuteron is treated as a collection of six free quarks. Here the nucleons are allowed to keep their identity as individual three quark states. This allows the contributions to the deuteron form factor that arise from the internal structure of each nucleon to be separated from the remaining part of the deuteron form factor. The soft interactions that occur within each nucleon can be removed by dividing out the form factors for each nucleon, assuming each nucleon absorbed half of the momentum transfer, leaving each nucleon a "point" particle inside the deuteron. This is the concept of the "reduced" form factor which is defined as

$$f_d(Q^2) = \frac{F_d(Q^2)}{F_p(\frac{Q^2}{4})F_n(\frac{Q^2}{4})} \tag{2.23}$$

where the nucleon form factors are calculated using the standard dipole formula [42]

$$F_N(Q^2) = \frac{1}{\left(1 + \frac{Q^2}{\Lambda^2}\right)^2}, \ \Lambda^2 = 0.71 \ GeV^2. \tag{2.24}$$

Figure 2.10 gives a pictorial version of one possible diagram for elastic deuteron scattering. After one quark is scattered by the virtual photon, it transfers half the photon momentum to another quark, and the remaining soft gluon exchanges occur within each nucleon. In order to keep each nucleon in a color singlet state, a quark interchange is necessary between the two nucleons.

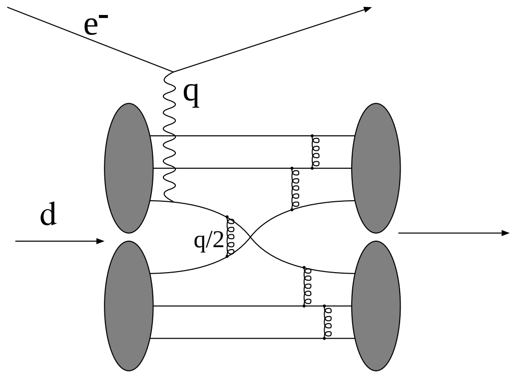

Figure 2.10: Quark-interchange diagram for electron-deuteron elastic scattering as described by the reduced form factor.

Now that the deuteron is reduced to a combination of two nucleons rather than six quarks, the reduced form factor looks similar to a meson form factor [16] which can be considered to consist of two point-like constituents. For high Q^2,

$$f_d(Q^2) \sim \frac{1}{(1+\frac{Q^2}{m_0^2})}. \tag{2.25}$$

The mass scale, $m_0^2 = 0.28\ \mathrm{GeV}^2$, is derived from a fit to data for the pion form factor. The actual mass scale becomes unimportant at very high momentum transfer.

This model has had remarkable success in showing that the energy dependence in the reduced deuteron form factor behaves in the same manner expected of a monopole form factor, where scaling begins at about $Q^2 \sim 1$ GeV as shown in Figure 2.11. This success led Brodsky and Hiller to generalize the method used in calculating the reduced deuteron form factor for use in any exclusive process [43].

Once again, the binding energies between nucleons involved in the reaction are ignored, and the internal structure of the nucleons is assumed to be contained entirely in their form factors. For any generic process with amplitude $\mathcal{M}$ that involves A incoming and outgoing nucleons, the "reduced nuclear amplitude" (RNA) is defined

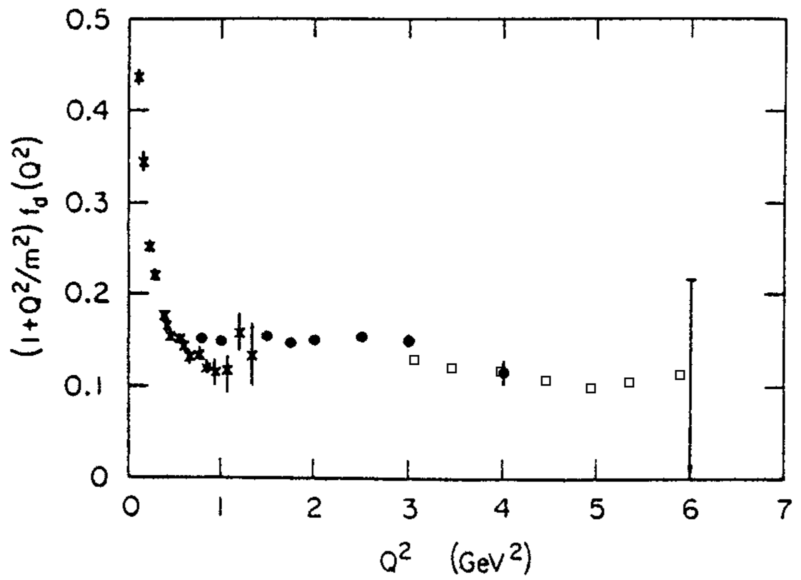

Figure 2.11: Measurement of reduced deuteron form factor. The figure is adapted from [43]. Additional data are from [41].

as

$$m(s,t) = \mathcal{M}(s,t)\left[\prod_{i=1}^{A} F_N(\hat{t_i} = q_i^2)\right]^{-1} \tag{2.26}$$

where $\hat{t_i} = q_i^2$ is the momentum transferred to each nucleon.

In the case of deuteron photodisintegration ($\gamma d \to pn$), there are $A = 2$ nucleons. By applying the RNA technique to this reaction, the reduced amplitude can be written as

$$m_{\gamma d \to np} = \frac{\mathcal{M}_{\gamma d \to np}}{F_n(\hat{t_n})F_p(\hat{t_p})} \tag{2.27}$$

The momentum transferred to each nucleon is determined by comparing the final momentum to the initial momentum, assuming that each nucleon carried half of the initial deuteron momentum,

$$\hat{t_p} = (p_p - \frac{1}{2}p_d)^2, \tag{2.28}$$

$$\hat{t_n} = (p_n - \frac{1}{2}p_d)^2, \tag{2.29}$$

where p_d, p_p, and p_n are the four-momenta of the deuteron and recoil proton and neutron respectively.

The fixed-angle energy dependence of the reduced amplitude at high momentum transfer is given by dimensional scaling [43] to be

$$m \sim p_T^{4-n} f(\theta_{cm}) \tag{2.30}$$

where p_T is the transverse momentum imparted onto the outgoing nucleons and n is the number of external elementary fields as in dimensional scaling except that each nucleon is now reduced to only one elementary field. For deuteron photodisintegration, there are a total of $n = 5$ external fields: the incoming photon, and the incoming and outgoing nucleons. According to Equation 2.30, the reduced amplitude should scale as

$$m \sim p_T^{-1} f(\theta_{cm}) \tag{2.31}$$

where θ_{cm} is defined as the angle of the proton with respect to the incoming photon in the center of mass frame and $p_T = \vec{p_p} \sin(\theta_{cm})$ is the transverse momentum of the proton (or the neutron).

Using the reduced amplitude, the differential cross section for $(\gamma d \to pn)$ in the center of mass frame is found by combining Equations 2.31, 2.27, and 2.11,

$$\frac{d\sigma}{d\Omega_{cm}} \propto \frac{1}{\sqrt{s(s-m_d^2)}} F_p^2(\hat{t_p}) F_n^2(\hat{t_n}) \frac{1}{p_T^2} f^2(\theta_{cm}) \tag{2.32}$$

where the nuclear form factors are similar to Equation 2.24 replacing Q^2 with t_N.

The method of reduced nuclear amplitudes would predict that deuteron photodisintegration would start to scale at $p_T^2 \sim 1$ GeV^2 for fixed θ_{cm} as this is roughly where scaling seems to begin for elastic electron-deuteron scattering. Figure 2.5 shows the result as a long dashed line of the RNA calculation applied to experimental data at $\theta_{cm} = 90°$ that is normalized to a data point near $E_\gamma = 1$ GeV. Agreement at higher energies is less favorable than that given by constituent scaling rules [38].

2.4 Quark-Gluon String Model

Recently, there has been an attempt to model the deuteron photodisintegration reaction by applying Regge phenomenology (described in [44]) and the quark-gluon string

(QGS) model [45]. Kondratyuk, De Sanctis, Rossi, *et. al.* [46] claim that this model is applicable at low $|t|$ and $|u|$, where t and u are the Mandelstam variables given in Equations 2.8-2.9. In the region of high momentum transfer ($|t| \gg 1$ GeV^2), the cross section would exhibit scaling in accordance with the constituent scaling rules given in Section 2.2. However, at high energies and low t or u ($s \gg m_D^2$, $|t|$ or $|u| \leq 1$ GeV^2), the reaction is dominated by a three valence quark exchange where three valence quarks absorb the photon, exchanging any number of gluons between them. The three quarks that are exchanged correspond to a Reggeon, which is an assembly of three quarks plus a collection of gluons (see Figure 2.12)[1]. The limitation placed on $|t|$ or $|u|$ is based on the considerations that the secondary singularities in the complex angular momentum plane will become significant at higher values. But the contribution cannot be quantified easily because phenomenological descriptions of reactions contain parameterizations of data which may include the contributions due to these secondary singularities [46]. So this concept may work for higher values of $|t|$.

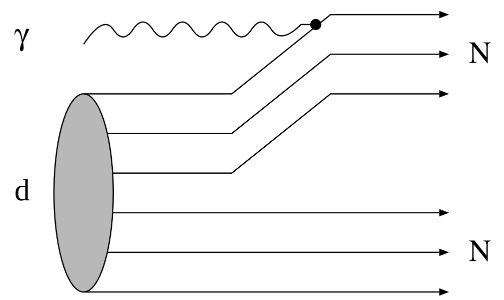

Figure 2.12: Three-quark exchange diagram for $\gamma d \to pn$, at high s and low $|t|$ or $|u|$. The three quarks that are exchanged along with any number of gluons that are exchanged between them correspond to a Reggeon.

The QGS model can be used to extend the predictions given by Regge phenomenology to higher values of momentum transfer. In the QGS model, the Regge singularities are fixed in each graph by the quark content. Thus the amplitude for each graph can

[1]It is useful to point out that although t is traditionally considered a momentum transfer in elastic scattering, in deuteron photodisintegration, the momentum transferred from the photon to the proton increases as $|t|$ decreases. Similarly for the neutron and $|u|$.

be considered for any value of s and t. This has shown to be successful in describing experimental data for other exclusive reactions [46]. This success led Kondratyuk to apply this method to describe deuteron photodisintegration starting at $E_\gamma \sim 0.4$ GeV. The cross section is parameterized in the form

$$\left(\frac{d\sigma}{dt}\right)_{Regge} = \frac{1}{64\pi s E_{\gamma,cm}^2}\left[|T(s,t)|^2 + \frac{1}{R}|T(s,u)|^2\right], \tag{2.33}$$

where $T(s,t)$ and $T(s,u)$ are the amplitudes for deuteron photodisintegration and R is the ratio of forward to backward cross section values defined by

$$R = \frac{(d\sigma/d\Omega)_{0^\circ}}{(d\sigma/d\Omega)_{180^\circ}}. \tag{2.34}$$

The value of R can be shown to be related to the charges of the u and d quarks [47],

$$R = \frac{2z_u^2 + z_d^2}{2z_d^2 + z_u^2} = 1.5. \tag{2.35}$$

In the QGS model, the ratio R increases up to 4 in the limit of infinite E_γ as the model accounts for the difference in momentum distributions in the u and d quarks. However, in this calculation, the ratio is taken to be 1.5.

The amplitude $|T(s,t)|^2$ can be written for a fermion Regge-pole exchange as

$$|T(s,t)|^2 \sim F^2(t)\left(\frac{s}{m_d^2}\right)^{2\alpha_N(t)}, \tag{2.36}$$

where $\alpha_N(t)$ is the trajectory for the nucleon Regge pole, and $F(t)$ is the residue of the pole. The amplitude $|T(s,u)|^2$ can be found by replacing t with u in the above relation. The Regge trajectory is found using data from πN backward scattering

$$\alpha_N(t) = \alpha_N(0) + \alpha_N'(0)t + \frac{1}{2}\alpha_N'' t^2, \tag{2.37}$$

with $\alpha_N(0) = -0.5$, $\alpha_N'(0) = 0.9$ GeV^{-2}, and $\alpha_N'' = 0.25$ GeV^{-4}. The residue, $F(t)$, is taken from [57] to be

$$F(t) = B\left[\frac{1}{m_N^2 - t}\exp(R_1^2 t) + C\exp(R_2^2 t)\right]. \tag{2.38}$$

The first term accounts for the nucleon pole in the t channel and the second term includes contributions from the non-nucleon degrees of freedom in the deuteron. In the calculation presented in [46], the values used were $R_1^2 = 1$ GeV^{-2}, $R_2^2 = -0.1$ GeV^{-2}, $C = 0.7$ GeV^{-2}, and $B = (C_1 + C_2 \sin^2(\theta_{cm}))$ with $C_1 = 6.99$ μb$^{0.5}$GeV^3 and $C_2 = 7.12$ μb$^{0.5}$GeV^3. The calculation also ignored interference terms between $T(s,t)$ and $T(s,u)$. They are expected to be small at forward and backward angles, but some contribution might remain around $\theta_{cm} = 90°$. However, additional cancelations over all the helicity amplitudes are expected to make the interference terms small [46].

Figure 2.13 shows the result of the calculation overlaid on the data from the SLAC NE17 experiment. For the forward angles, $\theta_{cm} = 37°$, $53°$, the contribution from the backward amplitude $|T(s,u)|$ is ignored as $|u|$ is considerably larger than $|t|$. For $\theta_{cm} = 90°$, both terms are included as $t = u$. The cross section given in Equation 2.33 is parameterized as $d\sigma/dt \sim s^{-n}$ where n is different for each angle. The values for n are given for the parameterization in [46] as $d\sigma/dt \sim s^{-9.1}$ at $\theta_{cm} = 37°$, $d\sigma/dt \sim s^{-10.3}$ at $\theta_{cm} = 53°$, and $d\sigma/dt \sim s^{-11.8}$ at $\theta_{cm} = 90°$

2.5 QCD Rescattering

In a recent paper, Frankfurt, Miller, Sargsian, and Strikman [17] describe deuteron photodisintegration by assuming that one quark absorbs the momentum from the photon, followed by a hard scattering of the struck quark from a quark in the second nucleon, producing a two nucleon state with large relative momentum. Figure 2.14 gives a pictorial representation of the reaction considered. Several kinematic conditions must be fulfilled for this picture to be valid. There are no baryon resonances in this model, so any intermediate state produced by the γN reaction must be larger than the threshold to reach the continuum. This threshold gives a minimum value for the photon energy, $E_\gamma \geq 2.4$ GeV [17]. The struck quark must transfer its momentum to the quark in the other nucleon without radiating low energy gluons, which is achieved at about $E_\gamma \geq 2.5$ GeV [17]. Also, the transverse momentum of the final

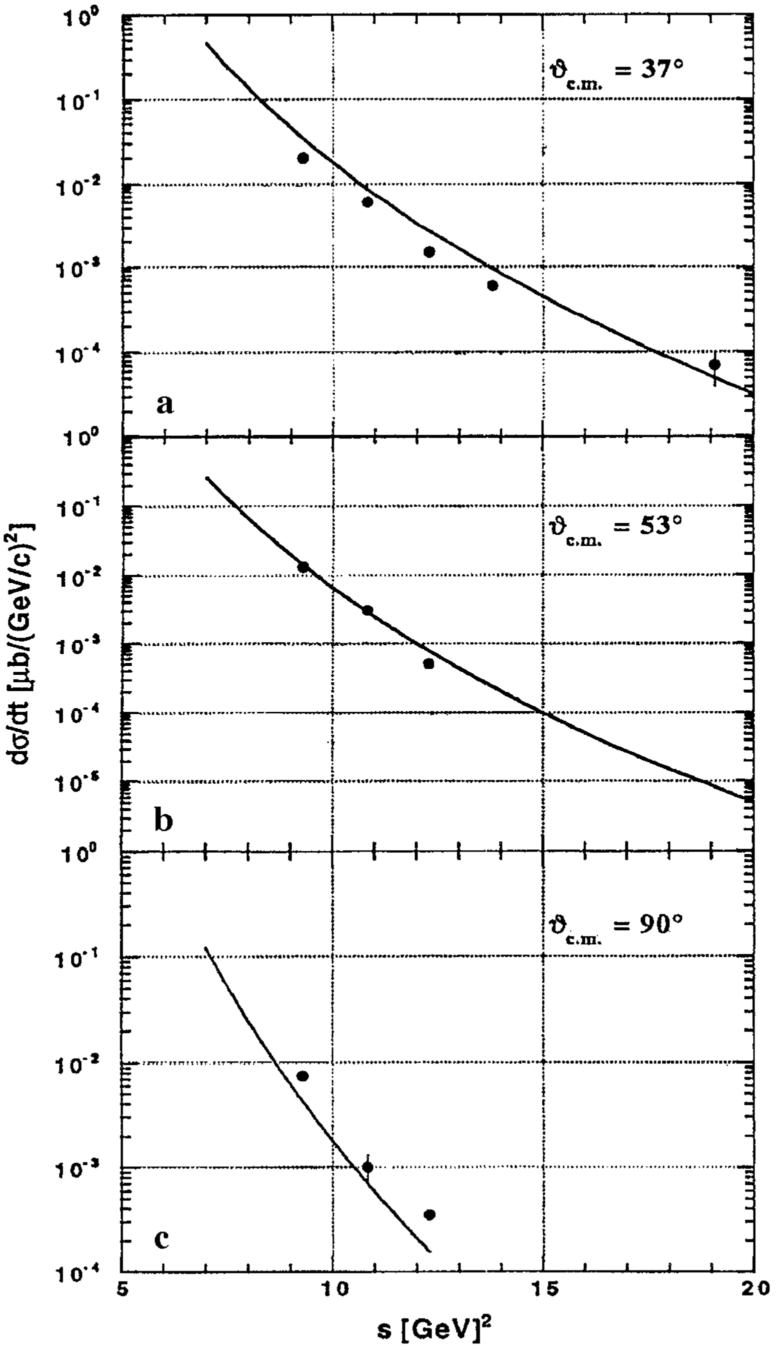

Figure 2.13: Differential cross sections for θ_{cm} = a) 37°, b) 53°, c) 90° from NE17. The solid line indicates the prediction given by the QGS model. Figure is adapted from [46].

state nucleons is required to be high to ensure that the momentum transferred from the first quark to the second is hard enough. The threshold given is $p_T \geq 1$ GeV, which corresponds to $-t \geq 2$ GeV^2. The derivation includes a quark interchange between the two nucleons through the exchange of the hard gluon. All other quark interactions are products of the structure of the nucleons.

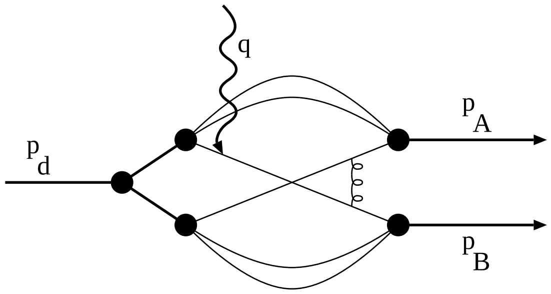

Figure 2.14: Quark rescattering diagram. The photon is absorbed by one quark which then performs a hard scattering with a quark from the other nucleon.

These authors find that the cross section for deuteron photodisintegration goes as [17]

$$\begin{aligned} \frac{d\sigma^{\gamma d \to pn}}{dt} &= \frac{4\alpha}{9}\pi^4 \frac{1}{s - m_d^2} C\left(\frac{t_N}{s}\right) \frac{d\sigma^{pn \to pn}(s, t_N)}{dt} \\ &\times \left| \int \Psi_d^{NR}(p_z = 0, p_\perp) \sqrt{m_N} \frac{d^2 p_\perp}{(2\pi)^2} \right|^2 . \end{aligned} \tag{2.39}$$

The cross section depends on the soft contributions of the deuteron wave-function and on the high p_T contribution of the $pn \to pn$ cross section.

2.6 Conventional Meson Theory

As some models try to explain the medium energy behavior of deuteron photodisintegration by extending PQCD theory from asymptotically high energies to lower limits while still using quark degrees of freedom, there are other models that try to extend traditional meson-exchange theories to higher energies. These models describe nuclear reactions in terms of baryon and meson degrees of freedom, where mesons are the mediators of the nuclear interaction.

There are a variety of such models, each taking into account different assumptions. Typically, the models focus on the exchange of the π meson, but some models also incorporate the ρ and ω mesons as well. Similarly, models allow for and try to calculate the effects of different intermediate excited nucleon states. Each model also assumes a certain nucleon potential for nucleon-nucleon (NN) interactions, such as the Paris potential [48] or the Reid soft-core potential [49]. The dominant contribution to the photodisintegration cross section at low energies comes from one nucleon absorbing the incoming photon. That nucleon then emits a pion (or other meson) which is then absorbed by the other nucleon. Final state interactions between the nucleons can also occur by the exchange of more mesons.

Laget uses a model whose derivation is detailed in [50] and improved upon in [18] where the Reid soft-core potential [49] is used to determine the deuteron wavefunction. He includes effects from both π-meson and the heavier ρ-meson exchange, as well as effects from final state interactions of the nucleons in the S-state only and ultimately the S and P-states. Because the emitted pion is far off mass-shell, the free pion photoproduction operator must be modified. A monopole form factor is used for the pion,

$$F_\pi(q_\pi^2) = \frac{\Lambda_\pi^2 - m_\pi^2}{\Lambda_\pi^2 - q_\pi^2}, \tag{2.40}$$

where q_π^2 is the mass of the off-shell pion, and Λ_π is a mass scale cutoff which acts like a parameter in the fit. For the calculation presented by Laget, $\Lambda_\pi = 1.2$ GeV is chosen as it best reproduces the cross section for $\theta_{cm} = 90°$ at $E_\gamma = 0.1$ GeV [18].

The contribution from the ρ-meson is added by fitting another parameter, the ratio of the coupling constants of the ρ and π. First the ρ form factor is modified to account for its off-shell character,

$$F_\rho(q_\rho^2) = \left[\frac{\Lambda_\rho^2 - m_\rho^2}{\Lambda_\rho^2 - q_\rho^2}\right]^2 . \tag{2.41}$$

The mass cutoff here is chosen to be $\Lambda_\rho = 2m_N$. The ratio of the coupling constants is fit to the data to best reproduce the cross section in the Δ resonance region, $E_\gamma = 0.3$

GeV which gives

$$\frac{G_\rho^2}{G_\pi^2} = 1.6. \tag{2.42}$$

Figure 2.15 gives the result of the calculation using these parameters. The fit gives good agreement with data up to $E_\gamma = 0.5$ GeV, but relativistic effects can be important in the high momentum region and must be investigated further [50].

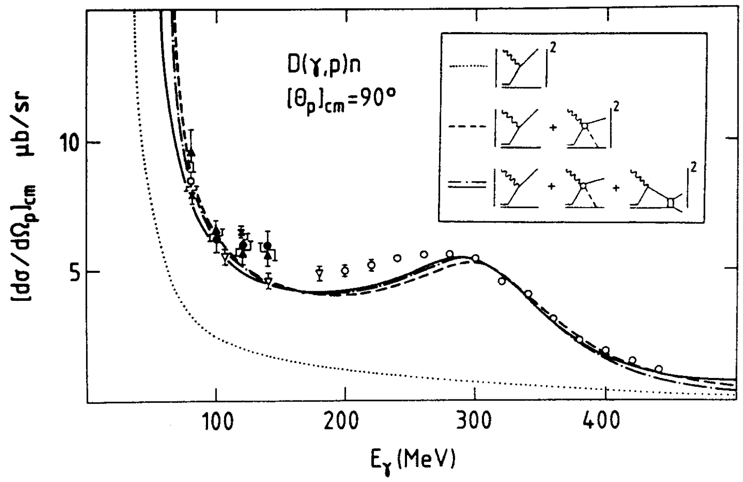

Figure 2.15: Meson exchange calculations using Reid soft-core potential. A cutoff mass of $\Lambda_\pi = 1.2$ GeV and a ρ-baryon coupling constant ratio of $G_\rho^2/G_\pi^2 = 1.6$ are chosen. The dotted line indicates the result for the calculation without any meson exchange current. The dashed line gives the result with the meson exchange current. The dash-dot and solid lines also include final state interactions between the nucleons in the S state only and the S and P states respectively. The figure is taken from [51].

Lee [19] considers a similar reaction method in the Coupled-Channel model which is pictured in Figure 2.16. In this model, one nucleon absorbs the photon, which is makes a transition to an intermediate excited state. The nucleon then emits a high-momentum meson which is absorbed by the other nucleon. The two nucleons undergo final state interactions by the exchange of further mesons. Lee begins by considering the model he developed previously [52] where he extends the Paris potential [48] to include the Δ and the N^* Roper resonance. The one and two-pion production mechanisms are described with the vertices $\Delta \leftrightarrow \pi N$, $N^* \to \pi N$, and $N^* \leftrightarrow \pi\Delta$. This model reasonably reproduces the NN phase shifts and cross sections up to 2

GeV [19] and is used to generate the amplitude for the final state interactions, t. The $\gamma N \to N +$ mesons amplitude, F, is described by a Born term from a field-theoretical Lagrangian taken from [51] and an additional term to describe the excitation of the Δ to account for $\gamma N \to \Delta \to \pi N$ [53]. This model is extended to also include the amplitudes for $\gamma N \to N^* \to \pi N$ and $\gamma N \to N^* \to \pi\Delta \to \pi\pi N$. To simplify the calculation, the two-pion channel is approximated with a fictitious particle, the σ meson–a method commonly used in meson-exchange models for NN interactions [19].

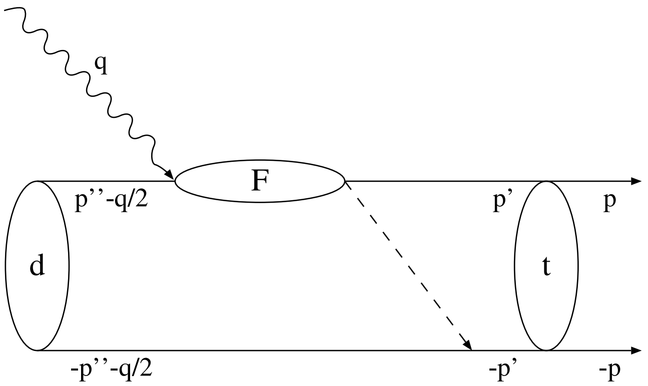

Figure 2.16: Meson exchange diagram for Lee's Coupled-Channel Model. The photon is absorbed by one nucleon, which goes into an intermediate excited state, F. It then emits a meson which is absorbed by the other nucleon. Finally, there are final state interactions shown in t in the form of meson exchange between the nucleons.

The result of the calculation is shown as a solid line on Figure 2.5. It accurately reproduces the experimental values for the cross section in the low energy region. The parameters in the calculation are constrained by NN reaction experimental data and experimental results from $\gamma d \to pn$ where $E_\gamma \leq 1$ GeV. Although this model does not offer a correct prediction at higher energies, meson-exchange models may still be useful if higher resonances and heavier meson exchange currents are considered more quantitatively. In addition, relativistic effects may play a greater role in this energy range and may need to be included in the meson-exchange models [19].

A more recent calculation by Lee [20] tries to incorporate nuclear dynamics within a relativistic calculation for deuteron photodisintegration. He defines a "front-form" coordinate system using a four-vector $n^\mu = [1, \vec{n}]$ with $|\vec{n}| = 1$. Choosing $\vec{n}$ to be along $\hat{z}$, any four-vector can be written in terms of $A^\mu = [A^0, A^1, A^2, A^3]$, giving $A^\pm = A^0 \pm A^3$, $\vec{A}_T = A^1\hat{x} + A^2\hat{y}$. For a two particle system, the front-form free particle Hamiltonian is written as

$$H_0 = \frac{M_0^2 + \vec{P}_T^2}{P^+} \tag{2.43}$$

where M_0^2 is the mass operator of the combined system, and the three-momentum $\vec{P} = [P^+, \vec{P}_T] = \vec{p}_1 + \vec{p}_2$ is the combined momentum of the two particles. The interaction is added by including a potential in the mass operator, $M_0^2 \to M_0^2 + 4mV_{12}$. The potential used in this formulation is the Paris potential, which solely uses a meson exchange two-nucleon model. Figure 2.17 shows the result of the calculation laid over the data points from the SLAC NE8 experiment at $\theta_{cm} = 90°$. The dotted line corresponds to the same calculation where the final state interactions between the neutron and proton are ignored. Lee states that the energy dependence in this calculation is not too different from the Coupled-Channel Model calculation [19]. However, he goes on to say that at high incident photon energy, $E_\gamma \geq 2$ GeV the Paris potential is no longer applicable, and a new NN model must be developed to increase the range in E_γ where this calculation may be used.

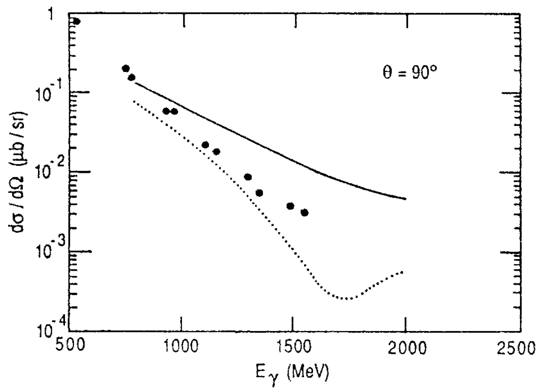

Figure 2.17: Predicted cross section for $\gamma d \to pn$ using a front-form calculation by Lee [20] laid over data taken at $\theta_{cm} = 90°$ in the SLAC NE8 experiment. The dotted line shows the results of the calculation if final state interactions are ignored.

2.7 Asymptotic Amplitudes

Traditional meson exchange models used to describe the deuteron photodisintegration process do fit experimental data at low energies. However, extending these approaches to higher energies ($E_\gamma > 1$ GeV) have failed to give an accurate representation. Nagornyĭ, Kasatkin, and Kirichenko [21] claim that this should be expected as such traditional models rely on realistic deuteron wavefunctions from the Reid soft-core or Paris potential. At high energies ($E_\gamma > 1$ GeV), the reaction starts to probe characteristic distances of $r_{eff} \leq 0.2$ fm. At these distances, the traditional meson theory potentials do not accurately determine deuteron wavefunctions in the nuclear core.

Assuming that at asymptotically high energies, only the lowest order diagrams need to be considered for the Fock-space wave function of the deuteron, these authors write

$$\Psi_D = \cos\phi|NN\rangle + \sin\phi|NN^*\rangle, \tag{2.44}$$

where N corresponds to the nucleon, and N^* is the Roper resonance (1440 MeV). Figure 2.18 gives a pictorial of the diagrams considered in this model.

Nagornyĭ develops a covariant Lorentz and gauge invariant field theory [54] to account for the internal structure of the deuteron. There, the dNN and dNN^* vertex couplings are calculated in the asymptotic limit using only meson and baryon degrees of freedom, which circumvents the problems caused by not knowing the deuteron wave function at small distances. After detailed calculations [54], Nagornyĭ states that in the asymptotic limit, the amplitude for deuteron photodisintegration is dominated by the form factors $G_{N}\gamma_\nu$ and $G_{N^*}\gamma_\nu$ where there is one virtual nucleon or nucleon resonance. The diagrams in Figure 2.18 a) through e) are evaluated in terms of the nucleon and deuteron masses, charges, and magnetic and quadrupole moments. The contact term, shown in Figure 2.18 f), ensures gauge invariance. The amplitude of the contact term is not zero because the deuteron wave function deviates from the asymptotic Yukawa form at short distances [54]. The contact term is particularly im-

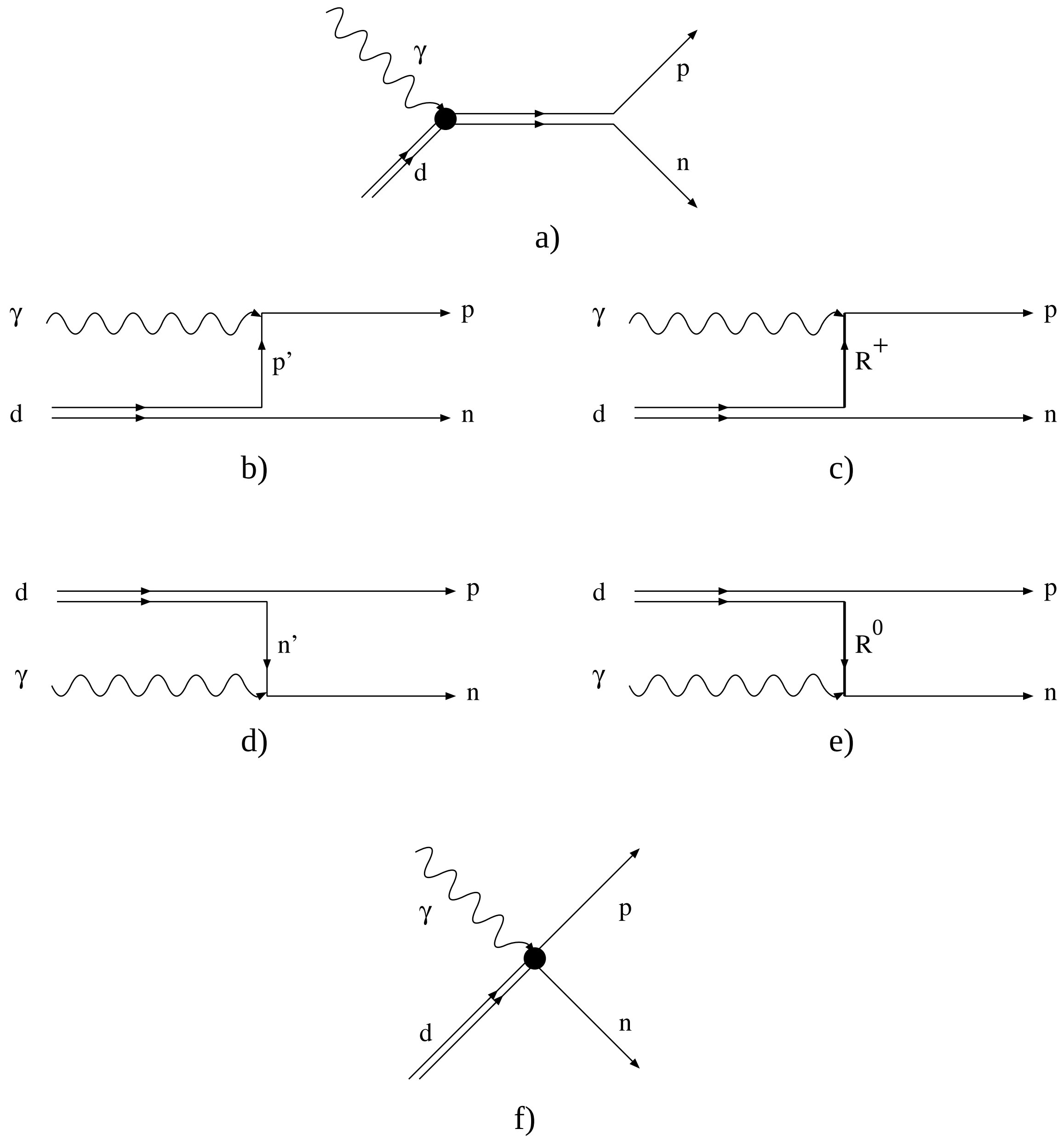

Figure 2.18: Tree level diagrams for deuteron photodisintegration at asymptotic energies considered in [21]. Figures a), b), d), and f) correspond to NN configurations of the deuteron. Figures c) and e) correspond to NN* configurations. Figure f) is the contact term and is important at asymptotic energies.

portant because it probes small internuclear distances, but realistic potentials are not suitable to evaluate the contact term at these distances. Thus, in analogy with [55], the form factor is approximated at high energies to have a three-pole form,

$$G_{N(N^*)}(-k^2) = C_{N(N^*)}\left[\frac{\beta^2_{N(N^*)}}{2} - k^2\right]^{-\epsilon}, \tag{2.45}$$

where $\epsilon = 3$ is a parameter that can be used to test the energy scaling behavior. The factor β^2 is identified with the mass of the pion, m_π^2. The relative four-momentum between the proton and the neutron is given by $k^2 = (p_p - p_n)^2/4$. The ratio, $\alpha \equiv C_{N^*}/C_N$ describes the ratio of the form factors in the dNN and dNN^* vertices. When the resonance is added ($\alpha \neq 0$), the nucleon electromagnetic moments are renormalized which changes the ratio of electric and magnetic transitions in the amplitude.

The energy dependence for the cross section is given by

$$\frac{d\sigma}{d\Omega_{c.m.}} \sim \frac{1}{s\,(s - m_d^2)^{2\epsilon-1}} f(\theta_{cm}, s);\;\; f(\theta_{cm} = 90^\circ, s) \equiv 1. \tag{2.46}$$

The function $f(\theta_{cm}, s)$ is defined to be

$$f(\theta_{cm}, s) = \frac{d\sigma/d\Omega(\theta_{cm}, s)}{d\sigma/d\Omega(90^\circ, s)}. \tag{2.47}$$

The function $f(\theta_{cm}, s)$ is expected to be independent of s only in a region of θ_{cm} near 90° ($50^\circ < \theta_{cm} < 130^\circ$). Outside of those limits, $f(\theta_{cm}, s)$ is modeled to be an increasing function in s.

The dotted line in Figure 2.5 shows the results of the calculation presented in [21] at $\theta_{cm} = 90^\circ$, normalized to experimental data at $E_\gamma = 1$ GeV. The curve assumes no contribution from the nucleon resonance ($\alpha = 0$) and uses the three-pole form for G_N ($\epsilon = 3$). In the intermediate region, $E_\gamma = 1.2$ - 3.3 GeV, the curve exhibits scaling similar to that predicted by dimensional scaling.

A more recent discussion by Dieperink and Nagornyǐ [56] compares a covariant approach and a light-front approach. For the lowest order Fock states, the models yield different results. The covariant approach yields the form factor given in

Equation 2.45. The light-front approach produces a form factor as a function of two variables,[2]

$$G^{lf}(\eta, -k^2) = C_N \left[\beta_N^2 - k^2\right]^{-\epsilon} \phi_\kappa(\alpha) \quad (2.48)$$

$$\alpha = 1 - \sqrt{\frac{s - 4m_N^2}{s}} \cos(\theta_{cm}), \quad (2.49)$$

where $\phi_\kappa(\alpha) = \alpha^{-\kappa}$, and κ is a parameter to help describe the angle dependence of the form factor. At $\theta_{cm} = 90°$, both formalisms lead to nearly the same result as $\alpha = 1$. However, at other angles, the dynamics change rapidly. Results from the light-front approach calculations are shown with the experimental data in Chapter 6.

[2]Note that here α does not represent the ratio of the form factors for dNN and dNN^* as discussed earlier. In [56], the variable α is equivalent to 2η as described in [21].

Chapter 3

Experiment

3.1 General Overview of Apparatus

Experiment E89-012 was completed between February and April 1996 in Hall C at the Continuous Electron Beam Accelerator Facility (CEBAF) in Newport News, Virginia. Additional data were taken during September 1997. A continuous wave electron beam, ranging in energy from 0.845 GeV to 4.045 GeV, was used to strike a copper radiator to produce a bremsstrahlung spectrum of photons. These photons then irradiated an aluminum cylinder target with length 15 cm filled with liquid deuterium (LD_2). Photo-protons from the $d(\gamma, p)n$ reaction are then detected in the High Momentum Spectrometer (HMS) over a nominal solid angle of ~6.7 msr. An illustration of this setup is shown in Figure 3.1.

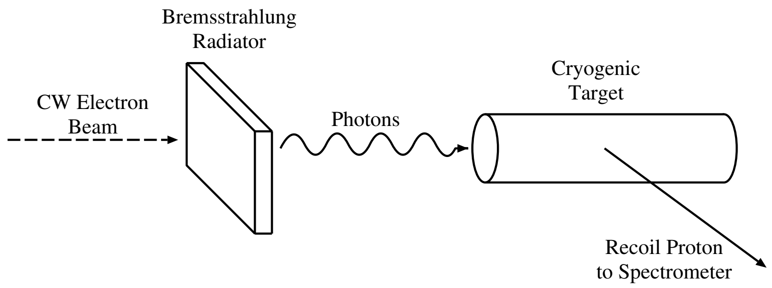

Figure 3.1: Schematic diagram of experimental setup. The electron beam strikes a copper foil radiator. The resulting bremsstrahlung photons strike the cryogenic deuterium target. Recoil protons from photodisintegration are then detected by the High Momentum Spectrometer.

During the experiment, a second spectrometer, the Short Orbit Spectrometer (SOS), was used to record deuteron photodisintegration data at other kinematic settings. The HMS was also used at times to record pion photoproduction $d(\gamma, d)\pi^{\circ}$ data. However, the analysis of these data are beyond the scope of this document.

3.2 Electron Beam

The CEBAF accelerator provides an unpolarized, continuous wave electron beam. Figure 3.2 shows a schematic of the layout of the electron beam path in the CEBAF accelerator. The injector produces a beam of electrons by thermionic emission. The electrons are bunched together so that they have a characteristic RF frequency of 1497 MHz. The electrons are then accelerated to 45 MeV where they enter the main accelerator area. The beam is accelerated through a recirculating linear accelerator (linac). There are two physical sets of linacs: one on the north side and one on the south side of the facility. Each linac increases the electron beam energy by 400 MeV in a series of superconducting RF cavities. After each linac, the beam is bent in an arc to enter the next linac. The beam can be recirculated through the linacs up to five times. The recirculated beams are combined as they enter each linac. At the exit of each linac, they are separated into their component beams before entering the bending arcs which steer the beams to the entrance of the next linac. At the end of the south linac, the beam can be extracted in the beam switchyard (BSY) and sent to any of three experimental halls: Hall A, Hall B, or Hall C. This allows for 5 different electron beam energies: 845, 1645, 2445, 3245, and 4045 MeV. The energy dispersion of the beam, $\Delta E/E$, is less than 10^{-4} and the angular emittance of the beam is less than 2×10^{-9} mrad [58]. For this experiment, the maximum beam current was 25 μA for the data taken in 1996. The maximum beam current was 45 μA for the data taken in 1997.

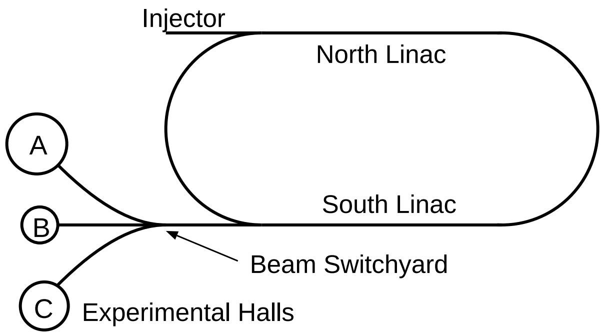

Figure 3.2: Overhead schematic of the accelerator at CEBAF.

3.3 Beam Charge Measurement

To properly normalize the data, the total beam charge deposited on the radiator and the target must be known. The charge is measured by using three cylindrical resonant cavities tuned to the RF structure of the beam. Associated electronics measures the signal from each resonant cavity, continuously recording the beam current during the experiment. A Bergoz Parametric Current Transformer is used to calibrate the resonant cavity signals and also provides continuous measurement of the beam current as a check on the performance of the resonant cavities. Details of each of the beam current measuring devices are presented in Appendix A.

3.4 Fast Rastering System

Due to the high intensity of the electron beam, with a nominal beam profile of $\leq$ 200 μm FWHM in both $\hat{x}_{beam}$ and $\hat{y}_{beam}$ (see Section 3.7.1), a rastering system is used to disperse the beam over a wider area to reduce the chance of localized boiling in the cryogenic target, which would produce a systematic reduction and fluctuations of the target density.

The fast raster system is located 25 meters upstream of the target. It operates by using two pairs of steering magnets which divert the beam in a sinusoidal pattern horizontally and vertically, respectively. The vertical bending magnets are driven at a frequency of 17.0 kHz, and the horizontal bending magnets are driven at a frequency of 24.2 kHz. The frequencies of each set of magnets are different to prevent correlation between the two independent bending magnets. In other words, the beam is distributed over the entire face of a square cross section once it reaches the target. The integrated profile of the beam is a 1 mm x 1 mm square.

3.5 Radiator

The bremsstrahlung radiator assembly consists of 5 sets of copper foils. Each foil is cut into rectangles approximately 1.5 by 0.75 inches, and each radiator is composed of a set of foils. The radiators have nominal thicknesses: 2%, 4%, 6%, 7%, and 8% of one radiation length. The assembly is located approximately 1.2 meters upstream of the target and can be positioned remotely to place the center of any one set or none of the copper radiators directly in the path of the electron beam.

For experiment E89-012, only the 4% and the 6% (nominal) copper radiators were used. The actual foil thicknesses for each of the two radiators were calculated [58] by measuring the total area and mass of each foil to determine the thickness. Table 3.1 lists the actual thickness of the two radiators used in the experiment, including the dimensions of each foil that is used in each radiator.

Nominal Thickness (% of radiation length)	Mass (g)	Area (cm^2)	Thickness (g/cm^2)	Total Thickness (% of radiation length)
4	1.5380	7.267	0.2117	3.489 ± 0.003
	1.5491	7.214	0.2147	
	0.1620	7.264	0.0223	
6	4.3316	7.260	0.5966	6.021 ± 0.003
	0.6283	7.064	0.0889	
	0.6443	7.264	0.0887	

Table 3.1: Nominal and actual thicknesses of copper radiators used in experiment E89-012, including thicknesses for each foil that form the radiators.

3.6 Target

The Hall C target at CEBAF includes a solid target ladder and a cryogenic target ladder. The experiment required only the cryogenic targets. Figure 3.3 shows a schematic of the cryogenic stack. The cryogenic stack consists of three different target loops, allowing for three different cryogens to be used as a target. For each cryogen there are two cells of differing nominal target lengths: 4.2 cm and 15.5 cm. The cryogen stack also includes two dummy positions consisting of only the endcaps for both target lengths to simulate an empty target for background measurements. The stack can be lifted remotely to choose any of the six cells or the dummy positions as the target.

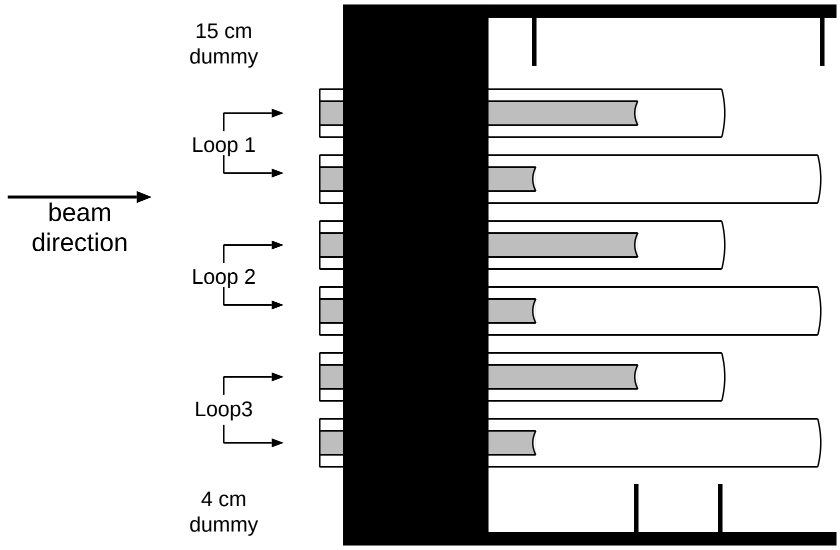

Figure 3.3: Schematic of the CEBAF Hall C cryogenic target stack.

The target cells are made of aluminum beer can stock and are 6.48 cm in diameter. The target windows are curved. Therefore a change in beam position will change the effective target length. The change in target thickness is estimated to be less than 0.5% for a 2 mm radial shift in the beam position from the center of the cell [59]. The dummy positions are two flat aluminum strips; they have no curvature. Table 3.2 gives the measured dimensions at cryogenic temperatures of each of the 15 cm cells used in this experiment [59]. The dummy target windows are thicker (about 1 mm) than their corresponding windows in the cryogen cells in order to record background measurements at a faster rate.

Target Loop	Measured Length (cm)	Entrance Window Thickness (cm)	Exit Window Thickness (cm)
1	15.34 $\pm$ 0.04	0.0071 $\pm$ 0.0003	0.0119 $\pm$ 0.0005
2	15.19 $\pm$ 0.04	0.0071 $\pm$ 0.0003	0.0130 $\pm$ 0.0005
3	15.12 $\pm$ 0.04	0.0071 $\pm$ 0.0003	0.0135 $\pm$ 0.0005

Table 3.2: Measured dimensions of nominal 15 cm target cells in the CEBAF cryotarget.

Target density depends on the temperature and pressure of the cryogen in the cell. Temperature control is more critical than pressure control because the liquid target is incompressible to first order. Pressure changes cause a $\frac{1}{\rho}\frac{d\rho}{dP} = 0.01\%/\text{PSIA}$ change in the target density. However, temperature changes cause a $\frac{1}{\rho}\frac{d\rho}{dP} = -1.25\%/\text{K}$ change in density. Therefore, temperature must be monitored precisely. Gaseous helium, supplied from the CEBAF Central Helium Liquefier at a nominal temperature of 15K, is used to cool the cryogen. Electrical heaters use feedback from Lakeshore Cernox heat-dependent resistors in each target loop of the cryogen to keep the temperature stable. For this experiment, a liquid deuterium target was used and the temperature was kept at 22.00 $\pm$ 0.05 K. Additional details of target operation and specifications can be found in [60].

3.7 High Momentum Spectrometer

After the bremsstrahlung photons strike the target, the reaction products are detected by the Hall C High Momentum Spectrometer (HMS). The main feature of the HMS is the ability to detect singly charged particles with a momentum up to 7.5 GeV/c over a large solid angle. Table 3.3 gives the performance limits of the HMS [61].

HMS Specification	Limits
Momentum Acceptance	± 9%
Momentum Resolution	< 0.1%
Solid Angle	< 6.74 msr
Scattering Angle Limits	12.5° - 90°
Scattering Angle Acceptance	± 27.5 mr
Scattering Angle Resolution	± 0.8 mr
Out of Plane Angle Acceptance	± 70 mr
Out of Plane Angle Resolution	± 0.8 mr
Target Length Acceptance	10 cm
Vertex Reconstruction Resolution	± 1 mm

Table 3.3: CEBAF Hall C HMS performance limits

Figure 3.4 shows a side view of the HMS magnets and the shield house containing the detectors. The HMS magnets operate in a QQQD array. Three superconducting quadrupoles act as focusing magnets, and a superconducting dipole with a bend angle of 25° provides momentum dispersion. Q1 and Q3 focus in the scattering angle direction; Q2 focuses in the out of plane angle direction.

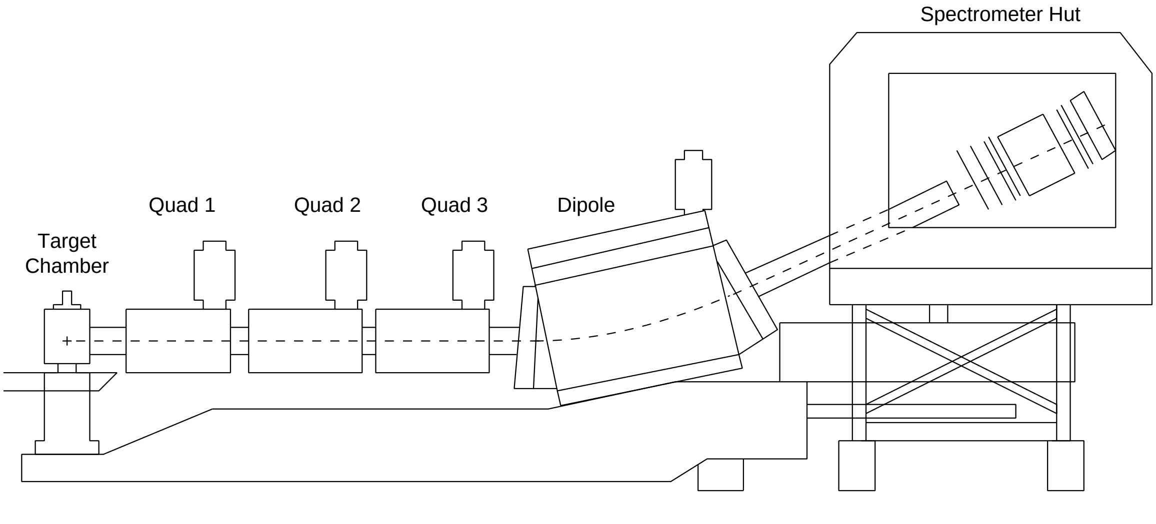

Figure 3.4: Side view of the High Momentum Spectrometer (HMS)

The HMS magnets are used in a point-to-point tune, wherein the magnets focus particles emanating from a point located at the target to a point in the focal plane located between the two drift chambers (discussed in Section 3.7.3). This tune provides optimal vertex reconstruction at the target.

The detectors are housed in a lead-lined concrete "shield house". Figure 3.5 shows the detectors used by the HMS and their locations relative to the nominal focal plane. The true focal plane can be approximated as a plane tilted about 85° from the nominal focal plane. However, it is more convenient to use the nominal focal plane in data analysis.

3.7.1 Coordinate Systems

The coordinate systems used for the HMS follow the conventions outlined in the TRANSPORT program [62]. Figures 3.6 and 3.7 give a graphical view of the coordinate systems at the target and for the HMS. The $\hat{z}_{HMS}$ axis lies along the central ray of the HMS. The $\hat{x}_{HMS}$ axis lies along the dispersive direction, with increasing x leading to higher momentum particles. To maintain a right-handed coordinate system, the $\hat{y}$ axis points horizontally to the left while looking downstream.

3.7.2 Collimator

In order to have a well-defined solid angle over the central part of the HMS acceptance, a collimator is used to reject particles that are outside of chosen limits.

The collimator is composed of machinable Heavymet material (90% Tungsten, 4% Copper, 6% Nickel, $\rho = 17$ g/cm^3) and is positioned 1.26 meters from the target along the HMS spectrometer z axis. It has an octagonal aperture in the center which allows the scattered photo-protons to pass through. This aperture restricts the solid angle of the spectrometer to a well-defined geometry in the center of the spectrometer acceptance.

Figure 3.8 shows the dimensions of the collimator. The aperture is flared on the exit side to allow for the angular dispersion of scattered particles from the target without striking the inner edge of the collimator. The collimator allows for a geometric

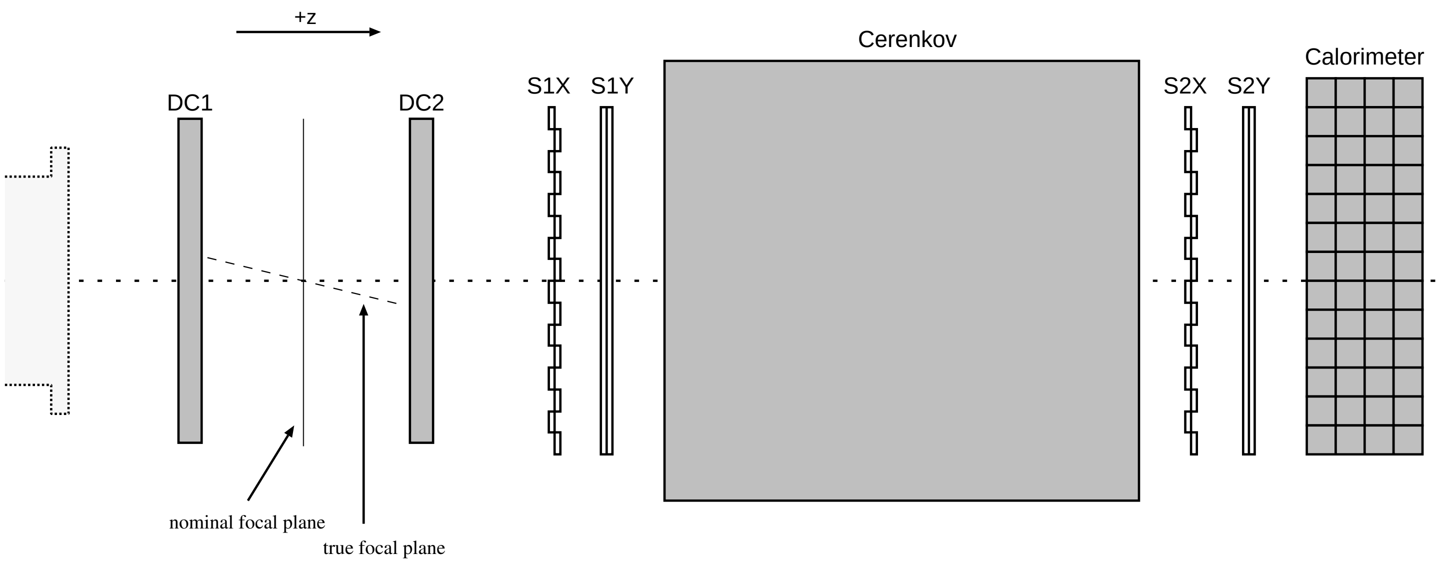

Figure 3.5: Schematic diagram showing the relative locations of the detectors in the High Momentum Spectrometer (HMS).

solid angle of 6.74 msr for a point source. However, for the extended target used for this experiment, the integrated geometric solid angle is reduced as scattering angle acceptance becomes smaller for reaction products originating some distance away from the center of the target. Other factors in HMS acceptance may also reduce total solid angle. See Section 5.4.1 for a description of the calculation for the HMS solid angle.

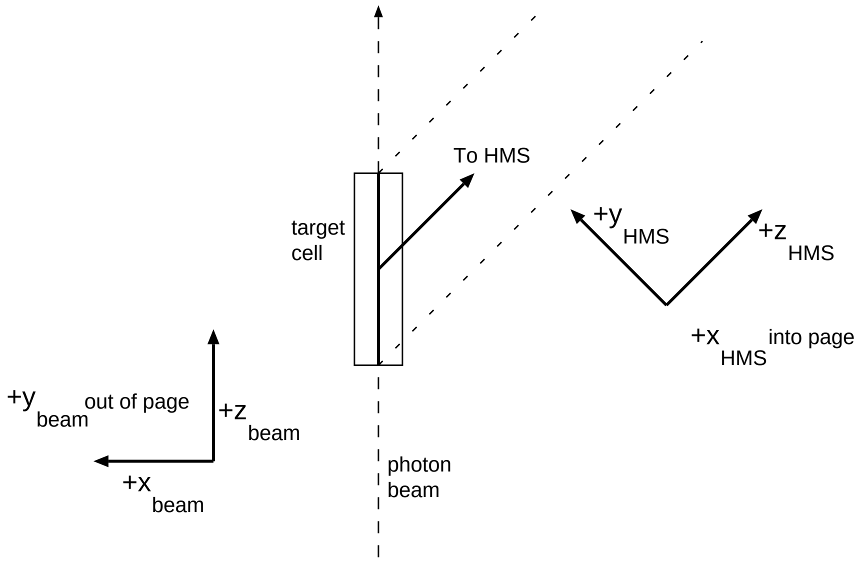

Figure 3.6: Coordinate systems as seen from above for the beam before it strikes the target, and for reaction products detected by the HMS.

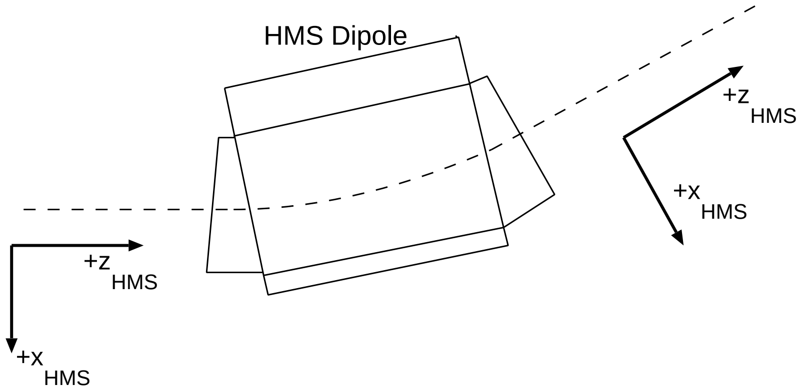

Figure 3.7: Coordinate system for the HMS as seen from the side before and after the dipole bend.

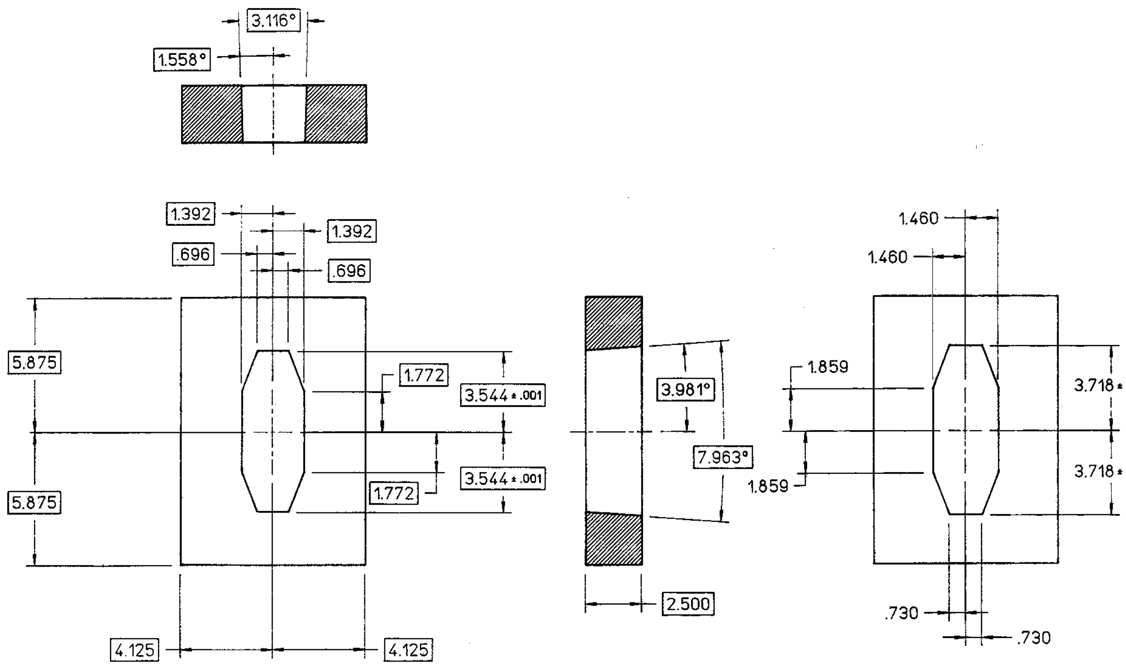

Figure 3.8: Schematic of HMS collimator. All dimensions are in inches.

3.7.3 Drift Chambers

Two drift chambers are used in the HMS to determine particle trajectories through the spectrometer. Each drift chamber contains six separate planes of grounded sense wires (25 μm diameter gold-plated tungsten) spaced 1.0 cm apart in a gas mixture of argon and ethane (50%-50% mixture by weight). The six planes are ordered x, y, u, v, y', x'. Figure 3.9 gives a pictorial representation of the order of each of the six planes. The x and x' planes offer two measurements of the particles trajectory in the dispersive direction. The y and y' planes offer two measurements in the transverse direction. The u and v planes are rotated 15° and -15° from horizontal. Figure 3.10 shows the direction of the wires in each plane.

The planes are spaced 1.8 cm apart. In between each sense wire is a field wire (150 μm gold-plated copper-beryllium) which is held at a high negative potential (-1800V to -2500V). On both sides of the sense planes is an additional plane of field wires, held at the same high negative potential. This creates a rectangular 'cell' around

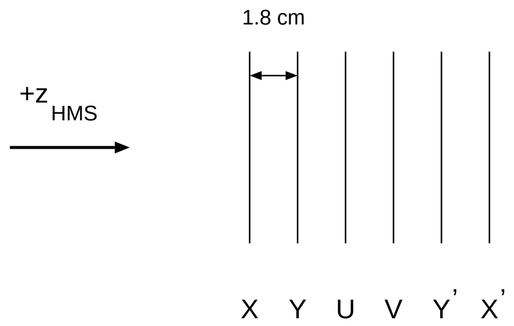

Figure 3.9: HMS drift chamber planes. An incoming particle traverses each of the six planes shown above from left to right.

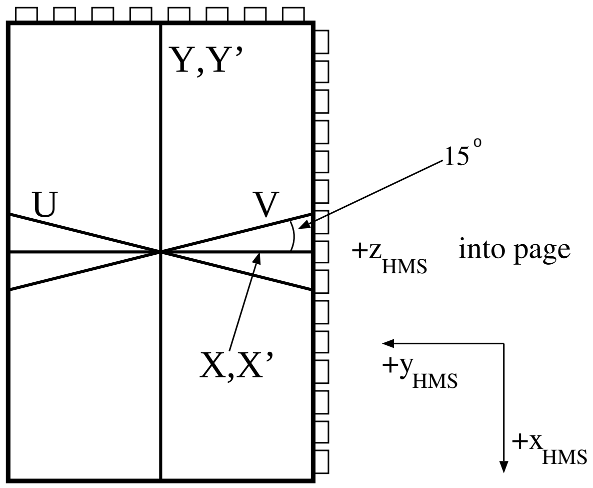

Figure 3.10: Front view of the HMS drift chamber wire layout. The lines show the direction the sense wires lay for each of the six planes.

each sense wire (see Figure 3.11). As a charged particle traverses the drift chamber, it ionizes the gas mixture in the chamber. The ionized electrons then drift through the electric field gradient generated by the chamber wires to the nearest sense wire and are detected. The drift time of the ionized electrons is used to determine the distance from the incoming particle to that sense wire [63].

The incoming particle can pass on either side of a sense wire. To help resolve this ambiguity, the x, x' planes and the y, y' planes are offset by one-half cell length. The coordinate information from both drift chambers is then used to determine the

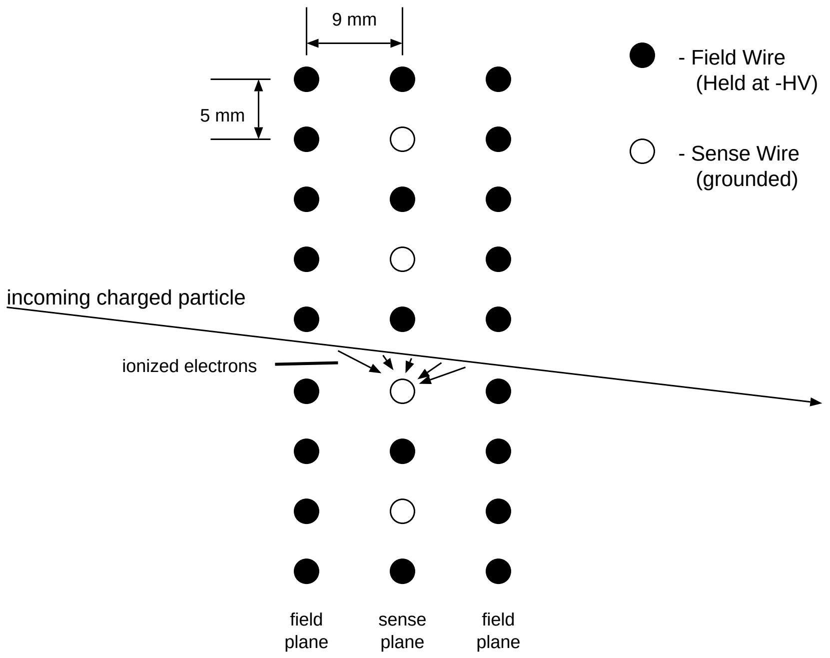

Figure 3.11: Wire layout for a typical plane in the HMS drift chamber. Electrons ionized by the charged incoming particle drift along the electric field gradient created by the field wires toward a grounded sense wire.

track of the incoming particle through the spectrometer. The two drift chambers are spaced 81.2 cm apart, and each has an active area of about 113 cm (x) by 52 cm (y). Further information on the HMS drift chambers can be found in [64].

3.7.4 Scintillator Hodoscopes

There are two pairs of scintillator hodoscope planes on either side of the Cerenkov chamber. The x planes have 16 individual strips of plastic scintillator (paddles) arranged horizontally. The y planes have 10 scintillator strips arranged vertically. The paddles are 8 cm wide, have a thickness of 1 cm, and are composed of BiCron BC404 plastic scintillator. Each scintillator paddle is wrapped in aluminum foil and Tedlar to make them light tight. Philips XP2282B phototubes are affixed to UVT lucite light guides and placed at each end of every paddle. The scintillator paddles are arranged in a staggered fashion as shown in Figure 3.12 with an overlap of about

0.5 cm to prevent gaps between elements. Each of the four planes has an active area of 120.5 cm by 75.5 cm. Figure 3.13 shows the layout of the four scintillator planes in the spectrometer. Each x-y pair of planes are spaced about 19.7 cm apart, and the front and back pair of planes are spaced about 220 cm apart.

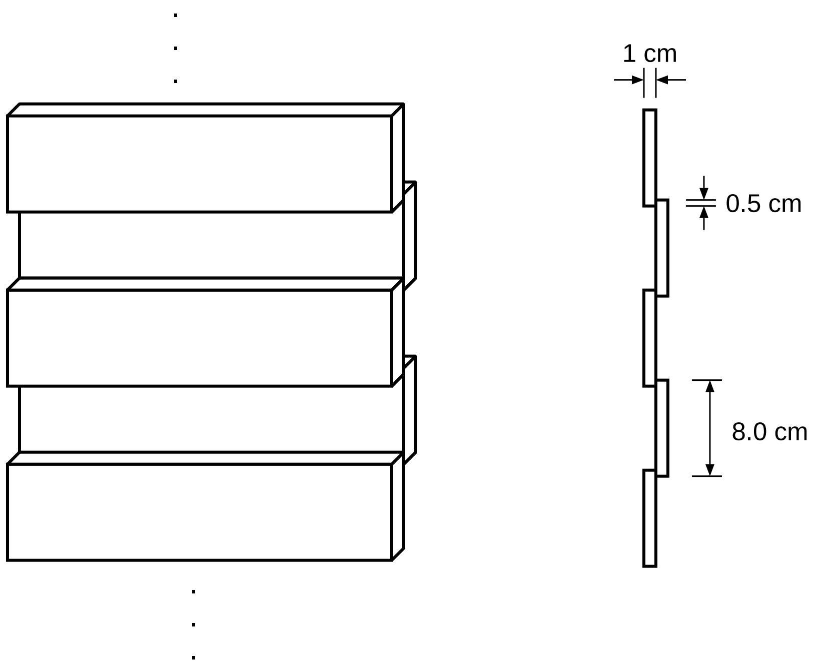

Figure 3.12: Layout for part of an HMS scintillator hodoscope plane. The x planes have 16 scintillators and the y planes have 10 scintillators staggered as above.

As the incoming charged particle traverses one of the paddles in each plane, it excites the atoms in the scintillator. These atoms radiate photons as they return to their ground state [65]. Some of these photons are reflected internally through the scintillator and are detected by photomultiplier tubes (PMTs) at either end of the paddle.

The signal pulses from the PMTs from each of the hodoscope planes are used to form a trigger. Event data is recorded once signals are detected in paddles in any 3-out-of-4 or 4-out-of-4 hodoscope planes, depending on the trigger requirements. Section 3.8 gives an explanation of how the scintillator planes are used in the trigger.

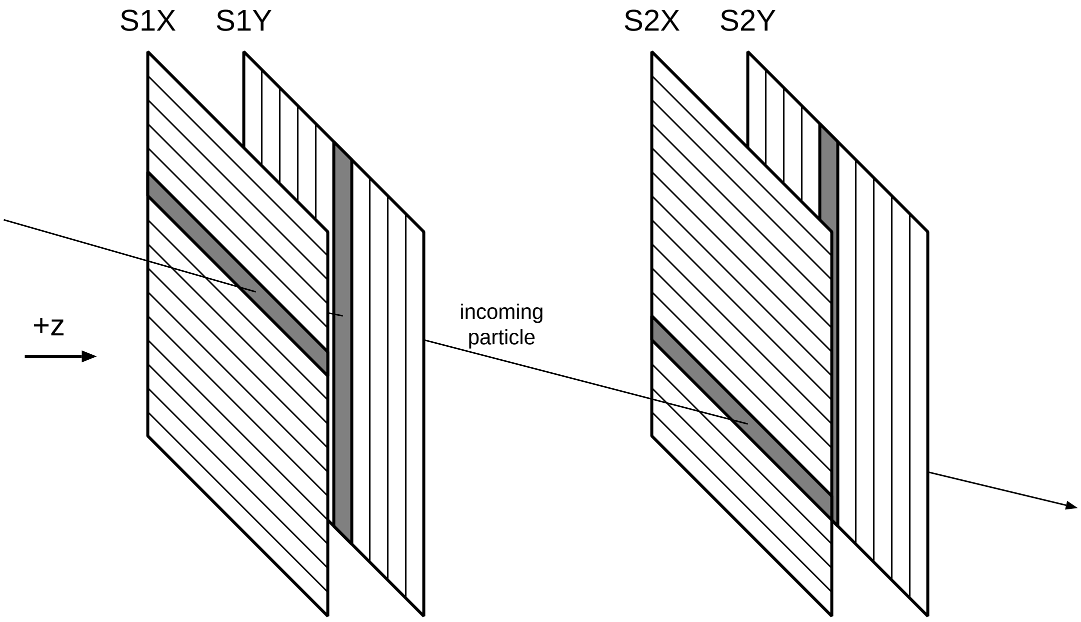

Figure 3.13: Layout of HMS hodoscope paddles in each of the four planes.

The fast time-response of the scintillators is also used in measurement of particle time-of-flight (tof). Information from the drift chambers gives the track of the particle through the spectrometer. Timing information from the hodoscope planes indicates the time when the particle traversed each plane. Using the time of flight and the distance of the particle track between each plane, the particle velocity is found. This is specifically useful in particle identification. Because incoming particles have momenta which are near the central spectrometer momentum setting, particles of different mass will have noticeably different velocities. Section 4.2.1 describes how the hodoscope is used for particle identification.

3.7.5 Cerenkov Detector

The HMS Cerenkov detector is a cylindrical steel tank with a diameter of about 150 cm and a length of about 165 cm. It is used in this experiment for particle identification purposes, specifically to separate pions and protons at high momenta, where the separation between the hodoscope planes is not large enough to give adequate resolution in time-of-flight measurements.

The Cerenkov detector operates by detecting Cerenkov radiation emitted by an incoming particle as it traverses a medium at a velocity greater than that of light in that medium [66]. This radiation, which is peaked in the ultraviolet range, is emitted in a cone and is directed towards two mirrors on the downstream end of the detector. The light is reflected by the mirrors and focused onto two 5-inch Burle 8854 PMTs. The PMT front surfaces have a wavelength-shifting coating applied to improve the efficiency in the ultraviolet wavelengths.

The velocity at which the incoming particle will start to emit Cerenkov radiation depends on the medium in the tank. That velocity corresponds to $\beta = c/n$ where c is the speed of light in a vacuum, and n is the index of refraction of the medium. For this experiment, the Cerenkov tank is filled with 1 atm of Perfluorobutane (C_4F_{10}) gas. The index of refraction, n, is 1.00143 for 1 atm at 300 K, which gives a threshold $\beta = 0.9986$. Charged pions reach the threshold velocity at $p_\pi = \sqrt{\frac{m_\pi^2\beta^2}{1-\beta^2}} = 2.6$ GeV. The threshold momentum for protons is $p_p = 17.5$ GeV, well beyond the maximum momentum of the HMS. Therefore the HMS Cerenkov detector can be used for π-p separation above $p = 2.6$ GeV.

3.7.6 Lead Glass Calorimeter

The final detector in the HMS is the calorimeter which consists of TF1 lead-glass blocks with dimensions (10 cm x 10 cm x 70 cm) wrapped in one layer of aluminized mylar and two layers of Tedlar. The blocks are stacked horizontally 13 layers high and 4 layers deep. The calorimeter assembly is rotated 5 degrees along the y_{HMS} axis to avoid loss due to finite distance between each block.

The calorimeter measures the energy deposited in each block as the incoming particle traverses the detector. If the incoming particle is an electron, it loses energy through bremsstrahlung, which then creates a shower of particles. The Cerenkov light emitted by this shower is detected by a Philips XP3462B 3-inch phototube located on one end of each block. The sum of the signals from the PMTs is proportional to the energy of the incoming particle.

This detector is used mainly for particle identification purposes to separate pions from electrons, and thus is not directly used in the analysis of this experiment. However, it is used in a limited way to calculate tracking efficiencies (see Section 4.3) and assist in calibration of the hodoscope time-of-flight (see Section 4.2.1).

Detailed information on the design and use of the lead-glass calorimeter will be published in another document [67].

3.8 Data Acquisition and Trigger

The HMS pretrigger for this experiment is set when a signal is received from a scintillator paddle in any 3 of the 4 hodoscope planes (S1X, S1Y, S2X, S2Y). At some kinematics, where the data rate is high, the pretrigger module is changed to accept a pretrigger only when a signal is received only from all 4 hodoscope planes. Figure 3.14 shows a layout of the pretrigger electronics before it is sent to the Trigger Supervisor (TS). This pretrigger logic diagram is a simplified version of the more general pretrigger that is used in Hall C. The portions of the pretrigger that are not important to this experiment are unused and are removed from the diagram.

The scintillator pretrigger SCIN is set high when signals are received from any 3 or 4 out of 4 scintillator planes. This also sets the gates ELLO, ELREAL, and PRETRIG high automatically. In other experiments, these gates have other inputs that can be used to set a veto on a pretrigger based on signals from the cerenkov detector and shower calorimeter. The signal from ELREAL is fanned out and recorded by scalers using gate widths in 30 ns increments up to 120 ns to test electronic dead time (see Section 5.4.7). The signal from each gate increments a hardware scaler and is sent to a TDC to record the time each gate occurred.

The pretrigger is sent to a LeCroy 8LM programmable logic module. An output for each pretrigger is sent to a hardware scaler to be incremented. When the data rate is very high and is beyond the capability of the data acquisition system to efficiently record the events, a prescale factor may be set where only a specified fraction of the events are sent to the TS.

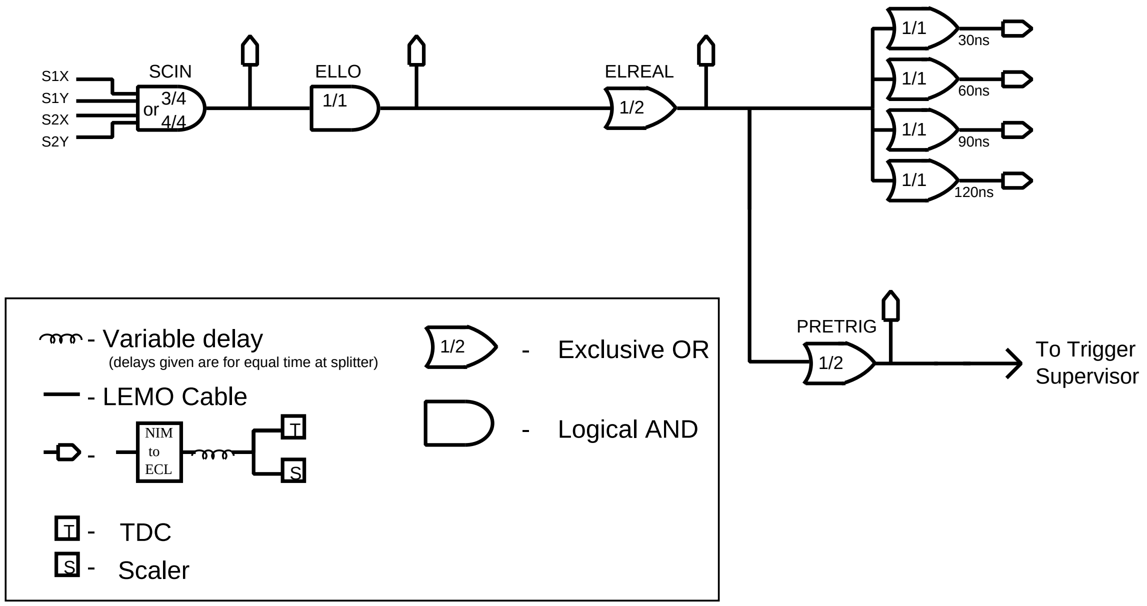

Figure 3.14: Schematic of the pretrigger electronics used in the experiment.

The pretriggers generated in the HMS and SOS are sent to a LeCroy 8LM programmable logic module (LC2365) which is the front end of the Trigger Supervisor electronics. Figure 3.15 shows a schematic of the Trigger Supervisor. When a run is started, TS GO is enabled. 1000 random pedestal triggers are generated by PED PRETRG and the data acquisition system records the readouts from the analog-to-digital converters (ADCs) to be used as a pedestal for the data. Then TS EN1 is enabled, which allows the data acquisition system to begin recording physics events. When a physics event is signaled by HMS PRETRG or SOS PRETRG, the data acquisition system records the readouts of the detector ADCs and TDCs. The Trigger Supervisor sets TS BUSY high while the data acquisition system records the readouts. This prevents an incoming pretrigger from prematurely recording another event. After the data acquisition system has completed recording the event information, TS BUSY is set low to allow for the next physics event. The eight outputs of the 8LM are given as four pretriggers and four triggers. The logic for each output is shown in Table 3.4. Detailed information about the operation of the Trigger Supervisor can be found in [68].

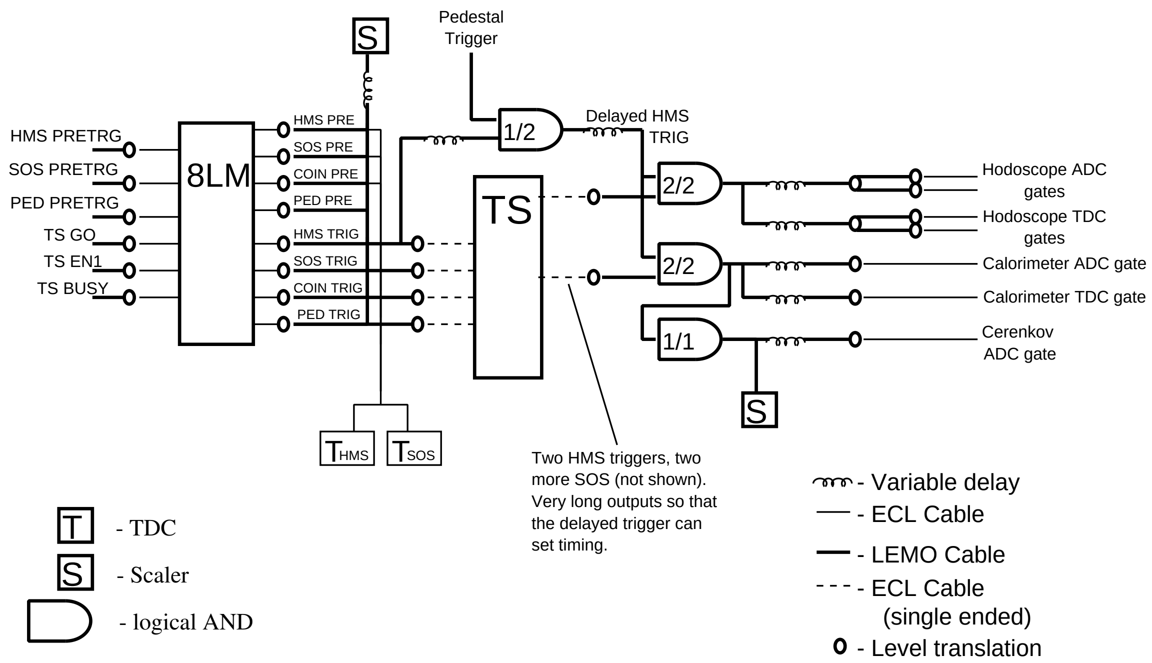

Figure 3.15: Schematic of the Trigger Supervisor.

Output	Logic
HMS PRE	HMS PRETRG ⊗ TS EN1
SOS PRE	SOS PRETRG ⊗ TS EN1
COIN PRE	HMS PRETRG ⊗ SOS PRETRG ⊗ TS EN1
PED PRE	PED PRETRG ⊗ $\overline{\text{TS EN1}}$
HMS TRIG	HMS PRETRG ⊗ TS EN1 ⊗ $\overline{\text{TS BUSY}}$
SOS TRIG	SOS PRETRG ⊗ TS EN1 ⊗ $\overline{\text{TS BUSY}}$
COIN TRIG	HMS PRETRG ⊗ SOS PRETRG ⊗ TS EN1 ⊗ $\overline{\text{TS BUSY}}$
PED TRIG	PED PRETRG ⊗ $\overline{\text{TS EN1}}$ ⊗ $\overline{\text{TS BUSY}}$

Table 3.4: The LeCroy 8LM output logic table. The symbol ⊗ implies a logical AND.

The CEBAF Online Data Acquisition (CODA) software [69] is used to record event data through a fiber-optic link to a Hewlett-Packard 9000/735 workstation.

There are many types of events that are recorded by CODA. Physics events describe those triggered by the detectors from either of the two spectrometers (HMS or SOS). When a physics event is generated by the TS, the control system reads data from a group of read-out controllers (ROCs) which are the CPUs in the VME and Fastbus crates that hold the ADCs, TDCs, and scaler information pertinent to each event. CODA then assembles the information from each ROC and builds the event that is recorded onto disk.

Other types of events include scaler events which are read out every two seconds. These are hardware data scalers that are reset to zero at the start of each run and increment throughout the run. They can be used for calibration purposes or to review rates when compared to a clock scaler that is included in these events. Slow control information, which includes slowly varying parameters such as high-voltage settings and beam line parameters, are read once every 30 seconds. The remaining events record the start of each run which includes information entered by the user about specific run information. An additional 1000 pedestal events are recorded at the start of each run in order to record the zero levels of each ADC. This is done by creating artificial trigger events for which there are no real events. Detailed information on the trigger and the data acquisition system can be found in [70].

3.9 Run Plan

The goal of the experiment is to measure $d(\gamma, p)n$ cross sections to within about 10% overall statistical accuracy. Table 3.5 shows the proposed statistical accuracy for the nominal kinematics studied in this experiment [71]. Data rates were estimated from the data from SLAC experiment NE17 and the rates for higher energies were extrapolated following the s^{-11} constituent scaling theory (see Section 2.2). The average beam current available from the CEBAF accelerator was limited to a maximum of about 25 μA CW. However, for the lower energy kinematics, the beam current was reduced to a nominal value of about 10 μA to reduce the data rate.

E_{beam}	HMS θ_{cm}			
(GeV)	37°	53°	70°	90°
0.845	5%			5%
1.645	5%	5%	5%	5%
2.445	5%	5%	5%	5%
3.245	5%	7%	7%	7%
4.045	5%	10%	15%	15%

Table 3.5: Expected statistical errors for each kinematics setting.

Background data using a hydrogen target were not taken due to problems with the CEBAF cryotarget. Only one target cell with deuterium was available for our main measurement. An empty target cell was used to measure background from the aluminum target windows (see Section 5.1.1).

Chapter 4

Event Level Analysis

Events that enter the spectrometer must be recorded in the data stream for later analysis. Signals from the scintillator hodoscope and the gas Cerenkov detector are used for particle identification. The drift chambers are used to determine particle trajectory through the spectrometer with help from hodoscope time of flight for timing information and the shower counter for crude particle identification. The particle track is then reconstructed through the use of optics matrix elements which use information about the focusing and bending magnets to find the position, trajectory, and momentum of the event at the target. All of this is done through the analysis software which distills the raw data into the quantities necessary to calculate the reaction cross section.

4.1 Analysis Software

Each event that is recorded contains information for analog-to-digital converters (ADCs) and time-to-digital converters (TDCs) for all drift chamber wires and photomultiplier tubes (PMTs) in the hodoscope, Cerenkov detector, and shower counter. The data streams includes events which read out incrementing scalers that are used for diagnostic and normalization purposes. The analysis of raw data for each event is completed using the Hall C analysis engine, discussed in detail in [70], which is run on an HP workstation in the HPUX 9.0 operating system. The results are stored as histograms and n-tuples generated with CERNLIB HBOOK libraries which are viewed with Physics Analysis Workstation (PAW) [72]. Text files are also generated to report the results for scalers which are read out for each run. The n-tuples are a series of variable values which detail the characteristics of each event. Calculation of the cross section is performed after analyzing the n-tuples with PAW, Physica [73], and other specialized routines.

4.2 Particle ID

Suitable particle identification methods must be applied to determine the type of particles that enter the spectrometer. Specifically, protons must be separated from pions and deuterons which result from other reactions occurring in the target.

For this experiment, a combination of particle time of flight (TOF) obtained from the scintillator hodoscope and signals from the gas Cerenkov detector are used for particle identification.

4.2.1 Hodoscope Time of Flight

A particle with low momentum can be identified by measuring the velocity, or equivalently, the time of flight, as it traverses the detectors in the spectrometer. This is accomplished using the HMS scintillator hodoscope (described in Section 3.7.4).

The hodoscope consists of two pairs of scintillator planes that are spaced approximately 220 cm apart. Each pair is segmented into 8 cm wide strips (paddles) in the $\hat{x}$ and $\hat{y}$ direction. PMTs are located on either end of each paddle. The PMTs detect the light that is produced in the paddle from ionization as the particle passes through each scintillator plane. The PMT signals are then sent to TDCs to record the time when the signal is detected.

The velocity is determined from the difference in time between the signals in each pair of scintillator planes and the distance traveled by the particle. The actual distance is calculated by including the particle trajectory angle determined by the tracking algorithm. The TOF velocity can be combined with the reconstructed momentum to calculate the particle mass,

$$M^2 = \frac{p^2(1-\beta^2)}{\beta^2}. \tag{4.1}$$

Figures 4.1 and 4.2 give examples of the mass spectrum that is obtained using TOF information for differing kinematics. Obvious peaks are seen for protons near ($m_p^2 = 0.88$ GeV^2) and for deuterons near ($m_d^2 = 3.52$ GeV^2). Figure 4.1 shows the mass spectrum for all events which track back to within the target, but Figure 4.2 has an additional cut on the reconstructed photon energy, E_γ, such that it only includes events that are expected from photodisintegration.

The peak for pions at ($m_\pi^2 = 0.02$ GeV^2) is not easily seen due to the large difference in magnitude when compared to the proton peak. An example of the pion peak is shown in Figure 4.3. The relative magnitude of the peak in Figure 4.3 is increased when background events from $Al(\gamma,\pi)X$ reactions in the aluminum target endcaps are included.

Some peaks may not be centered where expected due to limitations in the hodoscope calibration. Deuterons and pions have scintillator ionization signal characteristics that differ from protons. As the TOF calibration is optimized for detecting protons, the peaks for pions and deuterons may shift slightly due to the non-optimal measurement of their velocities.

As the central spectrometer momentum increases, the mass spectrum resolution becomes worse. This is due to the finite time resolution of each scintillator. The time resolution for each HMS hodoscope plane is ~100 ps, with an overall resolution of ~180 ps [74]. The timing resolution can be quickly estimated from this experiment by assuming the proton peaks in the mass spectra are gaussians. Figure 4.4 shows the width of the proton peak as a function of the central spectrometer momentum squared for all kinematics studied in this experiment. By finding the relation of the width of the gaussian to the central spectrometer momentum, the overall resolution of the HMS hodoscope is estimated to be ~210 ps. The value is in line with the expected

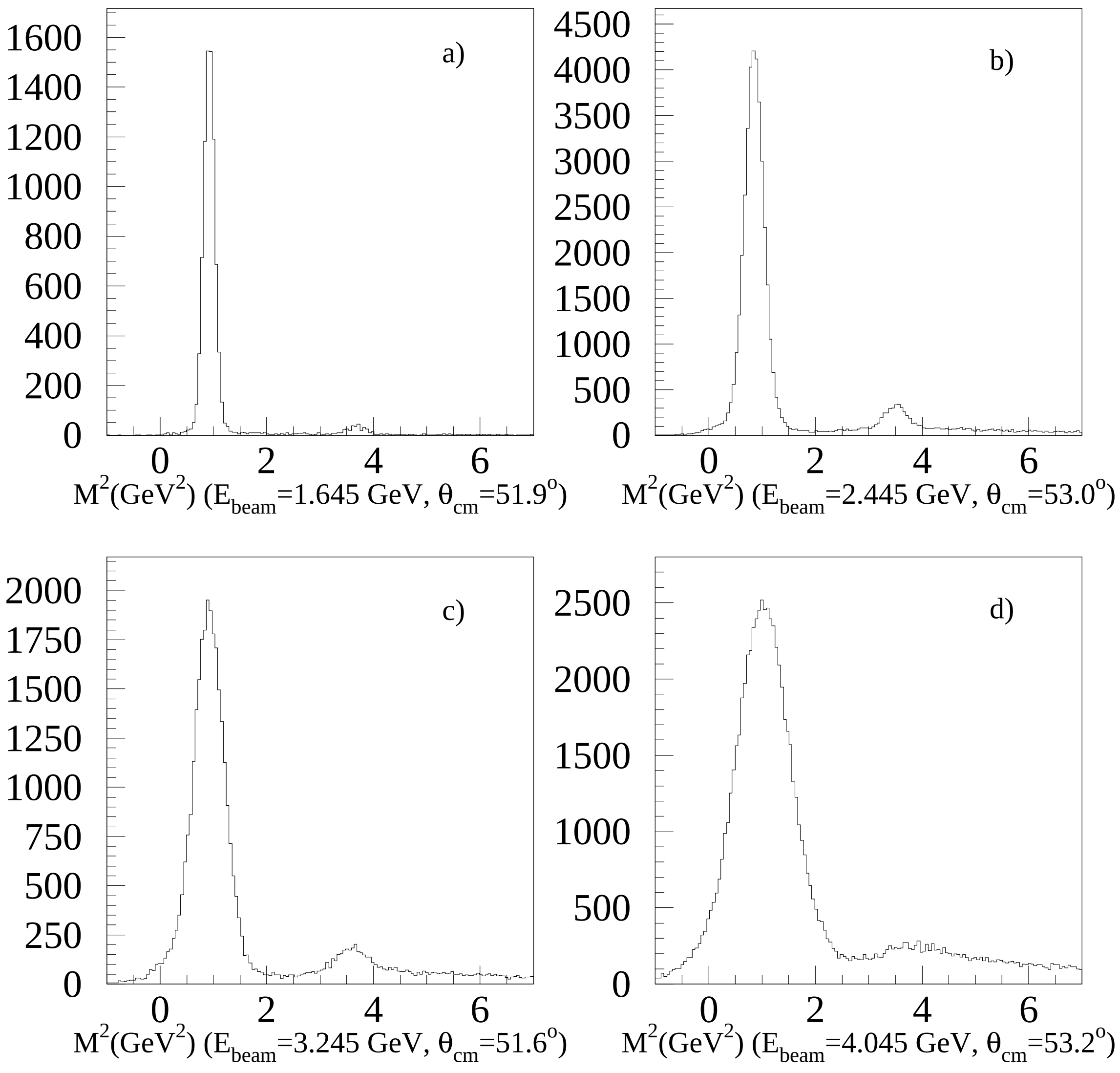

Figure 4.1: Raw particle mass spectrum. Figures a) through d) show the particle mass reconstructed from velocity determined through hodoscope time of flight and particle momentum reconstructed from tracking. Included are all events which reconstruct to a position within the target.

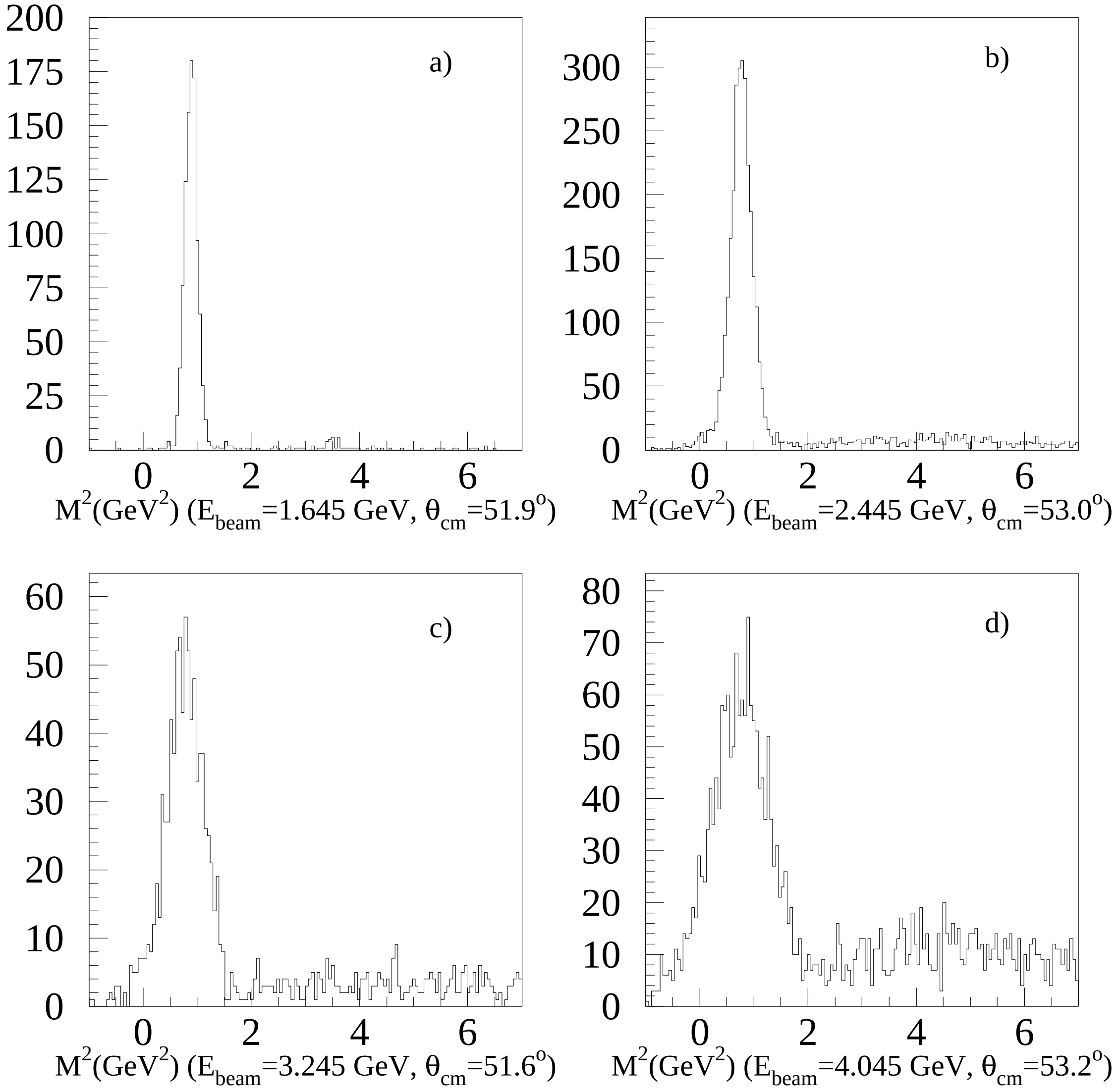

Figure 4.2: Raw particle mass spectrum. Figures a) through d) show the particle mass reconstructed from velocity determined through hodoscope time of flight and particle momentum reconstructed from tracking. These figures show the mass spectrum for events which reconstruct to a position within the target but only for -85 MeV $< E_\gamma - E_{beam} <$ -25 MeV.

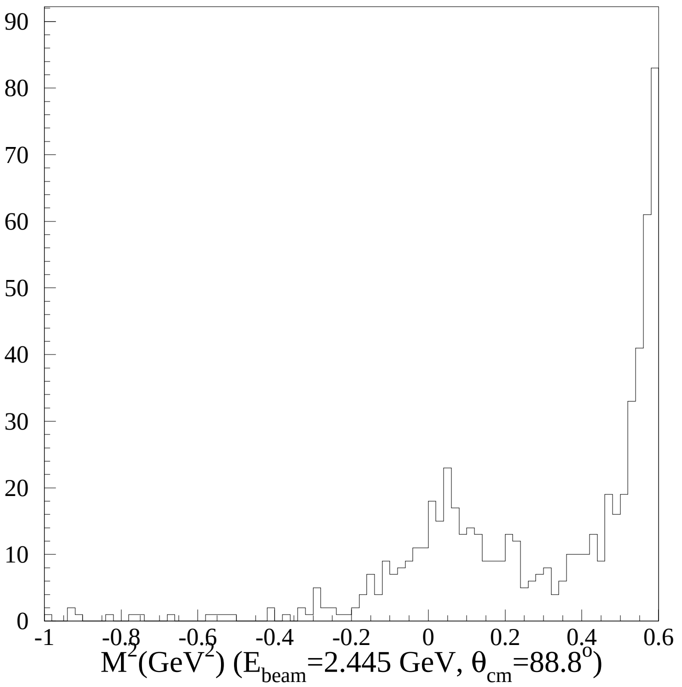

Figure 4.3: Example of the presence of pions in the raw particle mass spectrum for $E_{beam} = 2.445$ GeV, $\theta_{cm} = 88.8°$. The proton peak extends to the right. The height of the pion peak is enhanced in this figure by including background events which come from $Al(\gamma, \pi)X$ reaction from the target endcaps.

resolution given above, and is slightly higher due to limitations in the hodoscope calibration that is described below.

The finite time resolution limits the effectiveness of using time of flight as a sole method of particle identification. Above some threshold momentum, the peaks for pions and protons merge, making it difficult to separate the two peaks. This is seen at about $p_{HMS} \simeq 2.3$ GeV. Beyond that, other methods must be used to separate pions from protons. This is done with the HMS Gas Cerenkov described in the next section. Above $p_{HMS} \simeq 4.0$ GeV, the proton and deuteron peaks merge also, but no other method exists in this experiment to separate deuterons from protons. However, for both pions and deuterons, almost all pions and deuterons come from background processes. Separate background measurements, described in Chapter 5, are made to

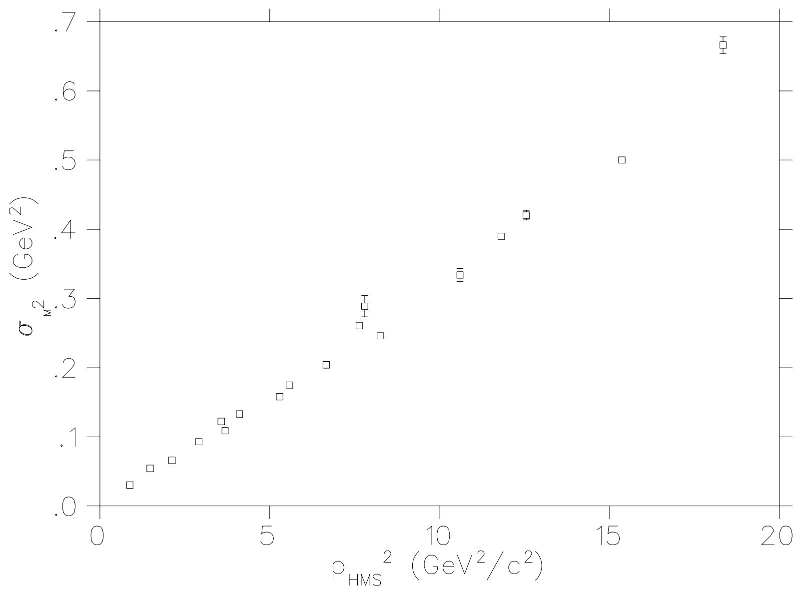

Figure 4.4: Relation between the width of the mass spectrum proton peak determined from TOF and p^2_{HMS} for all kinematics studied in this experiment. The relation can be used to determine the time resolution of the HMS hodoscope. Limitations in hodoscope calibration may give a value that is higher than expected.

help reduce deuteron and pion contamination.

Time of Flight Calibration

Measuring the time difference along the particle trajectory path length between the hodoscope scintillator planes requires very high precision. A particle with a velocity β near 1 travels the length of the hodoscope in less than 7.5 ns. The timing information from each scintillator paddle must be synchronized so that the time of flight is measured accurately.

Many factors need to be considered to adequately calibrate the hodoscope. Each PMT is connected via a cable to assorted discriminators, gates, and TDCs. There is a separate delay time associated with each PMT that corresponds to the different cable lengths and delay times of the electronics. These offsets must be eliminated. Also, as a particle travels through the scintillator, it deposits an amount of energy that depends on the velocity and type of particle. This energy travels through the scintillator as light to PMTs located on either end. Because the analog signal is sent to constant level discriminators, a large pulse triggers the TDC sooner than a smaller pulse. These pulse height variations can affect the overall time-of-flight measurements by several hundred picoseconds. As the scintillators have a time resolution of 70 - 100 ps when measured in a controlled environment [70], corrections must be applied for the varying pulse heights.

PMT pulse height corrections are determined by using a crossed set of scintillator paddles, one from the $\hat{x}_{HMS}$ plane and one from the $\hat{y}_{HMS}$ plane. This limits the region where the scintillator is hit, reducing the variations in the time it takes for the signal to reach the PMT. The mean time, which is the average of the times measured by both tubes on opposite sides of each paddle, is used to eliminate position dependence along the scintillator, leaving only the pulse height correction and an overall offset. After applying a rough pulse height correction to three out of the four PMTs, the remaining pulse height correction is given by the dependence on the ADC value for the fourth PMT that is fit to the form

$$\Delta t = PHC * \sqrt{max(0, (ADC/PHOFF - 1))} + t_0, \tag{4.2}$$

where ADC is the raw ADC value for the PMT, PHC and $PHOFF$ are the timing correction parameters, and t_0 is a timing offset between the two scintillators.

Additional corrections are applied for the velocity of light propagation within the scintillator. The propagation includes the path of the photons within each scintillator as most of the light bounces off the sides of the scintillator before reaching the PMT rather than taking a direct path. This average speed is calculated by comparing the time difference for PMT signals from opposite sides of each paddle as a function of the position of the track along the paddle. An average speed is calculated for each plane. All elements in that plane use the same offset.

Corrections for differences in cable lengths for each PMT are determined in a similar manner as for pulse height corrections. A mean time is generated for events for a crossed pair of scintillators with pulse height and velocity corrections included.

The offsets are then calculated to fit the velocity of the particle that is calculated from reconstructed particle momentum.

The standard calibration procedure uses a clean set of data which comes from electrons entering the spectrometer at a velocity $\beta \simeq 1$. For this experiment it is necessary to perform a calibration that is optimized to detect protons. Also, the pulse height characteristics of the proton as a function of proton momentum varies enough to require a new calibration for each kinematics. In most cases, it is sufficient to make a cut on protons given the initial set of timing offsets derived from the standard calibration for electrons. However, as proton momentum increases, it becomes more difficult to ensure that the events in the dataset for that calibration procedure are strictly protons. In these cases, a subset of the dataset is used. A cut is applied on the signal coming from the lead-glass calorimeter, similar to that outlined in Section 4.3 to determine tracking efficiency. As the calibration software relies on a high number of proton events to perform the procedure accurately, using a subset of the data results in a less than optimal calibration. This slightly increases the uncertainty in calculated particle mass beyond that expected from measured hodoscope time resolution.

Figure 4.5 shows the result of applying the hodoscope TOF calibration software for $E_{beam} = 3.245$ GeV, $\theta_{cm} = 68.7°$. It shows the reconstructed β spectrum for the protons used for the calibration and the distribution of the standard deviation of time measurements for each scintillator plane. For this example, the median value of 89 ps is near the expected resolution of the scintillators. Detailed information on the time of flight calibration software can be found in [75].

4.2.2 Gas Cerenkov Detector

The HMS Gas Cerenkov detector is useful in particle identification for those kinematics with high spectrometer momenta. Above $p_{HMS} = 2.3$ GeV, time-of-flight becomes an unreliable method to distinguish pions from protons. The HMS Gas Cerenkov chamber was filled with approximately 1 atm of C_4F_{10} gas at 300 K which

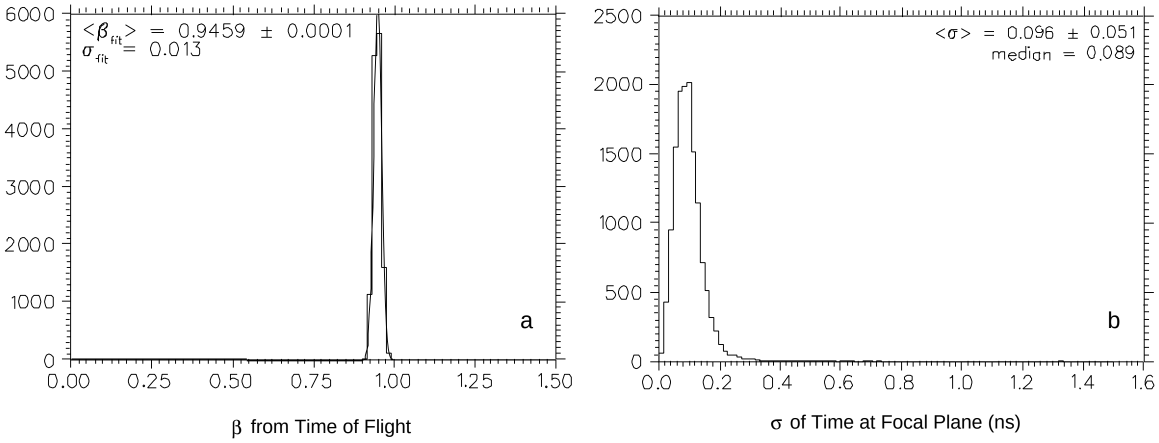

Figure 4.5: HMS time of flight and timing resolution for $E_{beam} = 3.245$ GeV, $\theta_{cm} = 68.7°$. Figure a) gives the velocity of the protons used in the calibration determined from tome of flight. Figure b) shows the distribution of standard deviations for time measurements made for each event. For each scintillator plane, a time is generated for the event to reach the focal plane. The standard deviation is calculated from the three or four measurements made by the hodoscope planes.

has an index of refraction of 1.00143. This gives a threshold velocity of $\beta = 0.9986$. Charged pions reach this threshold velocity at a momentum of $p_\pi = 2.6$ GeV. Above this threshold, pions emit Cerenkov radiation that is detected by PMTs installed on the sides of the chamber.

Figure 4.6 shows an example of how effective the Gas Cerenkov is at detecting pions and separating them from protons. The crosshatched area indicates those events which fire the Gas Cerenkov. The peak is centered around $M^2 \simeq 0.0$ GeV^2, as expected for pions. This pion peak is thus resolved with the Cerenkov detector despite being washed out by the large proton peak.

There is a small probability that a proton will also emit a photon that is detected by the PMTs as it travels through the Cerenkov tank due to scintillation in the Cerenkov gas. Protons can be misidentified as pions if these events with single photon counts were included. Therefore, a minimum of 3 photoelectrons must be detected by the PMTs in order to identify the event as a pion. There may be a possibility of misidentifying real pion events as protons due to setting this minimum. However, the ratio of pion events to proton events is small, and any misidentification is expected

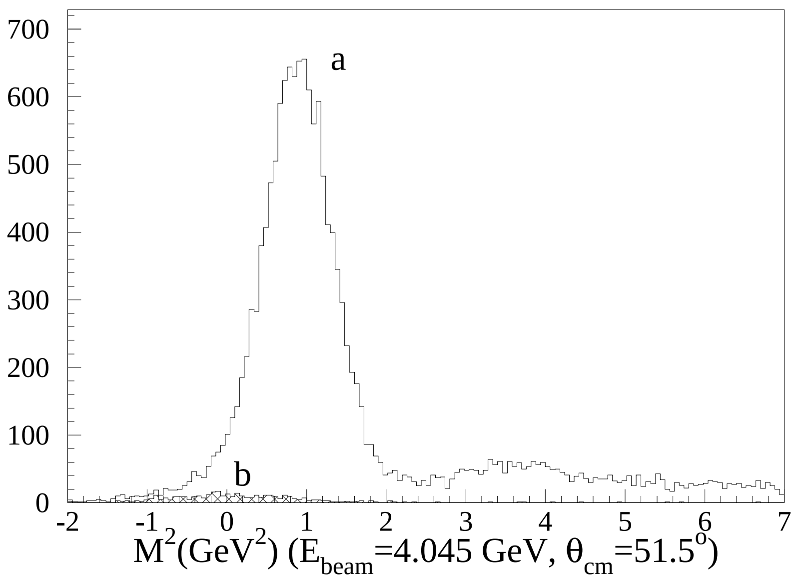

Figure 4.6: Raw mass spectrum for $E_{beam} = 4.045$ GeV, $\theta_{cm} = 51.5°$. The main curve (a) shows all events that reconstruct to the middle of the target region. The crosshatched area (b) shows those events which trigger the HMS Gas Cerenkov, identifying them as pions. Note that the peak is centered near $M^2 = 0.02$ GeV^2 where the pion peak is expected.

to be less than 0.1% after subtractions for background measurements are applied.

Figure 4.7 shows the ratio of pions to protons using time-of-flight and the Gas Cerenkov for particle identification. The ratio is calculated by considering those events which reconstruct back to a range of bremsstrahlung photon energies where only photodisintegration is expected. In the region where neither time-of-flight nor the Gas Cerenkov can be used for effective particle identification, an attempt was made to distinguish between the proton and pion peaks using time-of-flight to make an estimate of the ratio. For most kinematics, the number of pions is small ($< 1\%$). For $E_{beam} = 3.245$ GeV, the ratio is about 1 - 2%, and for $E_{beam} = 4.045$ GeV, the ratio is about 5 - 7%. Background measurements are made to significantly reduce the ratio of pions to protons such that misidentification of pion background as protons is no longer an issue.

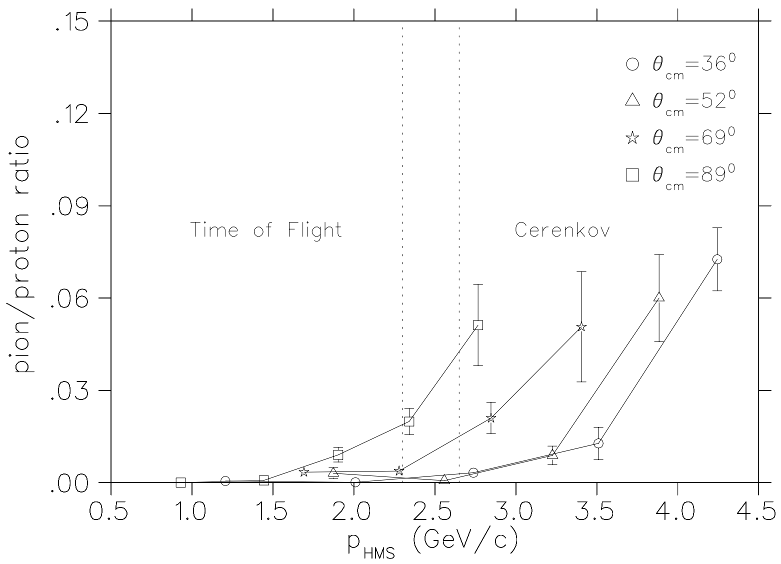

Figure 4.7: Ratio of total pions to total protons for each kinematics using time-of-flight and the Gas Cerenkov for particle identification. The ratio is calculated by considering the number of pions and protons in the region where only photodisintegration is expected. No subtractions are made for background measurements.

4.2.3 Particle ID Analysis Cuts

Software cuts are used in data analysis to include only those events that are identified to be protons. In all kinematics, the shape of the mass squared distribution is assumed to be gaussian. The cuts are placed at $\pm 2.5\ \sigma$. This includes all but 1.2% of the protons under the peak to minimize contamination from background and deuterons. For kinematics where there is very little background and the proton peak is well separated from the pion and deuteron peaks, the cuts are widened to accept a higher percentage of proton events. Table 4.1 gives the range in reconstructed mass squared that is considered for each kinematics.

To make an estimate of the systematic error for particle identification due to contamination by background sources, cross sections are measured for the kinematics at E_{beam} = 3.245 GeV and E_{beam} = 4.045 GeV (where residual background is at a maximum) are analyzed as follows. A particle identification cut is applied in the particle mass squared spectrum at $\pm 1.0\ \sigma$, $\pm 1.5\ \sigma$, $\pm 2.0\ \sigma$, and $\pm 2.5\ \sigma$ around the centroid of the gaussian proton peak. Cross sections for each set of cuts are corrected

E_{beam} (GeV)	θ_{cm}	M^2_{low} (GeV^2)	M^2_{high} (GeV^2)
0.845	36.2°	0.65	1.20
	88.7°, 89.5°	0.70	1.30
1.645	35.8°	0.30	1.30
	51.9°	0.50	1.30
	68.9°	0.50	1.30
	89.0°	0.50	1.30
2.445	35.6°, 37.1°	0.03	1.52
	51.6°, 53.0°	0.17	1.50
	68.8°, 70.1°	0.32	1.30
	89.0°	0.45	1.30
3.245	35.5°	-0.60	1.91
	51.6°	-0.22	1.78
	68.7°	0.09	1.55
	88.8°	0.31	1.36
4.045	35.4°	-1.56	2.44
	51.5°	-0.59	2.00
	53.0°	-0.46	2.03
	68.7°	-0.20	2.10
	70.2°	-0.40	1.80
	88.8°	-0.04	1.70

Table 4.1: Upper and lower limits in mass-squared used in data analysis for each kinematics.

for the part of the distribution that is left out of the calculation.

The cross sections for each of the four cuts are in good agreement with the mean of the four measurements. The overall systematic error for particle identification is found by averaging over the standard deviation from the mean for each kinematics at a given E_{beam}. This results in an estimate of particle identification systematic error of 1.3% for $E_{beam} = 3.245$ GeV and 2.6% for $E_{beam} = 4.045$ GeV. For all other kinematics, there is little contamination from pions or deuterons and the systematic error is less than 1%.

4.3 Tracking

The two HMS drift chambers are used to find the trajectory of the particle through the spectrometer. Each drift chamber contains six planes of wires. These planes measure the position of the particle as it moves through both chambers. The position and trajectory angles at the focal plane are calculated from this information. More information about the function of the drift chambers is located in Section 3.7.3.

4.3.1 Tracking Algorithm

For each event, position information is read out for all wires that are hit in the planes of both wire chambers. A best fit track is found using all the information from all the hits with an algorithm that is described in detail in [76].

The position along each plane is measured by using the position of the wire that is hit and adding to it the drift distance. This is the distance of the event to the wire that is hit. A TDC is used to determine the time when the event triggered the wire. The difference of this value to the time the event traveled through the plane (found from hodoscope time-of-flight) is used to determine the distance from the wire through a time-to-distance map that is determined through wire chamber calibration (see Section 4.3.3).

A space point is generated with information from each hit in a pair of "unlike planes". For the HMS, the $X-Y$, $U-Y$, $V-Y$ planes are considered unlike, but the $X-U$, $X-V$, $U-V$ planes are too nearly parallel to accurately define a space point (the U and V planes are 15° and -15° degrees offset from the X plane). A miniature track called a stub is fit through all space points that are sufficiently near each other. For each space point, the event may have passed each plane on either side of the sense wire, but that information is not definitively known. A stub is fit to each possible combination for both sides of the wire, and the stub with the least χ^2 is chosen as the best stub. To speed up the algorithm a small-angle approximation is used for the Y and Y' planes which are offset by one-half cell-width (0.5 cm). If there is a hit in both Y planes, then the ambiguity between left and right sides of the wire is eliminated by assuming the smallest trajectory angle in $\hat{y}_{HMS}$.

Stubs from both chambers which have slopes and positions such that they roughly point toward each other are linked together to form tracks. A χ^2 is calculated for each track against the stubs that are fitted, and in the case for multiple tracks, the track with the lowest χ^2 is chosen. The track gives the position and trajectory angles for the event at the focal plane (x_{fp}, y_{fp}, x'_{fp}, y'_{fp} in the plane equidistant from both wire chambers).

For many events, information is not available from all planes in each wire chamber. In the standard analysis software, wires in at least five out of six planes in each chamber must be hit for an attempt to be made to fit a track (5-out-of-6 tracking). For this experiment, however, a significant number of events hit only four out of the six planes (4-out-of-6 tracking). The conditions in the analysis are relaxed so a track is fit for a minimum of four out of six planes, provided at least one out of the two Y planes is also hit. The resolution becomes worse for fitting a track given information from only four out of six planes. However, the errors do not increase substantially for the events that would otherwise be lost [77].

4.3.2 Tracking Efficiency

Because the tracking algorithm requires a minimum number of hits in each wire chamber and sets a maximum number of hits per chamber as well, inefficient or noisy wires can prevent the tracking algorithm from finding a track for the event. The tracking efficiency relates the ratio of the number of tracks found to the number of events within the spectrometer acceptance. The data can be corrected for the number of events which are not tracked.

The tracking efficiency is calculated by placing a series of cuts on the data to narrow the collection to a group of relatively good events. First, the event must go through one scintillator in each of the four planes of the hodoscope. Further, the scintillator hit must be one of the central paddles in each plane. This defines the fiducial area, and guarantees that the particle passed through both wire chambers in the central portion of the spectrometer acceptance and should have been tracked. Such a method gives a better representation of the true tracking efficiency rather than using all trigger producing events [78]. For this experiment, the fiducial area is composed of paddles $5-12$ in the X planes, and $3-8$ in the Y planes. Figure 4.8 gives a graphic representation of the scintillators used to define the fiducial area. The fiducial area defined for this experiment is slightly larger than the standard fiducial area. This is done to increase statistical accuracy. An average of 1% variation is observed in the tracking efficiency by varying the size of the fiducial area in small amounts [60].

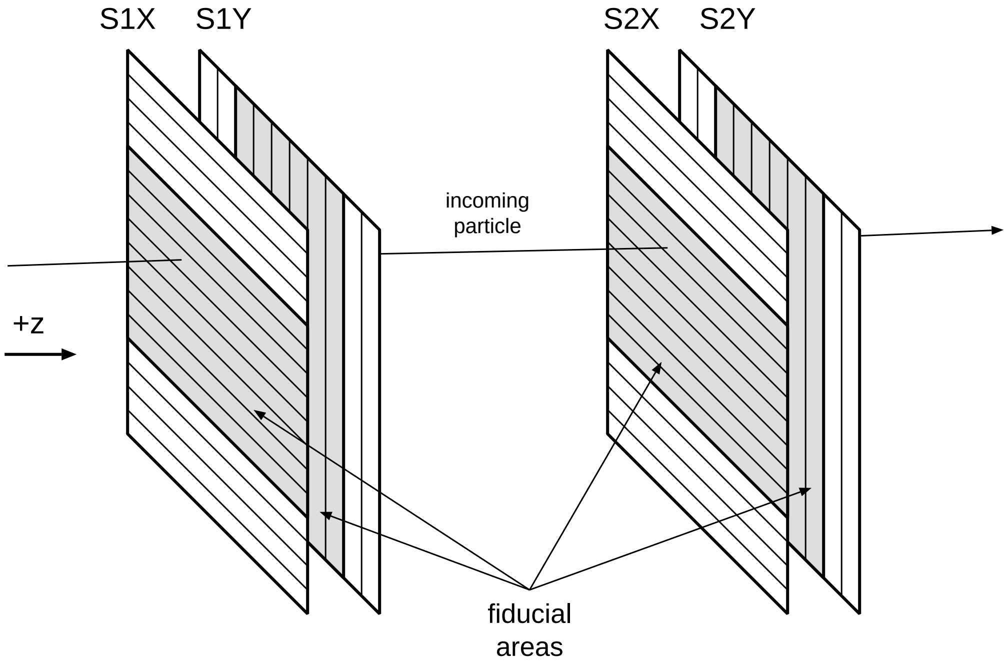

Figure 4.8: Fiducial area used to determine tracking efficiency. Tracking efficiency is calculated using only those events which fall within the central part of the spectrometer acceptance. The event must be triggered by hodoscope paddles in the shaded area.

For this experiment, the efficiency of tracking *protons* through the spectrometer is required for data analysis. A crude particle ID cut is used on the data to exclude those events which are definitely not protons. These cuts can be defined only by variables which do not depend on the tracking algorithm. A window is placed on the particle velocity determined from hodoscope time-of-flight, and the energy deposited by the particle in the shower calorimeter must meet some minimum value [60]. Figure 4.9 shows an example of the spectra for E_{cal} and β_{TOF}. The dashed curve in Figure 4.9 b) shows the remaining proton events which are used in the tracking analysis.

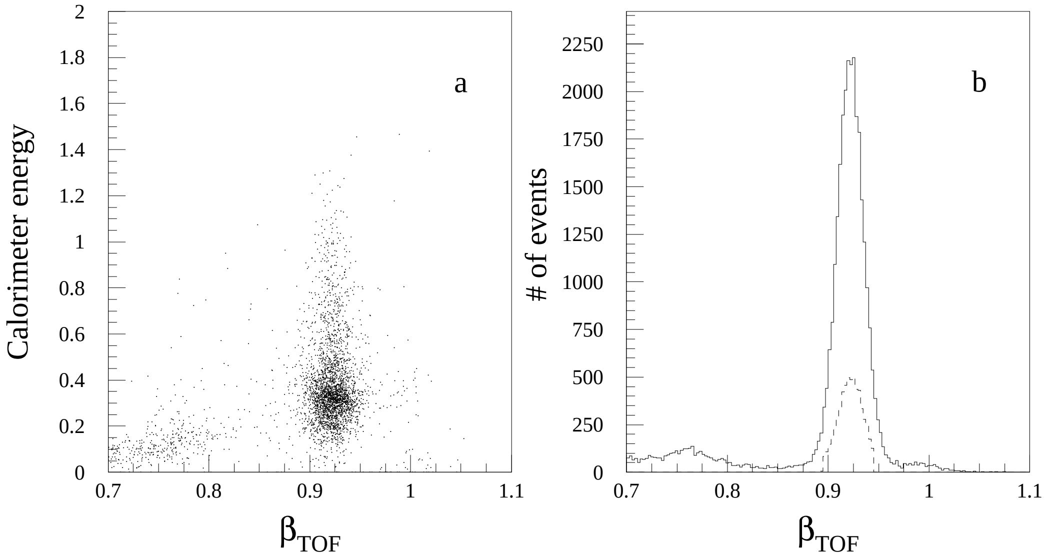

Figure 4.9: Figure a) shows the calorimeter energy spectrum for $E_{beam} = 3.245$ GeV, $\theta_{cm} = 88.8°$. Tracking efficiency calculations only include those events which are sure to be protons. This is done by requiring the events to be within a narrow window in β and that they deposit a minimum amount of energy in the calorimeter. For these kinematics, the value is $E_{cal} > 0.45$. The dashed curve in Figure b) shows the protons that pass both the β and the calorimeter energy cuts.

Table 4.2 gives a summary of the mean tracking efficiencies for each configuration. In some cases, a standard deviation for the mean cannot be calculated because only one run was taken for those configurations. The different configurations denote the main and background measurements taken during the experiment and are defined in Section 5.1.1.

E_{beam} (GeV)	θ_{cm}	$T^{in}_{LD_2}$	$T^{out}_{LD_2}$	T^{in}_{empty}	T^{out}_{empty}
0.845	36.2°	0.958 ± 0.009	0.962 ± 0.005	0.964 ± 0.066	0.967 ± 0.008
	88.7°	0.971 ± 0.009	0.835 -	0.973 -	0.972 ± 0.007
	89.5°	0.971 ± 0.009	0.835 -	0.973 -	0.972 ± 0.007
1.645	35.8°	0.808 ± 0.022	0.832 -	0.826 -	0.840 -
	51.9°	0.835 -	0.831 ± 0.018	0.837 -	0.844 -
	68.9°	0.862 ± 0.006	0.859 ± 0.028	0.859 ± 0.013	0.901 -
	89.0°	0.967 ± 0.001	0.970 ± 0.008	0.967 -	0.963 -
2.445	35.6°	0.764 ± 0.140	0.832 -	0.877 ± 0.009	0.859 -
	51.6°	0.959 ± 0.009	0.963 ± 0.007	0.290 -	0.305 -
	68.8°	0.884 ± 0.021	0.472 -	0.697 -	0.616 ± 0.099
	89.0°	0.960 ± 0.016	0.974 ± 0.008	0.969 ± 0.018	1.000 ± 0.000
3.245	35.5°	0.931 ± 0.008	0.954 -	0.885 ± 0.026	0.857 -
	51.6°	0.943 ± 0.011	0.946 ± 0.026	0.898 ± 0.041	0.912 -
	68.7°	0.946 ± 0.010	0.953 ± 0.025	0.939 ± 0.036	0.933 ± 0.059
	88.8°	0.957 ± 0.017	0.969 ± 0.016	0.964 ± 0.024	0.973 ± 0.006
4.045	35.4°	0.921 ± 0.009	0.925 ± 0.017	0.803 ± 0.013	0.681 -
	51.5°	0.907 ± 0.015	0.896 ± 0.058	0.728 ± 0.059	0.648 ± 0.109
	53.1°†	0.904 ± 0.022	0.949 ± 0.013	0.880 ± 0.116	0.864 -
	68.7°	0.918 ± 0.025	0.915 ± 0.050	0.909 ± 0.037	0.888 ± 0.093
	70.2°†	0.918 ± 0.034	0.921 -	0.918 -	1.000 -
	88.8°	0.923 ± 0.039	0.908 ± 0.044	0.973 ± 0.024	0.847 ± 0.192

Table 4.2: Charge weighted tracking efficiencies for the four measurement configurations of each kinematics. No standard deviations are given for those configurations where only one run is taken. For the kinematics marked with †, the tracking efficiencies T^{in}_{empty} and T^{out}_{empty} are replaced by $T^{in}_{LH_2}$ and $T^{out}_{LH_2}$ respectively, reflecting the configurations using a hydrogen target. See Section 5.1.1 for the list of configurations.

Average tracking efficiencies for protons were better than 90% in most cases. The observed performance for electrons is about 95% [70]. The efficiencies for this experiment are on average lower due to the presence of the gate valve which greatly increased the amount of background entering the spectrometer (see Section 5.3.1). Unusually low tracking efficiencies, particularly for data at E_{beam} = 2.445 GeV, are the result of the wire chamber threshold sensitivity experiment immediately prior to these kinematics, causing the wire chambers to be out of equilibrium. The accidental background levels were high at this time due to insufficient shielding along the HMS dipole, which greatly reduced the statistics for the empty configuration runs. Other anomalously low tracking efficiencies are attributed to a poor gas mixture in the wire chambers during that particular measurement.

The systematic uncertainty for the tracking efficiency is estimated by comparing the normalized proton yields for 4-out-of-6 tracking 5-out-of-6 tracking. The difference between the two algorithms should give an adequate value for the uncertainty in the tracking. Data from a number of kinematic points were tested in this manner and a systematic error of 3.3% is assigned to tracking efficiency from the mean variation of the two methods.

4.3.3 Drift chamber calibration

The HMS drift chambers provides a position resolution of 5 mm using only the information about which sense wire is hit. However, the resolution is greatly enhanced by including information about the time needed for the ionized electrons to reach the sense wire. For each wire hit, there is also a value in the TDC which can be transformed into a time. This time, when compared to the time obtained from the hodoscope time-of-flight, is used to determine the drift distance of the event from the sense wire. Calibration of the drift chambers is required to maintain an accurate drift time-to-distance map. By taking advantage of drift distance information, the position resolution for the HMS drift chambers is better than 300 μm per plane.

The calibration is performed by collecting the drift times for all the wires in each plane of the chambers for a high statistics data run ($>$ 50000 events). An example of the drift time distribution for one plane is given in Figure 4.10 a). Drift times can be negative because of an overall time offset between the drift chambers and the hodoscope that is not removed. Assuming that the drift distance distribution is uniform after averaging over all cells in the plane, the drift distance is given by

$$D = D_{max} \frac{\int_{t_{min}}^{T} F(\tau) d\tau}{\int_{t_{min}}^{t_{max}} F(\tau) d\tau}, \tag{4.3}$$

where $F(\tau)$ is the drift time distribution, t_{min}, t_{max} are the range of times to be included in the fit, T is the time given by the TDC, D is the distance of the event to the sense wire along the plane, D_{max} is the maximum drift distance allowed. D_{max} is set to 0.5 cm, which is one half of the distance between each sense wire. Figure 4.10 b) shows an example of the drift distance distribution that is formed by the calibration from the drift time distribution.

Because of long-term drifts in the electronics over the course of the experiment (eg. temperature variations) drift time-to-distance map calibrations were performed for each run.

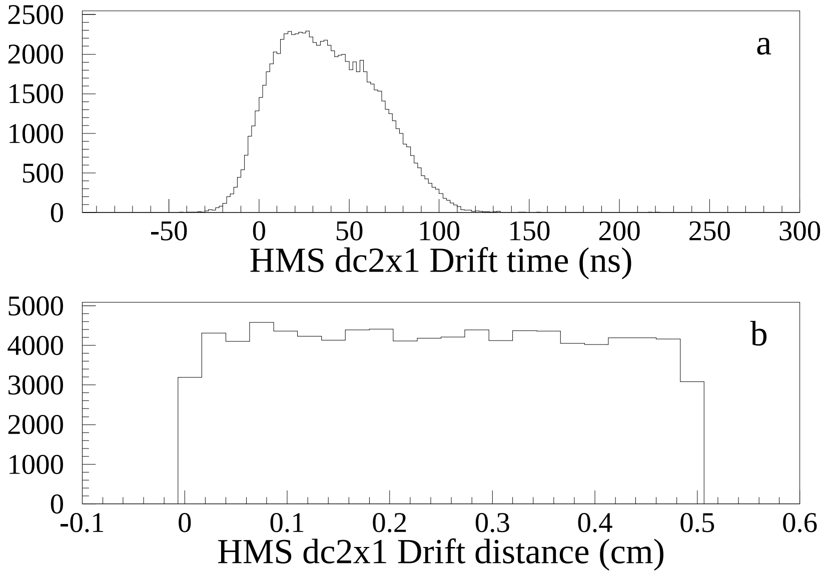

Figure 4.10: Drift time and drift distance spectra for events in the HMS drift chambers. Drift times are mapped into a uniform distribution of distances to the sense wire in the center of each cell.

4.4 Event Reconstruction

When a track is fit for an event in the HMS, four parameters are found for the event at the nominal focal plane. The nominal focal plane is located at an equal distance from both drift chambers and defines the origin of the HMS cooordinate system,

$\hat{z}_{HMS} = 0$. The parameters for each event are two positions (x_{fp}, y_{fp}) and two angles (x'_{fp}, y'_{fp}). A Taylor expansion in terms of the focal plane parameters can be used to reconstruct the event parameters at the target. The five target parameters are two positions (x_{tar}, y_{tar}), two angles (x'_{tar}, y'_{tar}), and particle momentum δ[1]. The matrix is under-determined as there are only four focal plane parameters and five possible target parameters. Because the beam spread along the $\hat{x}_{tar}$ is very small, that parameter is set to 0 ($x_{tar} = 0$), allowing for only four parameters to be considered in the transformation. Figures 4.11 and 4.12 show a pictorial representation of the target and focal plane position and angle parameters respectively in their coordinate systems.

4.4.1 Methods for event reconstruction

There are two methods that are used to determine coefficients in the Taylor expansion for the reconstruction matrix. One relies on a model of the properties of the dipole and quadrapole magnets. The other relies on a fit to real data that is used to refine the original model to account for inaccuracies of that model.

COSY

The COSY Infinity program [79] is used to model the magnetic elements of the spectrometer through field maps, effective lengths, and positions of the HMS dipole and quadrupole magnets. The COSY program uses these magnet properties to determine a forward matrix which transforms target parameters to focal plane parameters, and a reverse matrix which transforms focal plane parameters to target parameters. During data analysis, only focal plane parameters are available, so the reverse matrix is used to reconstruct quantities at the target. The Monte Carlo, discussed in Section 5.2, also uses the forward matrix to calculate the position of simulated events along the

[1]The quantity, $\delta = \frac{p-p_0}{p_0}$, refers to the difference in the particle momentum from the central spectrometer setting, p_0. The angles, x' and y', describe the angle of the event from the $\hat{z}$ axis projected onto the $\hat{x}$ and $\hat{y}$ axis respectively.

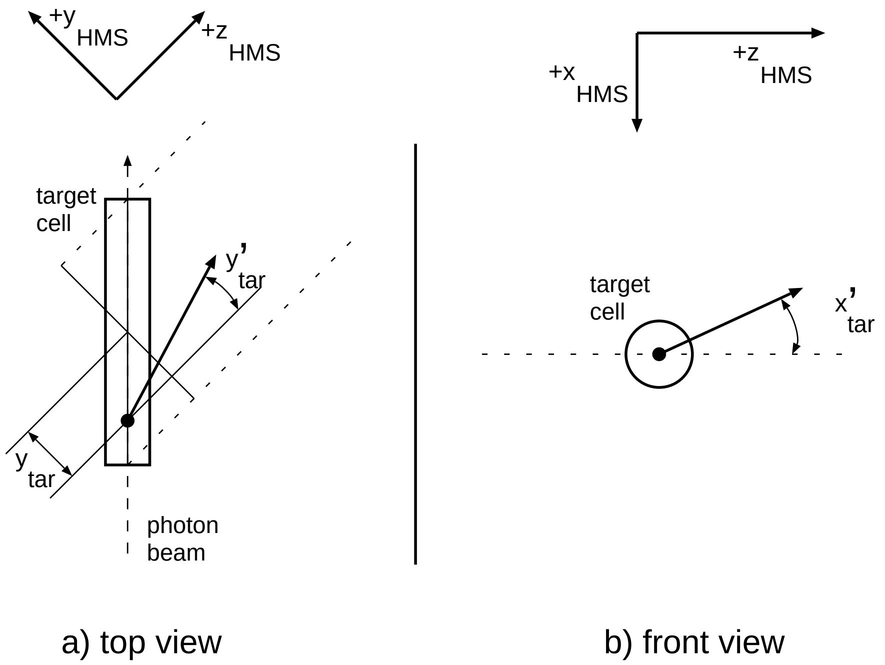

Figure 4.11: Pictorial of target position and angle parameters.

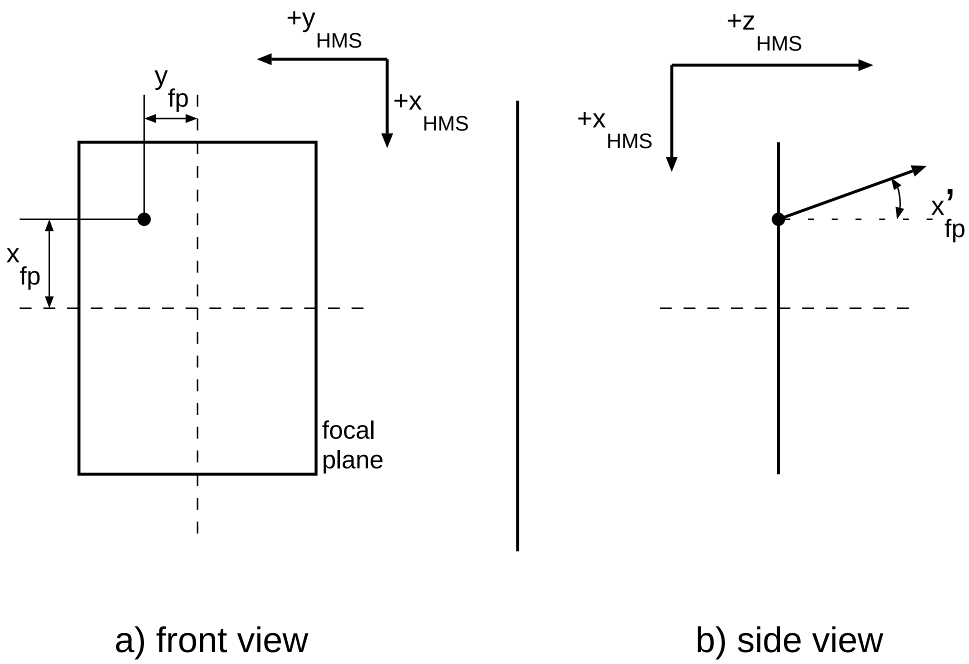

Figure 4.12: Pictorial of focal plane position and angle parameters.

path from the target to the detectors.

The forward matrix, F, is a Taylor expansion of order N over the target parameters. Each element in the matrix gives the coefficient for each term of the expansion. It is given in the form

$$\begin{bmatrix} x_{fp} \\ y_{fp} \\ x'_{fp} \\ y'_{fp} \end{bmatrix} = \sum_{ijklm} F_{ijklm}(x_{tar})^i (y_{tar})^j (x'_{tar})^k (y'_{tar})^l (\delta)^m, \ (1 \leq i+j+k+l+m \leq N) \quad (4.4)$$

where $N = 5$, the order of the expansion in the COSY generated matrix.

The reverse matrix is found in the same way. It is a Taylor expansion of order N over the focal plane parameters in the form

$$\begin{bmatrix} y_{tar} \\ x'_{tar} \\ y'_{tar} \\ \delta \end{bmatrix} = \sum_{ijkl} R_{ijkl}(x_{fp})^i (y_{fp})^j (x'_{fp})^k (y'_{fp})^l, \ (1 \leq i+j+k+l \leq N). \quad (4.5)$$

As mentioned earlier, because there are only four focal plane parameters, only four target parameters can be calculated with the reverse matrix. Because of the small range of the beam in $\hat{x}_{tar}$, the position in x_{tar} is assumed to be 0. This leaves only four remaining parameters to be found.

Fit to data

COSY is an adequate model of the HMS spectrometer to reconstruct events from the detectors back to the target. However, this model can be used as a starting point for further optimization using real data to refine the reverse matrix to possibly improve the final reconstruction.

The Hall C Matrix Element Optimization Package (CMOP) [80] is used to perform this refinement. High statistics runs are taken with a solid target with the sieve slit in place instead of the collimator used to define solid angle (Section 3.7.2). The sieve slit is a block of Heavymet (a machinable tungsten alloy) material with a thickness of 3.175 cm. Small holes with a diameter of 0.508 cm are bored into the block in a 9x9 grid. Two positions on that grid are left without holes to help visually guarantee correct vertical and horizontal orientation when viewing the results. The center hole has a diameter half the size of the other holes and is used to determine angular resolution. Figure 4.13 gives a pictorial representation of the sieve slit. The sieve slit helps optimize the x'_{tar} and y'_{tar} parameters. Further runs are taken with a slanted solid target to help optimize in y_{tar} and the central spectrometer momentum setting is changed in steps to optimize in δ.

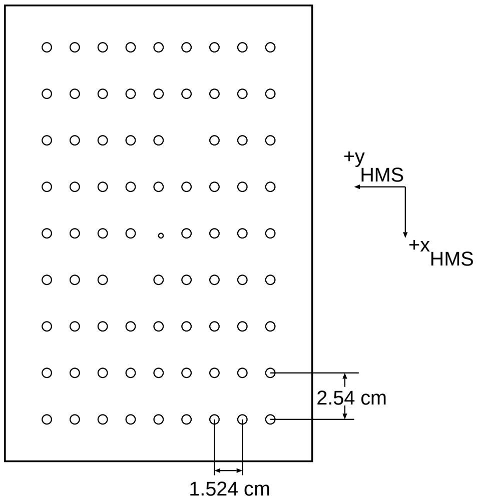

Figure 4.13: HMS sieve slit diagram. The sieve slit is used in fitting reverse optics matrix elements. Two holes are filled to visually guarantee correct orientation in the final reconstruction. The center hole is smaller to facilitate measurement of angular resolution.

As the first step in the optimization, the event is reconstructed back to the target with the COSY matrix. The event is then mapped to the position of the sieve slit. As the position of the holes in the sieve slit are known, the program determines the hole closest to that event and the trajectory angles are calculated from geometry. The geometric angles are compared to the angles found from the reconstruction matrix. A subset of these events, where the differences in the angles pass a certain cut, are then used to optimize the matrix through the singular value decomposition method

(SDV) [81]. Once the fit is made, new matrix elements are generated and can be used as a new starting point to iteratively fit the data until the matrix converges. Further details on the operation of CMOP can be found in [80] and [82].

4.4.2 Choice for data analysis

Either method can be used to reconstruct event parameters for use in data analysis. Presumably, the fitted matrix elements would make a better choice because they are directly related to data. They do not rely on a model of the magnets, but rather use a well-known reaction to map out the optical reverse matrix. However, problems occur when trying to reconstruct events which are scattered before reaching the detectors.

The fit is done for events within the acceptance of the spectrometer. Inside the acceptance, the resulting matrix is well-behaved. Outside the acceptance, the behavior of the matrix is not constrained. Events which are scattered (eg. along the path inside the spectrometer) may lie outside of the spectrometer acceptance and still be detected as follows. The acceptance is defined by the sequence of apertures of the dipole and quadrapole magnet, the vacuum pipes leading from the target chamber to the spectrometer, the collimator, and the active areas of each detector. However, events which punch through the collimator or scatter along the exit pipe from the dipole do not lie within this spectrometer acceptance, but can still hit all the detectors.

The consequence of the unconstrained nature of the fitted matrix elements in this case is that background events are mapped near the spectrometer acceptance. As a result, it becomes very difficult to identify and separate background events. The COSY matrix elements do not have this limitation because they not include the apertures when calculating the reverse matrix. Thus the matrix is well-defined over a much wider range of focal plane parameters. Background events which clearly come from outside of the spectrometer acceptance are mapped to target parameters which can be disregarded in data analysis.

An example of the behavior of the COSY and the fitted matrix elements is shown in Figures 4.14 and 4.15. Figure 4.14 a) shows the position for all tracked events in the plane of the collimator. The dark black octagon in the center is the collimator. The events surrounding the collimator are background events which are distributed more or less uniformly over the plane. Figure 4.14 b) shows the E_γ spectrum for each of the four measurements taken at $E_{beam} = 4.045$ GeV, $\theta_{cm} = 35.4°$ where a cut is placed to include only the region of the collimator. The different measurements are defined in detail in Section 5.1.1. The bremsstrahlung endpoint is clearly seen near the expected value of 4.045 GeV. The signal that remains beyond the endpoint is composed of the background events which are within the cut on the collimator area.

Figure 4.15 a) shows the same data using the fitted matrix elements. The result of using the fitted matrix elements is that the background events which were dispersed over the whole plane are now concentrated in the area of the collimator. Figure 4.15 b) shows the resulting E_γ spectrum. The increased concentration of background events is seen in the high yield beyond the bremsstrahlung endpoint.

This effect of the fitted matrix elements concentrating background events into the center of the acceptance is further illustrated during a test run shown in Figure 4.16. This Figure shows data taken for $E_{beam} = 4.045$ GeV, $\theta_{cm} = 53.2°$ with a 10 cm thick wall of lead stacked in front of the collimator blocking off the entire HMS acceptance. Figure 4.16 a) shows that the COSY matrix elements maps the distribution of the background over a wide area at the plane of the collimator. For the fitted matrix elements shown in Figure 4.16 b), the background events are concentrated near the center where they can be misidentified as real events.

Because of the relatively high background rates seen in this experiment, a choice was made to use the COSY matrix elements for data analysis, where background is minimized by a cut around the shape of the collimator. This problem is not seen in many other experiments because they rely on taking data in coincidence with another spectrometer which immediately rejects a large percentage of this type of background.

An estimate of the systematic error can be made by comparing the final yields

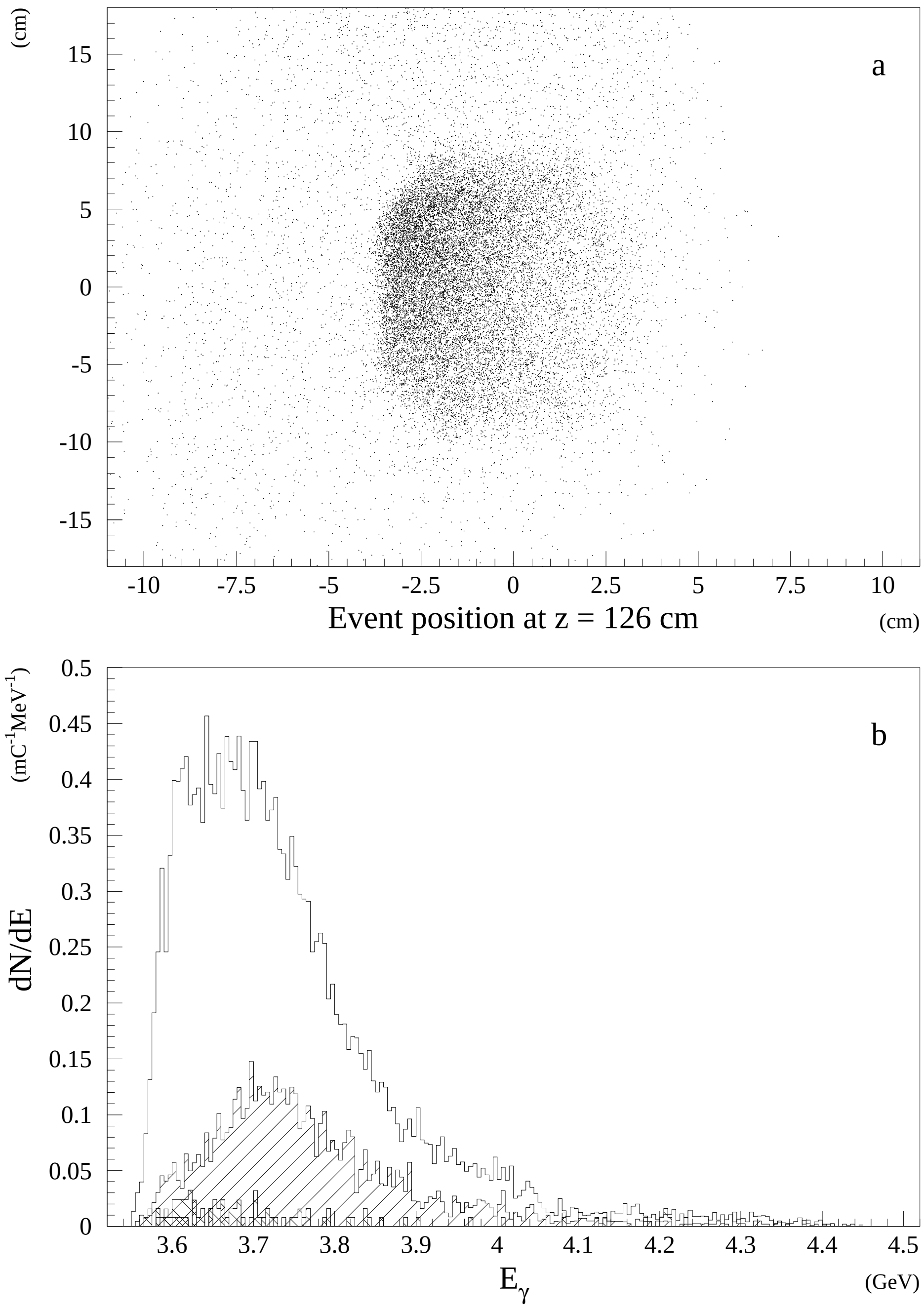

Figure 4.14: a) Position of events at the plane of the collimator (z = 126 cm) using the COSY model set of reconstruction matrix elements for $E_{beam} = 4.045$ GeV, $\theta_{cm} = 35.4°$. b) Corresponding reconstructed E_γ spectrum.

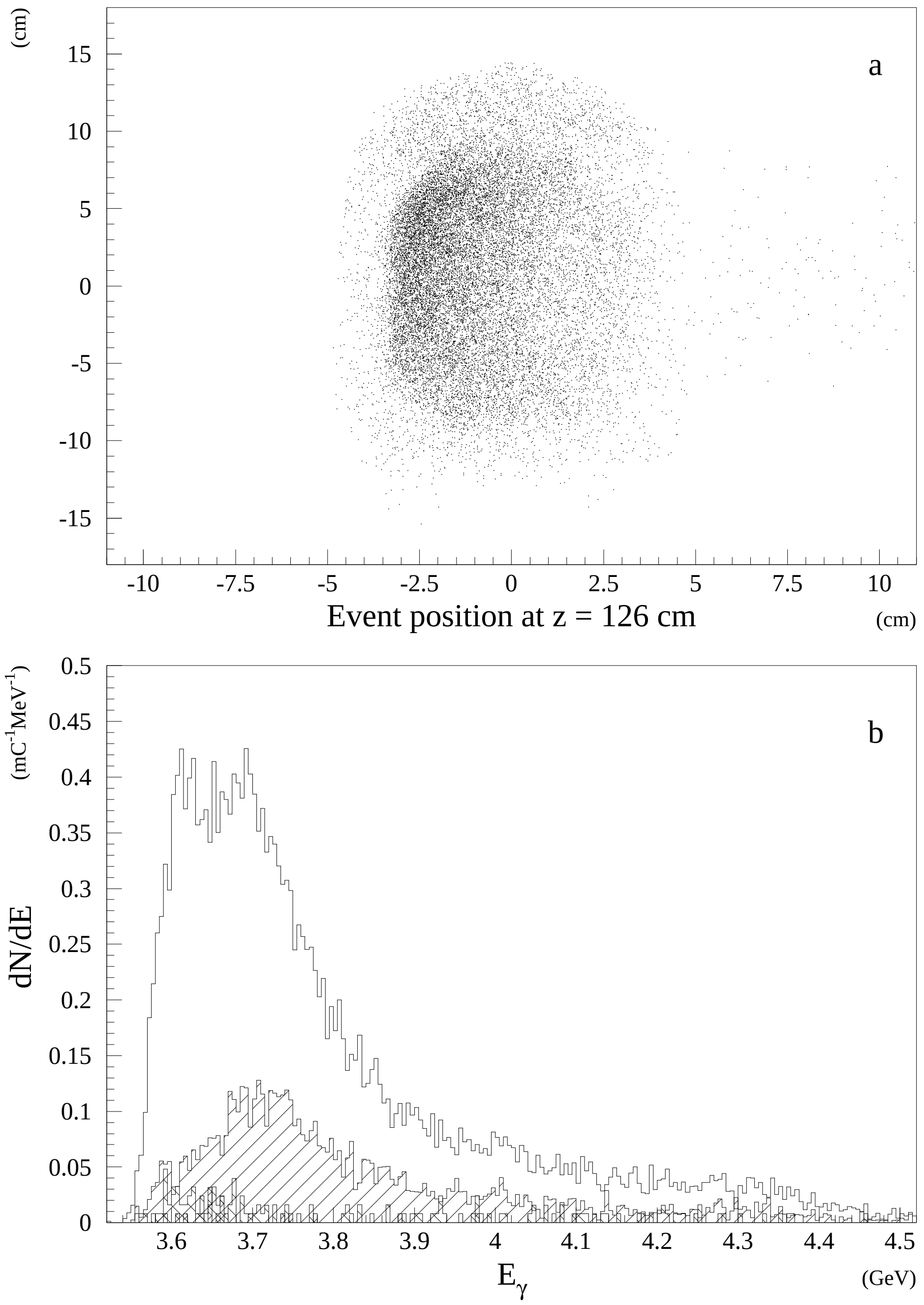

Figure 4.15: a) Position of events at the plane of the collimator (z = 126 cm) using the fitted set of reconstruction matrix elements for $E_{beam} = 4.045$ GeV, $\theta_{cm} = 35.4°$. b) Corresponding reconstructed E_γ spectrum.

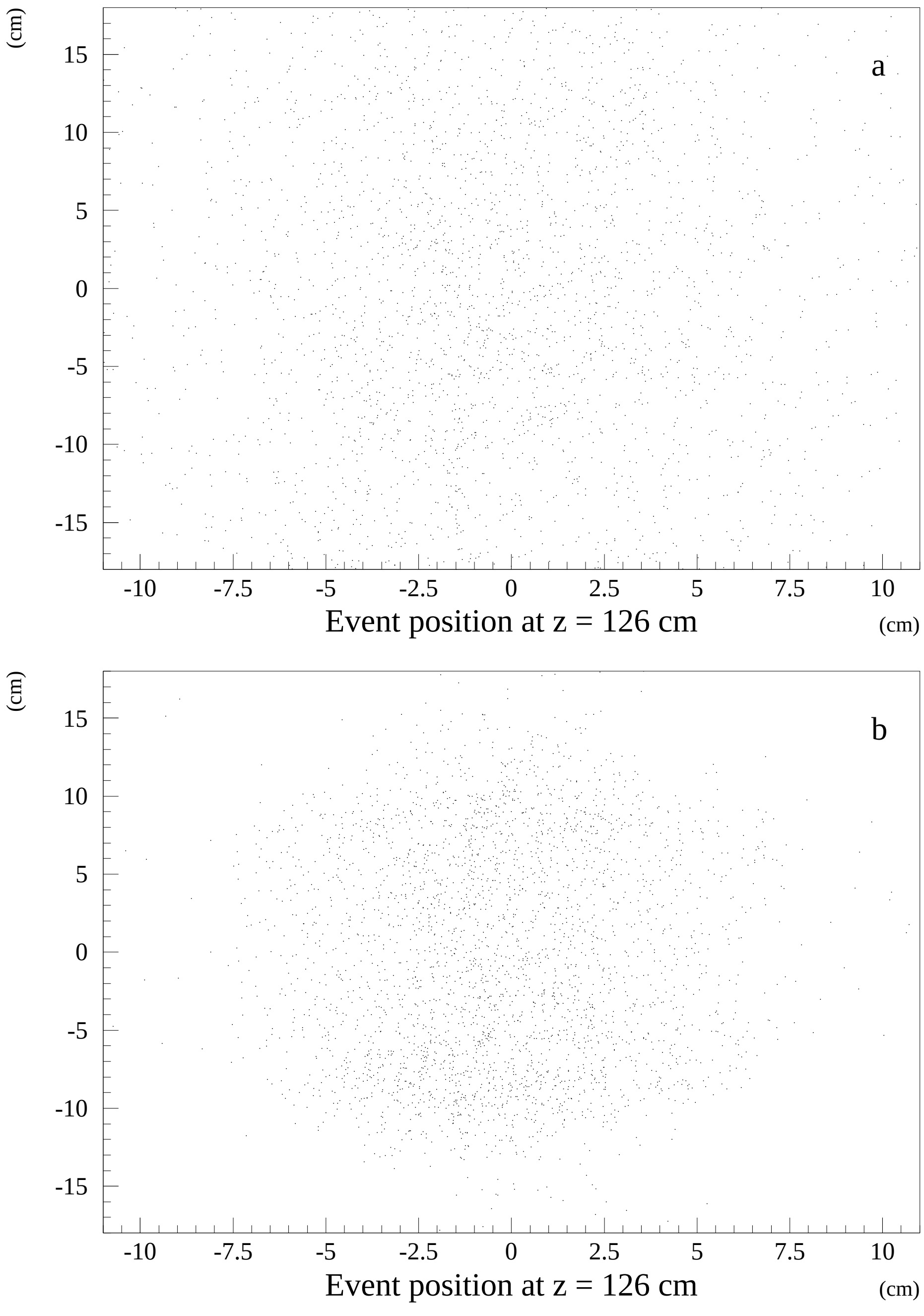

Figure 4.16: Position of events at the plane of the collimator (z = 126 cm) for $E_{beam} = 4.045$ GeV, $\theta_{cm} = 53.2°$. Figure a) shows the results for the COSY model of reconstruction matrix elements. Figure b) uses the fitted set of matrix elements.

obtained by using the different sets of matrix elements. A number of kinematics were tested where the background was minimal, and the differences were on the order of 3.5%.

Chapter 5

Measurement of the Cross Section

Once the events that enter the spectrometer are recorded in the data stream and identified as protons, the next step is to determine the yield of photo-protons arising from deuteron photodisintegration. This requires subtracting the background that results from other reactions occurring at the same time whose products enter the spectrometer acceptance. When the photodisintegration yield is determined, the differential cross section can be calculated.

5.1 Measuring Cross Section from Experimental Quantities

The electrons in the electron beam have an energy spread of about 0.1%. However, when the electron beam strikes the radiator, a continuous spectrum of photons is created of all energies up to the electron beam energy. The original energy of the photon is an important component in determining the photodisintegration yield because, as is explained later, only a small part of the bremsstrahlung spectrum near the endpoint can be used in the yield calculation.

When an event reaches the spectrometer that is identified to be a proton, two-body kinematics can be used to determine the original photon energy using only the recoil proton momentum and scattering angle,

$$E_\gamma = \frac{E_p m_d - \frac{1}{2}(m_d^2 + m_p^2 - m_n^2)}{m_d - E_p + p_p \cos\theta_p}, \tag{5.1}$$

where E_p and p_p are the energy and momentum of the recoil proton, θ_p is the recoil angle of the proton from the beam axis, and m_d, m_p, and m_n are the masses of the deuteron, proton, and neutron, respectively. All quantities are in the lab frame. The derivation of this relation can be found in Appendix B.5.

The photon energy, E_γ, for each event is histogrammed. Although the histogrammed photon energies are determined by assuming that the detected proton came from a deuteron photodisintegration reaction, protons can enter the spectrometer from a number of other sources as well. Although protons coming from $p(\gamma, p)X$ are kinematically forbidden in the energy range of interest, detected protons from reactions $Al(\gamma, p)X$ in the target endcaps contribute to the background.

5.1.1 Photodisintegration Yield

The photo-proton yield is determined using four separate measurements. The main configuration, (LD_2^{in}), uses the radiator to produce the bremsstrahlung photon spectrum which is incident on a liquid deuterium target[1]. Measurements with this configuration include the protons which are products of the $d(\gamma, p)n$ reaction. The other three configurations directly measure different types of background associated with the first configuration which can then be subtracted to obtain the photo-proton yield strictly from deuteron photodisintegration. The copper radiator is the main source of bremsstrahlung photons for this experiment, but the upstream aluminum target window and the deuterium target itself act as a radiator as well. The average material thickness of the deuterium is 1.0% of a radiation length. The aluminum entrance window has a thickness of 0.08% of a radiation length. Using a deuterium target with the radiator removed, (LD_2^{out}), measures the virtual photon yield from the electron beam and the real photon yield arising from bremsstrahlung photons created in the target. Using a liquid hydrogen target with the radiator inserted in the path of the electron beam, (LH_2^{in}), measures the background arising from the bremsstrahlung photons

[1]The electron beam passes through the target in all configurations.

and the electron beam striking the aluminum target endcaps. The final measurement uses a liquid hydrogen target with the radiator removed, (LH_2^{out}). This measures the background from the aluminum target endcaps that were over-corrected from the first two background configurations.

Ideally, liquid hydrogen would be used for the two final configurations, LH_2^{in} and LH_2^{out}. However, problems with the target during the experiment forced the use of only one target cell filled with deuterium. The other target cell, originally for use with liquid hydrogen, was run empty. A correction is later applied to account for the lack of hydrogen data. However, data taken at a later date includes background measurements taken with liquid hydrogen. These data are for the kinematics $E_{beam} =$ 4.045 GeV, $\theta_{cm} = 53.1°$ and $E_{beam} = 4.045$ GeV, $\theta_{cm} = 70.2°$. As most of the data used an empty cell instead of one with liquid hydrogen, the configuration labels LH_2^{in} and LH_2^{out} are changed to MT^{in} (MT for 'empty') and MT^{out}, respectively.

The photo-proton distributions are histogrammed according to the reconstructed photon energy using Equation 5.1 to create a raw histogram defined by

$$\frac{N_{E_\gamma}}{\Delta E_{\gamma,bin}}, \tag{5.2}$$

where $\Delta E_{\gamma,bin}$ is the width of each bin in E_γ and N_{E_γ} is the raw event count within each photon energy bin. The histograms are then normalized to the total charge deposited by the electron beam and the target density to give

$$\frac{dN_i}{dE_\gamma} = \frac{1}{(1-d.t.)Q}\frac{1}{n_{nucl}}\frac{N_{E_\gamma}}{\Delta E_{\gamma,bin}}\frac{1}{\epsilon}, \tag{5.3}$$

where i denotes the configuration of the measurement, $d.t.$ is the computer dead time, Q is the integrated electron beam charge, n_{nucl} is the target density (nuclei/nb), and ϵ is the product of all detector and tracking algorithm efficiencies. Figure 5.1 shows an example of the normalized yields for each of the four configurations, showing the average number of counts per MeV per mC for each bin.

The photodisintegration yield is determined by subtracting the background mea-

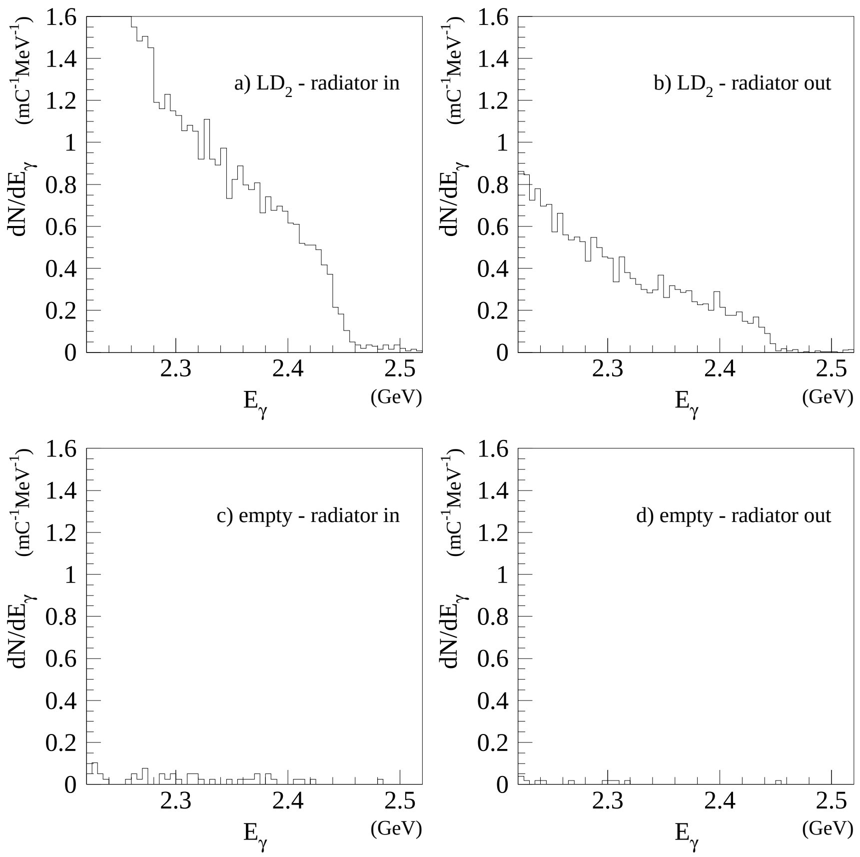

Figure 5.1: Normalized photo-proton yields as a function of E_γ for $E_{beam} = 2.445$ GeV, $\theta_{cm} = 51.6°$ for each of the four configurations, LD_2^{in}, LD_2^{out}, MT^{in}, MT^{out} in figures a), b), c), d), respectively.

surements from the initial LD_2^{in} configuration measurement which gives

$$\frac{dN_{d(\gamma,p)n}}{dE_\gamma} = \left[\frac{dN_{LD_2}^{in}}{dE_\gamma} - \frac{dN_{LH_2}^{in}}{dE_\gamma}\right] - f(E_\gamma)\left[\frac{dN_{LD_2}^{out}}{dE_\gamma} - \frac{dN_{LH_2}^{out}}{dE_\gamma}\right]. \tag{5.4}$$

Equation 5.4 is used for those kinematics where data is available from LH_2 configurations. However, most of the data only had configurations with an empty target rather then LH_2. Thus the yield subtraction must be modified to take that difference into account,

$$\frac{dN_{d(\gamma,p)n}}{dE_\gamma} = \left[\frac{dN_{LD_2}^{in}}{dE_\gamma} - \frac{7}{6}\frac{dN_{empty}^{in}}{dE_\gamma}\right] - f(E_\gamma)\left[\frac{dN_{LD_2}^{out}}{dE_\gamma} - \frac{7}{6}\frac{dN_{empty}^{out}}{dE_\gamma}\right]. \tag{5.5}$$

The factor $\frac{7}{6}$ is a correction for using an empty target rather than one filled with LH_2. Although photo-protons are kinematically forbidden, LH_2 provides a radiation length that is approximately 1%. This would provide an extra $\frac{1}{6}$ in the background event yield from the downstream target window. Since the target windows are cut out in the data analysis, the contribution is expected to be small, so the error in the correction is negligible.

The $f(E_\gamma)$ correction is the result of a change in the energy distribution of the electron beam after it passes through the bremsstrahlung radiator. The electron beam radiates energy as it passes through the radiator, causing the nearly monoenergetic electron beam to change into a continuous energy distribution. This alters the combined real and virtual photon spectrum that is created as the electron beam passes through the target. The correction factor, $f(E_\gamma)$, is defined as the ratio of the two photon spectra,

$$f(E_\gamma) = \frac{dN^{in}_{\gamma,target}}{dE_\gamma} / \frac{dN^{out}_{\gamma,target}}{dE_\gamma}. \tag{5.6}$$

With the radiator removed, the photon flux produced by the upstream target window and the cryogen target is given by

$$\frac{dN^{out}_{\gamma,target}}{dE_\gamma} = N_0 \int dE' \delta(E_0 - E') \left[\frac{d\sigma_{brem}}{dE_\gamma}(E', E_\gamma) + \frac{d\sigma^{eff}_{virtual}}{dE_\gamma}(E', E_\gamma) \right]. \tag{5.7}$$

The incident electron beam distribution is given by the delta function, $\delta(E_0 - E')$. The cross section $\frac{d\sigma_{brem}}{dE_\gamma}(E', E_\gamma)$ describes the production of a real photon of energy E_γ by an electron with energy E' in the target materials and $\frac{d\sigma^{eff}_{virtual}}{dE_\gamma}(E', E_\gamma)$ is the virtual photon spectrum. The form of this virtual cross section is described in [83].

The form of the photon flux with the radiator inserted is similar to Equation 5.7,

$$\frac{dN^{in}_{\gamma,target}}{dE_\gamma} = N_0 \int dE' I(E_0, E', Z, t_{rad}) \left[\frac{d\sigma_{brem}}{dE_\gamma}(E', E_\gamma) + \frac{d\sigma^{eff}_{virtual}}{dE_\gamma}(E', E_\gamma) \right]. \tag{5.8}$$

The electron energy delta function is replaced with the energy distribution of the electrons after it passes through the copper radiator. The form of the distribution is given by $I(E_0, E', Z, t_{rad})$, which is a function of the radiator material with atomic number, Z, and radiation thickness, t_{rad}. It describes the probability that the energy of an electron will change from E_0 to E' as it passes through the radiator. An analytical form is unavailable but a more detailed discussion of the calculation is available in [38].

The two photon distributions are calculated using an algorithm developed by Eric Belz [84]. It is based on the algorithm that is used to calculate the bremsstrahlung spectrum that is discussed in Section 5.4.3. This program includes effects from the finite energy spread of the initial electron beam and radiative straggling in the target.

The result is a table of corrections which list $f(E_\gamma)$ in steps of $\delta E_\gamma = 1$ MeV. Figure 5.2 shows a graph of $f(E_\gamma)$ as a function of E_γ for a 6.02% copper radiator and $E_{beam} = 4.045$ GeV.

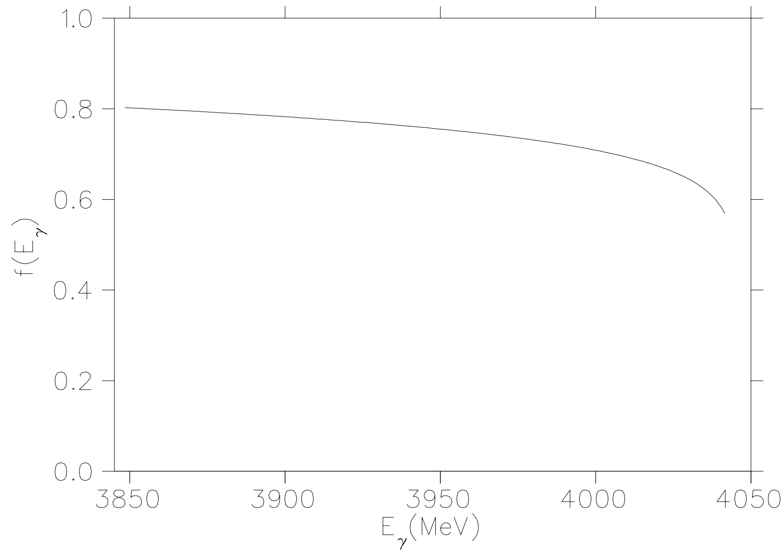

Figure 5.2: The correction factor $f(E_\gamma)$ for an electron beam with initial energy $E_{beam} = 4.045$ GeV striking a 6.02% copper radiator. This factor corrects for the difference in the photon spectra created by the electron beam in the target. This difference is caused by the change in the energy distribution of the incident electron beam as it passes through the copper radiator.

The normalized proton yields for each configuration are combined in Equation 5.5 to obtain the deuteron photodisintegration yield, $\frac{dN_{d(\gamma,p)n}}{dE_\gamma}$. Figure 5.3 shows the result of the combination for the configuration histograms shown in Figure 5.1.

Only a small portion of the photo-proton yield is used in determining the deuteron

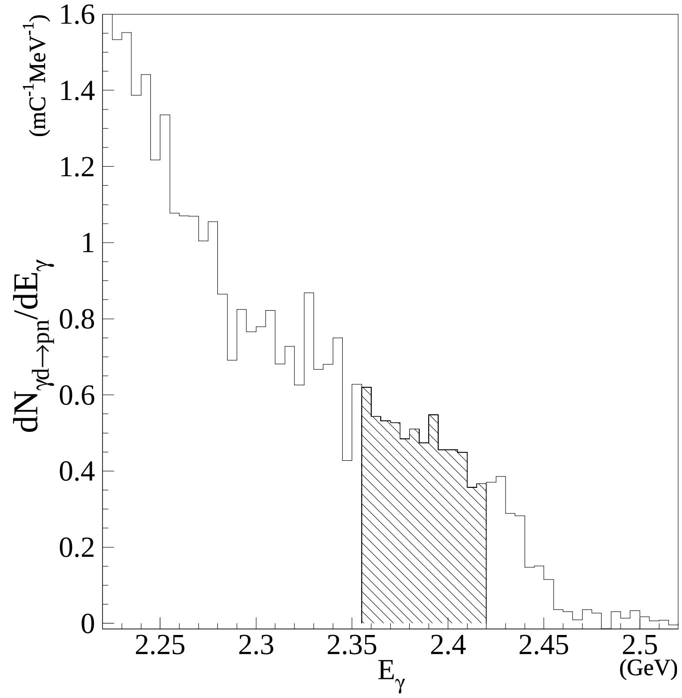

Figure 5.3: Photo-proton yield for $\theta_{cm} = 53.0°$, $E_{beam} = 2.445$ GeV as a function of E_γ. Background configurations have been subtracted in accordance with Equation 5.5. The crosshatched area shows the portion of the photo-proton yield that is used in calculating the deuteron photodisintegration cross section.

photodisintegration cross section. The upper limit in the window is set at $E_{\gamma,high} = E_{beam} - 25$ MeV. It is difficult to determine the expected bremsstrahlung photon yield above this point to an accuracy better than 3%. The lower limit is defined at the energy at which pion photoproduction begins. The description of how this lower limit is calculated is given in Section 5.3.2.

5.1.2 Cross Section

The photo-proton yield $Y(E_\gamma) = \frac{dN_{\gamma(d,p)n}}{dE_\gamma}$ for the photon energy range $E_{\gamma,low} < E_\gamma < E_{\gamma,high}$ is used to determine the average cross section for deuteron photodisintegration.

The differential cross section in the lab frame is given by

$$\frac{d\sigma}{d\Omega_{lab}}(E_\gamma) = \frac{Y(E_\gamma)}{N_\gamma(E_\gamma)\ \Delta\Omega\ A}, \tag{5.9}$$

where $\Delta\Omega$ is the total solid angle of the spectrometer, A is the correction for photo-proton absorption in the spectrometer, and $N_\gamma(E_\gamma) = \frac{dN_\gamma}{dE_\gamma}$ is the number of photons produced by the radiator per incident electron in an energy range dE_γ.

Although the cross section varies strongly with photon energy, low statistics do not allow a good measurement of the cross section *as a function of the photon energy* within the energy range $E_{\gamma,low} < E_\gamma < E_{\gamma,high}$. The average cross section is calculated by integrating over the photon energy range

$$\frac{d\sigma}{d\Omega_{lab}}(\bar{E}_\gamma) = \frac{1}{\Delta\Omega\ A}\int_{E_{\gamma,low}}^{E_{\gamma,high}} \frac{Y(E_\gamma)}{N_\gamma(E_\gamma)} dE_\gamma. \tag{5.10}$$

The photon flux is not constant over the photon energy range of interest, thus the mean photon energy, $\bar{E}_\gamma$, is given by

$$\bar{E}_\gamma = \frac{\int E_\gamma \frac{dN_\gamma}{dE_\gamma} dE_\gamma}{\int \frac{dN_\gamma}{dE_\gamma} dE_\gamma}. \tag{5.11}$$

However, the mean photon energy is not the photon energy appropriate for the average cross section measured in Equation 5.10. The actual photon energy that would normalize the measured cross section would satisfy the relation

$$\frac{d\sigma}{d\Omega}(E_\gamma^{proper}) = \frac{\int \frac{dN_\gamma}{dE_\gamma}\frac{d\sigma}{d\Omega}(E_\gamma) dE_\gamma}{\int \frac{dN_\gamma}{dE_\gamma} dE_\gamma}. \tag{5.12}$$

However this requires explicit knowledge of $\frac{d\sigma}{d\Omega}$ as a function of E_γ. Assuming that $\frac{d\sigma}{d\Omega}(E_\gamma) \propto s^{-10}$ as given by constituent scaling rules (see Section 2.2), E_γ^{proper} can be found numerically. The energies obtained this way are found to be smaller by about 0.5 MeV [38] which is less than the expected precision of measurement of E_γ. Therefore, the mean photon energy given by Equation 5.11 is used for the measured cross sections for each kinematics.

The differential cross section in the center of mass frame is given by

$$\frac{d\sigma}{d\Omega_{cm}} = \frac{d\sigma}{d\Omega_{lab}}\frac{d\Omega_{lab}}{d\Omega_{cm}} \tag{5.13}$$

where the Jacobian, $\frac{d\Omega_{lab}}{d\Omega_{cm}}$, is given by

$$\frac{d\Omega_{lab}}{d\Omega_{cm}} = \frac{\sin^2(\theta_{lab})}{\sin^2(\theta_{cm})}\left[\cos(\theta_{cm})\cos(\theta_{lab}) + \gamma_{cm}\sin(\theta_{cm})\sin(\theta_{lab})\right]. \tag{5.14}$$

where

$$\gamma_{cm} = \frac{1}{\sqrt{1-\beta_{cm}^2}}. \tag{5.15}$$

The center of mass frame moves relative to the lab frame at a velocity of

$$\beta_{cm} = \frac{\bar{E}_\gamma}{\bar{E}_\gamma + m_d}. \tag{5.16}$$

The energy dependence of the invariant cross section, $\frac{d\sigma}{dt}$ (where t is the Mandelstam variable), is a more useful form to study the energy dependent scaling properties of deuteron photodisintegration. The invariant cross section is given by

$$\frac{d\sigma}{dt} = \frac{d\sigma}{d\Omega_{cm}}\frac{d\Omega_{cm}}{dt} \tag{5.17}$$

$$\frac{d\Omega_{cm}}{dt} = \frac{\pi}{\bar{E}_{\gamma,cm}p_{p,cm}} \tag{5.18}$$

where $E_{\gamma,cm}$ and $p_{p,cm}$ are the photon energy and the proton momentum, respectively, in the center of mass frame. The derivations for $\frac{d\Omega_{lab}}{d\Omega_{cm}}$, β_{cm}, and $\frac{d\Omega_{cm}}{dt}$ are given in Appendix B.

5.2 Monte Carlo

A Monte Carlo program is available to simulate the behavior of the HMS [85]. Events are generated with initial conditions chosen randomly over user-definable ranges of particle momentum, δ, and particle position and trajectory angles, X_{beam}, Y_{beam}, Z_{beam}, X'_{beam}, Y'_{beam}. These are given in the beam coordinate system illustrated in Figure 3.6 where $\hat{Z}_{beam}$ lies along the direction of the beam, and $\hat{Y}_{beam}$ points vertically upward. These parameters are transformed into the spectrometer coordinate system (δ, x_{tar}, y_{tar}, x'_{tar}, y'_{tar}) and then projected forward through the spectrometer.

Figure 4.11 illustrates the transformed quantities in relation to the position of the target and the spectrometer.

The COSY Infinity program [79] is used to produce a series of matrices which transports the simulated event forward to various points along the spectrometer, including finding particle trajectories at the collimator, the entrance and exit of each quadrupole, and 2/3 of the way along the length of Q1 and Q2. If the event can be projected through the apertures at all these points, and if the event traverses the active area of the drift chambers and 3 out of 4 hodoscope planes, then it is considered a valid event; otherwise it is discarded.

The COSY forward matrix elements determine the event parameters at each point (x_p, y_p, x'_p, y'_p) along the event path up to the focal plane from the initial target parameters. The matrix F is an expansion of the form

$$\begin{bmatrix} x_p \\ y_p \\ x'_p \\ y'_p \end{bmatrix} = \sum_{ijklm} F^p_{ijklm} (x_{tar})^i (y_{tar})^j (x'_{tar})^k (y'_{tar})^l (\delta)^m, \ (1 \leq i+j+k+l+m \leq N) \quad (5.19)$$

where $N = 5$, the order of the expansion in the COSY generated matrix and p denotes the plane along the event path at which the event parameters are calculated.

An estimate of multiple scattering is applied to the event where it would pass through a scattering source as the event is projected forward through the spectrometer. These scattering sources include the target material, the target chamber exit window, the spectrometer entrance window, the detector materials, and the air within the spectrometer hut. The focal plane parameters are then smeared with the resolution of the drift chambers.

The Monte Carlo then uses the reverse matrix, R, which is generated by COSY. This is used to reconstruct the target parameters from the focal plane quantities and is given by

$$\begin{bmatrix} y_{tar} \\ x'_{tar} \\ y'_{tar} \\ \delta \end{bmatrix} = \sum_{ijkl} R_{ijkl}(x_{fp})^i (y_{fp})^j (x'_{fp})^k (y'_{fp})^l, \; (1 \leq i+j+k+l \leq N). \tag{5.20}$$

The initial, focal plane, and reconstructed quantities are then stored in an n-tuple for further analysis through PAW. The COSY reverse matrix is also used in analysis to find target parameters from focal plane quantities for real data. Presumably, the reverse matrix should give back the original target parameters that are randomly chosen. But this is not exactly the case in the Monte Carlo as multiple scattering is added to each event as well as the expected resolution in the drift chambers. Thus the reconstructed event deviates slightly from the original parameters.

The Monte Carlo code was modified to account for specific aspects of this experiment. Examples of these modifications include estimates of multiple scattering and energy loss from the event striking the collimator or the gate valve (see Section 5.3.1) and to weight the initial momentum distribution of events with the bremsstrahlung spectrum folded with a s^{-11} dependence on invariant cross section given by the constituent scaling model (see Section 2.2).

5.3 Background Sources

This experiment relies on measuring the cross section for deuteron photodisintegration by detecting the recoil protons from the reaction. However, there are many other reactions that occur in the deuterium target with the combined bremsstrahlung photon beam and electron beams. Some of the resultant reaction products are ejected into the acceptance of the spectrometer. This section describes sources of background which result from these other reactions. Methods of identifying the individual types of background are discussed as well as ways of removing their effect from the underlying photodisintegration data. Some sources of background, such as that from the aluminum target windows, are removed using the yield subtraction described in Section 5.1.1.

5.3.1 Gate valve

During part of the experiment, a gate valve near the front of the spectrometer failed and moved to a state where it partially obstructed the acceptance. This failure was discovered during offline analysis after all the data were taken.

The gate valve is located about 145 cm from the target. The gate valve shutter is composed of SST-316 Stainless Steel. The diameter is 37.58 cm and the thickness is 1.33 cm. Figure 5.4 shows a schematic of the gate valve assembly. Only the shutter was left in the spectrometer acceptance. No part of the remaining gate valve assembly moved into the view of the spectrometer.

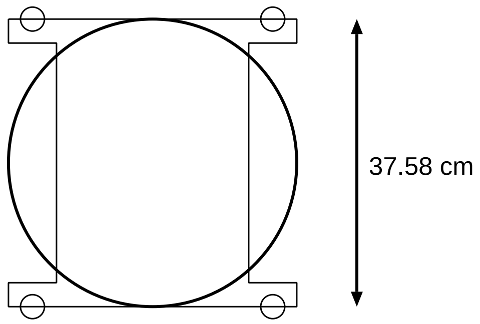

Figure 5.4: Schematic diagram of gate valve and mechanism.

The valve acts as a multiple scatterer for detected photo-protons. A Monte Carlo study, described below, was undertaken to understand the extent of this problem. Ultimately, the data in the acceptance that were occluded by the valve were not analyzed. Figure 5.5 shows the extent of the obstruction. An outline of the edge of the gate valve overlaid on the data clearly shows the boundary of the affected data.

The gate valve obstructed part of the spectrometer acceptance for all data analyzed here except for three measurements at $E_{beam} = 2.445$ GeV at angles $\theta_{cm} = 37.1°$, $53.0°$, and $70.1°$. Additional data were taken at a later time without the obstruction

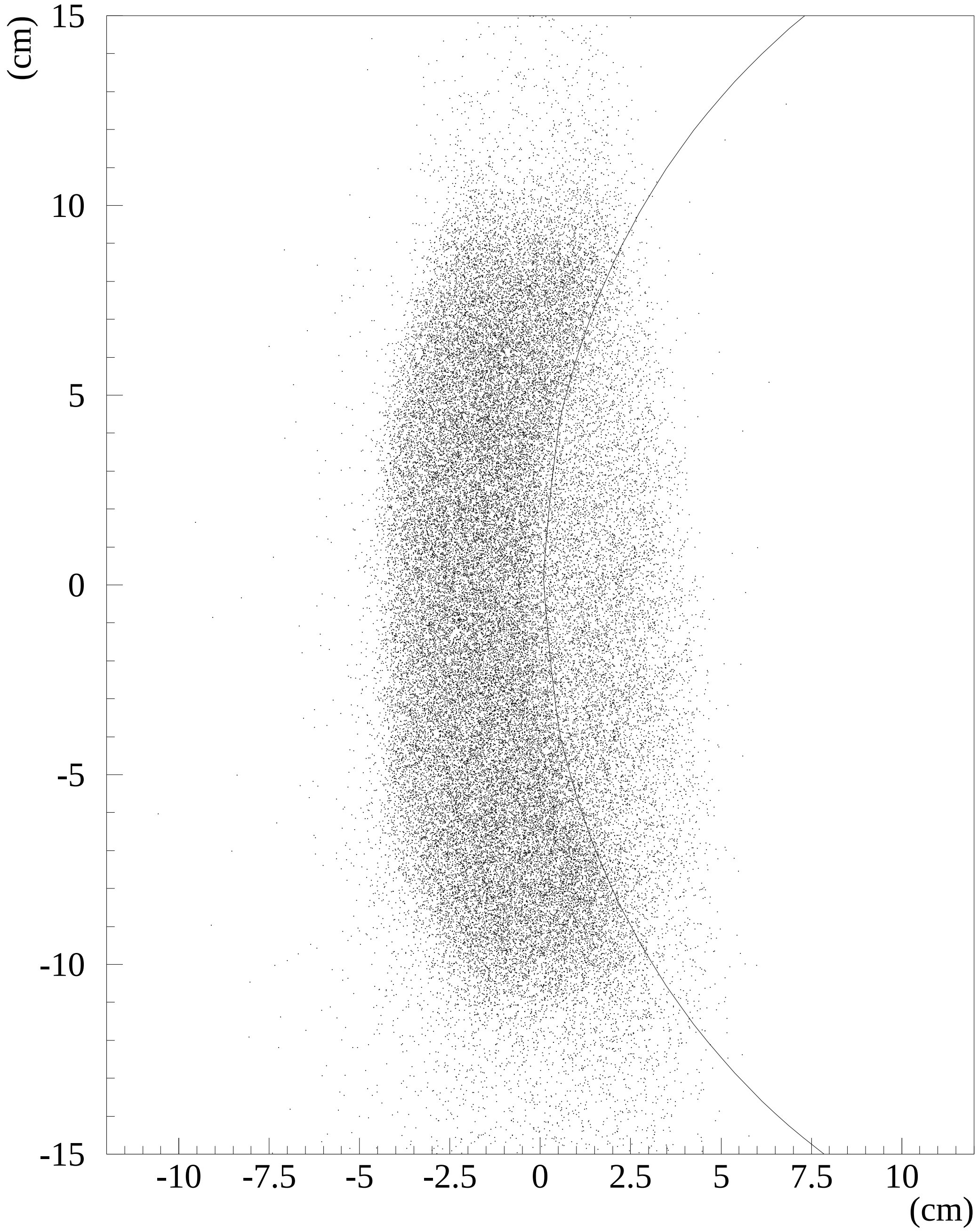

Figure 5.5: Attenuation from gate valve. Shown here are the reconstructed particle positions at (z_{HMS} = 145 cm) downstream from the target for data taken at $\theta_{cm} = 89.0°, E_{beam} = 1.645$ GeV. An outline of the edge of the valve is overlaid on the data.

at $E_{beam} = 4.045$ GeV, $\theta_{cm} = 53.0°$ and $E_{beam} = 4.045$ GeV, $\theta_{cm} = 70.2°$.

In an effort to determine what kind of effects are expected due to multiple scattering and energy loss of photo-protons traversing the gate valve, the Monte Carlo program was used to model the obstruction. When the Monte Carlo generates events which traverse the position of the gate valve, new event parameters are determined which include the multiple scattering and energy loss estimate. The event is then projected through the remainder of the spectrometer.

Multiple scattering is implemented using the composition and thickness of the gate valve plate over a gaussian distribution for angular scattering [86],

$$\theta_0 = \frac{13.6MeV}{\beta p} z \sqrt{\frac{x}{X_0}} \left[1 + 0.038 \ln\left(\frac{x}{X_0}\right)\right] \tag{5.21}$$

where β is the velocity of the particle, p is the momentum of the particle, and $\frac{x}{X_0}$ is the thickness of the scattering medium in radiation lengths. Two variables, z_1 and z_2, are chosen over a gaussian distribution of width 1 for each plane to find the scattered angle and linear offset as described in [86],

$$\delta y_{plane} = z_1 x \theta_0/\sqrt{12} + z_2 x \theta_0/2 \tag{5.22}$$

$$\delta \theta_{plane} = z_2 \theta_0. \tag{5.23}$$

The mean energy loss is calculated using the Bethe-Bloch formula [87]

$$-\frac{dE}{dx} = (0.1535MeV cm^2/g)\rho \frac{Z}{A}\frac{z^2}{\beta^2}\left[\ln\left(\frac{2m_e\gamma^2\beta^2 W_{max}}{I^2}\right) - 2\beta^2 - \delta - 2\frac{C}{Z}\right] \tag{5.24}$$

where m_e is the mass of the electron, β is the velocity of the particle, $\gamma = 1/\sqrt{1-\beta^2}$, I is the mean excitation potential, δ is the density correction, and C is the shell correction. The atomic number, the atomic weight and the density of the material are given by Z, A, and ρ respectively. For the gate valve material, effective parameters are calculated using the composition of SST-316 stainless steel. The values are $Z_{eff} = 26.36$, $A_{eff} = 56.72$, and $\rho_{eff} = 7.94$ g/cm^3. The maximum energy transfer in a single collision, W_{max}, is approximated for heavy incident particles as

$$W_{max} \simeq 2m_e\beta\gamma. \tag{5.25}$$

There is a probability that the incident proton event is absorbed due to nuclear reactions with the gate valve material. An estimate of the absorption probability is included in the Monte Carlo. The probability of absorption of a proton in a material of thickness X is given by [88]

$$A = 1 - e^{-X/\lambda} \tag{5.26}$$

where λ is the mean free path of the proton. The mean free path is taken to be the average mean free path for the two extremes, λ_I, the mean free path for inelastic collisions and λ_T, the mean free path for any type of collision.

Although the Monte Carlo only takes into account small angle scattering, the effects of the gate valve are evident. Figure 5.6 shows the results of a simulation for $E_{beam} = 1.645$ GeV, $\theta_{cm} = 89°$, which can be visually compared to data shown in Figure 5.5. In addition, multiple scattering and energy loss cause a smearing in the reconstructed target parameters and in the calculated photon energy. Figure 5.7 shows the change in the initial and reconstructed quantities in δ, y_{target}, and E_γ for events which are unobstructed by the valve and for events which pass through the valve and enter the spectrometer. The gate valve smears the events in the above three parameters well beyond the precision of the spectrometer. From this simulation it can be seen that events that penetrate the gate valve do not have reliable target parameters (e.g. the reconstructed E_γ has a width that is comparable to the window used to calculate the cross section as shown in Section 5.1.1) and cannot be corrected in data analysis.

Because the gate valve obstructs nearly one half of the HMS acceptance, only the half-acceptance without the gate valve is used in data analysis. The face of HMS collimator allows for a θ aperture of $\pm 1.6°$ from the central angle, θ_{HMS}. Utilizing only half of the θ acceptance shifts the central angle, θ_{HMS}, forward by $0.8°$ in the lab frame. New values for the central angle in the center of mass frame, θ_{cm}, are determined by projecting θ_{HMS} into the center of mass frame. Table 5.1 lists the values of the central angles in the center of mass frame for each kinematics where

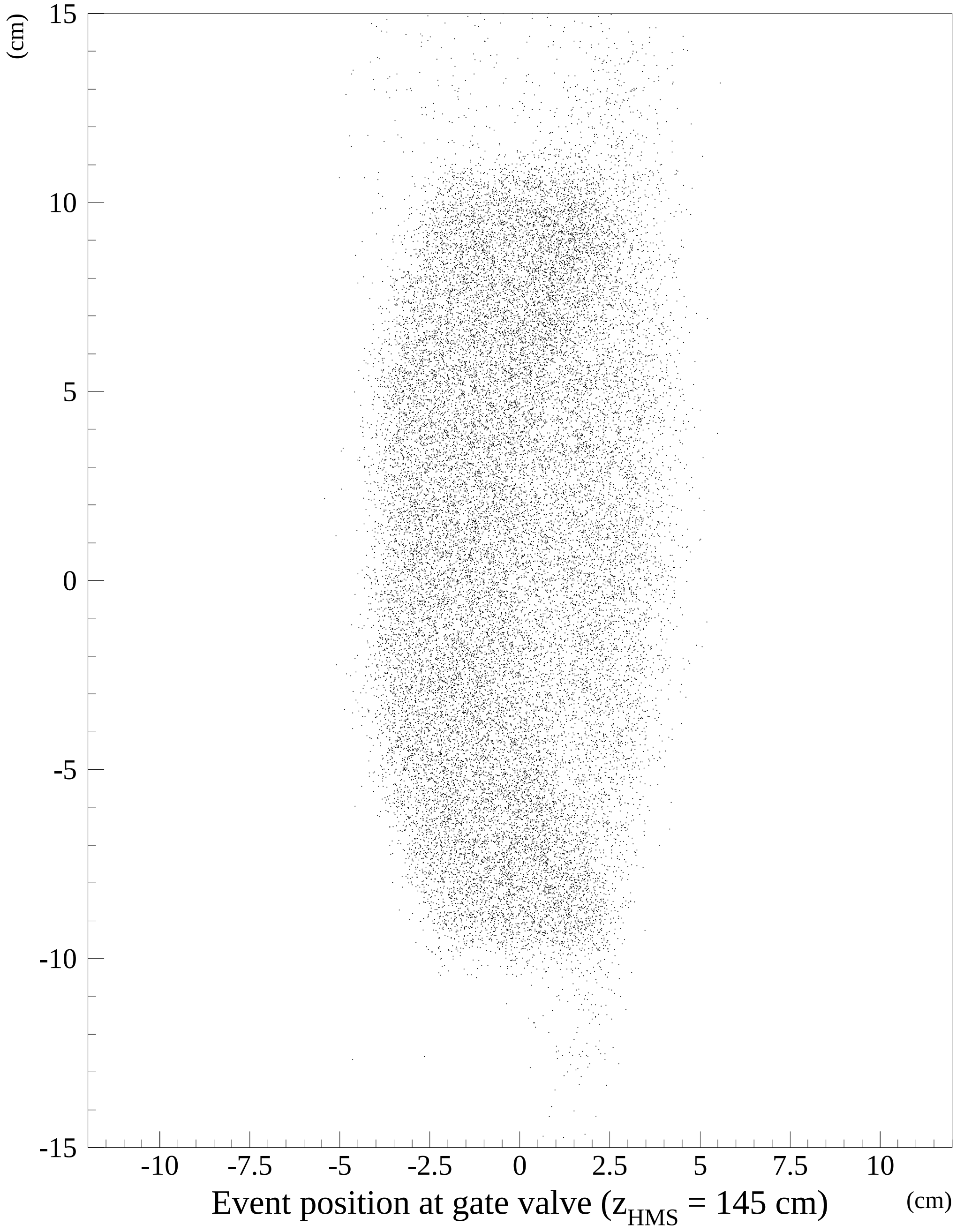

Figure 5.6: Reconstructed particle positions at ($z_{HMS} = 145$ cm) for a simulation of $E_{beam} = 1.645$ GeV, $\theta_{cm} = 89°$.

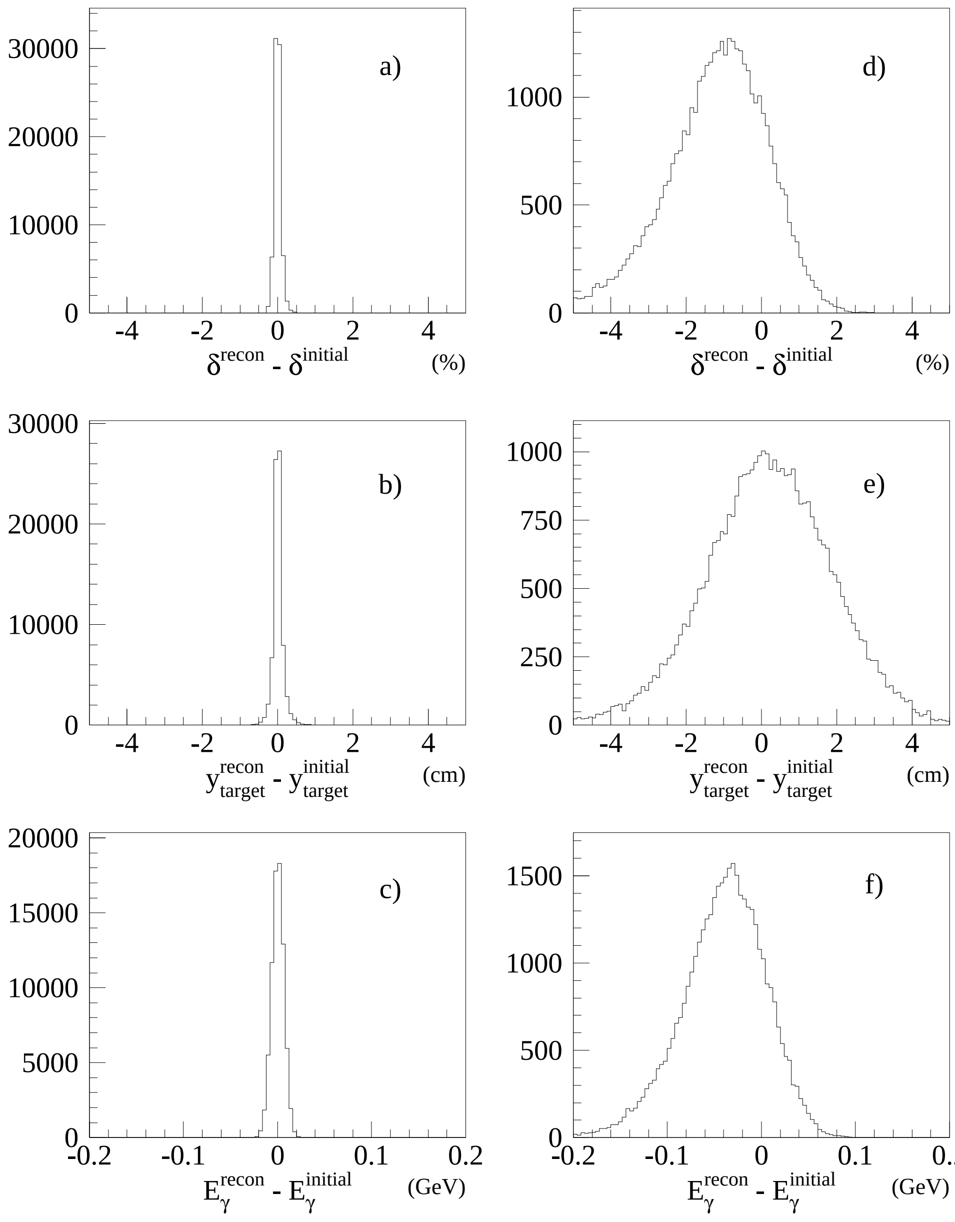

Figure 5.7: Difference in reconstructed and initial parameters for a simulation of E_{beam} = 1.645 GeV, θ_{cm} = 89°. Figures a), b), c) on left show the difference in δ, y_{target}, and E_γ, respectively, for events which are not obstructed by the gate valve. Figures d), e), f) on right show the difference in δ, y_{target}, and E_γ, respectively, for events for those events which pass through the gate valve and enter the spectrometer.

only half of the acceptance is used in data analysis. For the kinematics where the gate valve was not present, central angles for the full acceptance are listed at the bottom of the table.

E_{beam} (GeV)	Nominal θ_{cm}	Actual θ_{cm}
0.845	36°	36.2°
	89°_1	88.7°
	89°_2	89.5°
1.645	36°	35.8°
	52°	51.9°
	69°	68.9°
	89°	89.0°
2.445	36°	35.6°
	52°	51.6°.
	69°	68.8°
	89°	89.0°
3.245	36°	35.5°
	52°	51.6°
	69°	68.7°
	89°	88.8°
4.045	36°	35.4°
	52°	51.5°
	69°	68.7°
	89°	88.8°
2.445	36°	37.1°
2.445	52°	53.0°
2.445	69°	70.1°
4.045	52°	53.1°
4.045	69°	70.2°

Table 5.1: Actual center-of-mass angles in degrees for the half acceptance that is not obscured by the gate valve. The bottom portion of the table list the center-of-mass angles for the full acceptance for kinematic settings where the gate valve is not present. Note that for $E_{beam} = 0.845$ GeV, the data for $\theta_{nom} = 89^\circ$ are separated into two different regions in E_γ in the analysis (see Section 5.4.3), which correspond to different values for θ_{cm}.

Using only half of the acceptance cuts out most of the data that are affected by the gate valve. However, some events are scattered into the part of the acceptance

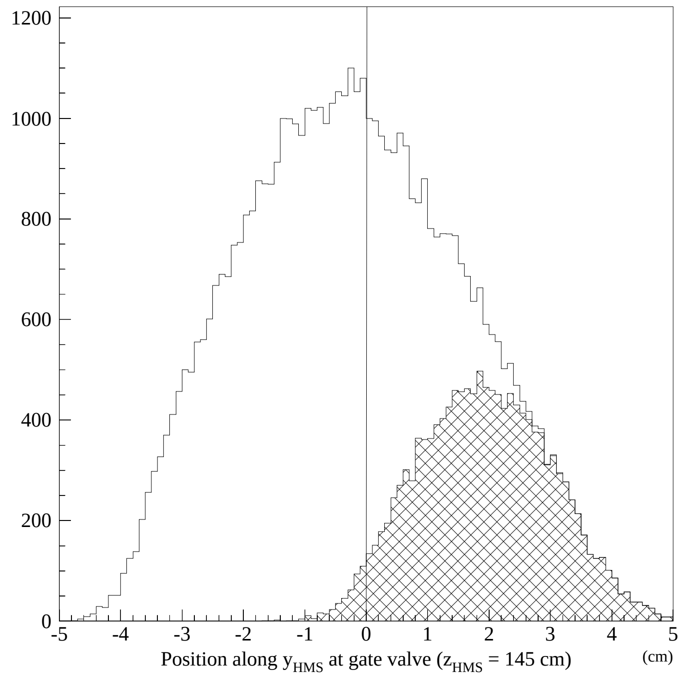

Figure 5.8: Monte Carlo simulation of the reconstructed position along $\hat{y}_{HMS}$ for E_{beam} = 1.645 GeV, $\theta_{cm} = 89°$, at the position of the gate valve (z_{HMS} = 145 cm). The main graph shows the histogrammed position for all events that are within the spectrometer acceptance. The 'unobstructed' half of the acceptance corresponds to the region $y_{HMS} < 0$. The crosshatched area shows the events which are scattered by the gate valve, showing the portion of those events which leak into the half-acceptance used in data analysis for those kinematics affected by the gate valve.

used in data analysis. Figure 5.8 shows an example of using the Monte Carlo to estimate the scattering that is caused by the gate valve. The left portion is the half-acceptance used in data analysis. The main graph shows the position along $\hat{y}_{HMS}$ at the position of the gate valve (z_{HMS} = 145 cm) for E_{beam} = 1.645 GeV,$\theta_{cm} = 89°$. The crosshatched area describes the events that pass through the gate valve. An estimated 1.5% of the events that are within the unobstructed region originate from the gate valve.

5.3.2 Pion production

The equation used to reconstruct the original photon energy (Equation 5.1) assumes that the detected proton is formed in the desired reaction $\gamma d \rightarrow pn$. However, if the detected proton were formed by the process $\gamma d \rightarrow pn\pi^0$ (see Figure 5.9), then Equation 5.1 would not apply, and the reconstructed photon energy would be incorrect.

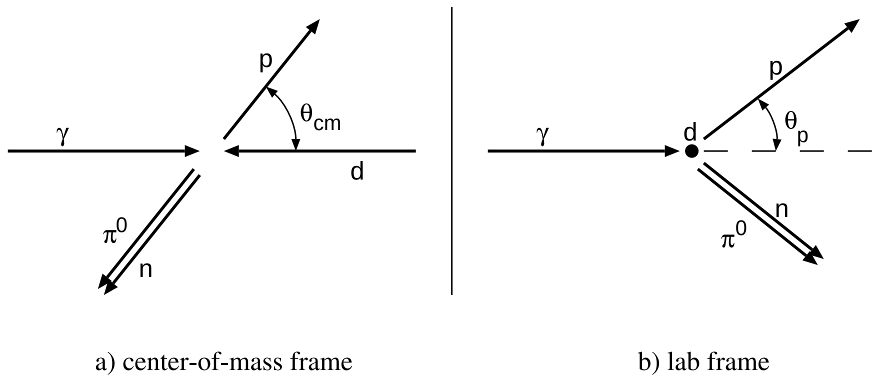

Figure 5.9: Pion production in the deuteron photodisintegration reaction in the center of mass and the lab frame.

As already mentioned, the cross section for $\gamma d \rightarrow pn$ is determined by considering only the region of E_γ near the endpoint. The lower end of the energy window is delineated by the threshold at which pion production begins in the range of reconstructed photon energies.

The threshold can be determined by calculating the maximum proton energy that can be achieved in the pion production reaction, and then reconstructing the photon energy using Equation 5.1. The detailed derivation is given in Appendix B.6. The maximum proton energy obtainable from a pion production event is given by

$$E_{p,cm}^{max} = \frac{E_{cm}^2 + m_p^2 - (m_n + m_{\pi^0})^2}{2E_{cm}}. \tag{5.27}$$

where $E_{cm} = \sqrt{s}$, and m_p, m_n, and m_{π^0} are the masses for the proton, neutron, and neutral pion, respectively.

After boosting the proton energy into the lab frame, the maximum reconstructed photon energy is different from the actual photon energy. Table 5.2 shows the difference in the two energies for the kinematics studied. In order to totally exclude all possible events from pion production, the proton angle used to determine the pion production threshold corresponds to the leading edge of the collimator aperture. The collimator aperture has an opening angle of $\pm 1.6°$ from the central angle, θ_{HMS}. Therefore, for the purposes of calculating the threshold using Equation 5.1, $\theta_p = \theta_{HMS} - 1.6°$.

E_{beam} (GeV)	θ_{cm}	$E_{\gamma d \to pn} - E_{\gamma d \to pn\pi^0}$ (MeV)
0.845	36.2°	93.4
	88.7°, 89.5°	138.2
1.645	35.8°	87.6
	51.9°	96.2
	68.9°	110.7
	89.0°	138.8
2.445	35.6°, 37.1°	85.1
	51.6°, 53.0°	93.8
	68.8°, 70.1°	108.9
	89.0°	138.7
3.245	35.5°	83.7
	51.6°	92.5
	68.7°	107.8
	88.8°	138.7
4.045	35.4°	82.8
	51.5°, 53.2°	91.6
	68.7°, 70.2°	107.1
	88.8°	138.6

Table 5.2: Thresholds for pion production for the kinematics studied. Above the threshold, all kinematically allowed events come from $\gamma d \to pn$. The angles shown above are central values. The actual proton angles used to find the thresholds correspond to the forward edge of the collimator aperture.

If the energy window is constructed to exclude events which may be generated by a pion production reaction, then all the events analyzed should come strictly from deuteron photodisintegration alone. The original energy windows used in analysis for cross section results shown in [89] included some of the region beyond the pion production threshold. In the worst case, 3.7% of the energy window included the region beyond the threshold. Because the photon flux is small at the endpoint, the number of events from pion production reactions is expected to be small compared to events from photodisintegration. Assuming the pion production yield is close to that of photodisintegration near the endpoint, the worst case kinematics would have overestimated the yield by 0.2%. The overestimation for all other kinematics is less. The energy windows used in the analysis presented here have been changed accordingly to exclude any proton events arising from pion production.

5.3.3 Background

Despite efforts to identify and subtract all expected sources of background from the data, additional events remain that are not a result of deuteron photodisintegration. These events come from particles which scatter off material along their path and are diverted into the spectrometer acceptance. Optics reconstruction of most background events map the particles to impossible target parameters. These are discarded in data analysis through software cuts. However, some background events are reconstructed back to points that lie within the software cuts, which results in misidentifying them as $\gamma d \rightarrow pn$ events.

Figure 5.10 shows the protons which pass detector cuts reconstructed back to the plane of the collimator for the LD_2^{in} configuration for $E_{beam} = 4.045$ GeV, $\theta_{cm} = 53.2°$. The octagonal borders of the collimator can clearly be seen. The events which are outside of those borders are background events of unknown origin. Most of the background is discarded from the data analysis by software cuts that are defined by the interior box. However, some number of background events remain within those cuts and are masked by real data.

It is difficult to determine precisely the magnitude of the background in the final yield determination by looking strictly at the area within the HMS acceptance. However, if it is assumed that the background events are uniformly distributed over the central area, then the size of the background contribution can be estimated by

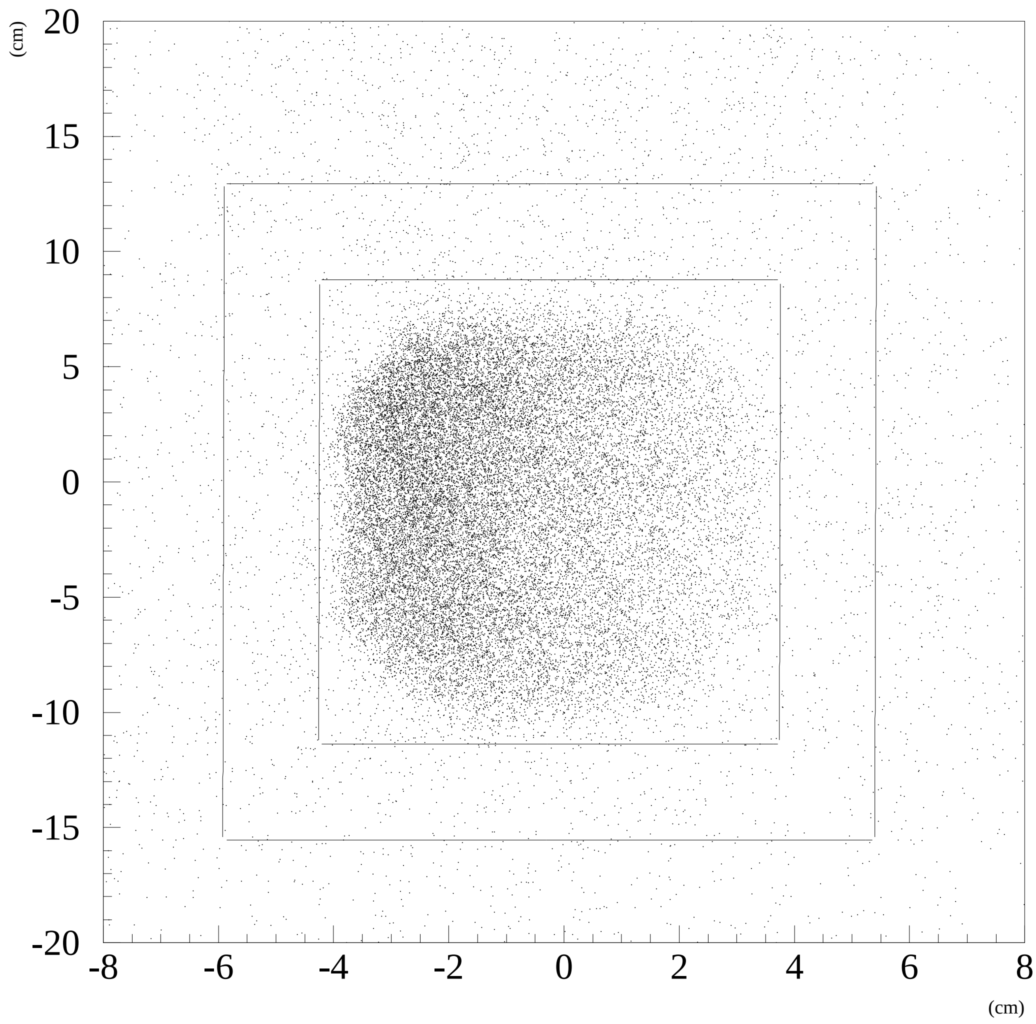

Figure 5.10: Proton events reconstructed back to the plane of the collimator (z_{HMS} = 126 cm) for the LD_2^{in} configuration for E_{beam} = 4.045 GeV, θ_{cm} = 53.2°. The inner box shows the software cuts used in data analysis. The area between the outer box and the inner box is equal in area to that of the inner box and is used to estimate the amount of accidental background which remains after all other background subtraction.

looking at a region of equal size where only accidental background events are evident.

The area between the inner box and the outer box in Figure 5.10 covers an equal area to that of the inner box which is used in data analysis, but this perimeter only contains accidental events. Figure 5.11 shows the histogrammed spectrum for E_γ for $E_{beam} = 4.045$ GeV, $\theta_{cm} = 35.4°$. The crosshatched area shows the spectrum for the perimeter area which contains only background events. Above the bremsstrahlung endpoint, where no signal is expected, the spectrum from the perimeter area closely resembles that of the central HMS acceptance. The background estimate continues to be small and uniform over the first 200 MeV below the endpoint. This 'evidence' that the accidental background is uniform over that range in E_γ gives a possible method of removing the contribution due to background. *Therefore in the data analysis, the accidental background is estimated by subtracting the average background yield above the bremsstrahlung endpoint.*

The accidental background is noticeable only at high energy settings. In these cases, there is a greater chance that particles can be scattered into the spectrometer acceptance. Figure 5.11 shows the case for the highest spectrometer momentum setting and smallest scattering angle, where the background event rate is expected to be maximum. For all other kinematics, the background rate drops off rapidly as the spectrometer momentum setting decreases and the scattering angle increases until the rate for background becomes negligible. For example, for the worst case kinematics, $E_{beam} = 4.045$ GeV, $\theta_{cm} = 35.4°$, the background level comprises 11$\pm$1% of the total photo-proton yield. For $E_{beam} = 3.245$ GeV, $\theta_{cm} = 35.5°$, the background level drops to 2.4$\pm$0.5% of the total yield.

5.4 Other Cross Section Factors

Differential cross sections require knowledge of spectrometer, beam, and target quantities in addition to event characteristics. This section describes how these normalizations and corrections are determined.

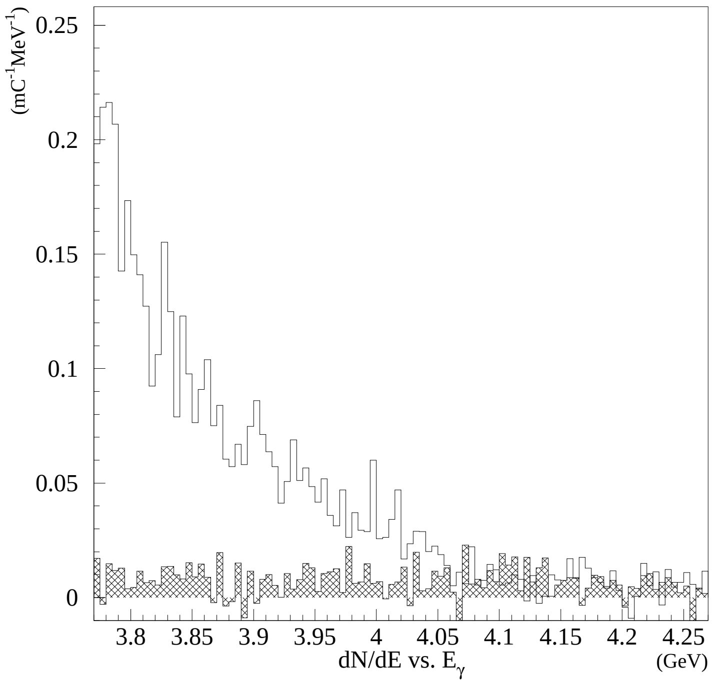

Figure 5.11: Normalized photo-proton yields for $E_{beam} = 4.045$ GeV, $\theta_{cm} = 35.4°$ as a function of E_γ. The crosshatched area shows the normalized spectrum for background events which lie in an area around the perimeter of the spectrometer acceptance.

5.4.1 Solid Angle

The HMS spectrometer is designed to detect particles originating within the target. The event can be described as originating at a position (x_{tar}, y_{tar}, z_{tar}) with a trajectory described by a momentum, δ, and angles x'_{tar}, y'_{tar} in the HMS coordinate system shown in Figure 3.6. However there is only a finite range in target parameters over which the spectrometer can detect events.

The spectrometer acceptance is defined as the probability that an event with initial parameters (x_{tar}, y_{tar}, z_{tar}, x'_{tar}, y'_{tar}, δ), will be detected. Therefore the spectrometer acceptance is a function of six variables, $A = A_6(x_{tar}, y_{tar}, z_{tar}, x'_{tar}, y'_{tar}, \delta)$.

The Monte Carlo model of the HMS (described in Section 5.2) is used to determine the acceptance function, A_6. Figure 5.12 shows the modeled acceptance for the HMS for parameters x'_{tar}, y'_{tar}, δ, and y_{tar}. The position parameter x_{tar} (transverse to the electron beam) is not considered important as it is confined to very small values (± 1 mm) by the size of the bremsstrahlung and rastered electron beam. The position value z_{tar} is projected onto the $\hat{y}_{tar}$ axis as shown in Figure 4.11. The Figure shows the histogrammed ratio of the number of final events to initial events for each of the four variables. Ratios of greater than 1 are possible because the event may be reconstructed to slightly different target parameters, due to multiple scattering estimates in the Monte Carlo..

The acceptance is relatively flat along a wide range of each parameter. Data cuts used in the analysis include only that central region over which the acceptance is well known and nearly one. In addition, the presence of the collimator restricts the values of x'_{tar} and y'_{tar} to an area where the acceptance is flat. Therefore it is unnecessary to calculate an acceptance function for different regions of the spectrometer parameter space.

In place of an acceptance function that varies over the initial parameter space, an effective solid angle can be calculated through use of the HMS Monte Carlo to properly normalize the data. The solid angle is a measure of the total angular area of the HMS acceptance. The solid angle for this experiment is defined as

$$\Delta\Omega = (\Delta x'_{tar} \Delta y'_{tar}) \frac{N_{final}}{N_{initial}} \tag{5.28}$$

where $N_{initial}$ is the number of events generated by the Monte Carlo, N_{final} is the number of events which pass into the spectrometer and are reconstructed back to the target successfully, and $\Delta x'_{tar}$ and $\Delta y'_{tar}$ are the ranges in angles used to determine the solid angle (± 80 mr x ± 55 mr). The angular range is increased slightly beyond the geometric boundaries to ensure that the edges of the collimator are not clipped off from the calculation for the solid angle.

The initial parameters of events are chosen using the same data cuts used in data analysis. Events are generated uniformly over the scattering and out of plane angles, y'_{tar}, x'_{tar}, and along the length of the target, Z_{beam}. Two additional position param-

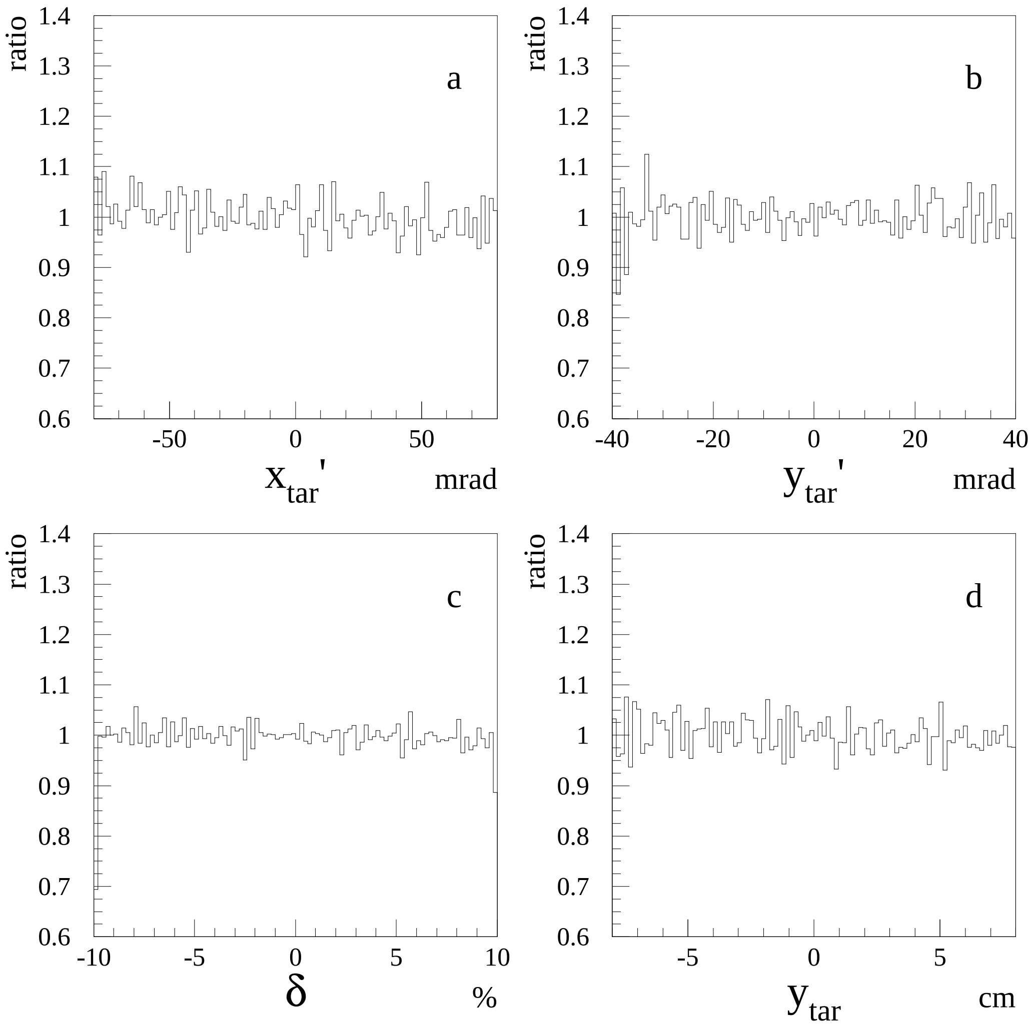

Figure 5.12: Acceptance for Monte Carlo for x'_{tar}, y'_{tar}, δ, and y_{tar}. Shown are the ratios of final reconstructed target parameters to the initial target parameters for a simulation run at $p_{HMS} = 1.920$ GeV, $\theta_{HMS} = 51.5°$. A ratio of 1 indicates that all events in that parameter space successfully track into the spectrometer.

eters, X_{beam} and Y_{beam} are generated within a very narrow range given by the size of the raster. The position parameters are transported using the angle parameters to the $\hat{y}_{tar}$ axis, shown in Figure 4.11, to give the initial event position, where $z_{tar} = 0$. The initial value for δ is determined by first randomly choosing a photon energy over the probability of photo-protons expected from the s^{-11} variation given by the constituent scaling model (see Section 2.2) folded with the shape of the bremsstrahlung spectrum generated by the radiator. The initial photon energy and scattering angle is used in Equation 5.1 to determine the initial particle momentum which defines δ.

The Monte Carlo was run for one million initial events for each kinematics and the values used in data analysis are given in Table 5.3. Values are given for the half acceptance for all kinematics for the half of the spectrometer acceptance that is not obscured by the presence of the gate valve. Solid angles for full acceptances are listed at the end of the Table for kinematics where the gate valve was not present. The statistical error for the Monte Carlo values of solid angle are about 0.5%. The reduced statistical accuracy on one million initial events is due to the number of events which are stopped along their path by the collimator, magnet, and detector apertures. In addition, solid angle calculations for half-acceptances reject about half of the events because they fall in the wrong half of the acceptance.

The largest changes in solid angle come from differing target length cuts used in data analysis. The HMS collimator is optimized for events originating at the center of the target. However, the extended target allows for events to originate anywhere along the length of the target. As the distance between the event and the center of the target increases along the y_{tar} axis, the size of the collimator opening decreases, leading to a decreasing total effective solid angle. Differing target length cuts were used for each kinematics based on the lab angle of the HMS, θ_{HMS}. A discussion of how software cuts are chosen for the target length is given in Section 5.4.4.

5.4.2 Total Charge

The total charge accumulated for each run is determined by making a sum of individual measurements taken by the data acquisition system every two seconds during the run. A more detailed description of the charge measurement system is given in Appendix A. Each measurement consists of an average scaler rate for all beam cur-

E_{beam} (GeV)	θ_{cm}	$\Delta\Omega$ (msr)
0.845	36.2°	3.184
	88.7°	2.875
1.645	35.8°	3.293
	51.9°	3.231
	68.8°	2.978
	89.0°	2.896
2.445	35.6°	3.288
	51.6°	3.230
	68.8°	2.983
	89.0°	2.896
3.245	35.5°	3.335
	51.6°	3.233
	68.7°	3.073
	88.8°	2.886
4.045	35.4°	3.338
	51.5°	3.227
	68.7°	3.061
	88.8°	2.877
2.445	37.1°	6.556
2.445	53.1°	6.421
2.445	70.1°	5.926
4.045	53.1°	6.491
4.045	70.2°	6.346

Table 5.3: Effective solid angles used for data analysis. Values are given for the half of the spectrometer acceptances that is not obscured by the presence of the gate valve. Values for full acceptances are given at the end of the table for kinematics where the gate valve was not present.

rent measuring devices. The scaler rates are converted to an average current using parameters calculated using the calibration procedure outlined in the Appendix.

To properly normalize the yield, the total charge is measured for each of the four yield measurements (LD_2^{in}, LD_2^{out}, MT^{in}, MT^{out}) for each kinematic setting.

During most of the experiment, the measurements from BCM1 are used to determine the total charge. Measurements from BCM1 and BCM2 are virtually identical, except for the beginning of the experiment, when BCM2 was connected to an untested measuring device. This device was removed after unsatisfactory performance and replaced with the device outlined in the Appendix. This also caused the signal from BCM1 to become unstable during that time, so for the kinematics at $E_{beam} = 2.445$ GeV, BCM3 is used to calculate the total charge. BCM1 offers superior linearity over BCM3 as a function of beam current, and overall measurement precision and the stability of the pedestal are superior to that of the Unser PCT. For those runs where BCM3 is used to calculate total charge, the poor linearity was minimized by performing additional calibrations for low beam current runs.

In addition, for data taken during September, 1997, BCM3 is used to determine total charge after new hardware was installed to improve the linearity of the response.

There are two sources of systematic error. A 0.2 μA systematic error comes from the calibration procedure due to statistical fluctuations of the signal from the Unser PCT [90]. As the calibration procedure is completed at a beam current of about 20 μA, the uncertainty in the calibration is about 1.0%. An additional 1.0% systematic error comes from the uncertainty in the gain of the power meter used to measure the beam current from BCM1 for a total estimated uncertainty of 1.4%. The systematic error for using BCM3 is comparable to BCM1 after performing additional calibrations to minimize the nonlinear response at low current.

5.4.3 Bremsstrahlung Photon Yield

As the electron beam strikes the copper foil radiator, it produces a continuous photon beam spectrum through the bremsstrahlung process. This photon beam is used for the photodisintegration reaction. The photons are not tagged in the experiment event by event. Therefore the photon energy spectrum must be calculated.

The method used to calculate the energy spectrum is based on the method of Matthews and Owens [91]. The photon yield for an infinitely thin radiator as a function of photon energy is given by

$$\frac{dN_\gamma}{dk} = \frac{X_0 N_A d\tau}{A} \frac{d\sigma_{brem}}{dk}(E_0, k) \tag{5.29}$$

where A is the atomic weight, X_0 is the radiation length of the radiator material, and $d\tau$ gives the thickness of the radiator in radiation lengths [38]. The bremsstrahlung cross section is given by

$$\frac{d\sigma}{dk} = \frac{\alpha r_0^2}{k}[Z^2\Phi_n(Z, E_0, k) + Z\Phi_e(Z, E_0, k)] \tag{5.30}$$

where $\alpha = 1/137$, $r_0 = e^2/mc^2$, Z is the atomic number of the radiator, E_0 is the incident electron energy, and k is the photon energy. This cross section includes electron-nucleon reactions with the nuclei of the radiator, and electron-electron reactions with the atomic electrons of the radiator.

The above photon yield (Equation 5.29) requires corrections due to the finite thickness of the radiator. This includes corrections for multiple scattering and energy loss of the electron beam and absorption of photons in the radiator and the target. Effects from the finite energy width of the electron beam also need to be included [92].

The photon yields for the data taken in this experiment are estimated using computer code developed by Eric Belz [93]. Given an initial electron beam energy and estimated beam energy width, this code calculates the photon yield per unit charge as a function of photon energy for an infinitely thin radiator and a radiator of finite thickness. In addition, the energy spectrum is calculated for the electron beam after it traverses the radiator. This is used to estimate the correction factor necessary to calculate the proton yield for data taken with the radiator removed (see Section 5.1.1). The details of the calculation used in the computer code are given in [38].

Figure 5.13 shows an example of the bremsstrahlung spectrum for an electron beam of 4.045 GeV incident on a 6.02% copper radiator.

Table 5.4 gives the integrated photon yields for the kinematics studied. This is informational only, as the final analysis uses the photon yield divided into 1 MeV bins.

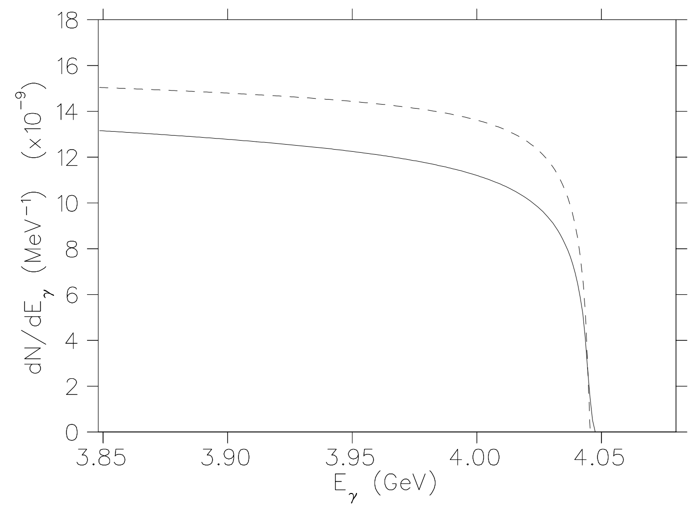

Figure 5.13: Bremsstrahlung energy spectrum for a 4.045 GeV electron beam incident on a 6.02% copper radiator. The dashed line corresponds to the spectrum in the thin radiator limit. The solid line includes corrections for finite radiator thickness.

5.4.4 Target Density

To determine the cross section, the photo-proton yield must be normalized to n_{nucl}, which gives the total nuclear density encountered by the photon and electron beams. The nuclear density is given by

$$n_{nucl} = fN_A A\rho l \tag{5.31}$$

where N_A is Avogadro's number, f is the number of atoms per molecule (2 for deuterium), A is the atomic weight of the cryogen, ρ is the volume density of the cryogenic target, and l is the length of the target used in data analysis.

The temperature and pressure of the cryogenic target is measured to within 50 mK and 0.1 psi. This leads to an uncertainty in the target density of less than 0.1% (see Section 3.6). However, the electron beam can cause localized temperature fluctuations as it passes through the target. To minimize localized effects, the electron beam is rastered to reduce power density on the target (see Section 3.4). The electron beam spot size is further enlarged during runs with the radiator in place due to multiple scattering from the radiator. In addition, flow diverters are installed in the target cells to create a turbulent flow to minimize localized fluctuations.

E_{beam} (GeV)	θ_{cm}	$E_{\gamma,high}$ (GeV)	$E_{\gamma,low}$ (GeV)	$\bar{E}_\gamma$ (GeV)	N_γ (x 10^9 γ/μ C)
0.845	36.2°	0.820	0.765	0.792	11.88
	89.5°	0.820	0.770	0.794	10.94
	88.7°	0.770	0.720	0.745	12.16
1.645	35.8°	1.620	1.565	1.592	9.99
	51.9°	1.620	1.555	1.587	11.94
	68.9°	1.620	1.540	1.579	14.93
	89.0°	1.620	1.510	1.563	21.05
2.445	35.6°	2.420	2.365	2.392	6.60
	51.6°	2.420	2.355	2.387	7.88
	68.8°	2.420	2.340	2.379	9.84
	89.0°	2.420	2.310	2.363	13.84
3.245	35.5°	3.220	3.165	3.192	4.90
	51.6°	3.220	3.155	3.187	5.85
	68.7°	3.220	3.140	3.179	7.30
	88.8°	3.220	3.110	3.163	10.26
4.045	35.4°	4.020	3.965	3.992	3.89
	51.5°	4.020	3.955	3.987	4.65
	53.2°	4.020	3.955	3.987	4.65
	68.7°	4.020	3.940	3.979	5.80
	70.2°	4.020	3.940	3.979	5.80
	88.8°	4.020	3.910	3.963	8.15

Table 5.4: Integrated photon yields per microcoulomb of electrons incident on a copper radiator. Radiator thickness is 3.49% radiation length for $E_{beam} = 0.845$ GeV, and 6.02% radiation length for all other kinematics. The photon energy window upper limit is $E_{\gamma,high} = E_{beam} - 25$ MeV, where E_{beam} is the bremsstrahlung endpoint, except for $E_{beam} = 0.845$ GeV, $\theta_{cm} = 89.1°$, where the window has been split into two regions of 50 MeV width. The average photon energy is calculated with Equation 5.11.

A study of localized boiling on a 15 cm deuterium filled cell showed that density changes are less than 0.5% for a raster amplitude of ± 1 mm and for beam currents less than 50 μA [94]. As the data for this experiment were taken at beam currents of less than 30 μA, no corrections are made to account for local density effects.

A chemical analysis of the components of the hydrogen and deuterium used in the experiment was completed by Lawrence Livermore National Laboratory [95]. Table 5.5 summarizes the results of the gas analysis. The purity of the deuterium was about 99.5%. Most of the contamination comes from hydrogen present in the deuterium supply. The purity of the hydrogen supply was about 99.8% with the main contaminants being oxygen and nitrogen. As these contaminants should freeze at the operating temperature of 19 K, no correction is made for the density of the hydrogen in the target. Table 5.6 gives the densities of the liquid hydrogen and deuterium in the target cells during the experiment [96, 97].

Target	Sample	Component	Abundance (%)
D_2	1	D_2	99.59 $\pm$ 0.01
		HD	0.301 $\pm$ 0.002
		N_2	0.070 $\pm$ 0.008
		O_2	0.037 $\pm$ 0.004
D_2	2	D_2	99.54 $\pm$ 0.013
		HD	0.220 $\pm$ 0.01
		N_2	0.183 $\pm$ 0.008
		O_2	0.060 $\pm$ 0.004
D_2	3	D_2	99.28 $\pm$ 0.01
		HD	0.616 $\pm$ 0.003
		N_2	0.072 $\pm$ 0.013
		O_2	0.037 $\pm$ 0.004
H_2	1	D_2	99.81 $\pm$ 0.01
		N_2	0.127 $\pm$ 0.008
		O_2	0.061 $\pm$ 0.004

Table 5.5: Results of target gas analysis by Lawrence Livermore National Laboratory.

Target	Temperature (K)	Density (g/cm^3)
H_2	19	0.07230 $\pm$ 0.0005
D_2	22	0.1670 $\pm$ 0.0012

Table 5.6: Densities of cryogenic targets used in the experiment. Errors include uncertainties in overall temperature and pressure, and localized temperature effects.

Target length

The aluminum target windows cause a large amount of background due to $Al(\gamma,p)X$ reactions. Due to limited resolution in reconstructing y_{tar}, some of this background is mapped to regions within the target. To minimize the contributions to the photo-proton yield from the aluminum endcap background, only the central region of the target is used in data analysis. The cuts used in data analysis for y_{tar} are given in Table 5.7. Because the spectrometer sees a projection of the target along $\hat{y}_{tar}$, the actual target length, Z, that is seen by spectrometer is given by

$$Z = \frac{y_{tar}}{\sin\theta_{HMS}}. \tag{5.32}$$

E_{beam} (GeV)	θ_{cm}	θ_{HMS}	y_{tar} (cm)
0.845	36.2°	25.1°	±2.0
	88.7°, 89.5°	65.6°	±4.0
1.645	35.8°	21.3°	±1.5
	51.9°	31.1°	±2.0
	68.9°	42.3°	±3.5
	89.0°	57.1°	±4.0
2.445	35.6°, 37.1°	18.9°	±1.5
	51.6°, 53.0°	27.7°	±2.0
	68.8°, 70.1°	37.9°	±3.5
	89.0°	51.5°	±4.0
3.245	35.5°	17.2°	±1.2
	51.6°	25.3°	±2.0
	68.7°	34.7°	±3.0
	88.8°	47.4°	±4.0
4.045	35.4°	15.9°	±1.2
	51.5°	23.4°	±2.0
	53.2°	23.4°	±1.8
	68.7°	32.2°	±3.0
	70.2°	32.2°	±2.2
	88.8°	44.2°	±4.0

Table 5.7: The region in y_{tar} used in data analysis for all kinematics.

To estimate the precision of choosing to use only the central portion of the target, the yields were calculated for different target lengths. Table 5.8 shows the results for two kinematics. The variation of the normalized yield is on the order of about 1.5%. A systematic uncertainty of that amount is assigned to the cross section.

Setting	$\|y_{tar}\|$ (cm)	$\left(\frac{d\sigma}{d\Omega}\right)_{lab}$ (nb/sr)
E_{beam} = 1.645 GeV	1.0	5.681±0.230
θ_{cm} = 89.1°	2.0	5.530±0.163
	3.0	5.433±0.135
	4.0	5.402±0.120
E_{beam} = 2.445 GeV	1.0	0.3953±0.0360
θ_{cm} = 88.8°	2.0	0.4005±0.0219
	3.0	0.3961±0.0213
	4.0	0.4004±0.0188

Table 5.8: Normalized integrated photo-proton yield for different target lengths. The errors given for the yield are statistical only.

Target length correction

The COSY matrix elements used to reconstruct target quantities from focal plane parameters provide an inaccurate measurement of the target length. The reconstructed target length is smaller for all kinematics. The source of this inaccuracy is unknown, but a correction must be applied to the data to account for the inaccuracy. Figure 5.14 shows the event yield for the empty configurations for four different kinematics settings at different beam energies and spectrometer angles. Since the target cells were empty for these data, the spectrometer can only see events which come from interactions with the aluminum target endcaps. The apparent target length was measured by determining the distance between the centroids of the peaks for each aluminum target window. Table 5.9 summarizes the apparent target lengths measured for the different kinematic settings.

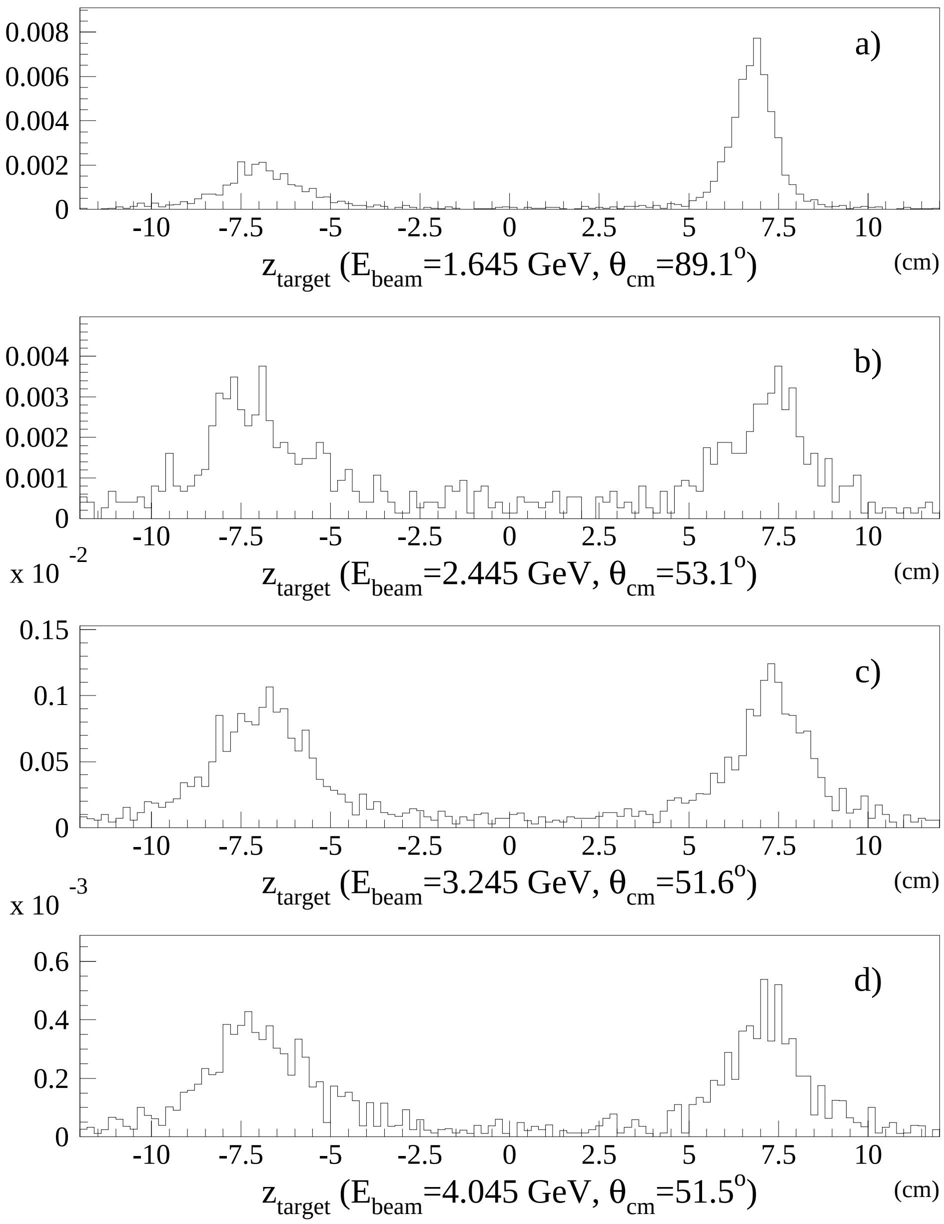

Figure 5.14: Event yields, $\frac{dN}{dZ}$, in arbitrary units over the length of the target. Empty target configurations are used which presents data that comes solely from the aluminum target windows. Figures a) - d) are labeled showing the kinematics that are histogrammed.

E_{beam} (GeV)	θ_{cm}	True Target Length (cm)	Apparent Target Length (cm)	Correction (%)
0.845	36.2°	15.12 ± 0.04	13.57 ± 0.04	11.4 ± 0.4
	89.1°	15.12 ± 0.04	13.42 ± 0.03	12.6 ± 0.4
1.645	35.8°	15.12 ± 0.04	13.94 ± 0.07	8.5 ± 0.6
	51.9°	15.12 ± 0.04	13.77 ± 0.08	9.8 ± 0.7
	68.8°	15.12 ± 0.04	13.87 ± 0.07	9.0 ± 0.6
	89.1°	15.12 ± 0.04	13.74 ± 0.04	10.0 ± 0.4
2.445	35.6°	15.34 ± 0.04	14.61 ± 0.08	5.0 ± 0.6
	51.6°	15.34 ± 0.04	14.70 ± 0.15	4.3 ± 1.1
	68.8°	15.34 ± 0.04	14.51 ± 0.07	5.7 ± 0.6
	88.8°	15.34 ± 0.04	14.23 ± 0.06	7.8 ± 0.6
3.245	35.4°	15.34 ± 0.04	14.22 ± 0.13	7.9 ± 1.0
	51.6°	15.34 ± 0.04	14.35 ± 0.10	6.9 ± 0.8
	68.7°	15.34 ± 0.04	14.43 ± 0.07	6.3 ± 0.6
	88.8°	15.34 ± 0.04	14.25 ± 0.04	7.7 ± 0.4
4.045	35.4°	15.12 ± 0.04	14.13 ± 0.20	7.0 ± 1.6
	51.5°	15.12 ± 0.04	14.10 ± 0.12	7.2 ± 0.9
	53.1°	12.48 ± 0.04	11.76 ± 0.10	6.1 ± 1.0
	68.6°	15.12 ± 0.04	14.25 ± 0.10	6.1 ± 0.8
	70.2°	12.48 ± 0.04	11.66 ± 0.07	7.1 ± 0.7
	88.8°	15.12 ± 0.04	14.19 ± 0.07	6.6 ± 0.6

Table 5.9: Apparent target lengths obtained by measuring the distance between the peaks for empty target cells for many kinematics settings. This shows the inaccuracy of the COSY matrix elements in reconstructing the position of the event at the target.

As the full target length is not used in the data analysis, the actual target length within the software cuts needs to be corrected by the ratio of actual to apparent target lengths. Figure 5.15 shows the ratio of the apparent target length to the actual target length with respect to the central momentum setting of the spectrometer. The error on the apparent target length is determined from the uncertainty in measuring the centroids of the peaks from the two aluminum target windows.

The cross section measured for each kinematic setting is reduced by the ratio of the two target lengths. The systematic error for each correction is added in quadrature to the uncertainty in target length due to yield fluctuations shown in Table 5.8 for

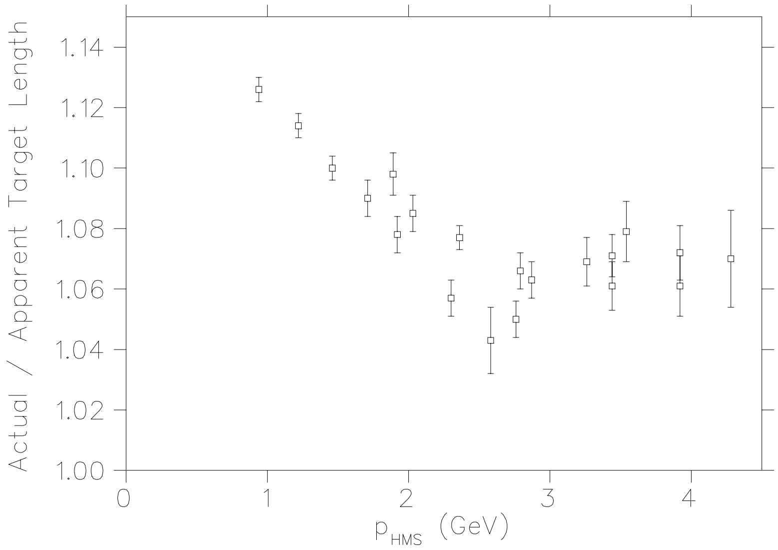

Figure 5.15: Correction for target length due to inaccuracy of COSY matrix element reconstruction of y_{tar}. Plotted is the ratio of actual target length to apparent target length as a function of the central spectrometer momentum. The errors include only the uncertainty of determining the centroids of the two target windows for each data set combined with the uncertainty of the physical measurement of the target lengths.

each kinematic setting to find the total systematic error for target length.

5.4.5 Proton Absorption

There is a finite probability that a proton undergoes a nuclear interaction within the materials between the reaction vertex and the detectors. If the interaction removes the proton from the spectrometer acceptance, the event is lost, and the proton yield is lower than expected. The probability that the proton will be 'absorbed' can be calculated given the nuclear interaction lengths and densities of the materials in the path of the proton. The fraction of protons absorbed is given by [88]

$$A = 1 - e^{-\sum_i X_i/\bar{\lambda}_i} \tag{5.33}$$

where X_i is the thickness of each material and $\bar{\lambda}_i$ is the nuclear interaction length of each material.

The interaction lengths describe the mean free path between nuclear reactions for the proton. Two different interaction lengths are given in [86]: λ_T gives the mean free path for all nuclear collisions, and λ_I gives the mean free path for inelastic collisions. The precise mean free path that would give the actual correction for proton absorption lies in between the two values as elastic nuclear reactions are typically very forward peaked and thus do not always remove the proton from the spectrometer acceptance. As the proton absorption is not measured directly, an average of the total and inelastic mean free path is used to estimate proton absorption.

Table 5.10 summarizes the materials that lie in the path of the proton from the center of the target to the detector stack. The estimate for the proton absorption using Equation 5.33 gives

$$A = 1 - e^{-0.1151} = 10.9\%. \tag{5.34}$$

For data taken where a signal must be received from four out of the four scintillator planes, proton absorption was estimated up to 1/4 of the way through the fourth scintillator plane (assuming that the proton is required to traverse only 1/4 of the scintillator to provide a valid trigger). Data taken with a three-out-of-four plane trigger would decrease the absorption estimate to 9.5%. In addition, the amount of liquid deuterium that the proton traverses depends on the spectrometer angle and varies from 3.6 cm at $\theta_{HMS} = 65.6°$ to 11.8 cm at $\theta_{HMS} = 15.9°$. This would vary the proton absorption estimate between 10.2% to 12.6%. However, as the target cell is only 15 cm long, the average amount of deuterium traversed in the very forward angles is less than the maximum of 11.8 cm as the proton exits the target through the forward endcap rather than the side of the target.

Direct measurements of the proton absorption for the HMS were performed using $H(e, e'p)$. They showed that the measured absorption rate of $5.5 \pm 2.0\%$ agreed with the estimate of 6.5% for the configuration used in the measurement [98]. Due to the uncertainty in the measurement and the uncertainty in estimating the correct average interaction length, $\bar{\lambda}$, an overall correction of 10.9% is made on all kinematics, with a systematic error of 2.0% assigned on the estimate of the correction.

Absorber	Density (g/cm^3)	Thickness (cm)	λ (g/cm^2)	X (g/cm^2)	X/λ (10^{-3})
LD_2 target (after scattering)	0.167	~6	50.2	1.0	19.9
5 mil Al target window	2.70	0.0127	88	0.0343	0.39
16 mil Al chamber window	2.70	0.0406	88	0.1096	1.24
Air	0.00121	~15	75	0.0182	0.24
Kevlar	0.74	0.0381	~70	0.0282	0.40
Mylar	1.39	0.0127	72	0.0177	0.25
Kevlar	0.74	0.0381	~70	0.0282	0.40
Mylar	1.39	0.0127	72	0.0177	0.25
Air (exit pipe through S2)	0.00121	~256	75	0.310	4.13
4 mil Mylar (entrance/exit)	1.39	0.0102	72	0.0142	0.20
Sense Wires (effective) 25μm W, 12 planes	19.3	0.000076	147.7	0.00146	0.010
Field Wires (effective) 150μm Al/Au (99/1) 18 planes	2.70	0.0068	89.1	0.0184	0.21
Ar/Ethane (50/50 weight)	0.00154	16.6	~70	0.0256	0.36
Field Wires (effective) 150μm Cu/Be (50/50) 18 planes	5.40	0.0068	87.9	0.0368	0.42
Polystyrene	1.03	2(1.067)(1.0)	70	2.198	31.40
Čerenkov windows 40 mil Al (entrance/exit)	2.70	2(0.102)	88.5	2(0.275)	6.22
Čerenkov gas C_4F_{10}	0.0106	150	78.8	1.59	20.18
Rohacell Mirror support	~0.05	~1.8	~70	0.09	1.3
Mirror SiO_2	2.20	0.3	83.1	0.66	7.94
Polystyrene	1.03	1.25(1.067)(1.0)	70	1.374	19.63
Total					115.1

Table 5.10: Materials in the HMS. The actual amount of LD_2 material depends on scattering angle.

5.4.6 Trigger Efficiency

The trigger for the experiment relies on the hodoscope to send signals as the event goes through the four scintillator planes. Inefficiencies in the hodoscope cause some fraction of those events to be lost as the trigger fails to fire.

The standard trigger for the experiment is to signal that an event has entered the spectrometer when at least one scintillator in three out of the four hodoscope planes detects an event. An efficiency can be given to each scintillator in the four planes, but it is easier to determine the total trigger efficiency by using the efficiencies of each scintillator plane as a whole,

$$\begin{aligned} P_{3/4} &= P_1 P_2 P_3 P_4 + P_1 P_2 P_3 (1 - P_4) + P_1 P_2 (1 - P_3) P_4 + \\ &\quad P_1 (1 - P_2) P_3 P_4 + (1 - P_1) P_2 P_3 P_4 \end{aligned} \tag{5.35}$$

where P_i is the probability that at least one scintillator in the hodoscope plane i detects the incoming event. The trigger efficiency for a three-out-of-four plane trigger for all kinematics is greater than 99.5%. For a four-out-of-four plane trigger, the efficiency is always greater than 99.2%.

5.4.7 Dead Time Corrections

To accurately measure cross sections, every event within the spectrometer acceptance must be recorded. However, if the event rate is high, the trigger and data acquisition system may be busy processing and recording a previous event, and incoming events may be lost. This loss rate is referred to as the dead time because it is the time fraction where the data acquisition is too busy to record incoming events, thus appearing 'dead'.

Electronic Dead Time

The electronic dead time is a result of the trigger system being busy as another event comes in. When the trigger is activated by an event, a logic gate is turned on for a finite time, τ (30 ns). If another event enters the spectrometer during that time, it does not activate the busy trigger system and is lost. Assuming that the event rate is constant over the length of each run and that the events occur randomly, the electronic dead time can be estimated. The probability distribution for the time between events is given by

$$P(t) = r\ e^{-rt} \tag{5.36}$$

where r is the mean event rate. Any events which enter the spectrometer when t is less than the trigger gate width, τ, it will be lost. Thus the fraction of events that are lost can be determined by integrating the probability distribution from 0 to the gate width, τ,

$$\text{Electronic dead time} = \int_0^\tau r\ e^{-rt} dt = 1 - e^{-r\tau}. \tag{5.37}$$

For this experiment, the data rates were small enough that the dead time can be approximated by $1 - e^{-r\tau} \approx r\tau$. The electronic dead time was measured by generating four different trigger gate widths (τ = 30, 60, 90, and 120 ns) and measuring the number of events which would be recorded for each of the four gate widths. A linear extrapolation back to zero gate width can be used to determine the electronic dead time for the real trigger width (τ = 30 ns).

In all kinematics, the dead time is less than 0.1%. Therefore, no correction is applied to the data for electronic dead time.

Computer Dead Time

A more significant source of dead time comes from the data acquisition system. Once a trigger is activated, there is significant delay in reading out the status of all of the detectors and recording it onto disk. The total processing time per event is on the order of 300-400 μs. While the data acquisition system is busy recording the event, subsequent events which enter the spectrometer are lost. The computer dead time can be measured by recording the number of triggers which are generated by events entering the spectrometer (called PRETRG) and comparing that to the number of events that are actually processed by the data acquisition system (denoted TRIG). The ratio of PRETRG to TRIG gives the fraction of time the data acquisition was 'live'. The computer dead time is the fraction of triggers which were lost. The total photo-proton yield corrects for the calculated computer dead time (see Equation 5.3).

The dead times for this experiment ranged up to 40% for high event rate runs. During the experiment, data were simultaneously taken for other reactions using the Short Orbit Spectrometer (SOS). This increased the load on the data acquisition system which processes events from both spectrometers, thereby increasing dead times for data taken with the HMS. For kinematics and target configurations where the event rate is high, a prescale factor is used which selects a set fraction of triggers to be processed. In most cases, the prescale factor is 1, so that there is an attempt to process all incoming events, but for $E_{beam} = 0.845$ GeV, the prescale factor is set up to 30, meaning only one out of every 30 events are sent to the data acquisition system to be processed.

5.5 Systematic Uncertainties

The measurement of the reaction cross section is limited to the measurement accuracy of the instrumentation and the detectors. Table 5.11 gives a summary of the systematic errors and their sources. The uncertainties can be loosely separated into two categories. Absolute errors affect all kinematics equally, stemming mostly from global estimates for corrections that apply to all kinematics equally. Point-to-point errors are uncertainties that affect each kinematics differently. Some sources of systematic error have contributions from both global and point-to-point errors, which will be discussed below.

The bremsstrahlung photon spectrum is strongly related to the electron beam energy. An uncertainty in the beam energy can lead to a shift in the spectrum, affecting the overall photon flux used to normalize the photo-proton yield. The beam energy is known to about 0.2% [99]. The systematic error in the cross section due

Description	Absolute Uncertainty	Point-to-Point Uncertainty
Beam Energy		0.2-2.1%
Total Charge	1.4%	
Bremsstrahlung Flux Calculation	3.0%	
Radiator Thickness	0.1%	
Radiator-Out Correction	1.0%	
Proton Absorption	2.0%	
Tracking Efficiency	3.4%	
Particle Identification		1.0-2.6%
Target Length	1.5%	0.4-1.6%
Target Density	0.7%	
Gate Valve Cut	3.0%	
Gate Valve Inscatter	0.5%	
Reconstruction/Acceptance	4.6%	
Solid Angle (statistical)	0.5%	
Background Subtraction		0.0-4.0%
Dead Time	<0.1%	

Table 5.11: Summary of systematic errors that affect calculation of the $\gamma d \rightarrow pn$ cross section.

to the uncertainty in the beam energy is estimated by comparing the photon flux calculations for electron beam energies that are shifted $\pm 0.2\%$ from nominal. This results in an uncertainty of 0.2% to 2.1%, depending on the nominal beam energy and the size of the window used in E_γ (see Section 5.4.3).

The uncertainty in the total charge from the electron beam has a number of components. The calibration runs taken during the experiment depends on the accuracy of the Unser PCT, which can measure the beam current to an accuracy of 0.2 μA over a short period of time [90]. Most calibrations were done at a beam current of about 20 μA, leading to a systematic error of 1.0%. An additional 1.0% systematic error comes from the overall uncertainty in the readings from the power meter used to measure the signal from BCM1. This leads to a combined uncertainty of about 1.4% (see Section 5.4.2).

A systematic error of 3% [91] is assigned to the total photon flux due to limitations of the algorithm used. Note that the first 25 MeV below the bremsstrahlung endpoint is excluded from the analysis due to large uncertainties in calculating the photon flux in such close proximity to the endpoint.

Errors in measuring the radiator thicknesses (see Section 3.5) also affect the bremsstrahlung spectrum, but as they are measured to an accuracy of about 0.1% [58], the total effect on the photon spectrum is minimal.

The factor used to correct for the change in the energy spectrum of the electron beam after it strikes the radiator, $f(E_\gamma)$, has an uncertainty that is comparable to that of the bremsstrahlung photon spectrum as it is calculated with the same algorithm (see Section 5.1.1). However, the systematic uncertainty on the cross section is only 1.0% as the correction is only applied to the configurations where the radiator is removed. The yield for these configurations is only about one third of the total yield.

The uncertainty in proton absorption comes from the comparison of the estimate of the absorption by calculating the probability of nuclear interactions between the photo-proton and the materials along the path to the detectors to direct measurements taken of the proton absorption [98]. The uncertainty in the direct measurements of 2.0% is used as the uncertainty in the proton absorption (see Section 5.4.5).

Tracking efficiency uncertainty is estimated by comparing the cross section using the five-out-of-six and four-out-of-six tracking algorithms (see Section 4.3.2). The average standard deviation for results using both algorithms gives a systematic error of 3.4%.

The source of the systematic error in particle identification comes from uncertainty in the separation of protons from pions and deuterons. For the kinematics with low proton momentum, the uncertainty is small, and is estimated to be about 1%. The uncertainty ranges up to 2.6% for the highest proton momentum where the separation from the pions and deuterons becomes more difficult. This uncertainty is estimated by comparing the normalized yields obtained by changing the time-of-flight proton mass-squared window used in data analysis (see Section 4.2.3).

There are two types of target length uncertainties. By comparing the normalized yields for changes in target length window used in data analysis, an estimate is made on the overall uncertainty of about 1.5% on the target length. There is an additional point-to-point error of about 0.4% to 1.6% that arises from the use of the COSY matrix elements (see Section 5.4.4). This uncertainty for the target length correction is estimated by considering the uncertainty on the centroids of the two gaussian peaks formed by the two aluminum target endcaps in the empty target configurations.

Target density effects include uncertainties in temperature, pressure, effects of localized boiling from the electron beam, and contamination in the cryogenic targets (see Section 5.4.4). This adds up to an overall uncertainty of about 0.7% for target density.

For the kinematics where only half of the acceptance is used in measuring the cross section, the collimator is not centered exactly at the origin. The data analysis cut is chosen by eye, along the center of the collimator using high statistics runs with low background. The center position of the collimator can be measured up to an accuracy of ± 1 mm. Moving the cut 1 mm in either direction changes the cross section by $\pm 3\%$. Therefore a systematic error of 3% is assigned on the cross section for those kinematics. An additional 0.5% systematic error is included for the uncertainty in the number of events that are scattered by the gate valve into the half-acceptance used in data analysis (see Section 5.3.1).

The largest uncertainty comes from acceptance. This was estimated by comparing the cross sections for various kinematics using both the COSY matrix elements and the fitted matrix elements. Only kinematics with low background were considered in this estimate. An average of 3.5% deviation is seen in cross sections calculated using the two different reconstruction matrices (see Section 4.4.2). An additional systematic error of 3% is included in the acceptance from the overall uncertainty in the calculation of the solid angle to give a total acceptance uncertainty of 4.6%. The measurement of the solid angle includes an additional 0.5% uncertainty due to statistical error in the Monte Carlo used to calculate the solid angle (see Section 5.4.1). This error could be reduced by taking more computer time to calculate the solid angle.

The background events that remain after all other subtractions are removed by a flat subtraction that is estimated by finding the average background level beyond the bremsstrahlung endpoint in the reconstructed photon energy histogram (see Section 5.3.3). For low momentum runs, there is no background evident, so no subtraction is made, and there is no additional uncertainty. For high momentum runs, the uncertainty is estimated by the uncertainty in the level of the background that is subtracted from the yield. This leads to a systematic error of up to 4.0% for the kinematics with the highest proton momentum.

All other uncertainties, including those from dead time and trigger efficiency are assumed to be less than 0.1%, and are not included here.

These systematic errors all affect the measurement of the cross section and were added in quadrature to find the total systematic error for the cross section. Additional uncertainties remain in the calculation of $s^{11}\frac{d\sigma}{dt}$. Spectrometer angle resolution is on the order of about 0.8 mr and proton momentum resolution is about 0.1%. These resolutions cause additional uncertainties in the calculation of total center of mass energy s and the transformation into the invariant cross section $\frac{d\Omega_{cm}}{dt}$. These uncertainties are calculated to be between 0.5 and 1.8% and were added in quadrature with the systematic error on the cross section to find the total systematic error in $s^{11}\frac{d\sigma}{dt}$.

Chapter 6

Experimental Results

The differential cross sections for $\gamma d \to pn$ were measured during CEBAF experiment E89-012 at center-of-mass angles near 36°, 52°, 69°, and 89° and incident photon energies near 0.8, 1.6, 2.4, 3.2, and 4.0 GeV. These measurements build upon results from previous experiments SLAC NE8 and SLAC NE17, and extend the angular differential cross section measurements out to $E_\gamma = 4.0$ GeV, giving the first measurements of the differential cross section at $\theta_{cm} = 69°$ at $E_\gamma > 1.0$ GeV.

6.1 Kinematic Variables

For each angle and energy setting, there are a set of kinematic variables that are used in the calculation of the measured cross section. The derivations for the Mandelstam variables s, t, u, and Jacobians $d\Omega/d\Omega_{cm}$ and $d\Omega_{cm}/dt$ are included in Appendix B. The values used for each setting are given in Tables 6.1 and 6.2. Table 6.1 gives the values for each angle and energy setting assuming that only half of the acceptance is being used. This is a necessity due to the gate valve (see Section 5.3.1) obscuring one half of the acceptance during most of the experiment.

Some of the data were taken with the gate valve completely removed, including the early kinematics at $E_{beam} = 2.445$ GeV and later data taken at $E_{beam} = 4.045$ GeV. For those kinematic settings, the cross section is calculated using the full acceptance. Table 6.2 gives the kinematic variables for those data where the gate valve does not

E_{beam} (GeV)	$\bar{E}_\gamma$ (GeV)	θ_{cm} (deg)	s (GeV^2)	t (GeV^2)	u (GeV^2)	$d\Omega/d\Omega_{cm}$	$d\Omega_{cm}/dt$ (sr/GeV^2)
0.845	0.792	36.2	6.49	0.205	-1.413	0.483	6.260
1.645	1.592	35.8	9.49	-0.185	-4.024	0.355	2.654
2.445	2.392	35.6	12.49	-0.514	-6.696	0.282	1.653
3.245	3.192	35.5	15.49	-0.820	-9.391	0.235	1.194
4.045	3.992	35.4	18.49	-1.116	-12.10	0.201	0.933
1.645	1.587	51.9	9.47	-0.640	-3.550	0.403	2.664
2.445	2.387	51.6	12.47	-1.243	-5.948	0.326	1.657
3.245	3.187	51.6	15.47	-1.837	-8.355	0.275	1.196
4.045	3.987	51.5	18.47	-2.409	-10.78	0.237	0.934
1.645	1.579	68.9	9.44	-1.235	-2.925	0.487	2.680
2.445	2.379	68.8	12.44	-2.215	-4.946	0.405	1.663
3.245	3.179	68.7	15.44	-3.177	-6.985	0.347	1.200
4.045	3.979	68.7	18.44	-4.144	-9.019	0.304	0.936
0.845	0.745	88.7	6.31	-0.495	-0.536	0.781	6.768
0.845	0.794	89.5	6.50	-0.599	-0.617	0.779	6.240
1.645	1.563	89.0	9.38	-2.009	-2.091	0.654	2.713
2.445	2.363	89.0	12.38	-3.474	-3.627	0.566	1.676
3.245	3.163	88.8	15.38	-4.941	-5.161	0.500	1.206
4.045	3.963	88.8	18.38	-6.408	-6.695	0.449	0.940

Table 6.1: Kinematic variables for all settings where only half of the acceptance is used in the analysis. This is necessary due to the gate valve obscuring half of the acceptance for most kinematics.

E_{beam} (GeV)	$\bar{E}_\gamma$ (GeV)	θ_{cm} (deg)	s (GeV^2)	t (GeV^2)	u (GeV^2)	$d\Omega/d\Omega_{cm}$	$d\Omega_{cm}/dt$ (sr/GeV^2)
2.445	2.392	37.1	12.49	-0.573	-6.637	0.286	1.653
2.445	2.387	53.0	12.47	-1.317	-5.875	0.331	1.657
2.445	2.379	70.1	12.44	-2.293	-4.868	0.412	1.663
4.045	3.987	53.2	18.47	-2.563	-10.63	0.242	0.934
4.045	3.979	70.2	18.44	-4.305	-8.858	0.312	0.936

Table 6.2: Kinematic variables for full acceptance settings. The failure of the gate valve mechanism did not affect these settings, allowing for data analysis for the full acceptance.

affect the data. The first set of entries include those settings at the beginning of the experiment before the failure of the gate valve mechanism led to the gate valve being inserted halfway into the acceptance. The second set of entries are for data taken in September 1997 after the main experiment.

6.2 Results

The results for the measurement of the differential cross sections for $\gamma d \rightarrow pn$ are given in Tables 6.3, 6.4, and 6.5. Included in the tables are the values for $s^{11}d\sigma/dt$ which are useful in testing the energy behavior of the cross section.

Table 6.3 gives the cross sections for the half-acceptance of each kinematic setting, regardless of the position of the gate valve. This allows for a comparison of results for data that are all analyzed in a consistent manner. The errors quoted give the statistical and systematic uncertainties. The total uncertainty is found by adding the two uncertainties in quadrature. The systematic uncertainties for $s^{11}d\sigma/dt$ include the systematic uncertainty in s and the Jacobians, $d\Omega/d\Omega_{cm}$ and $d\Omega_{cm}/dt$, due to the uncertainties in the spectrometer angle and central spectrometer momentum setting (see Section 5.5).

For some kinematic settings near the beginning of the experiment, the gate valve was not present in the acceptance, and therefore an analysis could be made for the entire spectrometer acceptance. The same is done for additional measurements taken at a later time where the gate valve was not present. Table 6.4 gives the differential cross sections for the analysis of the entire acceptance for those kinematic settings.

The cross section for $E_\gamma = 3.987$ GeV, $\theta_{cm} = 51.5°$ and $E_\gamma = 3.979$ GeV, $\theta_{cm} = 68.7°$ is a weighted mean of two separate half-acceptance measurements. One measurement was taken during 1996 where the gate valve obscured half of the acceptance. The second measurement was taken at a later time, September 1997, where the gate valve is completely removed from the acceptance. Table 6.5 gives the results for each measurement used to determine the weighted mean. The relative systematic

E_{beam} (GeV)	$\bar{E}_\gamma$ (GeV)	θ_{cm} (deg)	$d\sigma/d\Omega_{cm}$ (nb/sr)	$s^{11}d\sigma/dt$ (kb GeV^{20})
0.845	0.792	36.2	177.9± 2.9 ±14.0	0.957±0.016±0.075
1.645	1.592	35.8	10.19± 0.23 ±0.81	1.521±0.035±0.121
2.445	2.392	35.6	1.272± 0.044 ±0.101	2.430±0.084±0.194
3.245	3.192	35.5	0.213± 0.018 ±0.017	3.13± 0.26 ±0.26
4.045	3.992	35.4	0.0665± 0.0064 ±0.0058	5.37± 0.52 ±0.47
1.645	1.587	51.9	4.71± 0.23 ±0.37	0.691±0.034±0.055
2.445	2.387	51.6	0.482± 0.023 ±0.039	0.907±0.043±0.073
3.245	3.187	51.6	0.1062± 0.0053 ±0.0086	1.546±0.078±0.126
4.045	3.987	51.5	0.0228± 0.0015 ±0.0020	1.826±0.122±0.158
1.645	1.579	68.9	3.42± 0.16 ±0.27	0.486±0.023±0.039
2.445	2.379	68.8	0.332± 0.016 ±0.026	0.611±0.029±0.049
3.245	3.179	68.7	0.0407± 0.0028 ±0.0033	0.581±0.040±0.047
4.045	3.979	68.7	0.00620±0.00086±0.00058	0.487±0.068±0.046
0.845	0.745	88.7	221.8± 4.1 ±17.4	0.952±0.018±0.075
0.845	0.794	89.5	147.0± 5.7 ±11.6	0.798±0.031±0.065
1.645	1.563	89.0	3.54± 0.08 ±0.28	0.475±0.010±0.038
2.445	2.363	89.0	0.2216± 0.0105 ±0.0175	0.389±0.018±0.031
3.245	3.163	88.8	0.0282± 0.0020 ±0.0023	0.388±0.027±0.032
4.045	3.963	88.8	0.00573±0.00090±0.00051	0.437±0.068±0.039

Table 6.3: Center-of-mass differential cross sections for $\gamma d \to pn$ measured during the CEBAF experiment E89-012 for half-acceptance data analysis at all kinematics settings. The errors listed are for statistical and systematic uncertainties.

E_{beam} (GeV)	$\bar{E}_\gamma$ (GeV)	θ_{cm} (deg)	$d\sigma/d\Omega_{cm}$ (nb/sr)	$s^{11}d\sigma/dt$ (kb GeV^{20})
2.445	2.392	37.1	1.161± 0.031 ±0.086	2.217±0.060±0.164
2.445	2.387	53.0	0.487± 0.017 ±0.036	0.916±0.032±0.068
2.445	2.379	70.1	0.342± 0.011 ±0.025	0.629±0.021±0.047
4.045	3.987	53.2	0.02325±0.00135±0.00186	1.858±0.108±0.150
4.045	3.979	70.2	0.00887±0.00093±0.00071	0.698±0.073±0.057

Table 6.4: Center-of-mass differential cross sections for $\gamma d \to pn$ measured with full acceptance for those kinematic settings where the gate valve was completely removed from the acceptance. The errors listed are for statistical and systematic uncertainties.

uncertainty in each of the two measurements are roughly equal. Therefore, the systematic uncertainty given in the weighted mean is simply taken to be the larger of the two systematic uncertainties.

$\bar{E}_\gamma$ (GeV)	θ_{cm} (deg)	$d\sigma/d\Omega_{cm}$ (nb/sr)	$s^{11}d\sigma/dt$ (kb GeV^{20})	Data Set (year)
3.987	51.5	0.0212$\pm$ 0.0027 $\pm$0.0018	1.69$\pm$ 0.22 $\pm$0.15	1996
		0.0236$\pm$ 0.0018 $\pm$0.0020	1.88$\pm$ 0.15 $\pm$0.16	1997
3.979	68.7	0.00500$\pm$0.00120$\pm$0.00047	0.394$\pm$0.094$\pm$0.037	1996
		0.00746$\pm$0.00123$\pm$0.00065	0.587$\pm$0.097$\pm$0.052	1997

Table 6.5: Individual measurement of differential cross sections using data analysis for half-acceptance for two seperate measurements. The weighted mean of these values are used for their respective entries in Table 6.3.

The values for $s^{11}d\sigma/dt$ listed in Table 6.3 are plotted as a function of E_γ in Figures 6.1 - 6.4. Figures 6.1, 6.2, 6.3, and 6.4 show the scaled cross section as a function of E_γ for measurements taken in the range $\theta_{cm} = 87.9 - 91.0^\circ$, $\theta_{cm} = 68.7 - 68.8^\circ$, $\theta_{cm} = 51.5 - 53.8^\circ$, $\theta_{cm} = 35.4 - 37.5^\circ$, respectively. Additional scales are provided to show the cross section behavior as a function of s and transverse momentum p_T^2. Data from previous experiments [3, 33, 34, 37] are included as a comparison to the results of this experiment. The center-of-mass cross sections for all four angular ranges are plotted on the same scales in Figures 6.5 and 6.6 including the data from previous experiments which are graphed in Figures 6.1 - 6.4.

Figure 6.7 shows the angular dependence of the differential cross section for small ranges in the incident photon energy. Included are data from previous experiments [3, 37]. The data for this experiment are plotted at the central angle for the half-acceptance used in the analysis. These values are given in Table 6.3. The half-acceptance spans an angular area of $\pm 0.8^\circ$ in the lab frame. This angular coverage can be converted to center-of-mass angle coverage by use of the Jacobian $d\Omega/d\Omega_{cm}$ given in Table 6.1.

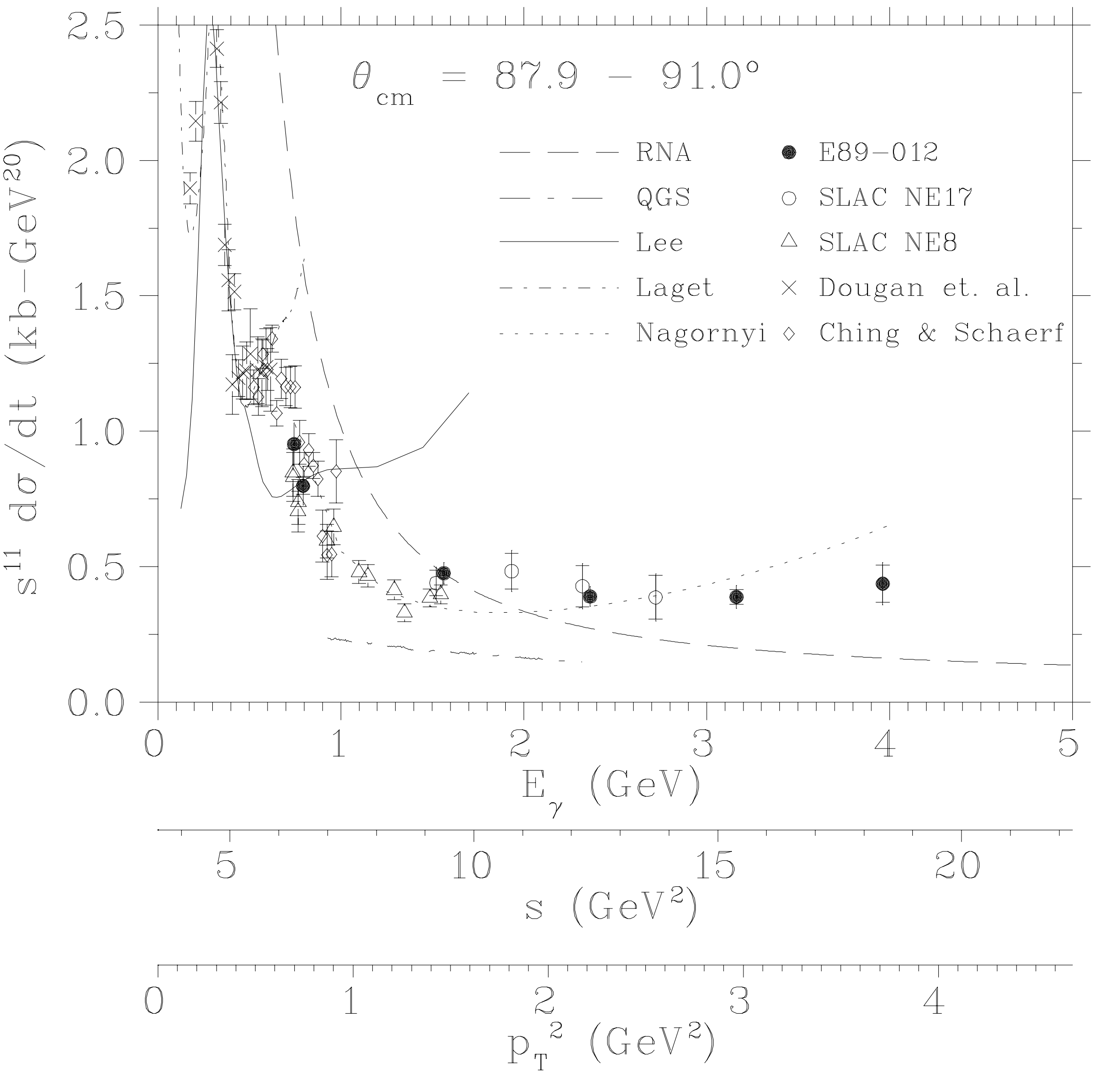

Figure 6.1: Results for $s^{11}d\sigma/dt$ for $\theta_{cm} = 87.9 - 91.0°$. Data for previous measurements are also shown [3, 33, 34, 37]. Data for E89-012 and SLAC NE17 include statistical and total uncertainties. For information regarding theoretical curves, see Section 6.3.

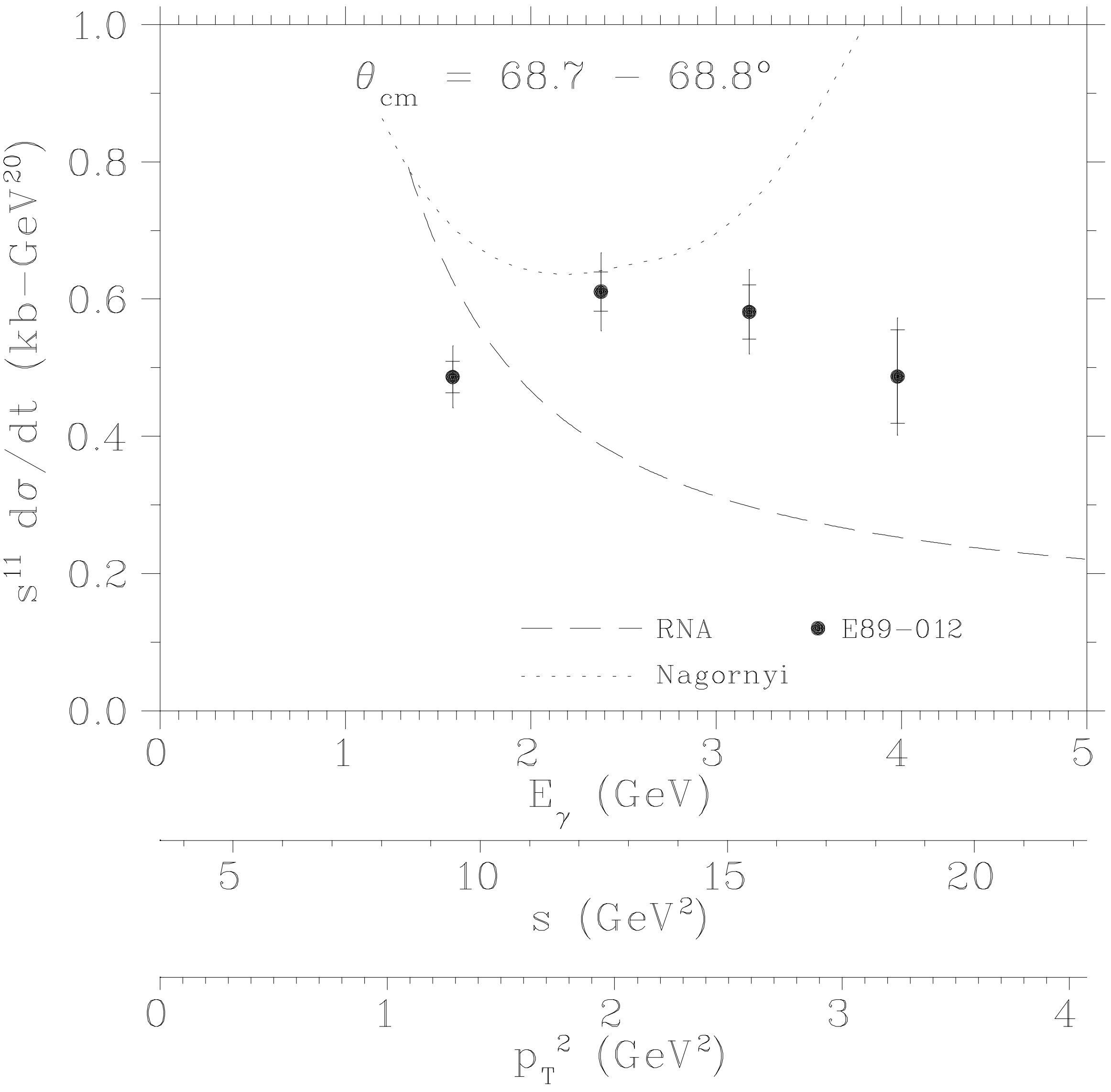

Figure 6.2: Results for $s^{11}d\sigma/dt$ for $\theta_{cm} = 68.7 - 68.8°$. Data for E89-012 include statistical and total uncertainties. For information regarding theoretical curves, see Section 6.3.

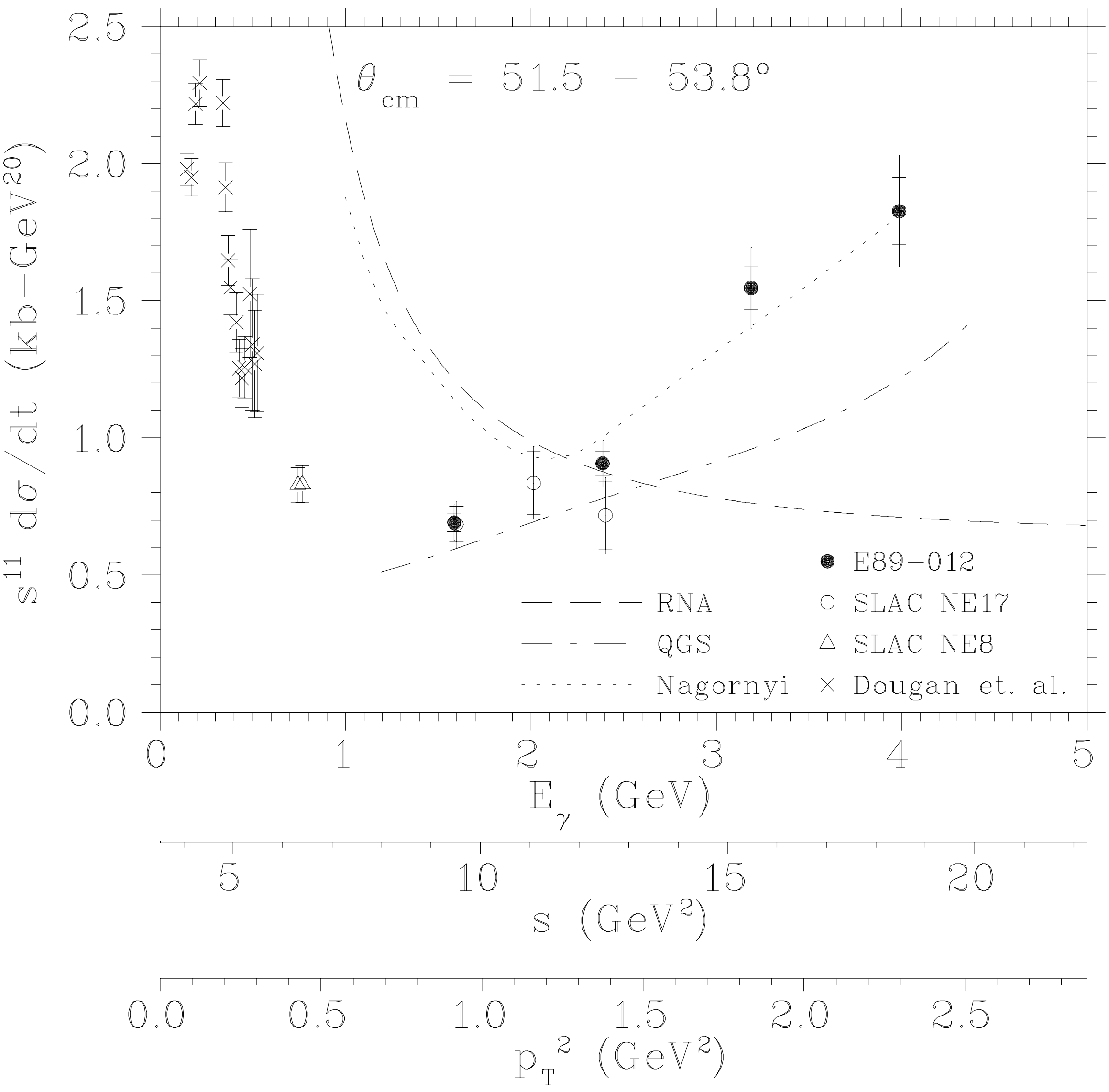

Figure 6.3: Results for $s^{11}d\sigma/dt$ for $\theta_{cm} = 51.5 - 53.8°$. Data for previous measurements are also shown [3, 33, 37]. Data for E89-012 and SLAC NE17 include statistical and total uncertainties. For information regarding theoretical curves, see Section 6.3.

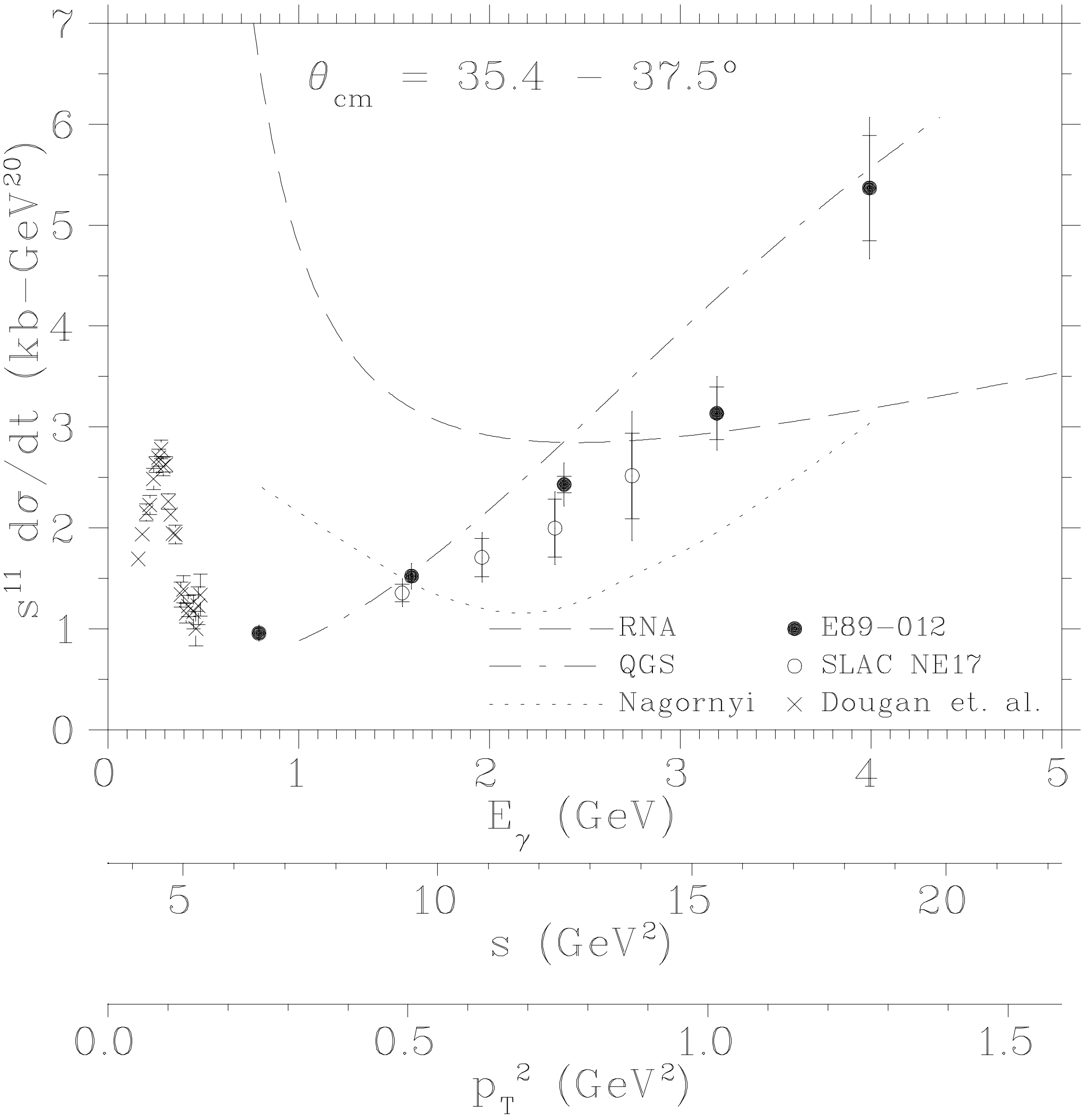

Figure 6.4: Results for $s^{11}d\sigma/dt$ for $\theta_{cm} = 35.4 - 37.5°$. Data for previous measurements are also shown [3, 33]. Data for E89-012 and SLAC NE17 include statistical and total uncertainties. For information regarding theoretical curves, see Section 6.3.

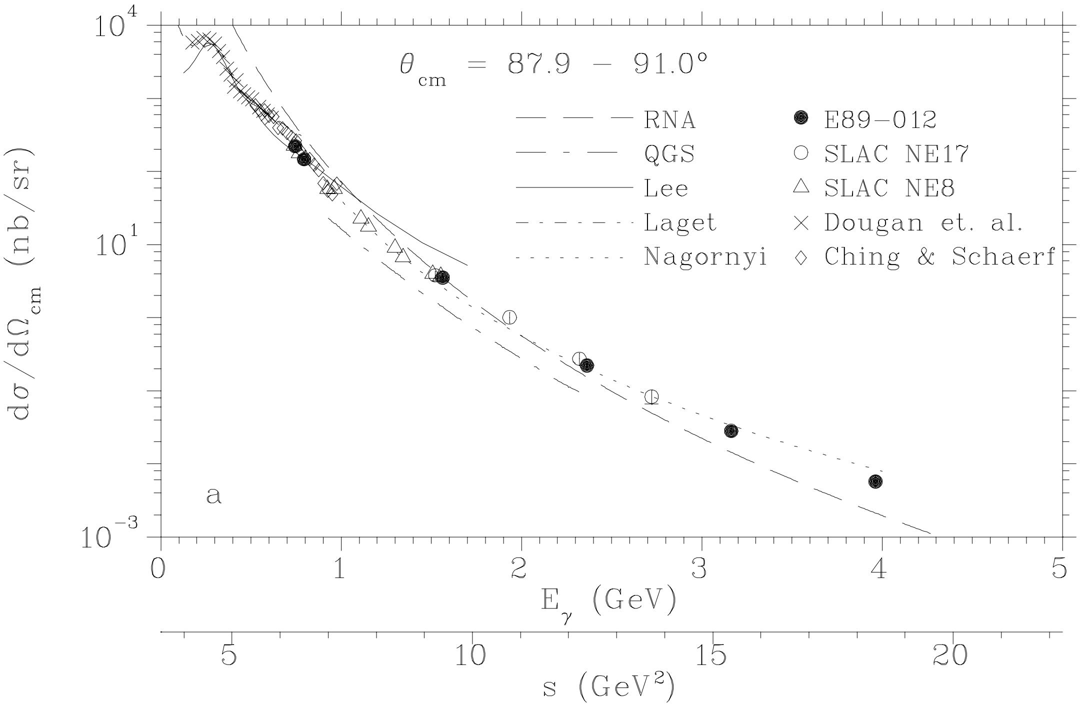

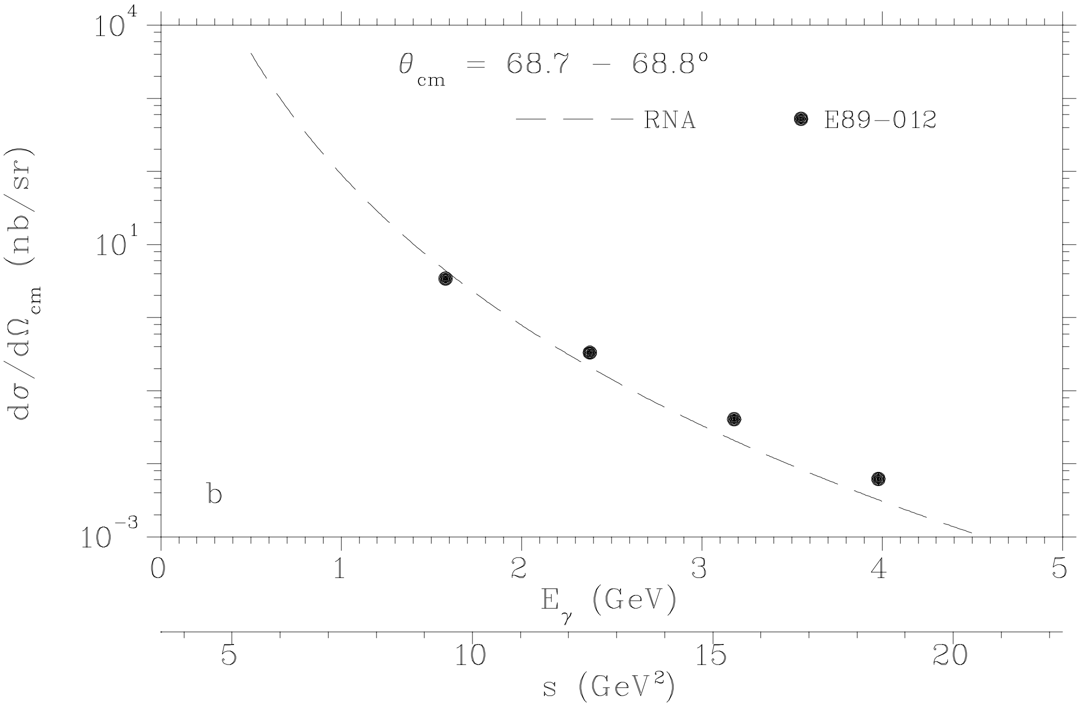

Figure 6.5: Results for $d\sigma/d\Omega_{cm}$ for a) $\theta_{cm} = 87.9 - 91.0°$ and b) $\theta_{cm} = 68.7 - 68.8°$. Data for previous measurements are also shown [3, 33, 34, 37]. Data for E89-012 and SLAC NE17 include statistical and total uncertainties. For information regarding theoretical curves, see Section 6.3.

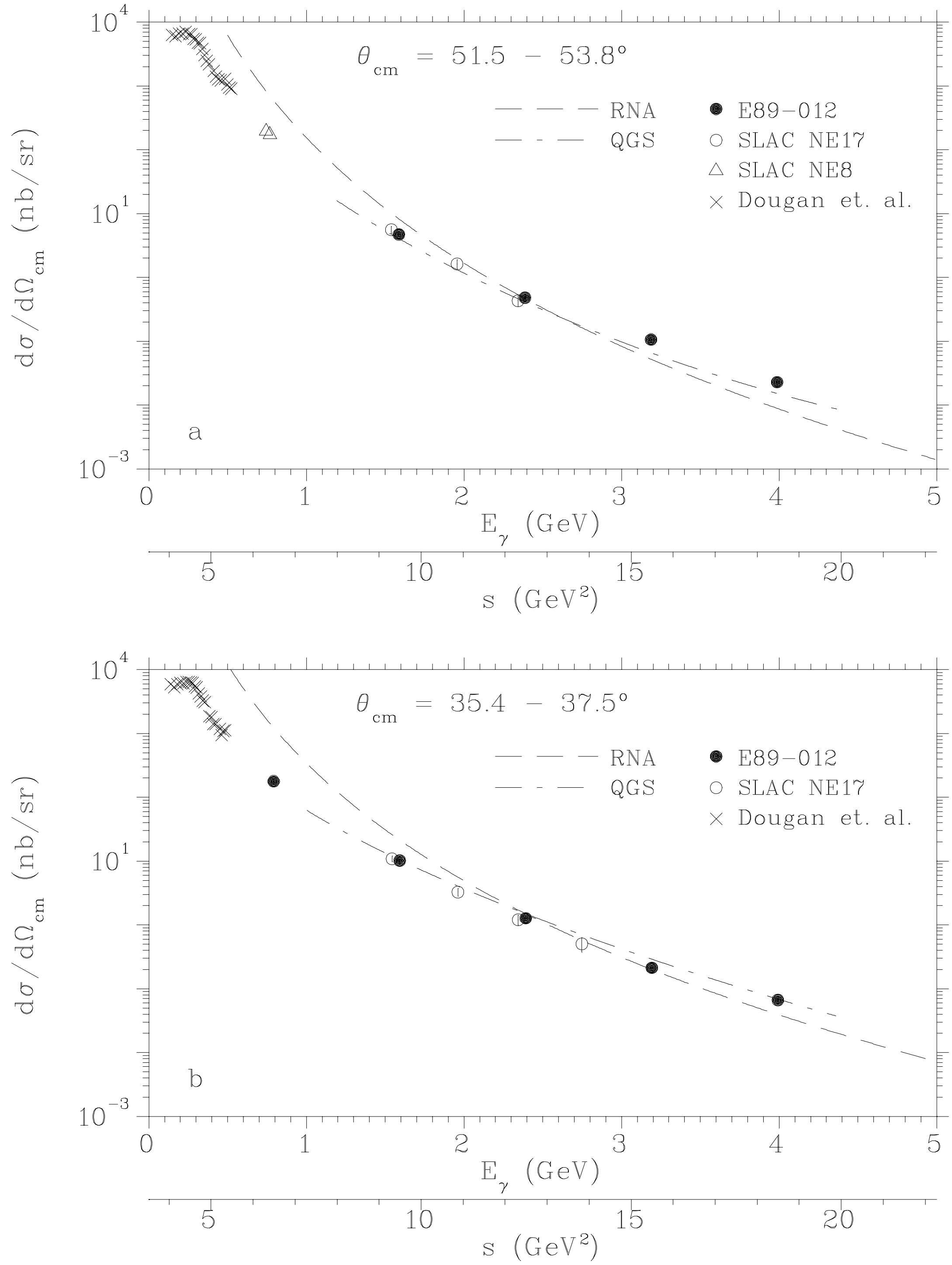

Figure 6.6: Results for $d\sigma/d\Omega_{cm}$ for a) $\theta_{cm} = 51.5 - 53.8°$ and b) $\theta_{cm} = 35.4 - 37.5°$. Data for previous measurements are also shown [3, 33, 37]. Data for E89-012 and SLAC NE17 include statistical and total uncertainties. For information regarding theoretical curves, see Section 6.3.

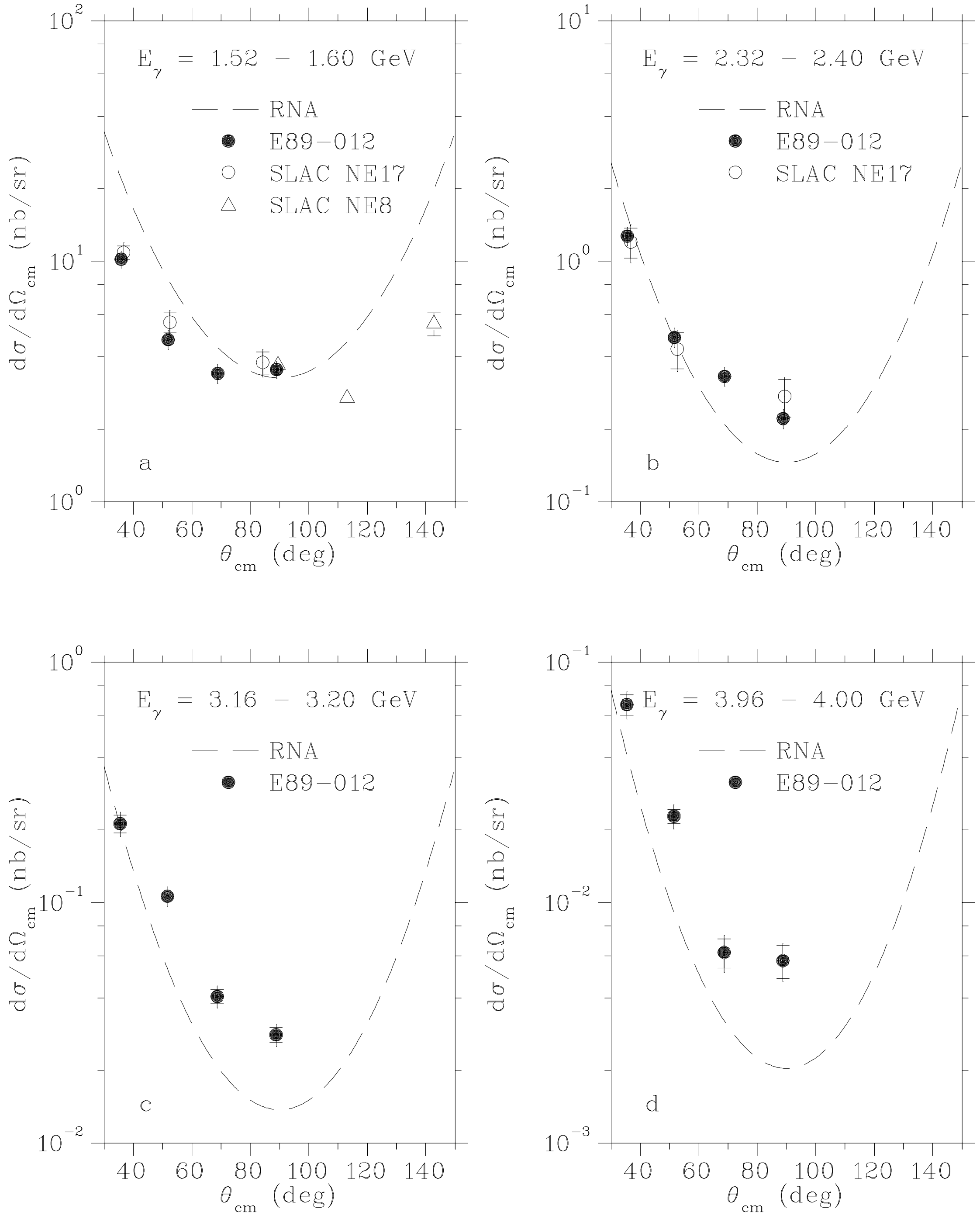

Figure 6.7: Angular behavior of $d\sigma/d\Omega_{cm}$ for a) $E_\gamma = 1.52 - 1.60$ GeV, b) $E_\gamma = 2.32 - 2.40$ GeV, c) $E_\gamma = 3.16 - 3.20$ GeV, d) $E_\gamma = 3.96 - 4.00$ GeV. Data for previous measurements are also shown [3, 37]. Data for E89-012 and SLAC NE17 include statistical and total uncertainties. For information regarding theoretical curves, see Section 6.3.

6.3 Comparison to Theoretical Models

There are many models to consider when comparing the predictions for the behavior of the $\gamma d \to pn$ cross section to the results of this experiment. The details of each model are described in Chapter 2.

6.3.1 Constituent Counting Rules

The constituent counting rules [13, 14] predict the energy dependence of the reaction cross section at asymptotically high energies. For the process $\gamma d \to pn$, the invariant cross section, $d\sigma/dt$, is expected to scale as

$$\frac{d\sigma}{dt} \propto s^{-11} f(\theta_{cm}) \tag{6.1}$$

where $f(\theta_{cm})$ is expected to depend solely on the center of mass angle. This relation is expected to hold only in the region of high energy ($s \gg m_d^2$), where perturbative QCD can be used to describe the dynamics of the reaction.

The onset of energy scaling according to the constituent counting rules relation in Equation 6.1 would manifest itself as a constant value when the scaled cross section $s^{11} d\sigma/dt$ is plotted as a function of energy. In Figure 6.1, the data for $\theta_{cm} = 87.9 - 91.0^\circ$ appears to start scaling at about $E_\gamma = 1.2$ GeV. Figure 6.2 shows that for $\theta_{cm} = 68.7 - 68.6^\circ$, the data appears to also show energy scaling behavior at about $E_\gamma = 1.6$ GeV. However, there are no earlier data to compare to the present results. Earlier in the SLAC NE17 experiment, asymptotic scaling at $\theta_{cm} = 51.5 - 53.8^\circ$ appeared to have started at about $E_\gamma = 1.6$ GeV [38], but Figure 6.3 shows that with measurements at extended energies, the apparent asymptotic scaling seen at larger angles has not yet begun. The data for $\theta_{cm} = 35.4 - 37.5^\circ$ in Figure 6.4 clearly show that scaling has not yet begun at even the highest energy measurement, $E_\gamma = 4.0$ GeV. The lack of scaling at forward angles may be due to the low momentum transfer from the incident photon to the recoil neutron, which could keep the reaction dynamics in the non-perturbative regime of QCD.

Using the results of this experiment from $E_\gamma = 1.6 - 4.0$ GeV, a fit can be made at each angle for the scaling behavior of the invariant cross section given by

$$\frac{d\sigma}{dt} \propto s^{-n} \tag{6.2}$$

where n is the parameter that is fit. Again, constituent scaling rules predict $n = 11$ for $\gamma d \to pn$. The results of the fits are given in Table 6.6 [100].

θ_{cm} (deg)	E_γ (GeV)	$\lvert t_p^{\gamma d}\rvert$ (GeV^2)	$\lvert t_n^{\gamma d}\rvert$ (GeV^2)	n	Reduced χ^2 of fit
88.8 - 89.0	1.563 - 3.963	1.48 - 3.78	1.44 - 3.64	-11.31$\pm$0.27	0.72
68.7 - 68.9	1.579 - 3.979	1.90 - 4.95	1.06 - 2.51	-10.86$\pm$0.22	1.47
51.5 - 51.9	1.587 - 3.987	2.21 - 5.83	0.76 - 1.64	-9.47$\pm$0.21	0.85
35.4 - 35.8	1.592 - 3.992	2.45 - 6.49	0.53 - 1.00	-9.28$\pm$0.24	0.83

Table 6.6: Fits to the energy behavior of $d\sigma/dt \propto s^{-n}$ where n is the parameter that is fit. Data used in the fit include only the results from the half-acceptance analysis given in Table 6.3.

6.3.2 Reduced Nuclear Amplitudes

The reduced nuclear amplitude model from Brodsky and Hiller [43] attempts to obtain the energy scaling behavior predicted by constituent scaling rules by factoring out the soft reaction mechanism present in the interactions within each nucleon. This is done by including the nucleon form factors in the amplitude, reducing the deuteron to two point-like constituents. The cross section is expected to scale in energy as

$$\frac{d\sigma}{d\Omega_{cm}} \sim \frac{1}{\sqrt{s(s-m_d^2)}} F_p^2(\hat{t}_p) F_n^2(\hat{t}_n) \frac{1}{p_T^2} f^2(\theta_{cm}). \tag{6.3}$$

The nucleon form factors used are the standard dipole form [42],

$$F_N(q^2) = \frac{1}{1+\frac{Q^2}{\Lambda^2}}, \tag{6.4}$$

with $\Lambda^2 = 0.71$ GeV^2. At high momentum transfer, the nucleon form factors are expected to scale as $F_N(t) \sim |t|^{-2}$. In the asymptotic energy region, the ratio t/s is fixed at fixed θ_{cm}. Therefore, the cross section given in Equation 6.3 will scale as

$$\frac{d\sigma}{d\Omega_{cm}} \propto s^{-10} \rightarrow \frac{d\sigma}{dt} \propto s^{-11} \tag{6.5}$$

which is the scaling behavior expected from constituent counting rules.

The theoretical predictions for RNA are plotted as long dashed lines in the graphs for $s^{11}d\sigma/dt$ in Figures 6.1 - 6.4 and for $d\sigma/d\Omega_{cm}$ in Figures 6.5 and 6.6. The curves are all normalized to the data point at $E_\gamma = 1.592$ GeV, $\theta_{cm} = 89.0°$. Assuming that the angular factor, $f^2(\theta_{cm})$, is constant for all angles when transverse photons are used [43], the normalization can be carried over for the other recoil angles. Figure 6.7 shows the angular behavior of the differential cross section predicted by RNA for data points in narrow ranges of E_γ.

The angular factor, $f^2(\theta_{cm})$ is expected to be independent of energy in the region where scaling occurs due to RNA. Figure 6.8 shows the calculated values for $f^2(\theta_{cm})$ for $\theta_{cm} = 87.9 - 91.3°$. The RNA model predicts that this function should be a constant when the cross section scales according to RNA. Clearly there is no substantial range where $f^2(\theta_{cm})$ is constant.

Given that each figure represents data taken in a range of angles, the theoretical curves presented in each figure are calculated for center-of-mass angles near the mean for the data from this experiment. Table 6.7 lists the angles where each RNA curve is calculated in the figures. The same is true in Figure 6.7, where the RNA curve in each figure is calculated at a photon energy, E_γ near the mean for the data from this experiment. The photon energies used to calculate each RNA curve in Figure 6.7 are also listed in Table 6.7.

At all angles, it seems that the RNA prediction falls short of predicting the energy behavior of the cross section. The cross section does increase for forward angles, but the measured increase is not as fast as that predicted by RNA.

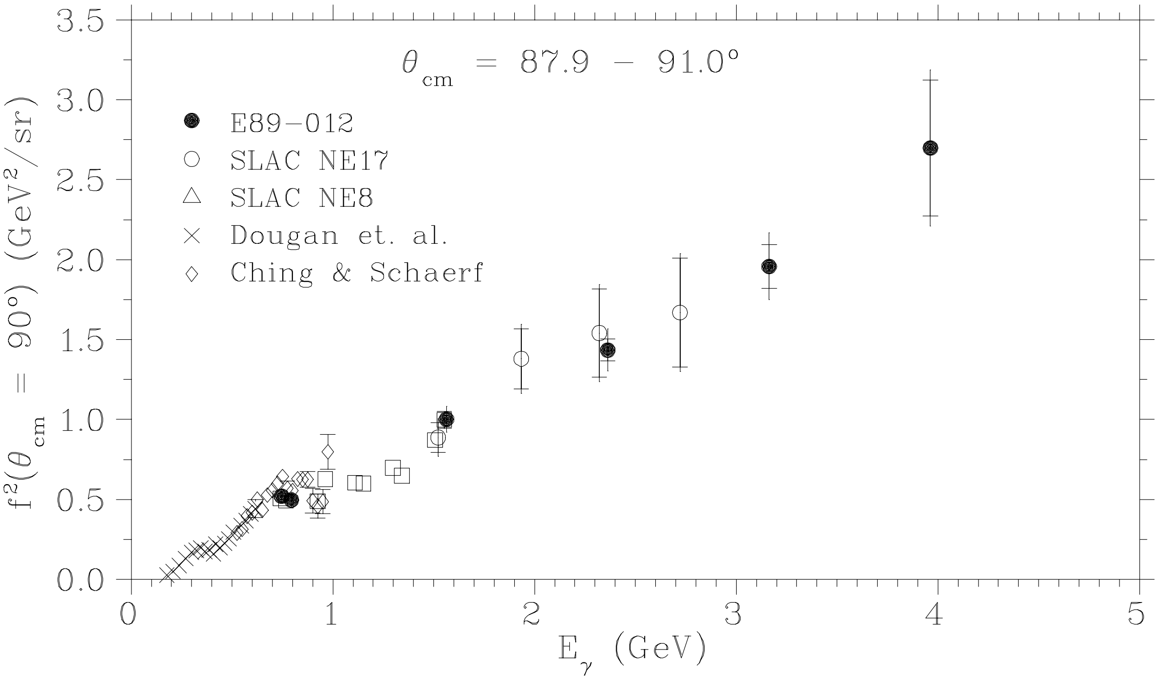

Figure 6.8: Graph for $f^2(\theta_{cm} = 90°)$, the angular factor in the differential cross section prediction of the reduced nuclear amplitude model.

Figures 6.1 - 6.6		Figure 6.7	
Range in θ_{cm} (deg)	RNA curve θ_{cm} (deg)	Range in E_γ (GeV)	RNA curve E_γ (GeV)
87.9 - 91.0	88.9	1.52 - 1.60	1.580
68.7 - 68.8	68.8	2.32 - 2.40	2.380
51.5 - 53.8	51.6	3.16 - 3.20	3.180
35.4 - 37.5	35.6	3.96 - 4.00	3.980

Table 6.7: Center-of-mass angles, θ_{cm}, used to calculate the RNA curves in Figures 6.1 - 6.6 and incident photon energies, E_γ used to calculate RNA angular dependence curves in Figure 6.7.

6.3.3 Traditional Meson-exchange Theory

Predictions for the energy dependent behavior of deuteron photodisintegration at $\theta_{cm} = 90°$ for two meson-exchange models are shown in Figure 6.1. The solid line shows the result for Lee's coupled channel model [19], and the short dash-dot line gives the result from Laget's meson-exchange model [18]. Although both models accurately predict the resonance region for the cross section, they fail to predict the energy dependence anywhere above $E_\gamma = 1$ GeV. This does not mean that meson-exchange models should be abandoned. Perhaps in the higher energy region, such models may better predict the energy dependence after further consideration of relativistic effects as well as higher nucleon resonances and heavier mesons that are exchanged between the nucleons.

6.3.4 Asymptotic Amplitudes

The asymptotic amplitude model proposed by Nagornyĭ [21] predicts an energy dependence at $\theta_{cm} = 89°$ similar to that expected by constituent counting rules in the energy range covered by this experiment. The dotted line in Figure 6.1 shows the results of a calculation based on this model using the data from this experiment [101]. Agreement with data is good from about $E_\gamma = 0.6$ GeV although there may be a deviation at the highest energy measurement which lies about two σ under the prediction. Calculations for other angles using the asymptotic amplitude model with the additional α parameter [56] are shown in Figures 6.2, 6.3, 6.4 for $\theta_{cm} = 69°$, $52°$, and $36°$, respectively. In general, the cross section increases for more forward angles faster than the model suggests.

6.3.5 Quark Gluon String Theory

The predictions by the quark-gluon string model [45] are presented in Figures 6.1, 6.3, and 6.4 for $\theta_{cm} = 90°$, $53°$, and $37°$, respectively. These values are obtained from the published graph which is shown in Figure 2.13. The prediction is too low in comparison to the cross section at $\theta_{cm} = 90°$, but agreement may be more favorable (as expected) for the more forward angles.

6.4 Changes from Published Data

Results from a preliminary analysis were presented in a letter [89]. Since publication, changes were made to the analysis as certain aspects of the analysis were more closely considered.

The target length correction, discussed in Section 5.4.4, changed from an overall correction of 7.0% to a point-by-point correction for each kinematics after it was discovered that the correction was dependent upon the kinematics.

The intervals in E_γ that are used in calculating the reaction yield were all reduced by an overall amount of 5 MeV. This was done after discovering that background protons arising from pion production may enter the spectrometer at the forward edge of the acceptance, as discussed in Section 5.3.2. The error introduced to the previously published data by having the interval extend into the pion production region is negligible. However, the change was made to ensure the pion photoproduction background is eliminated from the photo-proton yield.

The correction due to inscattering of proton events by the gate valve as discussed in Section 5.3.1 was increased from 1.0% to 1.5% after a more careful study with the Monte Carlo of the spectrometer.

The correction for proton absorption, as discussed in Section 5.4.5, was changed after a more thorough investigation of the materials along the path of the photo-proton from the target to the spectrometer. The original correction used is 5.5%. This correction was increased to 10.9% for all kinematics.

Finally, a change was made in the beam current monitor used to measure accumulated charge. Formerly, BCM3 was used exclusively to measure charge. However, the beam current linearity response of BCM3 is poor compared to that of BCM1. Some runs were taken with a lower beam current where the nonlinearity from BCM3 may cause the beam current readback to be inaccurate. In the analysis presented here, BCM1 is used for charge normalization for all kinematics except for two cases. For data taken at $E_{beam} = 2.445$ GeV, the response from BCM1 was affected by temperature irregularities of the measurement instrumentation. For those kinematics, BCM3 is used with careful calibrations for runs taken at significantly different beam currents. BCM3 is also used for later data taken during 1997 after hardware was upgraded to remove the nonlinearity. See Section 5.4.2 and Appendix A for more details.

The improvements to the data analysis changed the cross sections for the higher energy kinematics by an average of 3%. For E_{beam} = 0.845, 1.645 GeV, the results changed by an average of 9%, mostly due to the nonlinearity of BCM3. The current monitors are all calibrated at a beam current of about 20 μA. However, due to the high data rate, the beam current was reduced for the lower energy runs to 8 to 10 μA.

6.5 Summary

One of the important results of this experiment is the evidence of the apparent persistence of asymptotic scaling of the differential cross section for deuteron photodisintegration at $\theta_{cm} = 89°$ from 1 - 4 GeV. The results also show evidence of asymptotic scaling for $\theta_{cm} = 69°$. The onset of asymptotic scaling seems to occur near $E_\gamma = 1.0$ GeV for $\theta_{cm} = 89°$ and asymptotic scaling already seems to in effect by $E_\gamma = 1.6$ GeV for $\theta_{cm} = 69°$. Asymptotic scaling is not evident for the more forward angles; however, this may be due to the low momentum transferred to the neutron, which may preclude the use of perturbative QCD to describe the reaction.

Clearly more theoretical and experimental work needs to be done to clarify the situation further. The premature scaling of the data at $\theta_{cm} = 89°$ and 69° is not expected as perturbative QCD is expected to apply only in the high energy region ($s \gg m_d^2$). There has been disagreement over the applicability of PQCD methods in this intermediate energy range [9], stating the non-perturbative effects are still the main contribution to the reaction cross section. By extending the measurements out further in energy, perhaps the answer can be found.

There is little discussion in the theoretical literature regarding the angular behavior of the cross section compared to the energy behavior, possibly due to the lack of measurements at backward angles. Further measurements of the backward angle differential cross sections may be instrumental in the determination of a theory that accurately describes both the energy and angular behavior.

Chapter 7

Conclusions

The differential cross section for $\gamma d \to pn$ was measured at $\theta_{cm} = 36^\circ$, 52°, 69°, and 89° at incident photon energies from 1.6 - 4.0 GeV, with additional measurements at 0.8 GeV for $\theta_{cm} = 36^\circ$ and 89°. The results for $\theta_{cm} = 89^\circ$ and 69° are consistent with asymptotic scaling predicted by the constituent counting rules [13, 14]. However, asymptotic scaling is not evident for the more forward angles $\theta_{cm} = 36^\circ$ and 52°. Whether the results are indicative of scaling as predicted by PQCD is still unclear [9]. The results at all angles are in disagreement with the reduced nuclear amplitude theory [43]. Conventional meson-exchange theories fail to reproduce the differential cross section above 1 GeV. However, meson-exchange theories may still be useful with further considerations for higher nucleon resonances, heavier exchange mesons, and relativistic effects. The prediction given by the asymptotic amplitude model [21] is consistent with the differential cross section measurements at $\theta_{cm} = 89^\circ$; however, the cross section may be falling faster than predicted by the model at the measurement at the highest energy.

In the attempt to observe energy scaling behavior predicted by PQCD, high momentum transfers between the constituents are necessary in order for the reaction to be in the perturbative regime. Photo-reactions such as deuteron photodisintegration are an excellent means of such high momentum transfers as the entire momentum of the photon is absorbed by the target constituents.

7.1 Comments on Experiment Quality

The experiment was successful in measuring the differential cross sections at the kinematics considered, although many obstacles hampered the process. The loss of the hydrogen target during the experiment prevented an accurate measurement of background processes which could be detected in the spectrometer acceptance. In addition, the unfortunate position of the gate valve delayed analysis in order to further study the consequences of the position in the spectrometer acceptance. Statistical accuracy was considerably reduced as only half of the acceptance could be used in the analysis. In addition, overall background may have increased due to multiple scattering from the gate valve. Despite the failures of hardware, let it be said that no good experiment is flawless.

7.2 Future Considerations

There is still much more room to stretch out in the search for theoretical models for the behavior of exclusive reactions. There is already an experiment proposed that would extend the measurements of deuteron photodisintegration presented here out to higher energies [102]. In addition, measurements can be made for the angular behavior of the differential cross section, especially at backward angles [103]. Polarization observables may also be measured in an attempt to discover the reason for the scaling behavior [104] as the polarization of the recoil proton may vary greatly for different models where they only predict small changes in the differential cross section. Lastly, further consideration may be given to photodisintegration of other nuclei such as ^{3}He [105] in the energy range covered by this experiment. However, the increased number of constituents would cause the cross section to drop off with energy at a far faster rate, causing the measurement of such a cross section to become extremely difficult.

Appendix A

Beam Current Monitors

A.1 Description and Location

The Hall C beam current monitor (BCM) system is composed of a parametric current transformer (Unser toroid) and three resonant cavities located on the beam line in the hall.

There are four beam current monitors used in Hall C. The resonant cavities are labeled BCM1, BCM2, and BCM3. The Unser toroid is referred to as the Unser PCT. Figure A.1 shows the layout of the beam current monitors on the beamline.

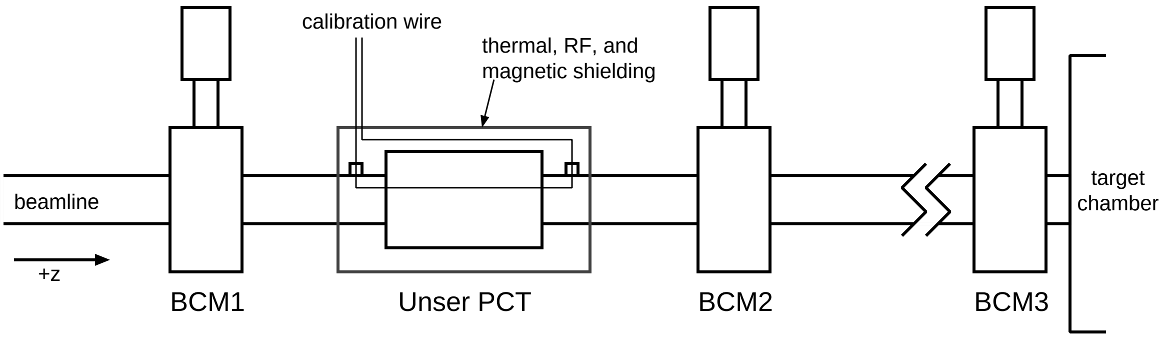

Figure A.1: Relative locations of the beam current monitors on the beamline. Distances are not to scale.

BCM1, BCM2, and the Unser PCT are located in Hall C along the transport channel approximately 28 meters upstream of the target chamber. BCM3 is located about 3 meters upstream of the target chamber. BCM3 is also used in conjunction with a similar cavity in the injector region as part of the accelerator beam accounting system.

A.2 Theory of Operation

A.2.1 Unser PCT

The Unser PCT is a parametric current transformer manufactured by Bergoz in Crozet, France. It consists of a toroid of magnetic material placed around the beam pipe. It operates as a DC transformer [90] which detects the beam current moving through the toroid and sends out a signal which is proportional to the detected current.

There are 4 separate windings to consider around the Unser toroid:

- The **beam** can be considered a one-loop winding around the toroid, adding to its magnetization when the beam is on.
- The **driver** is a winding which carries a 7 KHz AC signal with enough current to completely saturate the toroid at each half-cycle.
- The **receiver** winding serves to detect the magnetization of the toroid induced by the driver and the beam.
- The **feedback loop** attempts to nullify the magnetization caused by the beam by carrying an equivalent opposing current.

While the beam is off, the toroid would saturate at the same magnitude of driver current at both halves of the AC cycle. However, when the beam is on, the beam adds to the magnetization, making the toroid saturate earlier at one half of the cycle and later at the other half. The receiver detects this asymmetry and the feedback circuitry attempts to restore the symmetry by sending an opposing feedback current to cancel out the beam magnetization. This feedback current is returned by the instrument in the form of a DC voltage that is linearly proportional to the beam current.

This mechanism allows for detection of current from DC to 500 Hz. An additional conventional AC transformer allows for the detection of AC currents up to 100 kHz.

Measurements from the Unser PCT are affected by changes in temperature and by external RF and magnetic fields. Although the Unser PCT already has some magnetic shielding around the toroid, it is further encased in an RF shield and additional μ-metal magnetic shielding. To reduce effects from changes in temperature, the assembly is kept at an elevated temperature with heating tape around the magnetic shielding. Custom fitted thermal blankets surrounding the entire assembly reduce heat loss from the heating tape.

A.2.2 Resonant cavities

The resonant cavities for BCM1 and BCM2 are single port stainless steel cylindrical cavities with the fundamental resonant mode at 1497 MHz. BCM3 is similarly constructed except that it has two ports instead of one. They are positioned on the beamline such that the beam moves along the z-axis of the cylinders.

The electron beam, with an RF frequency of 499 MHz, excites the TM_{010} mode of the cavities, which is insensitive to beam position [106]. This mode describes magnetic field lines which are transverse to the z-axis of the cavity, and the magnetic field varies by one half cycle between both boundaries along the radial axis of the cylinder [107].

A pickup antenna located inside the cavity detects the stored power and sends an AC signal linearly proportional to the stored power to the support electronics.

Quality Factor

The quality factor, Q_0, of a resonant cavity is the ratio of the resonant frequency, f_0, to the frequency range, Δf, where the differential stored power is attenuated by 3 dB [106],

$$Q_0 = \frac{f_0}{\Delta f}. \tag{A.1}$$

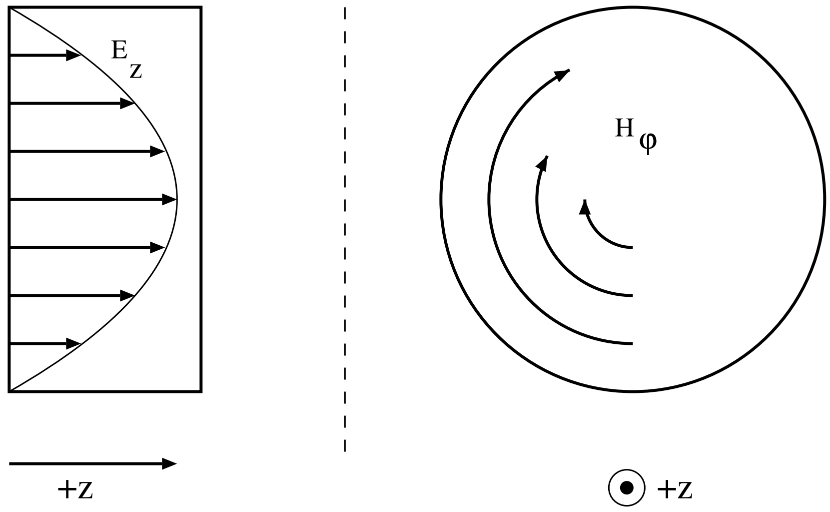

Figure A.2: Pictorial of TM_{010} mode in cylindrical cavity.

This quantity, Q_0, is also referred to as the unloaded quality factor as there is no load to detect the stored power within the cavity. The factors that go into determining Q_0 include the resonant frequency, the length of the cavity, and the skin depth of the stored power in the walls of the cavity. For these cavities, the skin depth is estimated to be 1.12 μm [106]. For this reason, the surface finish of the interior of the cavity can play a large role in determining the final unloaded quality factor.

The loaded quality factor, Q_L, measures the quality factor of a resonant cavity with an antenna coupled to it, removing some of the stored power. The loaded Q is related to the unloaded Q by a coupling factor

$$Q_L = \frac{Q_0}{1+\beta}. \tag{A.2}$$

This coupling factor, β, has a critical value of 1 where the total power detected by the antenna is at a maximum and is equal to the total power dissipated along the walls of the resonant cavity.

For the resonant cavities used in this experiment, Q_0 was estimated and Q_L was determined from direct measurement [108]. Table A.1 lists the values of the quality factors for BCM1 and BCM2.

	BCM1	BCM2
Q_0	3000	3000
Q_L	538	635

Table A.1: Estimated quality factors and measured loaded quality factors for resonant cavities BCM1 and BCM2

Temperature effects

Ambient temperature changes can affect the resonant frequency of a cylindrical cavity by causing the cavity to expand or contract.

A small change in temperature changes the radius of the resonant cavity by

$$\Delta r = \alpha r \Delta T \tag{A.3}$$

where α is the coefficient of thermal expansion for the material composition of the microwave cavity. For BCM1 and BCM2, the cavities were constructed of Type 304 Stainless Steel.

The resonant frequency of the TM_{010} mode in a cylindrical cavity is given by

$$f_{010} = \frac{c}{2\pi}\frac{\chi_{01}}{r} \tag{A.4}$$

where c is the speed of light, r is the radius of the cavity, and χ_{01} is the 1st root of the Bessel function J_0. A small change in the radius will change the resonant frequency of the cavity by

$$\Delta f = -\frac{c}{2\pi}\frac{\chi_{01}}{r^2}\Delta r. \tag{A.5}$$

One of the corrections to the power generated by the beam in the resonant cavity is the detuning factor. This describes the reduction in the emitted power for a signal that is Δf away from the resonant frequency [106]. The power generate by the beam is given by

$$P_{em} \propto \frac{1}{1 + (2Q_L\frac{\Delta f}{f})^2}. \tag{A.6}$$

By combining the above, the change in generated power and beam current is given by

$$\frac{\Delta P_{em}}{P_{em}} = (2Q_L \alpha \Delta T)^2. \tag{A.7}$$

Thus, for a critical coupled cavity with $Q_L = 1500$, a $\pm 1°$C change in temperature causes a change of approximately $\pm 0.36\%$ in beam current [106].

Although the generated power is reduced by lowering Q_L, a benefit of doing so reduces the sensitivity to changes in temperature. In order to further reduce ambient temperature change effects, each cavity is kept at an elevated temperature of 110° F through the use of a heating tape wound around the outer edge of each cavity and are then encased in custom fitted thermal insulation blankets.

A.2.3 Support Electronics

Along with each type of detector used to measure the beam current, there is a series of support electronics used to translate that signal into data used to record the beam current as a function of time.

Figures A.3 and A.4 shows a block diagram of the manipulation of the signal from each beam current measuring instrument.

Unser electronics

The Unser PCT comes with custom electronics used to detect the signal from the Unser monitor. The final output of the electronics is in the form of an analog voltage linearly proportional to the beam current.

The front end electronics is located in the BCM rack in the Hall C Counting Room. The back end electronics is located in the Hall C transport channel near the Unser toroid. The back end electronics is sensitive to radiation [90], so a lead brick shield is built around it to minimize radiation damage.

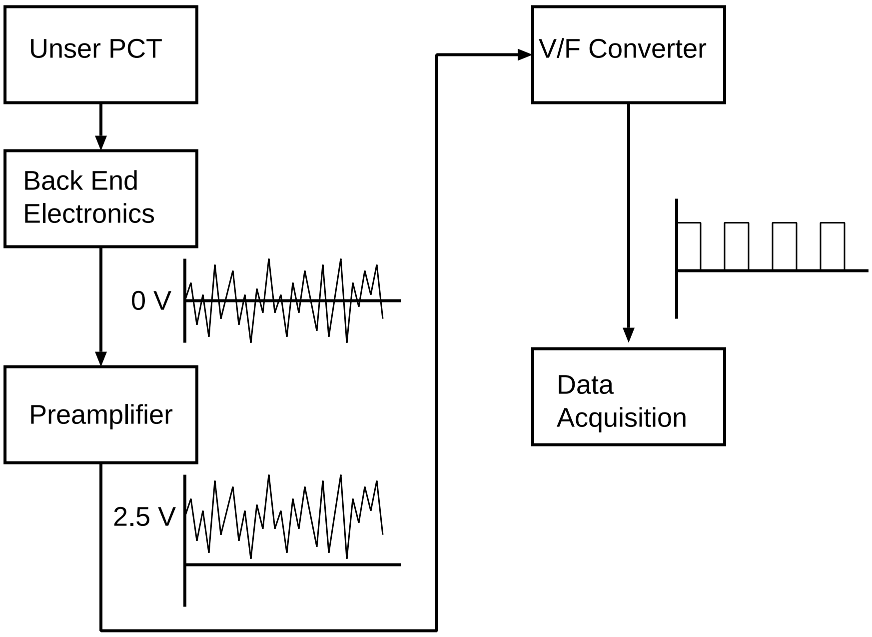

Figure A.3: Block diagram of electronics associated with the signal from the Unser PCT.

Power Meter

The signals from two of the three resonant cavities (BCM1, BCM2) are sent from the experimental hall via 1/2 inch heliax cable to a Gigatronics 8542 power meter. The power meter has a bandwidth from 10 MHz to 40 GHz [109]. The 1497 MHz signal from the resonant cavities are well within those boundaries. The signal is then sent to the preamplifiers in the form of an analog voltage linearly proportional to the power detected from the cavity.

Mixer/rms-dc converter

The 1497 MHz signal from BCM3 is mixed down to 1 MHz and sent through a 1/2 inch heliax cable to an rms-dc converter. The output signal is then an analog voltage which is linear with the beam current.

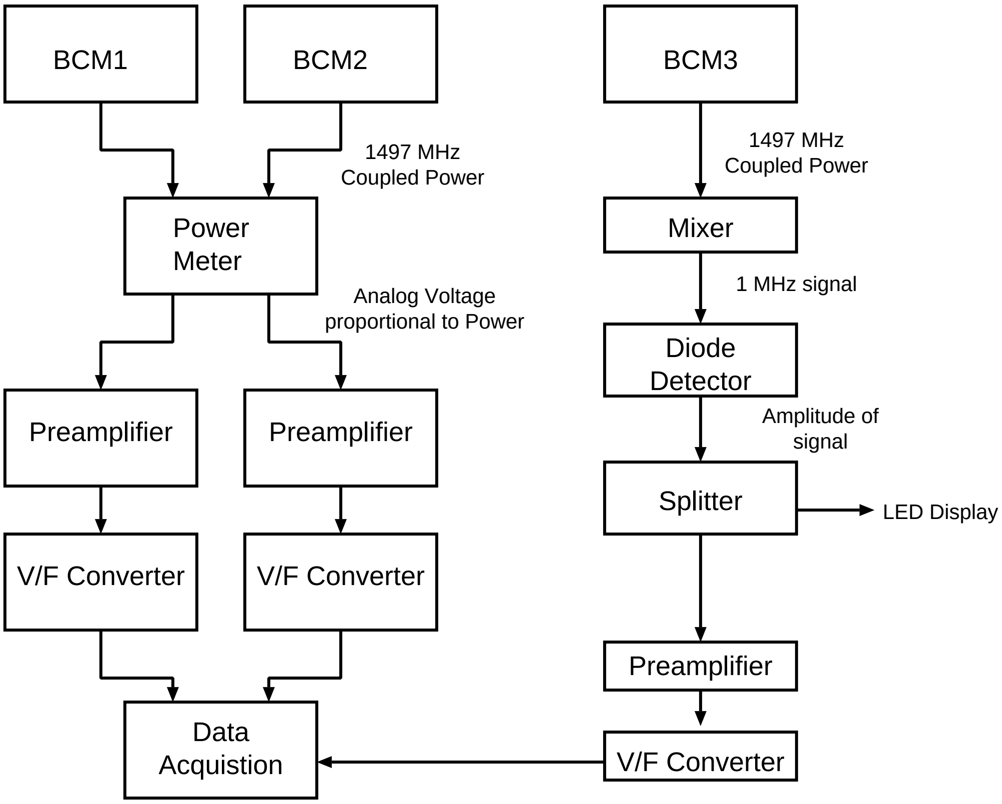

Figure A.4: Block diagram of electronics associated with the signal from the resonant cavities.

Preamplifiers

Preamplifiers are used to amplify the signal coming from the detector if necessary. The preamplifier also adds a 2.5 V positive voltage offset which is used as a 'pedestal' for when the beam current is 0. The pedestal ensures that the signal will never drop below 0 V.

Voltage-Frequency Converters

Voltage-Frequency (V/F) converters are used to change the analog voltage into a pulsed signal. An input voltage between 0 and 10 V is fed into the module and the output is in the form of pulses with a frequency between 0 and 1 MHz with a relation of 100 $\frac{kHz}{V}$.

Scalers

The pulses from the V/F converters are fed into scalers which count the number of pulses and are read in 2 second intervals by the data acquisition system during data-taking.

Temperature stability system

BCM1 and BCM2, as well as the Unser monitor, are thermally insulated and have heating coils which keep the monitors stable at an elevated temperature of 110 $\pm$ 1° F. A strip chart recorder records the temperatures of six thermocouples located at various points near the BCMs as a monitor for the temperature stability of each current measuring device. The locations of each of the thermocouples are listed in Table A.2.

Thermocouple	Location
1	BCM1
2	Unser toroid
3	Power meter
4	Mumetal shielding around toroid
5	BCM2
6	Hall C Transport Channel

Table A.2: Location of the Temperature stability system thermocouples

A.3 Calibration

The beam current monitors require a regular calibration schedule to reduce systematic error caused by time-dependent drifts.

A.3.1 Absolute Calibration

The Unser PCT requires calibration about once every month to make sure that the overall performance of the Unser device meets manufacturer specifications. This is done through the use of a calibration wire which sits permanently in the beam line and which goes through the toroid. This calibration wire sends a DC current through the opening of the toroid which serves to mimic the conditions of the electron beam. It is assumed that the Unser is incapable of detecting the underlying 1497 MHz frequency structure of the electron beam as that frequency is far beyond the specified AC frequency limit of 500 kHz. Precision resistors are used with a high-precision voltage source to send a well-known current in a range between 0 and 200 μA through the wire. The signal voltage is then read from the Unser PCT and compared to the actual current.

The calibration procedure suggests measuring the signal for two minutes at a particular current, followed by a two minute period with no current. This is repeated for a number of different currents, and then the entire procedure is repeated again. The signals from each two minute time period are averaged and compared to the zero offset reading. A longer time period is not advisable due to the probability of Unser PCT signal drift in the measurement time.

A.3.2 Relative Calibration

The resonant cavities cannot be calibrated in the same manner as the Unser PCT. There is no high-precision current source available that can mimic the 1497 MHz RF structure of the electron beam. To calibrate the resonant cavities, we use the electron beam from the accelerator in conjunction along with the previously calibrated Unser PCT. However, due to the increased sensitivity to temperature of the resonant cavities, this calibration is done once every one or two days.

The calibration procedure is similar to that for the Unser PCT. The CEBAF accelerator provides a fixed beam current for two minutes, followed by two minutes of no beam. This is done for a number of beam currents from 0 to 30 μA. Because the beam current is not as well known as the high-precision current source, we use the Unser PCT to determine the true beam current and calibrate the signals from the resonant cavities to that reading.

A.4 Performance

A.4.1 Definitions

Short-term Noise Changes in the signal that are on a short time scale—on the order of up to a few seconds, including statistical noise.

Long-term Drift Changes in the signal that are on a longer time scale which shift the average signal by some significant amount. This is a systematic change. It can not be described as noise.

Gain Drift A change in the relation between the actual beam current and the signal received from the current monitoring instruments.

Linearity A description of how closely the beam current and the signal received from a current monitor follows a linear relation. Any systematic deviation from that is called a nonlinearity.

A.4.2 Unser

Short-term Noise

According to the Bergoz PCT Manual charts [90], the Unser PCT should exhibit a short-term noise of about 600 $\frac{nA}{\sqrt{Hz}}$. This means the beam current, determined from a 1 second sample of the signal from the Unser PCT would have a statistical error of 600 nA.

Tests were done to measure the short term noise for the Unser monitor. Figure A.5 shows an example of the short term noise for a part of one test run. There is a

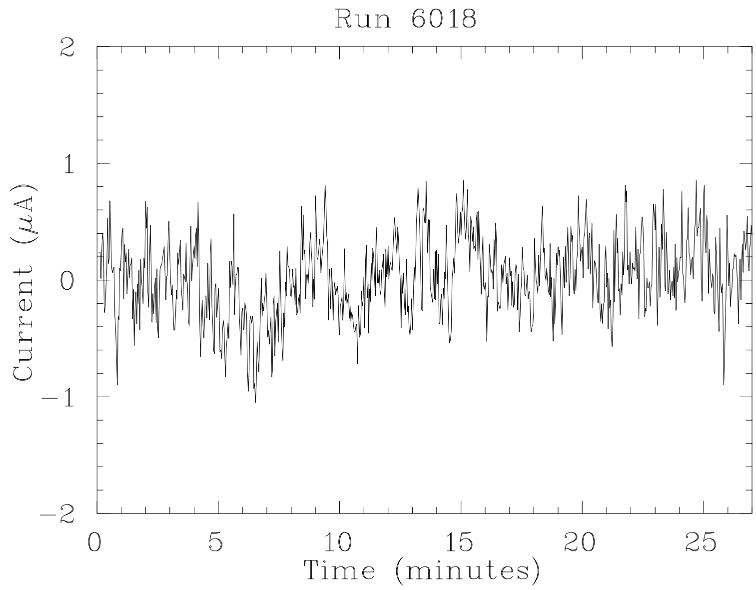

Figure A.5: Example of short term noise in the Unser monitor.

statistical part that can be fitted to a gaussian, as shown in Figure A.6. For this particular test, the width of that gaussian was 330 nA, and each sample was 2 seconds long. Therefore, the noise factor for the Unser is

$$\text{Noise factor} = 330\ nA\ \sqrt{2\ \text{sec}} = 470\frac{nA}{\sqrt{Hz}}.$$

There are longer term variations which would artificially increase calculated statistical error. These variations cause the signal to move over the course of minutes rather than seconds.

Long-term Drift

For unknown reasons, the offset of the signal from the Unser can drift up to 2 μA or more within several hours [110]. In practice, this drift can take place very quickly and for many qualifiable reasons. The average signal level is highly susceptible to stray RF fields, magnetic fields, temperature, and even mechanical vibrations. Changing the orientation of the toroid within the earth's magnetic field causes huge variations of over 100 μA in the average signal level. During initial tests with thermally stabilizing the Unser toroid at an elevated temperature, the signal from the Unser PCT changed

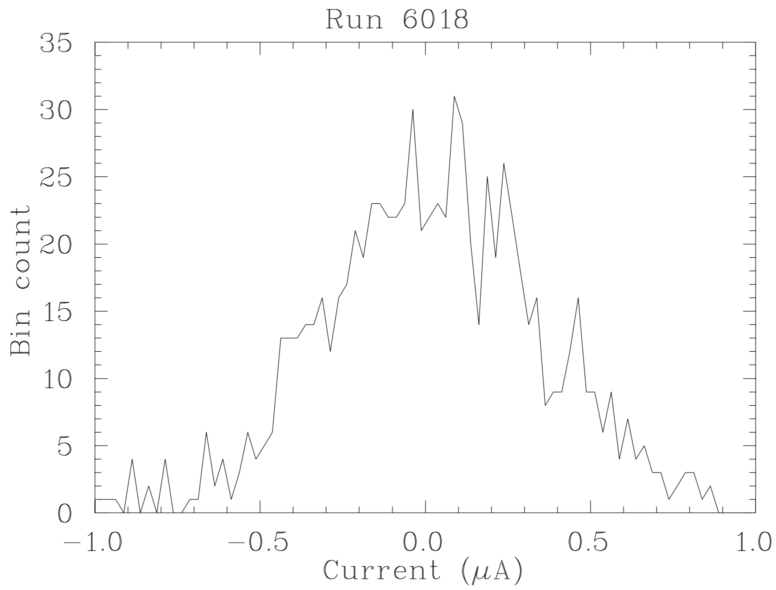

Figure A.6: Histogram of current readings from the Unser PCT from data shown in Figure A.5.

by as much as 40 μA as the toroid heated to its new equilibrium temperature. These effects have been minimized by surrounding the Unser toroid with heating tape to keep it at an elevated temperature, a copper RF shield, a mu-metal magnetic shield, and a passive thermal shield. Long-term drift remains despite the additional shielding, but the effect is not as pronounced as initial tests indicated.

Gain Drift

The gain of the Unser monitor while the front end electronics is set at **Range B** is quoted at 4 $\frac{mV}{\mu A}$ [90], which, after additional processing through the associated electronics, is equal to a scaler counting rate of 4000 $\frac{Hz}{\mu A}$. Measurements of the gain taken months apart have consistently stayed within about 0.1% of the above rate. Table A.3 lists the gains that were found for 4 different Unser calibrations.

Linearity

The Unser PCT has demonstrated an acceptable linearity over a range of 0 to 200 μA to within the statistical error of the calibrations. One method to demonstrate the

Date	Unser gain ($\frac{Hz}{\mu A}$)
6-3-95	4003.7 $\pm$ 10.7
11-10-95	4002.0 $\pm$ 6.7
2-22-96	3999.9 $\pm$ 1.6
7-19-96	3997.7 $\pm$ 0.8

Table A.3: Results from absolute Unser PCT calibrations over the course of several months.

linearity of the device is to look at its response as a function of beam current, and plot the residuals of the measurements compared to the expected signal given by the absolute calibration. Figures A.7 and A.8 show the residuals from two separate absolute Unser calibrations. To within statistical error, the device appears to be linear over the range of measurement.

A.4.3 Power Meter

Short-term Noise

The short term statistical noise of the power meter during normal data acquisition is low compared to that of the Unser monitor. However, the noise is correlated with the beam current as the power meter measures power, not current. When the beam current is high, the short term noise is on the order of a few nA. When the beam current is low, the short term noise can be on the order of a few hundred nA.

Because the beam current varies from the injector with time, it is more instructive to show the relative noise between BCM1 and BCM2. Figure A.9 shows an example of the short term noise of BCM1 and BCM2 with respect to each other. This particular run was taken at about $I_{beam} \approx 25$ μA, with integrated samples taken every two seconds.

Also, when the power levels drop below a certain point in the power meter (-48 dBm) [109], the power meter output signals change less frequently as it averages the power it detects in order to reduce the noise level of the output signal.

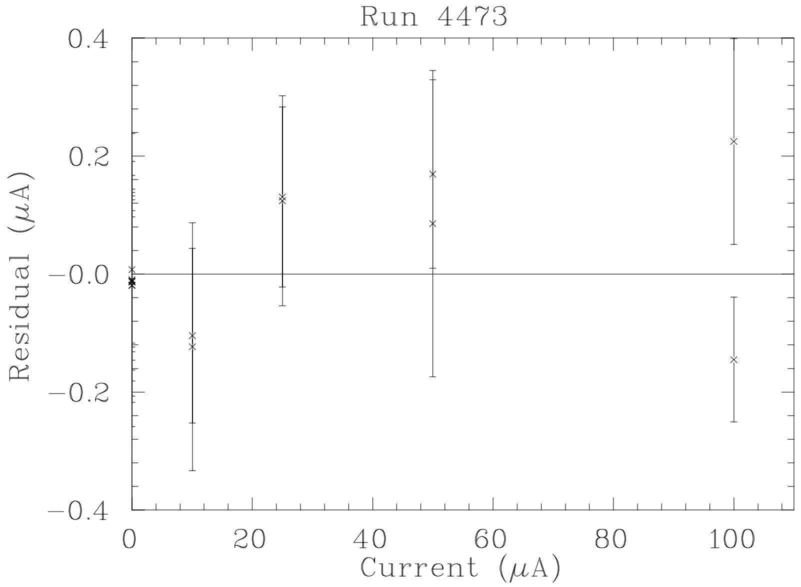

Figure A.7: Residuals from a linear fit for the absolute calibration of the Unser PCT in November 1995.

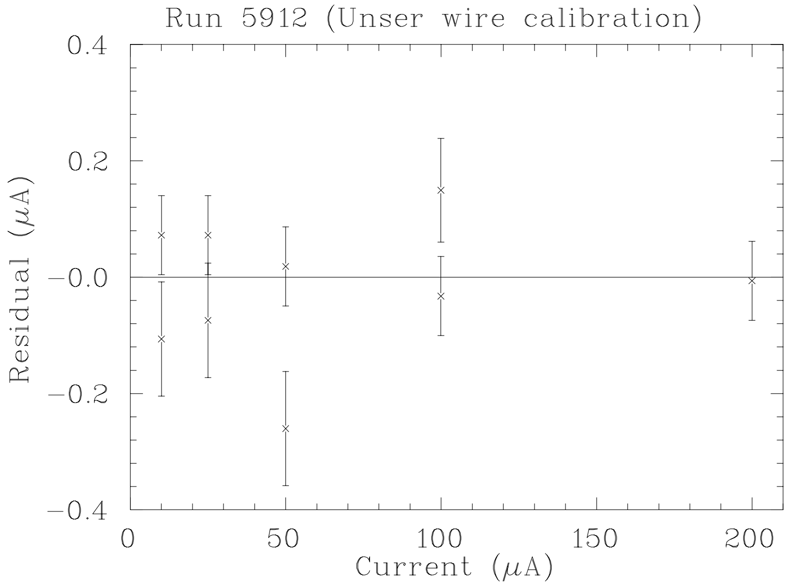

Figure A.8: Residuals from a linear fit for the absolute calibration of the Unser PCT in February 1996.

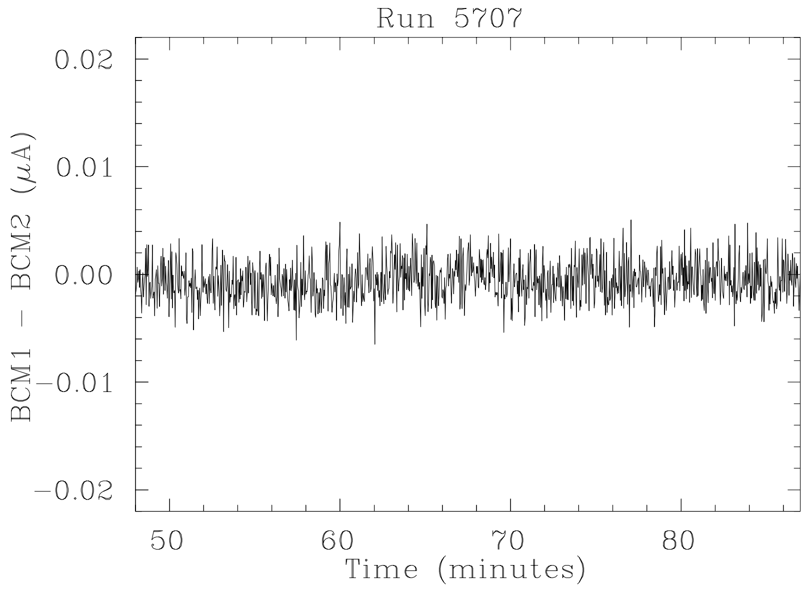

Figure A.9: Relative short-term noise between BCM1 and BCM2 at $I_{beam} \approx 25\mu$A.

Long-term Drift

The zero offset level for BCM1 and BCM2 is much more stable than for the Unser. Within the 7.5 V dynamic range of the preamplifier, the offset level changes on the order of only about 100 nV over a few days. Figures A.10 and A.11 show an example of how the offset level changed over time for BCM1 and BCM2. This variation in the offset level causes very little systematic error when the beam is on. The power meter detects power which is proportional to beam current squared. This in turn means that as the beam current increases, a systematic offset in the signal voltage causes a smaller systematic error in the current measurement.

Gain Drift

The gain of the system comprising of the resonant cavity and the power meter is a function of many variables, some of which are hard to control. The Gigatronics power meter readings have an accuracy of about $\pm 1\%$ [109]. This correlates well with the type of variation seen in the gain from the power meter over time. Figure A.12 shows

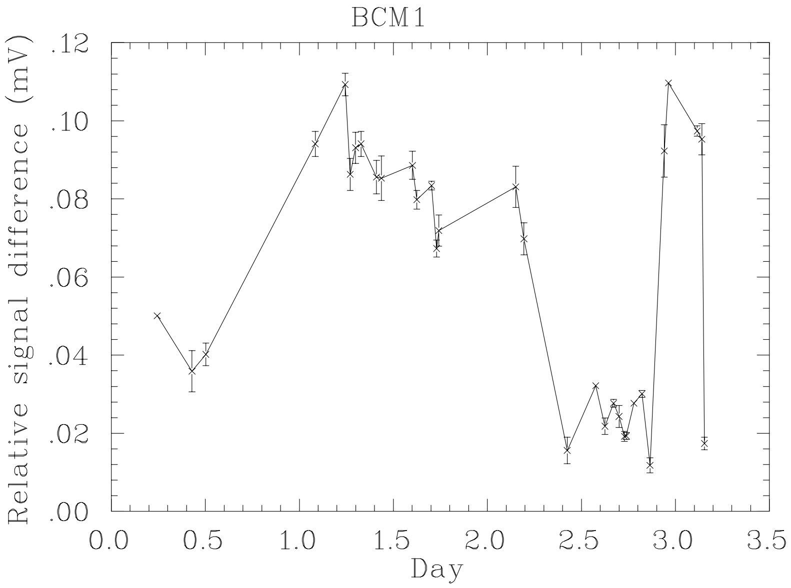

Figure A.10: Changes in the zero offset with respect to time for BCM1.

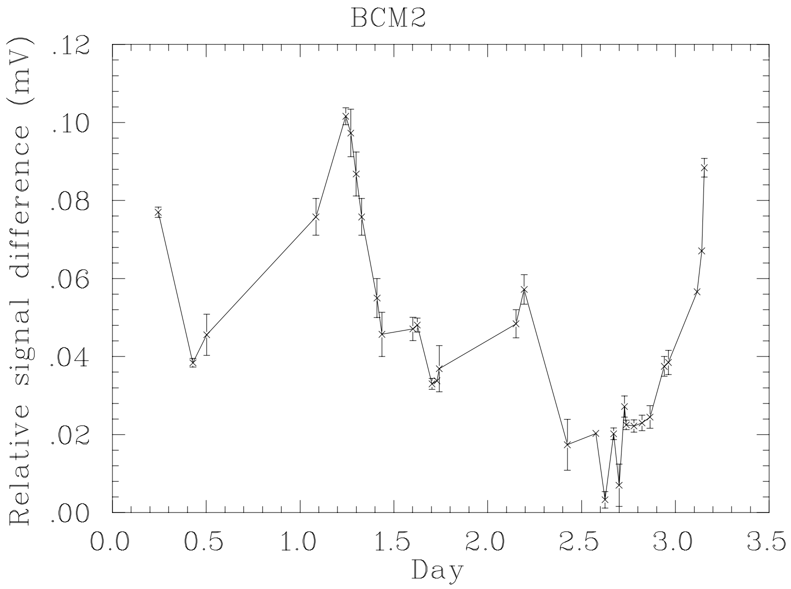

Figure A.11: Changes in the zero offset with respect to time for BCM2.

the typical variation of the gain for BCM1 over a series of runs.

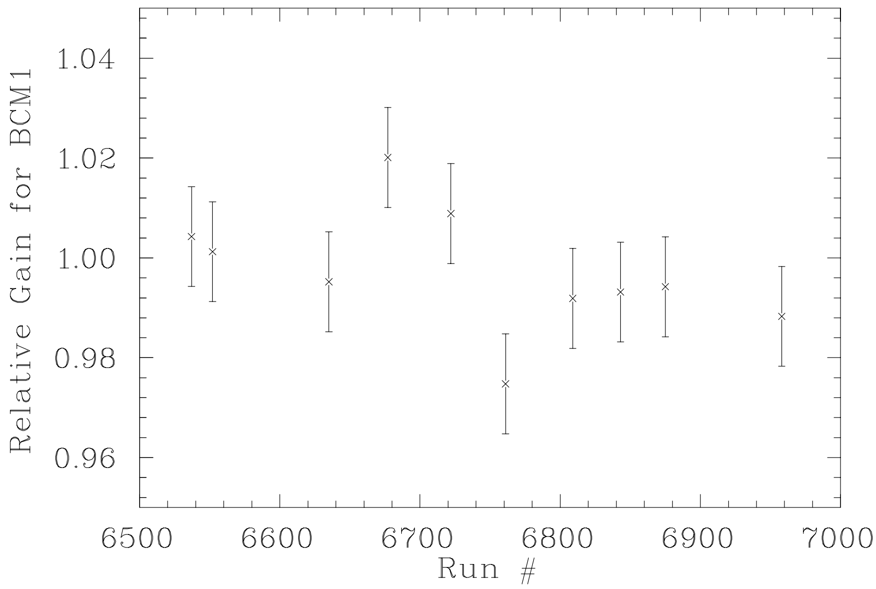

Figure A.12: Relative gain of BCM1 for successive calibrations.

The gain is also a function of temperature of the resonant cavity. As the temperature of the resonant cavity changes, the steel cavity expands and contracts, causing the cavity to go out of tune. As the cavity temperature deviates from where it was tuned, the signal coming from the cavity is reduced.

There was evidence of this temperature correlation during late 1995. Thermocouples were attached to each of the resonant cavities and the temperature was recorded on a strip-chart recorder. Over two months, a number of calibrations were made, and the gains of each cavity were plotted with respect to the temperature. Figures A.13 and A.14 show the gains for BCM1 and BCM2 as a function of temperature.

While there are not enough data to definitively say that a correlation exists between gain and temperature, further evidence points to that correlation because the cavities were tuned at a temperature: $T_{BCM1} = 72°\text{F}$, $T_{BCM2} = 70°\text{F}$, near the minima of both graphs, where the maximum signal is being delivered to the power meter from the cavity. The gain is a minimum here because the gain measures the factor needed to convert a detected power level to a corresponding current. As a cavity

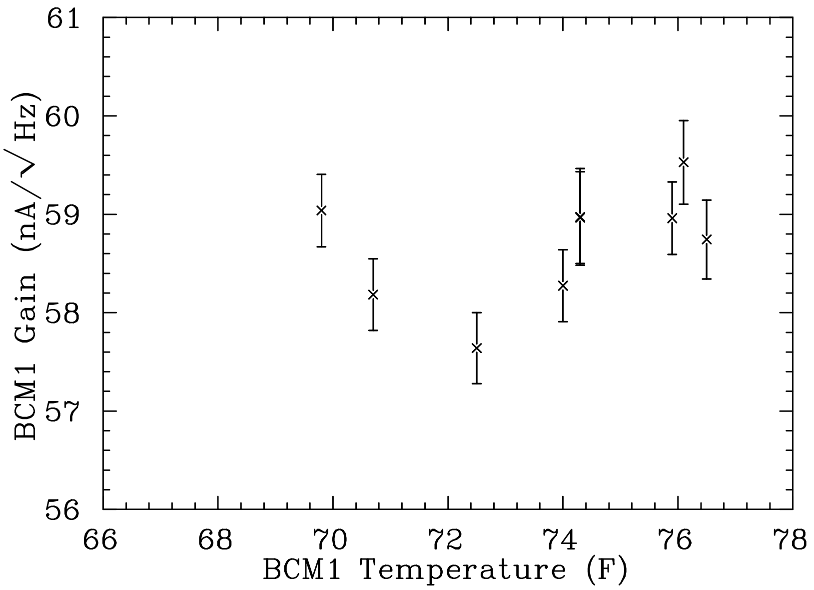

Figure A.13: Gain of BCM1 as a function of cavity temperature for calibrations made during late 1995.

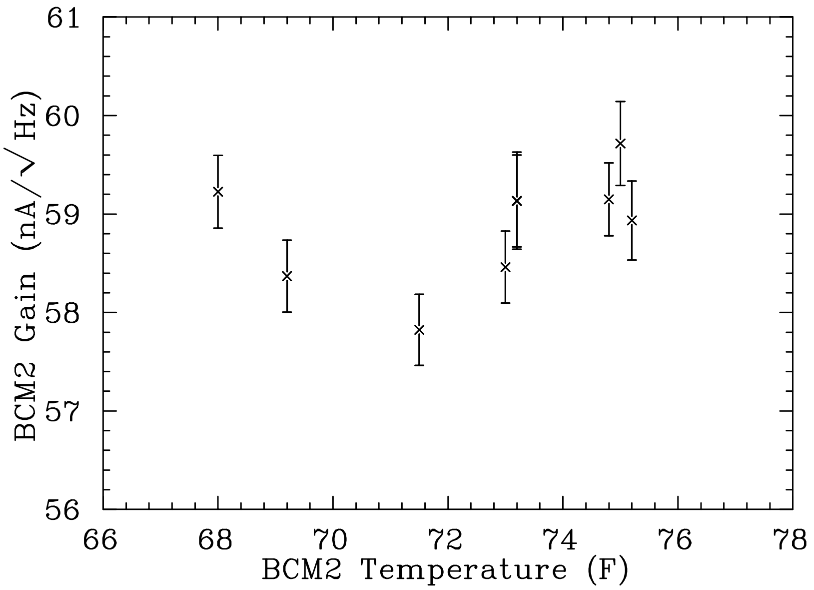

Figure A.14: Gain of BCM2 as a function of cavity temperature for calibrations made during late 1995.

becomes detuned, the power stored in the cavity decreases and the gain to convert the reduced power reading to the equivalent current must be increased. When the cavity is tuned, the gain is at a minimum.

Variations of this type were suppressed once the cavities were thermally insulated and kept at an elevated temperature of $110 \pm 1°$F. The loaded Q of each cavity was also lowered prior to the experiment in order to further reduce temperature dependent effects.

Errors in average current from non-linear signal

Beam current from the resonant cavity monitors is measured by integrating detected power over time. If there are any variations in the beam current while the power is being sampled, then there will be a systematic error induced in the translation from average power to average current because power is not linearly proportional to current.

This effect is most evident when the beam drops suddenly to zero, or when the beam returns to original levels as illustrated in Figure A.15. This drastic change in the current causes the greatest error.

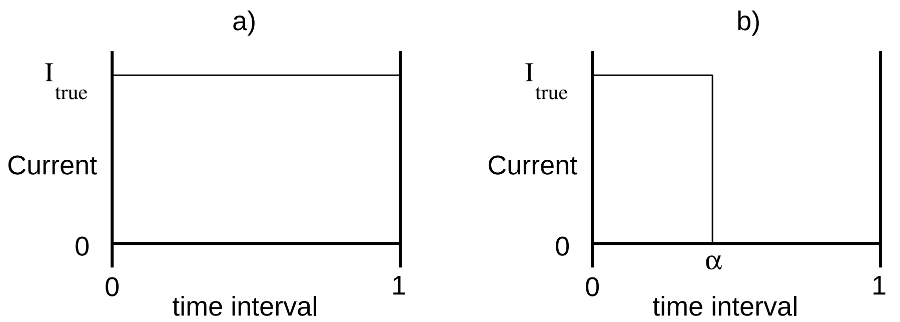

Figure A.15: Figure a) Expected behavior of beam current during measurement interval. Figure b) Sudden drop in beam current during a measurement interval. The quantity, α, is the fraction of the time interval that the beam remains on.

For a constant current, the average power $\langle P \rangle = \frac{\int_0^t P dt}{t} = RI_{true}^2$, where t is the length of the time interval, and R is a constant 'resistance'. The average current is then $\langle I\rangle = \sqrt{\langle P\rangle/R} = I_{true}$. The charge measured over that time interval is $C_{meas} = \langle I\rangle t = I_{true}t$. This charge measurement is the correct value.

However, assume the beam drops from a constant level to zero during a measurement interval, illustrated in Figure A.15 b). The measured average power for that measurement interval is

$$\begin{aligned}\langle P\rangle &= \frac{\int_0^t P(t)dt}{t} &\text{(A.8)}\\ &= \alpha R I_{true}^2 &\text{(A.9)}\end{aligned}$$

where α is the fraction of the interval the beam is on. The measured average current would then be

$$\begin{aligned}\langle I\rangle_{meas} &= \sqrt{\frac{\langle P\rangle}{R}} &\text{(A.10)}\\ &= \sqrt{\alpha I_{true}^2} \\ &= I_{true}\sqrt{\alpha}. &\text{(A.11)}\end{aligned}$$

The actual charge deposited on target is $C_{true} = I_{true}\alpha t$. However, due to the limitations in this measurement technique, the measured charge for this time interval is

$$\begin{aligned}C_{meas} &= \langle I_{meas}\rangle t &\text{(A.12)}\\ &= I_{true}\sqrt{\alpha}t. &\text{(A.13)}\end{aligned}$$

Therefore the systematic error in the charge measurement for that time interval is given by

$$\begin{aligned}\delta C &= C_{meas} - C_{true} &\text{(A.14)}\\ &= I_{true}\sqrt{\alpha}t - I_{true}\alpha t \\ &= I_{true}(\sqrt{\alpha} - \alpha)t. &\text{(A.15)}\end{aligned}$$

The maximum error occurs when $\alpha = 0.25$ where the measured charge is twice the actual charge.

As the beam can drop out at any time during a measurement interval, the average systematic error can be determined by integrating over all possible α,

$$\langle \delta C \rangle = I_{true} t \int_0^1 (\sqrt{\alpha} - \alpha) d\alpha \tag{A.16}$$

$$= \frac{1}{6} I_{true} t. \tag{A.17}$$

Assuming a 20 μA beam current, and a two second time for each measurement interval, the average systematic error in charge measurement for any time interval where the beam goes to zero is 6.7 μC.

For a typical 30 minute run, assuming a stable beam current of $I_{beam} = 20$ μA for the length of the run, a total of 36000 μC is deposited on the target. Each time the beam drops out in the middle of the run and comes back shortly thereafter, an additional 0.03% systematic error is introduced for the charge measurement for that run which is negligible compared to the overall uncertainty of the current measurement.

This error appears whenever the beam current changes, including minor variations in the beam current from the injector. A systematic error is induced when the beam current changes by even small amounts. The measured average current for a stable beam with current I_1 suddenly changing in current by some fixed amount and becoming stable again with current I_2 in the middle of an integration interval is

$$\langle I \rangle_{meas} = (I_1 \alpha + I_2 (1 - \alpha)) \frac{\sqrt{\alpha + (1 - \alpha) \frac{I_2^2}{I_1^2}}}{\alpha + (1 - \alpha) \frac{I_2}{I_1}}. \tag{A.18}$$

Assuming the beam drops suddenly from 25 to 20 μA one-quarter into a two second measurement interval, the error caused in that two second interval is only 0.5%. In the context of a run with many hundreds of measurements, this error is insignificant. Since fluctuations in beam current rarely reach such high levels, typical fluctuations in the beam current cause significantly less measurement error.

A.4.4 Mixer/rms-dc converter

The CEBAF Accelerator Operations Division has full control of this set of electronics, so the only analysis that could be done was to test the output signal of the mixer/rms-dc converter with the beam. No changes could be made for testing purposes.

Linearity

BCM3 shows signs of nonlinearity which would significantly increase systematic error if not corrected. A linearity scan was made for beam currents between 5 μA and 30 μA, with all BCMs calibrated at 30 μA.

This nonlinearity is shown in Figure A.16. The ratio of the beam current readings of BCM3 and BCM1 are given as a function of the beam current reading from BCM1. The signals are normalized at $I_{beam} = 25$ μA. If BCM3 were linear, the ratio in Figure A.16 would remain flat at 1.0. However the beam current reading from BCM3 drops off rapidly as the actual beam current decreases. At 7 μA, BCM3 reads 16% lower than BCM1. The readings from BCM3 can still be used to measure beam current with reasonable accuracy at low beam currents if the relative calibration procedure is performed to normalize all BCM signals to the beam current used in data production runs.

A.4.5 Preamplifiers

The voltage reference used in the preamplifier modules has remained stable to better than 0.1%. There is no evidence of any unstable or time-varying behavior in any of the modules. The output voltage exhibits an acceptable linearity between 0 to 10 V at both the x1 and x10 gain settings. The x100 and x1000 gain settings have never been tested.

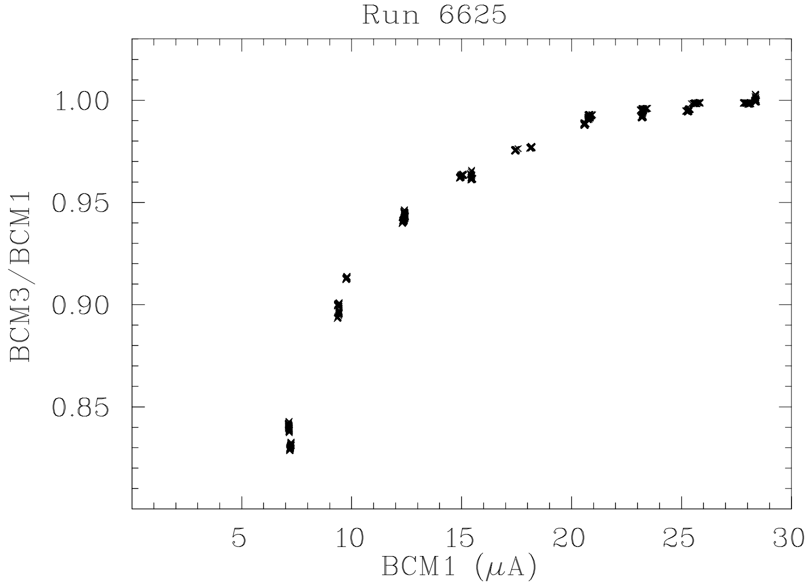

Figure A.16: Ratio of beam current readings from BCM3 to BCM1 normalized at $I_{beam} = 25\ \mu$A.

A.4.6 Voltage-Frequency Converters

Linearity

The Voltage-Frequency converters offer a linear response from 0 to 10 V, offering an output pulse frequency of 0 to 1 MHz. However, the V/F converters are capable of measuring signals outside of that range up to about 13.5 V. Early tests show that with an input signal 0 to 10 V, the output frequency has a linearity of better than 0.1%. The linearity of the module above 10 V has not been tested.

Cross-talk

When an input signal is applied to one of the V/F converters, the output signal of the other modules in that crate dropped by some amount, possibly due to some minor voltage drop in the power supply for the other modules.

Tests show that the pulse rate for each module dropped by about 7 Hz for each volt applied. The effect is also cumulative. So that if the maximum of 10 V were applied to each of the 4 modules, the cumulative effect would be that each of the modules would have an output pulse rate of (4 modules) $\left(10\frac{V}{\text{module}}\right)\left(7\frac{Hz}{V}\right) = 280$ Hz lower than expected. 280 Hz corresponds a voltage difference of 2.8 mV, or only about a 0.03% systematic error.

A.4.7 Temperature Stability System

The temperature stability system starts heating when the temperature of the magnetic shielding around the Unser falls to 109° and shuts off when the temperature reaches 111°, allowing the BCMs to cool. A strip chart recorder is used to continuously keep a record of the temperature of the 6 thermocouples. At all times, the temperatures were within 1°F of 110°. The typical period for heating and cooling was about 17 minutes per cycle. The Unser toroid was encased in a magnetic and RF shield. This extra shielding helped keep the toroid temperature stable to within ±0.2°. The resonant cavities, however, had no thermal barrier with the heating tape, and thus were cycling between 109° and 111°. As the quality factor of the cavities, Q_L were lowered prior to the experiment, a temperature variation of this magnitude would cause negligible error. For a coefficient of thermal expansion for stainless steel type 304 of $\alpha = 9.6\text{x}10^{-6}/°$ F [111], and a temperature fluctuation of ±1 °C = ±1.8 °F, Equation A.7 gives an uncertainty of

$$\frac{\delta I}{I} = \frac{1}{2}\frac{\delta P}{P} = \frac{(2Q_L\alpha\delta T)^2}{2} \approx 0.02\%. \tag{A.19}$$

Appendix B

Derivation of Kinematic Quantities

Many of the quantities that are used to describe the kinematics of deuteron photodisintegration are derived here. Focus is drawn to two different frames of reference, the "lab" frame and the "center-of-mass" frame. A general two-body reaction in the lab frame is pictured in Figure B.1. The center-of-mass frame is shown in Figure B.2. Here the total three-momentum of the reaction is always zero. Most calculations are easier to perform in the center-of-mass, so this is a particularly useful frame to consider. Also, the center-of-mass frame is the standard frame of reference when quoting reaction cross sections, so measurements in the lab frame must be transformed into the center-of-mass frame for results consistent with that of other experiments.

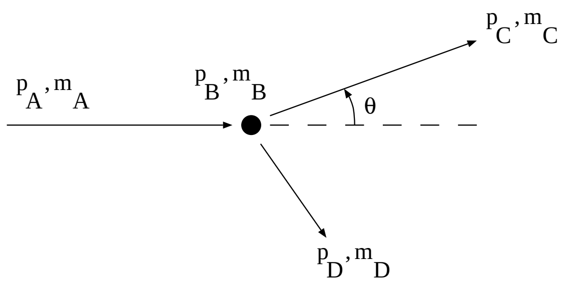

Figure B.1: General diagram for $AB \to CD$ in the lab frame.

Here, the center-of-mass frame quantities and the lab frame quantities are distinguished by the subscript cm. For example, θ_{cm}, $p_{p,cm}$, $E_{\gamma,cm}$ correspond to quantities in the center-of-mass frame, while the equivalent quantities in the lab frame are given

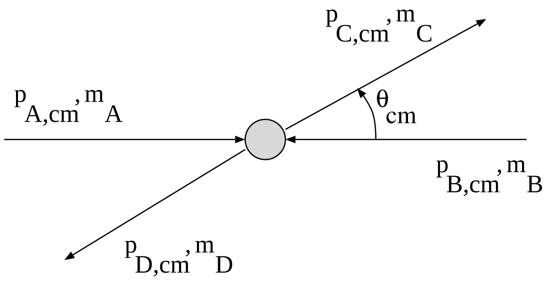

Figure B.2: General diagram for $AB \rightarrow CD$ in the center-of-mass frame.

as θ, p_p, E_γ. Also, the subscript *cm* will be used to label quantities relating the center-of-mass frame itself to the lab frame. For example, the quantities γ_{cm} and β_{cm} relate the velocity of the center-of-mass frame to the lab frame. Figures B.3 and B.4 show the lab and center-of-mass frame views of deuteron photodisintegration.

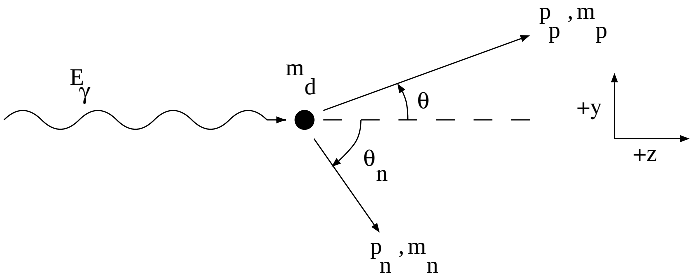

Figure B.3: Pictorial of $\gamma d \rightarrow pn$ in the lab frame.

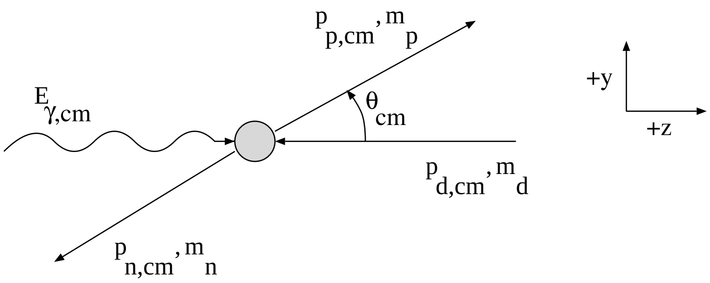

Figure B.4: Pictorial of $\gamma d \rightarrow pn$ in the center-of-mass frame.

B.1 Center of Mass Quantities

The Mandelstam variables are given by

$$s = (p^\mu_A + p^\mu_B)^2 \tag{B.1}$$

$$t = (p^\mu_A - p^\mu_C)^2 \tag{B.2}$$

$$u = (p^\mu_A - p^\mu_D)^2 \tag{B.3}$$

where p^μ_i is the four momentum of the particle given by $[p^0, p^1, p^2, p^3]$ where $p^\mu p_\mu = (p^0)^2 - (p^1)^2 - (p^2)^2 - (p^3)^2$. The Mandelstam variables are invariant under Lorentz transformation. Thus they can be calculated in either frame and they yield the same result.

The center-of-mass energy squared is given by s, and it is used extensively in the theory and analysis. In the lab frame, it is given by

$$\begin{aligned} s &= (p^\mu_\gamma + p^\mu_d)^2 && \text{(B.4)} \\ &= \left([E_\gamma, 0, 0, E_\gamma] + [m_d, 0, 0, 0]\right)^2 && \text{(B.5)} \\ &= [E_\gamma + m_d, 0, 0, E_\gamma]^2 && \text{(B.6)} \\ &= (E_\gamma + m_d)^2 - E^2_\gamma && \text{(B.7)} \\ &= m^2_d + 2m_d E_\gamma. && \text{(B.8)} \end{aligned}$$

For a general reaction in the center-of-mass frame,

$$\begin{aligned} s &= (p^\mu_{A,cm} + p^\mu_{B,cm})^2 && \text{(B.9)} \\ &= ([E_{A,cm}, 0, 0, p_{A,cm}] + [E_{B,cm}, 0, 0, p_{B,cm}])^2. && \text{(B.10)} \end{aligned}$$

But in the cm frame, the total three-momenta of the system must equal zero, so $\vec{p}_{A,cm} = -\vec{p}_{B,cm}$. Making the substitution in the above,

$$\begin{aligned} s &= [\sqrt{p^2_{A,cm} + m^2_A} + \sqrt{p^2_{A,cm} + m^2_B}, 0, 0, 0]^2 && \text{(B.11)} \\ &= \left(\sqrt{p^2_{A,cm} + m^2_A} + \sqrt{p^2_{A,cm} + m^2_B}\right)^2. && \text{(B.12)} \end{aligned}$$

The initial momentum, $p_i = p_{A,cm}$, is a quantity that is used to calculate the reaction cross section and can be solved from the above in terms of s and the particle masses,

$$p_i^2 = \frac{s^2 - 2s(m_A^2 + m_B^2) + (m_A^2 - m_B^2)^2}{4s}. \tag{B.13}$$

For $\gamma d \to pn$, $p_i = E_{\gamma,cm}$ and is given by the above to be

$$p_i^2 = \frac{(s - m_d^2)^2}{4s} \tag{B.14}$$

$$E_{\gamma,cm} = p_i = \frac{E_\gamma m_d}{\sqrt{s}}. \tag{B.15}$$

Because s is invariant, it describes the center of mass energy after the reaction has taken place as well, so

$$s = (p_C^\mu + p_D^\mu)^2. \tag{B.16}$$

The final momentum $p_f = p_{C,cm}$ is also used to calculate the reaction cross section and can be calculated in an analogous manner to p_i,

$$p_f^2 = \frac{s^2 - 2s(m_C^2 + m_D^2) + (m_C^2 - m_D^2)^2}{4s}. \tag{B.17}$$

For $\gamma d \to pn$,

$$p_f^2 = \frac{s^2 - 2s(m_p^2 + m_n^2) + (m_p^2 - m_n^2)^2}{4s}. \tag{B.18}$$

As $m_d \approx m_p + m_n$ and $m_p \approx m_n$,

$$p_f^2 \approx \frac{s - m_d^2}{4}. \tag{B.19}$$

The Mandelstam variable t and u can be found for a general two-body reaction in the center-of-mass frame from the above relations,

$$\begin{aligned}
t &= ([E_{A,cm}, 0, 0, p_{A,cm}] - [E_{C,cm}, 0, p_{C,cm}\sin\theta_{cm}, p_{C,cm}\cos\theta_{cm}])^2 && \text{(B.20)}\\
&= m_A^2 + m_C^2 - 2E_{A,cm}E_{C,cm} + 2p_{A,cm}p_{C,cm}\cos\theta_{cm}, && \text{(B.21)}\\
u &= ([E_{A,cm}, 0, 0, p_{A,cm}] - [E_{D,cm}, 0, p_{D,cm}\sin\theta_{cm}, p_{D,cm}\cos\theta_{cm}])^2 && \text{(B.22)}\\
&= m_A^2 + m_D^2 - 2E_{A,cm}E_{D,cm} + 2p_{A,cm}p_{D,cm}\cos\theta_{cm}. && \text{(B.23)}
\end{aligned}$$

For $\gamma d \to pn$,

$$t = m_p^2 - 2E_{\gamma,cm}E_{p,cm} + 2E_{\gamma,cm}p_{p,cm}\cos\theta_{cm}, \tag{B.24}$$

$$u = m_n^2 - 2E_{\gamma,cm}E_{n,cm} + 2E_{\gamma,cm}p_{p,cm}\cos\theta_{cm}, \tag{B.25}$$

where $E_{n,cm} = \sqrt{m_n^2 + p_{p,cm}^2}$.

B.2 Center-of-Mass Frame Velocity

The center-of-mass frame moves at a velocity β_{cm} with respect to the lab frame. The easiest way to determine the velocity is to note that in the lab frame, the deuteron is at rest, while in the cm frame, it has a momentum $-p_i\ \hat{z}$. Thus, the cm frame must move at the same velocity in the opposite direction to the deuteron. Using the relations above,

$$\beta_{cm} = -\beta_d = \frac{p_{d,cm}}{E_d} \tag{B.26}$$

$$= \frac{p_i}{\sqrt{p_i^2 + m_d^2}} \tag{B.27}$$

$$= \frac{E_\gamma}{E_\gamma + m_d}. \tag{B.28}$$

Another relation, γ_{cm}, is useful for Lorentz transformations between frames,

$$\gamma_{cm} = \frac{1}{\sqrt{1 - \frac{1}{\beta_{cm}^2}}} \tag{B.29}$$

$$= \frac{E_\gamma + m_d}{\sqrt{s}}. \tag{B.30}$$

B.3 Jacobian $\frac{d\Omega_{cm}}{dt}$

The Jacobian $\frac{d\Omega_{cm}}{dt}$ is used to relate the center-of-mass cross section to the invariant cross section. The differential solid angle is given by

$$d\Omega_{cm} = 2\pi\sin(\theta_{cm})d\theta_{cm} \tag{B.31}$$

where the quantity has already been integrated over $d\phi_{cm}$. Thus,

$$\frac{d\Omega_{cm}}{d\theta_{cm}} = 2\pi \sin(\theta_{cm}). \tag{B.32}$$

The Mandelstam variable, t, is given in Equation B.21. Differentiating it with respect to θ_{cm} gives

$$\frac{dt}{d\theta_{cm}} = 2\,|p_{A,cm}|\,|p_{C,cm}|\sin(\theta_{cm}). \tag{B.33}$$

Dividing Equation B.32 by Equation B.33 gives the Jacobian

$$\frac{d\Omega_{cm}}{dt} = \frac{\pi}{|p_{A,cm}|\,|p_{C,cm}|}. \tag{B.34}$$

For deuteron photodisintegration, the transformation is

$$\frac{d\Omega_{cm}}{dt} = \frac{\pi}{|p_i|\,|p_f|}. \tag{B.35}$$

B.4 Jacobian $\frac{d\Omega}{d\Omega_{cm}}$

The differential cross section that is measured in the lab must be transformed into the center-of-mass frame which is the standard frame of reference used for differential cross sections. This is done using the Jacobian $\frac{d\Omega}{d\Omega_{cm}}$. Using the relation in Equation B.31, the Jacobian is given by

$$\frac{d\Omega}{d\Omega_{cm}} = \frac{2\pi\sin(\theta)d\theta}{2\pi\sin(\theta_{cm})d\theta_{cm}} = \frac{\sin(\theta)}{\sin(\theta_{cm})}\frac{d\theta}{d\theta_{cm}}. \tag{B.36}$$

Now, only the relation $\frac{d\theta}{d\theta_{cm}}$ needs to be found. First, consider the Lorentz transformation for a particle, α, in the center-of-mass frame with $E_{\alpha,cm}$, $\vec{p}_{\alpha,cm}$ into the lab frame using the center-of-mass frame velocity given in Appendix B.2,

$$\begin{pmatrix} E_\alpha \\ p_{\alpha,y} \\ p_{\alpha,z} \end{pmatrix} = \begin{pmatrix} E_\alpha \\ p_\alpha \sin(\theta) \\ p_\alpha \cos(\theta) \end{pmatrix} = \begin{pmatrix} \gamma_{cm} & 0 & \gamma_{cm}\beta_{cm} \\ 0 & 1 & 0 \\ \gamma_{cm}\beta_{cm} & 0 & \gamma_{cm} \end{pmatrix} \begin{pmatrix} E_{\alpha,cm} \\ p_{\alpha,cm}\sin(\theta_{cm}) \\ p_{\alpha,cm}\cos(\theta_{cm}) \end{pmatrix}. \tag{B.37}$$

This matrix gives the three equations

$$p_\alpha \sin(\theta) = p_{\alpha,cm} \sin(\theta_{cm}) \tag{B.38}$$

$$p_\alpha \cos(\theta) = \gamma_{cm} p_{\alpha,cm} \cos(\theta_{cm}) + \gamma_{cm}\beta_{cm} E_{\alpha,cm} \tag{B.39}$$

$$E_\alpha = \gamma_{cm}\beta_{cm} p_{\alpha,cm} \cos(\theta_{cm}) + \gamma_{cm} E_{\alpha,cm}. \tag{B.40}$$

Solving Equation B.38 for p_α and substituting that into Equation B.39 gives

$$p_{\alpha,cm} \sin(\theta_{cm}) = \tan(\theta)(\gamma_{cm} p_{\alpha,cm} \cos(\theta_{cm}) + \beta_{cm}\gamma_{cm} E_{\alpha,cm}). \tag{B.41}$$

Differentiating it with respect to θ_{cm} gives

$$p_{\alpha,cm} \cos(\theta_{cm}) = \tan(\theta)(-\gamma_{cm} p_{\alpha,cm} \sin(\theta_{cm})) + \tag{B.42}$$

$$\frac{\frac{d\theta}{d\theta_{cm}}}{\cos^2(\theta)}(\gamma_{cm} p_{\alpha,cm} \cos(\theta_{cm}) + \beta_{cm}\gamma_{cm} E_{\alpha,cm}) \tag{B.43}$$

$$= \tan(\theta)(-\gamma_{cm} p_{\alpha,cm} \sin(\theta_{cm})) + \frac{d\theta}{d\theta_{cm}} p_{\alpha,cm} \frac{\sin(\theta_{cm})}{\sin(\theta)\cos(\theta)}. \tag{B.44}$$

Solving for $\frac{d\theta}{d\theta_{cm}}$ gives

$$\frac{d\theta}{d\theta_{cm}} = \frac{\sin(\theta)}{\sin(\theta_{cm})}[\cos(\theta_{cm})\cos(\theta) + \gamma_{cm} \sin(\theta_{cm})\sin(\theta)]. \tag{B.45}$$

Substituting that back into Equation B.36 gives the Jacobian

$$\frac{d\Omega}{d\Omega_{cm}} = \frac{\sin^2(\theta)}{\sin^2(\theta_{cm})}[\cos(\theta_{cm})\cos(\theta) + \gamma_{cm} \sin(\theta_{cm})\sin(\theta)]. \tag{B.46}$$

B.5 Reconstructed Photon Energy E_γ

The spectrometer detects the proton momentum, p_p, and the scattering angle θ in the lab frame. From these two quantities the energy of the photon, E_γ, can be reconstructed.

Starting with Figure B.3, conservation of energy and momentum gives

$$p_p \sin\theta + p_n \sin\theta_n = 0 \tag{B.47}$$

$$p_p \cos\theta + p_n \cos\theta_n = E_\gamma \tag{B.48}$$

$$E_p + E_n = E_\gamma + m_d. \tag{B.49}$$

Solving the above for the neutron quantities gives

$$p_n \sin\theta_n = -p_p \sin\theta \tag{B.50}$$

$$p_n \cos\theta_n = -p_p \cos\theta + E_\gamma \tag{B.51}$$

$$E_n = E_\gamma + m_d - E_p. \tag{B.52}$$

Squaring Equations B.51 and B.52 and adding them gives

$$p_n^2 = E_\gamma^2 + p_p^2 - E_\gamma p_p \cos\theta. \tag{B.53}$$

Squaring Equation B.52 and expanding E_n^2 gives

$$p_n^2 + m_n^2 = (E_\gamma + m_d - E_p)^2. \tag{B.54}$$

Substituting Equation B.53 into Equation B.54 and solving for E_γ give the reconstructed photon energy

$$E_\gamma = \frac{E_p m_d - \frac{1}{2}(m_d^2 + m_p^2 - m_n^2)}{m_d - E_p + p_p \cos\theta_p}. \tag{B.55}$$

B.6 Pion Production Threshold

The reconstructed value for $E_\gamma^{\gamma d\to pn}$ assumes that the proton that is detected came from a deuteron photodisintegration reaction. If, on the other hand, a pion was produced at the same time, then the value for E_γ would be wrong. There is no easy way to determine if a proton event is a product of strict photodisintegration, but there is an upper limit in the reconstructed $E_\gamma^{\gamma d\to pn}$ spectrum for pion production events. Above this threshold, pion production events are excluded.

Figure B.5 is a pictorial of the pion production reaction in the center-of-mass frame and the lab frame. The technique is to determine the highest possible proton energy allowed in this reaction. Then, by inserting that quantity into Equation B.55, the highest possible reconstructed value for $E_\gamma^{\gamma d\to pn}$ is obtained.

The total center of mass energy squared is given by

$$s = E_{cm}^2 = m_d^2 + 2E_\gamma^{\gamma d\to pn\pi^0} m_d. \tag{B.56}$$

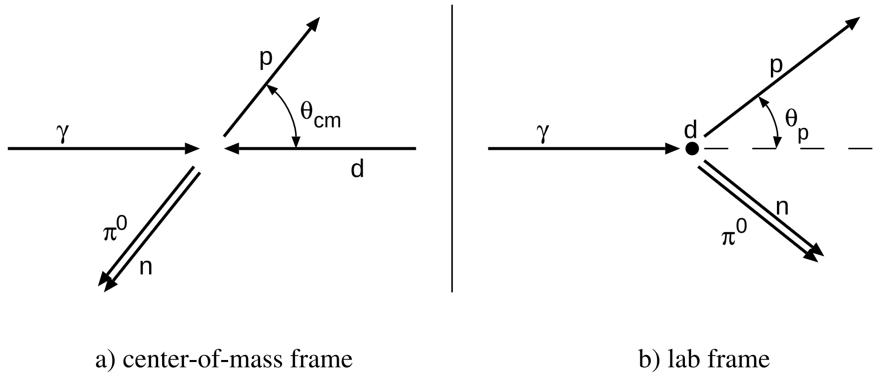

Figure B.5: Pion production in the deuteron photodisintegration reaction in the center of mass and the lab frame.

The value for $E_\gamma^{\gamma d \to pn\pi^0}$ should be the maximum value possible for E_γ. This is given by the electron beam energy, E_{beam}.

Momentum and energy conservation for the pion production reaction give

$$p_{p,cm} + p_{n,cm} + p_{\pi^0,cm} = 0 \tag{B.57}$$

$$E_{p,cm} + E_{n,cm} + E_{\pi^0,cm} = E_{cm} = \sqrt{s} \tag{B.58}$$

The momenta and energies of the pion and neutron are related but unconstrained. The maximum proton energy is found by taking the partial derivative of $E_{p,cm}$ with respect to $p_{n,cm}$ and setting it to 0

$$\frac{\partial E_{p,cm}}{\partial p_{n,cm}} = \frac{\partial}{\partial p_{n,cm}}\left(E_{cm} - \sqrt{m_n^2 + p_{n,cm}^2} - \sqrt{m_{\pi^0}^2 + p_{\pi^0,cm}^2}\right) = 0 \tag{B.59}$$

$$-\frac{p_{n,cm}}{\sqrt{m_n^2 + p_{n,cm}^2}} - \frac{\frac{\partial}{\partial p_{n,cm}}(p_{\pi^0,cm}^2)}{2\sqrt{m_{\pi^0}^2 + p_{\pi^0,cm}^2}} = 0 \tag{B.60}$$

$$-\beta_{n,cm} + \frac{p_{\pi^0,cm}}{\sqrt{m_{\pi^0}^2 + p_{\pi^0,cm}^2}} = 0 \tag{B.61}$$

$$\beta_{n,cm} = \beta_{\pi^0,cm}. \tag{B.62}$$

Thus the proton energy is maximum when the neutron and pion are moving directly away from the proton at the same velocity. This is equivalent to a composite particle with mass $m = m_n + m_{\pi^0}$ and momentum $p = p_{n,cm} + p_{\pi^0,cm} = -p_{p.cm}$ moving away from the proton at velocity $\beta = \beta_{n,cm} = \beta_{\pi^0.cm}$.

Using this relation in Equation B.58, the maximum proton energy is given by

$$E_{p,cm}^{max} = \frac{E_{cm}^2 + m_p^2 - (m_n + m_{\pi^0})^2}{2E_{cm}}. \tag{B.63}$$

Then, after boosting the proton energy back into the lab frame using the Lorentz transformation in Equation B.37, and substituting the proton energy and momentum into Equation B.55, the pion production threshold is obtained.

References

[1] J. Chadwick, M. Goldhaber, Nature, **134**, 237 (1934).

[2] J. Napolitano *et. al.*, Phys. Rev. Lett. **61**, 2530 (1988).

[3] J. E. Belz, *et. al.*, Phys. Rev. Lett. **74**, 646 (1995).

[4] S. J. Brodsky, G. P. Lepage, Nucl. Phys. **A353**, 247c (1981).

[5] B. Povh, K. Rith, C. Scholz, F. Zetsche, Particles and Nuclei, (Springer-Verlag: Berlin), p. 100, (1995).

[6] Review of Particle Properties, Phys. Rev. D, **50**, 1297 (1994).

[7] C. E. Carlson, J. R. Hiller, R. J. Holt, Annu. Rev. Nucl. Part. Sci. **47**, 395 (1997).

[8] D. Sivers, Ann. Rev. Part. Sci., **32**, 149 (1982).

[9] N. Isgur, C. H. L. Smith, Nuc. Phys. **B317**, 526 (1989).

[10] L. L. Frankfurt, M. I. Strikman, Phys. Reports **76**, 215 (1988).

[11] M. Harvey, Nucl. Phys. **A352**, 301 (1981), **A352**, 326 (1981).

[12] S. J. Brodsky, C. R. Ji, SLAC-PUB-3747, p. 56, (1985).

[13] S. J. Brodsky, G. R. Farrar, Phys. Rev. Lett. **31**, 1153 (1973).

[14] V. A. Matveev *et. al.*, Lettere al Nuovo Cimento **7**, 719 (1973).

[15] S. J. Brodsky, B. T. Chertok, Phys. Rev. **D14**, 3003 (1976).

[16] S. J. Brodsky, B. T. Chertok, Phys. Rev. Lett. **37**, 269 (1976).

[17] L. L. Frankfurt, G. A. Miller, M. M. Sargsian, M. I. Strikman, LANL preprint hep-ph/9904222.

[18] J. M. Laget, Rapport DPh-N Saclay n°2146, (1984).

[19] T. S. H. Lee, ANL-PHY-5253-TH-88.

[20] T. S. H. Lee, Few Body Systems, Suppl. **6**, 526 (1992).

[21] S. I. Nagornyǐ, Yu. A. Kasatkin, I. K. Kirichenko, Sov. J. Nucl. Phys. **55**, 189 (1992).

[22] R. J. Holt, Phys. Rev. **C41**, 2400 (1990).

[23] R. J. Holt, Argonne National Laboratory, CEBAF Proposal PR-89-012, (1989).

[24] S. J. Brodsky, G. R. Farrar, Phys. Rev. **D11**, 1309 (1975).

[25] F. Halzen, A. D. Martin, Quarks and Leptons: An Introductory Course in Modern Particle Physics, (John Wiley and Sons: New York), p. 91, (1984).

[26] P. V. Landshoff, Phys. Rev. **D10**, 1024, (1974).

[27] P. V. Landshoff, J. C. Polkinghorne, Phys. Lett. **44B**, 293 (1973).

[28] M. A. Shupe, *et. al.*, Phys. Rev. **D19**, 1921 (1979).

[29] R. L. Anderson, *et. al.*, Phys. Rev. **D14**, 679 (1976).

[30] S. J. Brodsky, B. T. Chertok, Phys. Rev. Lett. **37**, 269 (1976).

[31] C. White, *et. al.*, Phys. Rev. **D49**, 58 (1994).

[32] D. Meekins, *et. al.*, in preparation.

[33] P. Dougan, *et. al.*, Z. Phys. **A276**, 55 (1976).

[34] R. Ching and C. Schaerf, Phys. Rev. **141**, 1320 (1966).

[35] H. Myers, *et. al.*, Phys. Rev. **121**, 630 (1961).

[36] J. Arends, *et. al.*, Nucl. Phys. **A412**, 509 (1984).

[37] S. J. Freedman *et. al.*, Phys. Rev. **C48**, 1864 (1993).

[38] J. E. Belz, doctoral thesis, California Institute of Technology, unpublished, (1994).

[39] C. E. Carlson, Nucl. Phys. **A508**, 481c (1990).

[40] S. Rock, *et. al.*, Phys. Rev. Lett. **49**, 1139 (1982).

[41] L. C. Alexa, *et. al.*, Phys. Rev. Lett. **82**, 1374 (1999).

[42] D. H. Perkins, Introduction to High Energy Physics, (Addison-Wesley: Menlo Park, CA), (1987).

[43] S. J. Brodsky, J. R. Hiller, Phys. Rev. **C28**, 475 (1983).

[44] P. D. B. Collins, An Introduction to Regge Theory and High Energy Physics, (Cambridge University Press:Cambridge), (1977).

[45] A. B. Kaidalov, Z. Phys. **C12**, 63 (1982).

[46] L. A. Kondratyuk, *et. al.*, Phys. Rev. **C48**, 2491 (1993).

[47] E. DeSanctis, A. B. Kaidalov, L. A. Kondratyuk, Phys. Rev. **C42**, 1764 (1990).

[48] M. Lacome, *et. al.*, Phys. Rev. **C21**, 861 (1980).

[49] R. V. Reid, Jr. Annals of Phys. **50**, 411 (1968).

[50] J. M. Laget, Nucl. Phys. **A312**, 265 (1978).

[51] J. M. Laget, New Vistas in Electro-Nuclear Physics, (New York:Plenum Press), p. 361, (1986).

[52] T. S. H. Lee, Phys. Rev. **C29**, 195 (1984).

[53] C. R. Chen, T. S. H. Lee, Phys. Rev. **C38**, 2187 (1988).

[54] S. I. Nagornyĭ, Yu. A. Kasatkin, E. V. Inopin, I. K. Kirichenko, Sov. J. Nucl. Phys. **49**, 465 (1989).

[55] F. Gross, B. D. Keister, Phys. Rev. **C28**, 823 (1983).

[56] E. L. Dieperink, S. I. Nagornyĭ, LANL preprint nucl-th/9904058.

[57] A. B. Kaidalov, Sov. Phys. Usp. **20**, 691 (1977).

[58] D. Meekins, doctoral thesis, College of William and Mary, (1998).

[59] J. Dunne, Internal CEBAF Report, (1997).

[60] B. P. Terburg, doctoral thesis, Univerisity of Illinois, (1999).

[61] http://www.jlab.org/Hall-C/equipment/HMS/performance.html, TNJAF web-page.

[62] D. C. Carey, K. L. Brown, F. Rothacker, TRANSPORT, A Computer Program for Deisgning Charged Particle Beam Transport Systems, SLAC-R-95-462, (1995).

[63] W. R. Leo, Techniques for Nuclear and Particle Physics Experiments, (Springer-Verlag:Berlin), p. 149, (1994).

[64] O. K. Baker, et. al., Nuc. Inst. and Methods, **A367**, 92 (1995).

[65] W. R. Leo, Techniques for Nuclear and Particle Physics Experiments, (Springer-Verlag:Berlin), p. 157, (1994).

[66] W. R. Leo, Techniques for Nuclear and Particle Physics Experiments, (Springer-Verlag:Berlin), p. 35, (1994).

[67] H. Mkrtchyan, (unpublished).

[68] Trigger Supervisor Users Guide, Internal CEBAF document.

[69] CEBAF Online Data Acquisition User's Manual 1.2, (1993).

[70] J. Arrington, doctoral thesis, California Institute of Technology, (1998).

[71] B. P. Terburg, private communication (1994).

[72] Physics Analysis Workstation 2.03, CERN Long Writeup Q121 (1993).

[73] J. L. Chuma, Physica Reference Manual, TRI-CD-93-01 v1.3, TRIUMF, (1997).

[74] J. Arrington, Optimizing the Performance of the Hall C Detectors, Internal CEBAF Report, (1996).

[75] C. A. Armstrong, Hall C Time-of-Flight Fitting Code, Internal CEBAF document, (1995).

[76] D. F. Geesaman, Tracking in the SOS Spectrometer, Internal CEBAF Report, (1993).

[77] D. van Westrum, Measurement of Tracking Errors in the Regular and 4 out of 6 Tracking Algorithms, Internal CEBAF Report, (1996).

[78] D. van Westrum, Measurement of the Tracking Efficiency, Internal CEBAF Report, (1998).

[79] M. Berz, COSY Infinity Version 7 Reference Manual, MSCL Technical Report MSUCL-977, Michigan State University, (1995).

[80] K. A. Assamagan, D. dutta, P. Welch, Hall C Matrix Element Optimization Package, Internal CEBAF Document, (1997).

[81] W. H. Press, B. P. Flannery, S. A. Teukolsky, W. T. Vettering, Numerical Recipes, (Cambridge University Press:Cambridge), (1989).

[82] D. Dutta, doctoral thesis, Northwestern University, (1998).

[83] L. E. Wright, L. Tiator, Phys. Rev. **C26**, 2349 (1982).

[84] J. E. Belz, F-CEBAF, photon flux simulation program.

[85] CEBAF Hall-C HMS simulation program, mc-hms-single, internal CEBAF document.

[86] Review of Particle Properties, Phys. Rev. D, **50**, 1253 (1994).

[87] W. R. Leo, Techniques for Nuclear and Particle Physics Experiments, (Springer-Verlag:Berlin), p. 24, (1994).

[88] T. G. O'Neill, doctoral thesis, California Institute of Technology, (1994).

[89] C. Bochna, B. Terburg, et.al., Phys. Rev. Lett., **81**, 4756 (1998).

[90] J. Bergoz, Parametric Current Transformer Instruction Manual, (1991).

[91] J. L. Matthews, R. O. Owens, Nuc. Inst. and Methods, **111**, 157 (1973).

[92] J. L. Matthews, R. O. Owens, Nuc. Inst. and Methods, **180**, 573 (1981).

[93] J. E. Belz, SUPER-BREM, photon flux simulation program.

[94] K. Gustaffson, Cryotarget Density Dependence on Beam Current, Internal CEBAF Report, (1996).

[95] B. P. Terburg, The Target Gas Analysis Vademecum, Internal CEBAF Report, (1996).

[96] J. Dunne, Memorandum Regarding the Survey of the Cryotargets Pre-T20, Internal CEBAF Report, (1996).

[97] J. Dunne, Memorandum Regarding the Survey of the Cryotargets for T20, Internal CEBAF Report, (1997).

[98] D. vanWestrum, doctoral thesis, University of Colorado, (1998).

[99] P. Gueye, M. Tiefenback, C. Yan, Hall C Beam Energy Measurement, Internal CEBAF Document, (1996).

[100] M. Miller, private communication.

[101] S. I. Nagornyĭ, private communication.

[102] R. J. Holt *et. al.*, TJNAF Proposal PR-96-003, (1996).

[103] R. Gilman, R. J. Holt, Z. E. Meziani, CEBAF Proposal PR-99-008, (1999).

[104] R. Gilman, R. J. Holt, Z. E. Meziani, CEBAF Proposal PR-89-019, (1989).

[105] S. A. Wood, CEBAF Proposal PR-91-018, (1991).

[106] G. Niculescu, Resonant Cavities Used as Beam Current Monitors, Internal CEBAF Report.

[107] C. Armstrong, Beam Current Measurement in Hall C, Internal CEBAF Report.

[108] C. Piller, Internal CEBAF Communication, (1995).

[109] Gigatronics 8542 Power Meter Manual, Giga-tronics Inc.

[110] K. B. Unser, CERN SL/91-42 (BI) (1992).

[111] CRC Handbook of Tables for Applied Engineering Science, p. 118. (CRC Press: Boca Raton, FL), (1987).

Vita

Christopher Waldemar Bochna was born in Passaic, New Jersey on August 21, 1970 to Stefan and Jadwiga Bochna. He picked up his first book on physics from the school library in the second grade and his career progressed from there. He received a Bachelor of Science (B.S.) degree with University Honors in the field of Physics/Computer Science Track from Carnegie-Mellon University in May, 1992. He also received a Master of Science (M.S.) degree from the University of Illinois Urbana-Champaign in 1993. He won the Merck Fellowship in 1991, and was chosen as an Andrew Carnegie Society Presidential Scholar in 1992 while at Carnegie-Mellon. At the University of Illinois, he qualified for a University Fellowship in 1992 and won the Felix T. Adler Fellowship in 1999.

Publications:

Quasifree (e, e'p) Reactions and Proton Propagation in Nuclei, D. Abbott, *et. al.*, Phys. Rev. Lett. **80**, 5072 (1998).

Measurements of Deuteron Photodisintegration up to 4.0 GeV, C. Bochna, *et. al.*, Phys. Rev. Lett. **81**, 4576 (1998).

Inclusive Electron-Nucleus Scattering at Large Momentum Transfer, J. Arrington, *et. al.*, Phys. Rev. Lett. **82**, 2056 (1999).

Coherent π^0 Photoproduction on the Deuteron up to 4 GeV, D. G. Meekins, *et. al.*, submitted for publication.

Evidence for Valence Quark-Hadron Duality, I. Niculescu, *et. al.*, in preparation.

Experimental Verification of Quark-Hadron Duality, I. Niculescu, *et. al.*, in preperation.

Talks Presented:

Absolute Beam Current Monitoring in Endstation C, 1995 Joint April Meeting of the American Physical Society and American Association of Physics Teachers, April 1995.

Deuteron Photodisintegration up to 4 GeV, Sixth Conference on the Intersections of Nuclear and Particle Physics, May 1997.